Quantification of aleatory and epistemic uncertainties in the prediction of aeroelastic instabilities

Christian Thomas Nitschke

THÈSE DE DOCTORAT
DE SORBONNE UNIVERSITÉ

Spécialité : Mécanique

École doctorale : "Sciences Mécaniques, Acoustique, Électronique, Robotique SMAER 391"

réalisée

à l'Institut Jean le Rond ∂'Alembert

présentée par

Christian Thomas Nitschke

pour obtenir le grade de :

DOCTEUR DE SORBONNE UNIVERSITÉ

Sujet de la thèse :

Quantification d'incertitudes aléatoires et épistémiques dans la prédiction d'instabilités aéroélastiques

soutenue le 1er février 2018

devant le jury composé de :

M.	Christophe CORRE	Rapporteur
M.	Christian GOGU	Rapporteur
Mme	Paola CINNELLA	Examinatrice
M.	Rodolphe LE RICHE	Examinateur
M.	Corrado MAURINI	Examinateur
M.	Fabrice POIRION	Examinateur
M.	Jean-Camille CHASSAING	Directeur de thèse
Mme	Angela VINCENTI	Co-directrice de thèse

Acknowledgements

After more than three years of hard work, I would like to thank the many people who have made this work possible, better or at least more pleasant.

First, I would like to thank my supervisors Jean-Camille Chassaing and Angela Vincenti, who discovered and shaped the subject and supported me all the way through my work. I would like to thank them for the help they gave me when I had questions and the numerous discussions that were very fruitful, their patience with me when I was stuck, misunderstood them or things did not go as intended, and generally the time I spent working with them.

I also would like to express my gratitude for the members of my jury, who agreed to evaluate my work. This is especially important as they were asked on a very short notice, and the time of the evaluation of my thesis fell into the very busy time of the end of the year. With the multiple domains included, the thesis moreover certainly was not an easy read, which is why I am thankful to the jury as not everyone would have had the courage to assess it.

Important thanks go to the École Doctorale 391, who granted me a scholarship for my thesis and made this work possible. I also have to thank their team for closely watching the respect of best practices and measures to open my horizon alongside the thesis, which definitely enriched my experience.

Of course, I would also like to thank the Institut Jean le Rond d'Alembert led by Professor Stéphane Zaleski, who welcomed me during the more than three years and which provided the environment for my work. I especially would to thank the administrative team of the laboratory, where I notably want to mention Anne Marchal, who was the secretary of my working group during most of my time at the laboratory and who helped me to get through the forests of paperwork associated with the thesis, conferences etc., but also Simona Otarasanu, who also helped me with some administrative problems and who, moreover, was very engaged to create a good spirit in the institute, and Olivier Labbey, the always helpful site manager. At this point, I also have to mention my colleagues and fellow students, with whom I had a great time, who were open-minded, who never hestitated to help and among whom I have made many friends.

My friends - they were the important part who reminded me of the very necessity that there is life outside of the lab and beyond the equations. I would like to thank them for the many, many great moments I spent with them when I was not in front of my screen,

which were either fun or deep, wild or calm, inspired me and made my life so much richer during the time of the thesis and beyond.

Last but not least, I would like to thank my parents for their support - despite their amazement about my choice of profession and subjects of study, they encouraged me to carry on and helped me through all the difficult times I encountered during the thesis, were patient with me when I hang over during the holidays spent with them and helped me out in my life outside the thesis when I needed it. Thank you !

List of Figures

List of Tables

Acronyms

PAPA Pitch And Plunge Airfoil

LCO Limit Cycle Oscillations

CLPT Classical Laminated Plate Theory

pdf Probability Density Function

cdf Cumulative Density Function

MLP MultiLayer Perceptron

SVM Support Vector Machine

PCE Polynomial Chaos Expansion

gPC Generalised Polynomial Chaos

ME-gPC MultiElement-Generalised Polynomial Chaos

aPC Arbitrary Polynomial Chaos

FEM Finite Element Method

RANS Reynolds-Averaged Navier Stokes

DLM Doublet Lattice Method

VLM Vortex Lattice Method

UVLM Unsteady Vortex Lattice Method

BMA Bayesian Model Averaging

MLE Maximum Likelihood Estimation

MC Monte Carlo

MCMC Markov Chain Monte Carlo

Nomenclature

α	Angle of attack
$\delta\alpha$	Virtual angular displacement in α
δW	Virtual work of the virtual displacements
δw	Virtual displacement in z direction
$\mathbb{A}$	CLPT membrane stiffness tensor
$\mathbb{B}$	CLPT membrane-bending coupling tensor
$\mathbb{D}$	CLPT bending matrix tensor
$\mathbb{Q}$	CLPT base layer stiffness tensor
$\mathbf{0}$	Zero matrix
$\mathbf{A}$	CLPT membrane stiffness matrix in Voigt notation
$\mathbf{B}$	CLPT membrane-bending coupling matrix in Voigt notation
$\mathbf{D}$	CLPT bending stiffness matrix in Voigt notation
$\mathbf{I}$	Unity matrix
$\mathbf{Q}$	CLPT base layer stiffness matrix in Voigt notation
μ	Mass ratio $\frac{m}{\pi\rho_a b^2}$
ω	Natural angular frequency
ω_α	Natural angular frequency for degree of freedom in α
ω_z	Natural frequency for degree of freedom in z
$\overline{\omega}$	Nondimensional structural frequency parameter $\frac{\omega_z}{\omega_\alpha}$
ρ	Density of the plate material
ρ_a	Air density
τ	Nondimensional time $\frac{V}{b}t$
ζ_α	Damping ratio for degree of freedom in α

ζ_z	Damping ratio for degree of freedom in z
b	Half chord of the wing
c	Chord of the wing
d_α	Rotational damping about the elastic axis in α
d_z	Damping in z direction
h	Total thickness of the plate
I_α	Rotational mass moment of inertia about the elastic axis
k	Reduced frequency $\frac{\omega b}{V}$
k_α	Rotational spring stiffness in α
k_z	Spring stiffness in z direction
L	Aerodynamic lift at the aerodynamic centre (a quarter of the chord from the leading edge)
M	Aerodynamic moment
m	Mass of the wing
r_α	Nondimensional gyration radius $\sqrt{\frac{I_\alpha}{mb^2}}$ (reference length scale is b)
S	Half span of the wing
T	Kinetic energy
t_p	Ply thickness
U	Potential energy
u	Displacement in direction of x
V	Airspeed
v	Displacement in direction of y
V^*	Nondimensional speed index $\frac{V}{b\omega_\alpha}$
V_f	Critical flutter velocity
V_f^*	Nondimensional flutter speed index
w	Displacement in direction of z
w	Displacement in vertical direction
x_α	Nondimensional static imbalance; distance between the centre of gravity and the elastic axis divided by b

Publications

Journal Articles

[1] C. Nitschke, P. Cinnella, D. Lucor, and J.-C. Chassaing. Model-form and predictive uncertainty quantification in linear aeroelasticity. *Journal of Fluids and Structures*, 73:137–161, August 2017. ISSN 08899746. doi: 10.1016/j.jfluidstructs.2017.05.007.

Conference talks

[1] C. Nitschke A. Vincenti, J-C Chassaing, Uncertainty quantification in the vicinity of mode switches in the flutter response of a composite cantilevered wing, International Forum on Aeroelasticity and Structural Dynamics, IFASD 2017, 25-28 June, Como, Italy, 2017

[2] C. Nitschke, J.-C. Chassaing, Acceleration of Bayesian calibration for predictive uncertainty quantification in aeroelastic flutter, ECCOMAS Congress, June 5-10, Creete, Greece, 2016

[3] C. Nitschke, J. Maruani, A. Vincenti, J.-C. Chassaing, D. Lucor, Influence of elastic coupling and anisotropy on uncertainty quantification in the aeroelastic response of idealized composite wings ,ICCS18, 15-18 June , Lisbon, Portugal, 2015

[4] C. Nitschke, J. Maruani, A. Vincenti, D. Lucor, and J.-C. Chassaing. UNCERTAINTY QUANTIFICATION IN AEROELASTIC RESPONSE OF AN IDEALIZED COMPOSITE WING. In *International Forum on Aeroelasticity and Structural Dynamics*, volume 2, pages 970–983, Moscow, Russia, 2016. Central Aerohydrodynamic Institute. Presentation held on July 1st, 2015 at IFASD, St. Petersburg, Russia.

[5] C. Nitschke, J.-C. Chassaing, P. Cinnella, D. Lucor, Bayesian calibration and uncertainty analysis for airfoil flutter predictions, UNCECOMP 2015, 25 - 27 May, Crete Island, Greece, 2015

[6] C. Nitschke, D. Lucor, P. Cinnella, and J.-C. Chassaing. Efficiency improvements in Bayesian analysis of uncertainties in aeroelastic flutter predictions, International workshop on Uncertainty Quantification in CFD, 18 - 20 May, Paris, France, 2015.

Contents

Chapter I

Introduction

Aeroelasticity studies the interaction between aerodynamic and elastic forces on deformable bodies subject to a flow [15, 42]. The whole domain is often described by "Collar's triangle" [42] which symbolises the different interplays between the different forces at work.

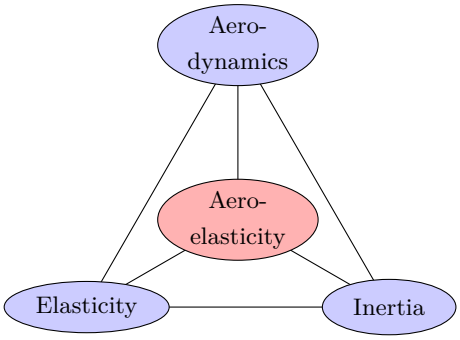

Fig. I.1 *Collar's triangle*

Collar's triangle also includes the inertial forces and consequently includes dynamic aeroelasticity [42]. The edges of the triangle stand for different subproblems that are linked to the phenomena that will be studied in this work. The lower edge represents free vibration problems, a domain which studies the interactions of elasticity and inertia without external influences. On the right edge, mostly flight dynamic phenomena like body freedom flutter [72] can be found [42]. The left edge represents static aeroelasticity, which is mostly about in-flight performance in deformed state as well as control reversal and aeroelastic divergence [55, 146]. The term "aeroelasticity" in the center of the triangle should be called "dynamic aeroelasticity", as it involves inertial forces inherent to movement. In this category, phenomena like buffeting, flutter and limit cycle oscillations are to be found. The present work will mostly study the flutter phenomenon, which is placed in the center of Collar's triangle, although in the given setting, divergence may occur. Although aeroelasticity is also of concern for other domains such as civil engineering and turbomachinery, this work will make reference to problems in aeronautical applications, where it remains a challenge today.

I.1 Motivation: Flutter problems in aeronautics

Despite being studied for a long time, aeroelastic phenomena still represent a major challenge in aeronautic construction [146]. The first systematic study of flutter was performed on the Handley-Page O 400 bomber from World War I, which suffered from tail flutter [146]. Garrick and Reed [44] provide an excellent overview over aeroelastic problems encountered in early aviation. A theoretical approach to the flutter problem was developed by Theodorsen [124]. However, the possibility of study did not prevent further flutter problems to occur. Through to the 1950s, multiple airplane prototypes encountered flutter problems [44]. One of the most spectacular cases is the case of the Lockheed Electra, which suffered two losses of production aircraft due to a phenomenon called "whirl flutter". In the accidents, the aeroelastic modes of the wing became coupled with the modes of the propeller discs due to defects in the mounting of the engine nacelles [18, 19]. Also modern aircraft continue to suffer from aeroelastic problems. One of the most severe, well-known and well-studied examples is the General Dynamics F-16, where the entire wing structure is subject to limit cycle oscillations (LCO) in certain flight regimes due to store configurations (e. g. [46]). In additon to that, edge cases such as stabiliser flutter [73], or fluttering winglets [103] are common. With increased interest in high-flying unmanned aerial vehicles, which often have wings of an extremely high aspect ratio, however, aeroelasticity on wings becomes a new concern. Recent reports of drone crashes suggest that ultimate failure was due to aeroelastic effects [38, 39].

Due to the high failure potential when aeroelastic phenomena occur, there is a strong motivation to determine their nature and their onset. Flutter testing is an important part of aircraft qualification today (e. g. [41]). The onset of aeroelastic phenomena, however, is highly dependent on the underlying parameters and thus very sensitive to uncertainties [13]. Aeronautical structures made of composite materials appearing more and more frequently, the complexity of composite laminate materials and the numerous sources of uncertainties connected to their manufacturing makes the prediction of aeroelastic instabilities even more challenging. At the same time, there is a variety of models for aeroelastic simulation in use, which may require separate parametrisation. The modelling differences also yield deviations in the result for the flutter onset velocity. This is why this work aims at the development of an approach to quantify uncertainties from different sources in order to give robust predictions of the linear flutter velocity.

I.2 Overview of aeroelastic prediction methods

As aeroelastic phenomena can lead to failure of aircraft either through fatigue or immediate runaway of the coupled forces, efforts to calculate them have been important for a long time. Especially the aerodynamic modelling involved, which has to account for the unsteady effects, still represents a great challenge. Early attempts for unsteady aerodynamic modelling to predict the dynamic lift of airfoils based on potential-flow theory are due to Wagner [139], whose work later led to the Theodorsen model [124] which was specifically designed for the modelling of flutter.

With the introduction of computers in aerodynamic calculus, it was possible to deploy discrete models. A method notably used in aeroelasticity is the Doublet Lattice Method (DLM) introduced by Albano and Rodden [2]. Later, vortex-sheet methods were also generalised to unsteady problems, where Murua et al. [92] cites [11, 108] as the beginning, and later articles where similar methods finally appear as Unsteady Vortex Lattice Method (UVLM) [79, 71]. As available computational power increased, the complexity of the flows solved also got more important. In the end of the 1980s, aeroelastic solutions using the transonic small disturbance equation appeared [12]. In the early 1990s the first approaches coupling computational fluid dynamics methods, such as finite volume method computation of Euler and Navier-Stokes flows, and structural models employing the finite element method followed. Schuster et al. [115] used a Reynolds-Averaged Navier Stokes (RANS) aerodynamic code to evaluate the static aeroelastic response of fighter aircraft in the transonic flight regime, while [52] used a finite-difference Euler solver coupled to a finite element model to study the dynamic response of a cantilevered rectangular wing (both found in [67]), [111]. The development went on to more and more complex predictions, so that today, transonic wing LCOs can be simulated using a full FEM wing model and Unsteady RANS (URANS) (e.g. [122]).

While on the high end, phenomena are treated that need investigation using Computational Structural Dynamics (CSD) and Computational Fluid Dynamics (CFD) methods, potential flow modeling is still in use in the domain of aeroelasticity. The DLM and the UVLM methods are often used in design and optimisation (e.g. [120, 17]) although more complex models also come into use for the domain (e.g. [65]). Approximated versions of Theodorsen's theory are used again since [68] showed their usability in control theory. More accurate approximations have been developed until recently, as for example by [20] who provided state-space models for aeroelasticity by using a harmonic balance development. However, due to ever-increasing computational power, the DLM has been used in flutter control recently by [72], who use it for body freedom flutter prediction and control via control surfaces.

The structural models also evolved at the same time. Early aeroelastic studies were limited to wing section models with a limited number of degrees of freedom, as for example in Theodorsen's report [124], which describes calculations for wing section reduced to a flat plate with pitch and plunge motion freedoms, and with a flap that has a rotational degree of freedom. This quickly evolved to wings modelled as a beam [51], which is especially valid for classical wing designs including a spar. Also other structural models like panels (e.g. [32, 3]) and plates (e.g. [31]) which only require simple structural models, were used in aeroelastic computations. Today, mostly finite element models are used to calculate the structural dynamic properties of wings. As it is applicable to a variety of geometries, the finite element method permitted to calculate the dynamic properties of more complex wing configurations. Common model types based on finite elements include for example plates, as used by [5] for demonstration of aeroelastic tailoring of composites. Finite element beam models enjoy popularity for more complex configurations in order to simulate partial or complete airframes. For example, Nayfeh et al. [95] use them to simulate store configurations under a fighter wing. Kotikalpudi et al. [72] employs a beam model to simulate a complete flying wing configuration for a body freedom flutter study. To obtain more realistic models, wing box models find entry into the optimisation domain,

such as in [45], where the sensibility of the aeroelastic behaviour of a wing structure to damage is assessed in a stochastic framework. Shell models are used as an alternative, such as in [122] where they are used to calculate transonic limit cycle oscillations of a high-aspect-ratio wing. In static aeroelasticity, more detailed models up to full, realistic wing structures come into use. A recent example is the study of Yi et al. [151], who optimize a wing structure of a UAV including ribs and spars in an aeroelastic framework.

The increasing use of composite laminated materials in aircraft construction has become another special challenge for the simulation of aeronautical structures. On one hand, these materials have very interesting properties, such as their high strength-to-weight and stiffness-to-weight ratios, but, on the other hand, they are anisotropic. This directional behaviour complicates the design process, but can also be used to control the stiffness properties of the wing to prevent flutter, a method referred to as aeroelastic tailoring. Early studies on the free vibration behaviour [4, 99] led to investigations in aeroelasticity [106, 57], before attempts to actively exploit these properties [142]. Especially, aeroelastic tailoring enables advanced aircraft configurations like forward-swept wings. For this particular purpose, the concept appears in a flight testing proposal by Mourey [91], before Weisshaar uses aeroelastic tailoring for prevention of divergence [142]. Consequently, there is activity in optimisation specific to composite structures with respect to aeroelastic behaviour (e. g. [80]). Composite materials also enable the construction of higher-span wings, which introduces geometric nonlinearities. Afonso et al. [1] give an overview about the broad research activity associated to this problem.

I.3 Uncertainty quantification

The complex interactions that lead to flutter are highly sensitive to uncertainties [13], which is why there is special interest in uncertainty quantification in this area. The recent review [13] cites a number of additional reasons why uncertainty quantification is compelling, one of the most important being the classical 15% safety margin on the airspeed which is required as of the date of the writing of these lines for qualification of airframes (e. g. [41]).

In this work, uncertainties shall be categorised into two types, namely, aleatory and epistemic uncertainties, (e. g. [59], of which the definitions are retained in the following). Epistemic uncertainties are uncertainties that are due to a lack of knowledge. By addition of information, they can thus be reduced. Aleatory uncertainties are due to natural variation and, contrary to epistemic uncertainties, irreducible by addition of knowledge. Although there is some debate if it makes sense to distinguish the two types [70], this distinction will be adopted in the present work.

The perhaps simplest uncertainty quantification method is Monte Carlo simulation (MCS), which consists in drawing random parameters and propagate them through a response function, in this case the aeroelastic solver. It has become feasible with the apparition of reasonably powerful computers and has found application in uncertainty quantification in aeroelasticity, with one of the first examples given by Vaicaitis et al. [129] who used MCS to model pressure fluctuations along a wing. However, Monte Carlo simulations are

computationally costly, which prevents its use in more complex scenarios and which is why surrogate modelling techniques have been developed.

I.3.1 Surrogate modelling

To lower the computational cost, surrogate models have been developed which approximate the stochastic response in place of the original solver. Wang [141] cites several surrogate model techniques, which will be summarised in the following.

Perhaps the oldest surrogate modelling technique is polynomial chaos, which goes back to an article by Wiener [143]. The original approach built surrogates for responses to Gaussian random variables by a spectral expansion using Hermite polynomials, which are orthogonal with respect to normal distributions. The expansion can either be used non-intrusively, using integration techniques, or be directly injected in Galerkin-method-type or finite element solvers. It became popular for stochastic finite elements [47]. In order to be able to use the polynomial chaos approach on non-Gaussian distributions, Xiu and Karniadakis [147] generalised it using the Askey scheme, which gives a set of families of probability distributions with the corresponding orthogonal polynomials. This approach was quickly used for problems in CFD [148] and fluid-structure interactions [149, 83].

A further extension of the method to arbitrary probability measures was described by Soize and Ghanem [118]. Again, the approach quickly found its way into applications in fluid-structure interactions, such as in [144], where stall flutter of turbine blades was investigated. Recently, the arbitrary polynomial chaos was demonstrated to work with correlated variables [94]. Wan and Karniadakis [140] developed the method into a multi-element approach, improving the performance of the method for scenarios with strong gradients (used for example by Le Meitour et al. [75] in uncertainty quantification on limit cycle oscillations). Blatman and Sudret [16] tried to expand the usability of the method from small to moderate numbers of variables by using sparse grid quadrature. Another approach is to drop variables of insignificant sensitivity, which is for example used by Congedo et al. [26] for shape optimisation of an airfoil in nonclassical flows.

The approaches have been applied to uncertainty quantification on composite wings. Manan and Cooper [84] used polynomial chaos to model uncertainty in the frequency response function of a composite wing with uncertain logitudinal Young's modulus and shear modulus. Scarth et al. [114] quantified the uncertainty in critical flutter velocity due to ply angle uncertainty, where the number of dimensions was reduced using lamination parameters [126] and the correlation was treated using a Rosenblatt decomposition. To avoid a high number of parameters, the study was restricted to laminates without membrane-bending coupling, which introduces an artificial symmetrisation of the layup. Moreover, it assumes plies identical in base material and thickness. An alternative approach to the lamination parameters is the polar method, which was first developed by Verchery [138] and reformulated later by Vannucci [133]. The polar method directly works on stiffness tensors, which allows to circumvent the restriction of the lamination parameters.

Collocation methods appeared later in the uncertainty context [60]. The most common

form was developed by [86] for the purpose of uncertainty quantification in CFD and demonstrated on a Riemann problem. The stochastic collocation method uses Lagrange polynomials at defined points, the so-called collocation points, to interpolate the stochastic response. Sparse grids were introduced by [150, 98]. Witteveen and Iaccarino [145] presented a multi-element approach for stochastic collocation based on simplex elements, already with the motivation to solve the problem of correlated variables. An alternative formulation for treating correlated variables in collocation without the need for a multi-element approach was later developed byNavarro Jimenez et al. [93]. Edeling et al. [36] brought sparse grids to multi-element approaches to enable the treatment of higher-dimensional problems.

Both stochastic collocation and polynomial chaos expansions suffer from the curse of dimensionality because of dependence on cubature. Several approaches to provide relief from this problem. Doostan and Iaccarino [29] aim to replace the quadrature rules with optimised versions of least-squares approximation. Another approch tries to improve sparse-grid rules [131], from which both methods would benefit.

Other non-intrusive technologies in use for uncertainty quantification include Kriging [33], mixed forms of polynomial methods and Kriging [25], Karhunen-Loève decompositions [47] and different types of chaos expansions like for example Fourier chaos expansions [87] (found in [13]) or Wiener-Haar expansions [74, 105]. A new approach aiming directly at the curse-of-dimensionality problem are non-intrusive low-rank separation techniques [30].

I.4 Quantification of epistemic uncertainties

Stochastic inverse problems have been solved in structural mechanics for a long time, Bayesian updating being one of the first techniques employed (e. g. [24]). In the beginning, the distributions were calculated using approximations (e.g. [8]). Full Markov-Chain Monte Carlo techniques came up with more computational power available [10, 7]. Since, authors have tried to reduce computational cost of bayesian methods. In order to improve the efficiency of the sampling in an effort to update coefficients in the computational model of a building Cheung and Beck [22] employed hybrid Monte Carlo. Marzouk et al. [85] used polynomial chaos on the prior distribution in a contaminant source identification problem. Gogu et al. [48] used fitted polynomial models in a study on elastic properties of orthotropic plates from free vibration data. Later, Gogu et al. [50] employed a reduced-order model for the same purpose, where interferometry data was used. Congedo et al. [27] used polynomial chaos in a backwards uncertainty propagation for the prediction of shockwaves. In order to adapt a polynomial chaos model to the posterior in Bayesian inference, making the approximation more efficient, Birolleau et al. [14] proposedan iterative technique.

Cheung et al. [23] applied that methodology to turbulence modelling, bringing it to the CFD domain. Edeling et al. [34] performed Bayesian Model Averaging (BMA) [56], where the averaging was also performed between different scenarios. In aeroelasticity, Riley [109] finally performed BMA on a set of aeroelastic models, alongside a simpler adjustment

factors approach, but without model updating.

From a mathematical point of view, epistemic uncertainty gets reduced by experimental data in the Bayesian framework. However, the experiments are rarely free from uncertainties of the underlying physical parameters, which are due to manufacturing errors or measurement errors and consequently of aleatory nature. The two types of uncertainties have thus to be treated at the same time. Jakeman et al. [61] solved the problem for discrete aleatory uncertainty by drawing realisations of the aleatory variables and sampling the Cumulative Distribution Function (CDF) of the other variables for each of the realisations, which is essentially the same mechanism as proposed by Eldred et al. [37]. However, other authors (e. g. Oden et al. [100]) argue that in the Bayesian framework, the two uncertainties need not to be treated differently.

I.5 Thesis layout

This work aims at quantifying several uncertainties occuring in aeroelastic problems.

In the second chapter, the different aeroelastic modelling approaches that are used in the thesis will be presented. For simplicity and to permit Monte Carlo simulations within reasonable computation time, the choice of aeroelastic models is limited to common potential flow-based methods for incompressible flows. Energy methods will be used to provide a common framework for Pitch and Plunge Airfoil (PAPA) and plate wings despite the different structures.

In the third chapter, propagation of uncertainties in the composite materials and the study of their effect on the critical flutter velocity of a straight rectangular composite wing will be performed. A preliminary deterministic parametric study will be carried out in the domain of orthotropic laminates. Both uncertainties in ply angles and ply thicknesses will be applied. In order to reduce the number of uncertain parameters, like in [96], the polar method will be used. The individual effects of ply angle and ply thickness uncertainties on the critical flutter velocity will be examined separately, and later on the response to the combination of the two uncertainties will be studied. Finally, the uncertainty quantification will be accelerated by using an arbitrary polynomial chaos surrogate in order to handle the correlation between the polar parameters serving as uncertain entry variables. Eventual discontinuities in the random space will be treated by splitting the domain in smooth partitions by machine learning and applying separate surrogates on the different parts.

The fourth chapter will be dedicated to epistemic uncertainty regarding the modelling choices. The first model studied is a quasi-steady approach by Wright and Cooper [146] already used in the forward uncertainty quantification in chapter III. Furthermore, a consolidated stochastic version of the approximations to Theodorsen's model [20] will be used in the study. Both models will be applied to a PAPA model and calibrated with the help of the original validation data from [124]. Bayesian Model Averaging (BMA) will be performed to compare the two models.

In the fifth chapter, the uncertainty studies laid out in the previous chapters will be

brought together in a combined study. First, the models will be applied to a composite plate wing and calibrated with the materials considered deterministic. Data from a flutter experiment from Hollowell and Dugundji [58] will be used for calibration. In a second step, the aleatory uncertainty from chapter three will be added to the problem. The combined study will be refined by adding data from a free vibration experiment also from [58] and the PAPA experimental data from the fourth chapter.

The last chapter will present the conclusions drawn from this work, and discuss its perspectives.

Finally, the appendices will give some numerical details and auxiliary studies in addition to the main work of the thesis. Appendix A will give details on the mathematical development of the Rayleigh-Ritz system matrices used in the aeroelastic solvers. Appendix B will provide some validation cases and convergence studies for the aPC method used in the third chapter. Finally, Appendix C gives details to a Bayesian calibration of material parameters using free vibration data, which is later incorporated into a combined study in chapter five.

Chapter II

Aeroelasticity for incompressible flows

In this chapter, the aeroelastic models are described as they will be used later on in this work for the uncertainty quantification studies. To be able to validate accelerated techniques with the help of Monte Carlo simulations, the study is restricted to traditional aeroelastic problems, that is, flutter of typical airfoil sections and cantilevered plates.

All the models in this framework are based on the Rayleigh-Ritz formalism. The equations of motion are derived from the Lagrange equation [117]

$$\frac{d}{dt}\frac{\partial T}{\partial \dot{\mathbf{q}}} - \frac{\partial T}{\partial \mathbf{q}} + \frac{\partial U}{\partial \mathbf{q}} = \frac{\partial(\delta W)}{\partial\,(\delta \mathbf{q})} \tag{II.1}$$

where T is the kinetic energy, U is the potential energy and δW is the virtual work of the non-conservative forces. The vector of generalised coordinates is denoted by $\mathbf{q}$. While the kinetic and potential energy are associated to the structure, the aerodynamic terms are part of the non-conservative forces and go into the virtual work. The Lagrange equation sets the common framework. However, the terms of the equation II.1 have to be expressed in a different manner following the different models, which largely depend on the type of the structure. All the aerodynamic models in this framework are based on incompressible potential flow theory.

II.1 Pitch And Plunge Airfoil problems

The most simple example problem which permits the study of aeroelastic phenomena is an airfoil section model with two degrees of freedom, namely pitch and plunge motion. This is why this canonical problem is often abbreviated as Pitch And Plunge Airfoil (PAPA). Despite its relative simplicity, the PAPA model is capable of demonstrating aeroelastic phenomena such as divergence, limit cycle oscillations and flutter [78].

The Figure II.1 shows an example of a typical scheme of a PAPA aeroelastic model.

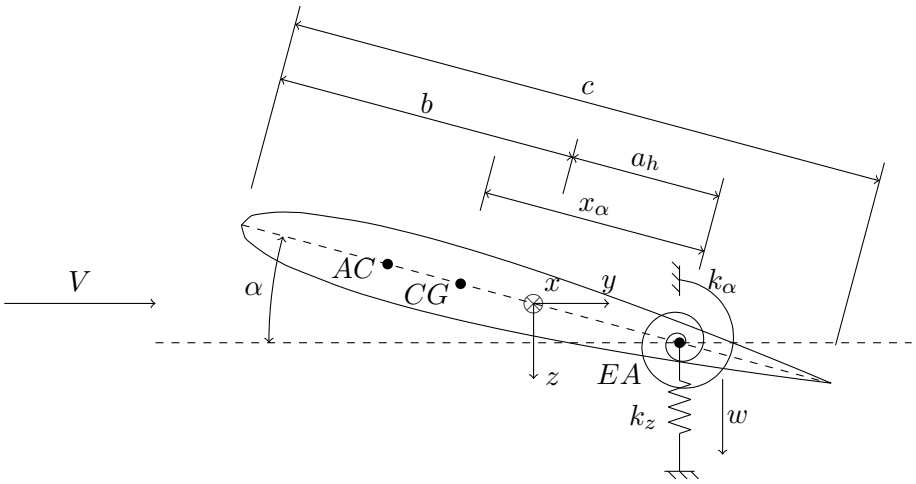

Fig. II.1 *Scheme of a typical wing section in a Pitch And Plunge Airfoil. The two degrees of freedom are the vertical displacement of the elastic axis w and the pitch angle α.*

The kinetic energy T of this aeroelastic configuration is expressed with respect to the center of gravity as [55]

$$T = \frac{1}{2}m\left(\dot{w}^2 + 2bx_\alpha\dot{w}\dot{\alpha}\right) + \frac{1}{2}I_\alpha\dot{\alpha}^2 \tag{II.2}$$

where w is the displacement of the elastic axis in z direction and α is the angular displacement, which coincides with the angle of attack in the scheme of Figure II.1. Coefficient b denotes the half chord. Coefficient x_α is the adimensional distance between the centre of gravity and the elastic axis, also called the nondimensional static imbalance, and is positive towards the rear of the wing section. Finally, m is the mass of the wing, and I_α is the rotational moment of inertia about the elastic axis.

The potential energy U due to the elastic forces is given by [55]

$$U = \frac{1}{2}k_z w^2 + \frac{1}{2}k_\alpha\alpha^2 \tag{II.3}$$

where k_z and k_α denote the spring stiffnesses in the plunge and pitch degrees of freedom, respectively.

The virtual work of the non-conservative forces contains the aerodynamic forces and the damping effects

$$\delta W = L(-\delta w) + M\delta\alpha + d_z\dot{w}(-\delta w) + d_\alpha\dot{\alpha}(-\delta\alpha) \tag{II.4}$$

The constants d_z and d_α are the corresponding damping coefficients. As frequently done in the aeroelastic analysis of PAPA models [15], the airfoil is modelled as a flat plate. Consequently, the aerodynamic centre is always assumed to be at a quarter of the chord, measured from the leading edge. The aerodynamic lift and moment are noted L and M.

Injecting Equations (II.2)-(II.4) into Equation (II.1), the equation of motion is obtained

$$m\ddot{w} + mbx_\alpha\ddot{\alpha} + k_z w = -L - d_z\dot{w} \tag{II.5}$$
$$I_\alpha\ddot{\alpha} + mbx_\alpha\ddot{w} + k_\alpha\alpha = M - d_\alpha\dot{\alpha} \tag{II.6}$$

These equations are rendered dimensionless by dividing through mb in case of the plunge displacement and through mb^2 in the case of the equation II.6 in pitch

$$\frac{\ddot{w}}{b} + x_\alpha\ddot{\alpha} + \omega_z^2\frac{w}{b} = -\frac{L}{mb} - 2\zeta_z\omega_z\frac{\dot{w}}{b} \tag{II.7}$$
$$r_\alpha^2\ddot{\alpha} + x_\alpha\frac{\ddot{w}}{b} + r_\alpha^2\omega_\alpha^2\alpha = \frac{M}{mb^2} - 2\zeta_\alpha r_\alpha^2\omega_\alpha\dot{\alpha} \tag{II.8}$$

This removes the dimensions from the equation, so that the effects of the stiffness now appear in terms of the natural angular frequencies in pitch and plunge ω_α and ω_z. Moreover, the nondimensional gyration radius $r_\alpha = \sqrt{\frac{I_\alpha}{mb^2}}$ emerges, of which the reference length scale is the half chord b.

These equations can be written in matricial form

$$\underbrace{\begin{bmatrix} 1 & x_\alpha \\ x_\alpha & r_\alpha^2 \end{bmatrix}}_{\text{Mass matrix } \mathbf{M}} \begin{bmatrix} \frac{\ddot{w}}{b} \\ \ddot{\alpha} \end{bmatrix} + \underbrace{\begin{bmatrix} \omega_z^2 & 0 \\ 0 & r_\alpha^2\omega_\alpha^2 \end{bmatrix}}_{\text{Stiffness matrix } \mathbf{K}} \begin{bmatrix} \frac{w}{b} \\ \alpha \end{bmatrix} = \begin{bmatrix} -\frac{L}{mb} \\ \frac{M_\alpha}{mb^2} \end{bmatrix} - \underbrace{\begin{bmatrix} 2\zeta_z\omega_z & 0 \\ 0 & 2\zeta_\alpha r_\alpha^2\omega_\alpha \end{bmatrix}}_{\text{Damping matrix } \mathbf{D}} \begin{bmatrix} \frac{\dot{w}}{b} \\ \dot{\alpha} \end{bmatrix} \tag{II.9}$$

Note that there is not yet an explicit expression for the terms L and M of the aerodynamic lift and moment. Despite computers being powerful enough to compute these terms using Unsteady Reynolds-Averaged Navier-Stokes models, modelling based on potential flow is still common and widely used in research, especially in the framework of uncertainty quantification [13]. As breaking potential flow models down to linear systems is analytical, this has the advantage of being very rapid. They are thus well-suited for use in applications needing a high number of computations such as optimisation and stochastic analysis. Two common modelling approaches based on potential flow, which will be used in this work, are presented in the following.

II.1.1 Wright's quasi-steady approach

The model presented in this section is taken from Wright and Cooper [146]. It is based on an earlier model by Hancock [54], who suggests the use of unsteady derivatives to augment steady potential flow aerodynamics. Wright and Cooper [146] simplify the model so that it is essentially composed of a steady potential flow model, with the plunge motion taken into account by using $\dot{w} \approx V\sin\alpha^* \approx V\alpha^*$ with α^* an effective angle of attack [42], and derivatives $L_{\dot{\alpha}}$ and $M_{\dot{\alpha}}$.

The equations for lift and moment, in dimensional form, are given as [146]

$$L = 2\rho_a\pi bV^2\left(\alpha + \frac{\dot{w}}{V}\right) \tag{II.10}$$
$$M = 2\rho_a V^2 b^2\left[\frac{1}{2}\pi\left(\alpha + \frac{\dot{w}}{V}\right) + M_{\dot{\alpha}}\frac{\dot{\alpha}b}{2V}\right] \tag{II.11}$$

where ρ_a is the density of the air, and V is the airspeed. Expressions (II.10) and (II.11) are written considering that the aerodynamic centre is at a quarter of the chord.

Rewriting equations (II.10)(II.11) in matricial form and dividing by the adimensionalising parameters mb and mb^2, respectively, the nondimensional equations for the lift and moment are then

$$\begin{bmatrix} \frac{-L}{mb} \\ \frac{M}{mb^2} \end{bmatrix} = \underbrace{\frac{2}{\mu}\frac{V^2}{b^2}\begin{bmatrix} 0 & -1 \\ 0 & \left(a_h + \frac{1}{2}\right) \end{bmatrix}\begin{bmatrix} \frac{w}{b} \\ \alpha \end{bmatrix}}_{\text{Aerodynamic "stiffness" matrix } \mathbf{K}_a} + \underbrace{\frac{2}{\mu}\frac{V}{b}\begin{bmatrix} -1 & -\frac{1}{\pi}L_{\dot{\alpha}} \\ \left(a_h + \frac{1}{2}\right) & \frac{1}{2\pi}M_{\dot{\alpha}} \end{bmatrix}}_{\text{Aerodynamic damping matrix } \mathbf{D}_a} \begin{bmatrix} \frac{\dot{w}}{b} \\ \dot{\alpha} \end{bmatrix} \tag{II.12}$$

The additional $\frac{1}{\pi}$ factors before the unsteady derivatives come from the efforts to render the equations dimensionless. The mass ratio is $\mu = \frac{m}{\rho_a \pi b^2}$ and a_h is the distance between the centre of gravity and the midchord, which is taken positive towards the trailing edge.

In their examples as well as some publications [123, 114], Wright and Cooper [146] fix the value of the unsteady derivatives to $L_{\dot{\alpha}} = 0$ and $M_{\dot{\alpha}} = -1.2$. While it is stated that $L_{\dot{\alpha}}$ does not have a big influence and is thus neglected, Wright and Cooper [146] argue that the value of $M_{\dot{\alpha}}$ may depend on the frequency. This raises the question of how general the value for $M_{\dot{\alpha}}$ used in the aforementioned publications is.

Making the common assumption that structural damping is negligible and using Equation (II.12) for the lift and moment, the full system of equations (II.9) can now be written as

$$\mathbf{M}\ddot{\mathbf{q}} + \mathbf{K}\mathbf{q} = \mathbf{D}_a\dot{\mathbf{q}} + \mathbf{K}_a\mathbf{q} \tag{II.13}$$

To solve the system for aeroelastic instabilities, i. e. for the critical velocity at which divergence or flutter occurs, the p method is used [55]. It uses an approach such that

$$\frac{w}{b} = \frac{\overline{w}}{b}\exp(pt) \tag{II.14}$$

$$\alpha = \overline{\alpha}\exp(pt) \tag{II.15}$$

with $p = s\omega_\alpha$ and s is an artificial parameter. The approach taken here deviates from [55] as dimensional time is used instead of the nondimensional time $\tau = \frac{V}{b}t$.

Factoring out ω_α and introducing the nondimensional speed index $V^* = \frac{V}{b\omega_\alpha}$, the aerodynamic stiffness matrix $\mathbf{K}_a$ and the aerodynamic damping matrix $\mathbf{D}_a$ from Equation (II.13) can be rewritten as

$$\mathbf{K_a} = \frac{2\omega_\alpha^2}{\mu}V^{*2}\begin{bmatrix} 0 & -1 \\ 0 & \left(a_h + \frac{1}{2}\right) \end{bmatrix} \tag{II.16}$$

$$\mathbf{D_a} = \frac{2\omega_\alpha^2}{\mu}V^{*2}\begin{bmatrix} -1 & -\frac{1}{\pi}L_{\dot{\alpha}} \\ \left(a_h + \frac{1}{2}\right) & \frac{1}{2\pi}M_{\dot{\alpha}} \end{bmatrix} \tag{II.17}$$

Moreover, inserting Equations (II.14), (II.15) in Equation (II.13), and dividing by ω_α^2

gives

$$s^2 \underbrace{\begin{bmatrix} 1 & x_\alpha \\ x_\alpha & r_\alpha^2 \end{bmatrix}}_{\mathbf{M}} \mathbf{q} + \underbrace{\begin{bmatrix} \overline{\omega}^2 & 0 \\ 0 & r_\alpha^2 \end{bmatrix}}_{\mathbf{K}^*} \mathbf{q} = \underbrace{\frac{2}{\mu} V^{*2} \begin{bmatrix} 0 & -1 \\ 0 & \left(a_h + \frac{1}{2}\right) \end{bmatrix}}_{\mathbf{K}_a^*} \mathbf{q} + s \underbrace{\frac{2}{\mu} V^{*2} \begin{bmatrix} -1 & -\frac{1}{\pi} L_{\dot{\alpha}} \\ \left(a_h + \frac{1}{2}\right) & \frac{1}{2\pi} M_{\dot{\alpha}} \end{bmatrix}}_{\mathbf{D}_a^*} \mathbf{q} \tag{II.18}$$

where , $\mathbf{K}^*$, $\mathbf{K}_a^*$ and $\mathbf{D}_a^*$ are the system matrices with further dimensional parameters removed by dividing by ω_α^2.

The resulting problem is a quadratic eigenvalue problem [125] with eigenvalues s, which can be written in matricial form asas

$$\begin{bmatrix} \mathbf{I} & \mathbf{0} \\ \mathbf{0} & -\mathbf{M}^* \end{bmatrix} s \begin{bmatrix} \mathbf{q} \\ s\mathbf{q} \end{bmatrix} = \begin{bmatrix} \mathbf{0} & \mathbf{I} \\ \mathbf{K}^* - \mathbf{A}^* & \mathbf{B}^* \end{bmatrix} \begin{bmatrix} \mathbf{q} \\ s\mathbf{q} \end{bmatrix} \tag{II.19}$$

which is equivalent to the system given in [146].

The complex conjugate eigenvalues s can be interpreted as [125]

$$s = \frac{-\zeta\omega \pm \imath\omega\sqrt{1-\zeta^2}}{\omega_\alpha} \tag{II.20}$$

where ζ is a nondimensional damping ratio and ω is the frequency of the aeroelastic mode. In the instability limit case, the damping ζ is zero and the eigenvalues consequently become $s = \pm\imath\frac{\omega}{\omega_\alpha}$. For small values of ζ, the eigenvalue s can be shortened to [55]

$$s = \frac{\Gamma \pm \imath\omega}{\omega_\alpha} \tag{II.21}$$

Practically, the flutter speed index V_f^* is solved for by increasing the speed index until the real part Γ of one of the eigenvalues becomes positive. The V_f^* value is then refined by a bisection algorithm, which drives Γ closer to zero. Finally, the frequency value is determined by using the imaginary part of the eigenvalue.

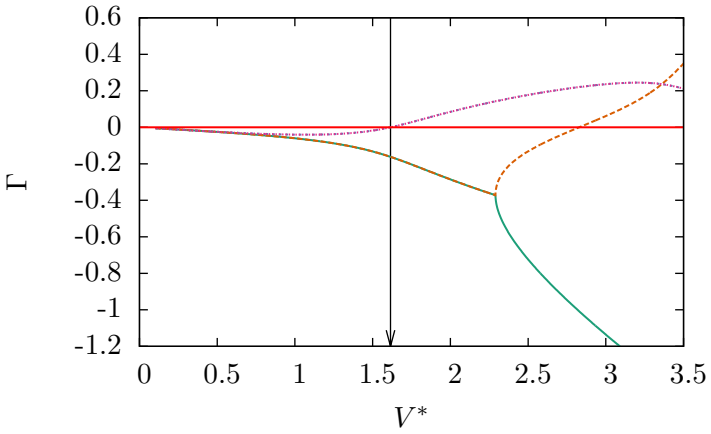

Fig. II.2 *$V-\Gamma$ diagram for the example from [55, p. 123] obtained using the p-method flutter solution and Wright aerodynamics for a PAPA configuration with $\overline{\omega}=0.4, r_\alpha^2=\frac{6}{25}, x_\alpha=0.1, \mu=20, a_h=-0.2$. The magenta line represents the fluttering mode. The nondimensional critical flutter velocity of $V_f^*=1.615$ is given by the black vertical arrow.*

For demonstration purposes, the computation for the example from [55, p. 123] is repeated for the Wright model with $L_{\dot{\alpha}}=0$ and $M_{\dot{\alpha}}=-1.2$, which is the same choice for the parameter values as in [146]. The corresponding velocity-damping diagram, which is often used to graphically demonstrate flutter problems, is given in Figure II.2. The red line indicates the stability limit (i.e. zero damping). The vertical arrow indicates the critical flutter velocity index $V_f^*=1.615$, which is the point where the unstable mode, depicted in the diagram as magenta-coloured dotted line, crosses the zero line.

II.1.2 Theodorsen approach

The quasi-steady approach assumes that the flow follows the wing perfectly at all times. That approximation becomes problematic in the case of a moving wing. In the previous model, the problem was solved by adding unsteady derivative parameters. Another approach consists in modelling wake effects. The work of Wagner [139] was one of the first approaches to calculate the unsteady lift of an airfoil by modelling a wake flow by vortex transport for wings in angular movement. Later, Theodorsen [124] developed a frequential model of unsteady aerodynamic forces for sinusoidal movement in pitch and plunge airfoils. Theodorsen's model can be shown to be equivalent to the Laplace transform of Wagner's when applied to angular motion without aileron only [43, 20].

In this work, only pitch and plunge motion will be considered. The point of departure is again the equation of motion (II.9). The unsteady lift and moment are given by

Theodorsen [124] as

$$L = \rho_a \pi b^2 \left(V\dot{\alpha} + \ddot{w} - b a_h \ddot{\alpha}\right) + 2\pi\rho_a V b C(k)\left[V\alpha + \dot{w} + b\left(\frac{1}{2} - a_h\right)\dot{\alpha}\right] \quad \text{(II.22)}$$

$$\begin{aligned} M &= -\rho_a b^2 \left[\pi\left(\frac{1}{2} - a_h\right) V b\dot{\alpha} + \pi b^2\left(\frac{1}{8} + a_h^2\right)\ddot{\alpha} - a_h \pi b \ddot{w}\right] \\ &\quad + 2\rho_a V b^2 \pi\left(a_h + \frac{1}{2}\right) C(k)\left[V\alpha + \dot{w} + b\left(\frac{1}{2} - a_h\right)\dot{\alpha}\right] \end{aligned} \quad \text{(II.23)}$$

where k is the reduced frequency

$$k = \frac{\omega b}{V} \quad \text{(II.24)}$$

and $C(k)$ is Theodorsen's lift function [124]

$$C(k) = \frac{-J_1(k) + \imath Y_1(k)}{-(J_1(k) + Y_0(k)) + \imath(Y_1(k) - J_0(k))} \quad \text{(II.25)}$$

which is also referred to as "circulation function". The real and imaginary parts of the function Equation (II.25) are plotted in Figure II.3.

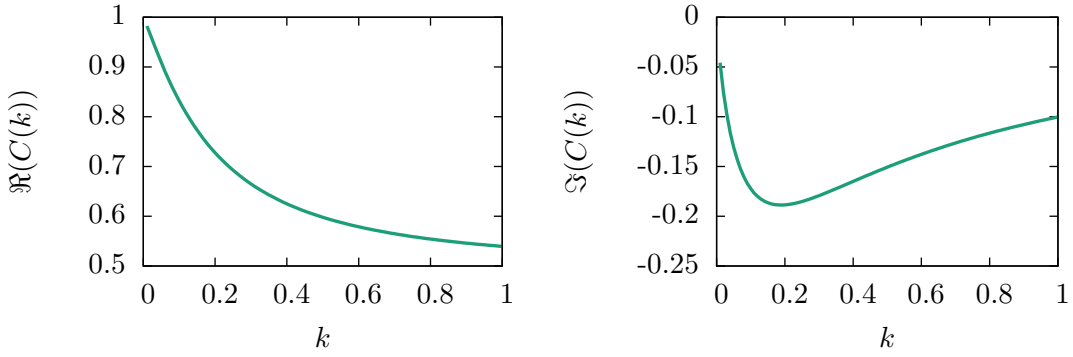

Fig. II.3 *Real and imaginary part of Theodorsen's function [124] plotted over the reduced frequency k*

As before, the lift equation (II.22) is divided by mb and the moment equation (II.23) by mb^2 in order to obtain dimensionless quantities.

$$\frac{L}{mb} = \frac{1}{\mu}\left(\frac{V}{b}\dot{\alpha} + \frac{\ddot{w}}{b} - a_h\ddot{\alpha}\right) + \frac{2}{\mu}\frac{V}{b}C(k)\left[\frac{V}{b}\alpha + \frac{\dot{w}}{b} + \left(\frac{1}{2} - a_h\right)\dot{\alpha}\right] \quad \text{(II.26)}$$

$$\begin{aligned} \frac{M}{mb^2} &= -\frac{1}{\mu}\left[\left(\frac{1}{2} - a_h\right)\frac{V}{b}\dot{\alpha} + \left(\frac{1}{8} + a_h^2\right)\ddot{\alpha} - a_h\frac{\ddot{w}}{b}\right] \\ &\quad + \frac{2}{\mu}\frac{V}{b}\left(a_h + \frac{1}{2}\right)C(k)\left[\frac{V}{b}\alpha + \frac{\dot{w}}{b} + \left(\frac{1}{2} - a_h\right)\dot{\alpha}\right] \end{aligned} \quad \text{(II.27)}$$

are obtained. In matricial form, the aerodynamic operator given by expressions (II.26),(II.27)

with the correct signs can be written in the time domain as

$$\begin{aligned}\begin{bmatrix} -\frac{L}{mb} \\ \frac{M}{mb^2} \end{bmatrix} &= \frac{1}{\mu}\begin{bmatrix} -1 & a_h \\ a_h & -\left(\frac{1}{8}+a_h^2\right) \end{bmatrix}\begin{bmatrix} \frac{\ddot{w}}{b} \\ \ddot{\alpha} \end{bmatrix} \\ &+ \frac{1}{\mu}\begin{bmatrix} -2\frac{V}{b}C(k) & -2\frac{V}{b}\left(\frac{1}{2}-a_h\right)C(k)-\frac{V}{b} \\ 2\frac{V}{b}\left(a_h+\frac{1}{2}\right)C(k) & -\left(\frac{1}{2}-a_h\right)\frac{V}{b}+2\frac{V}{b}\left(a_h+\frac{1}{2}\right)\left(\frac{1}{2}-a_h\right)C(k) \end{bmatrix}\begin{bmatrix} \frac{\dot{w}}{b} \\ \dot{\alpha} \end{bmatrix} \\ &+ \frac{1}{\mu}\begin{bmatrix} 0 & -2\frac{V^2}{b^2}C(k) \\ 0 & 2\frac{V^2}{b^2}\left(a_h+\frac{1}{2}\right)C(k) \end{bmatrix}\begin{bmatrix} \frac{w}{b} \\ \alpha \end{bmatrix}\end{aligned} \tag{II.28}$$

and finally, by using the reduced frequency k, this aerodynamic operator is expressed in the frequency domain as

$$\begin{bmatrix} -\frac{L}{Mb} \\ \frac{M}{Mb^2} \end{bmatrix} = \omega^2 \underbrace{\frac{1}{\mu}\begin{bmatrix} l_h & l_\alpha \\ m_h & m_\alpha \end{bmatrix}}_{\mathbf{A}}\mathbf{q} \tag{II.29}$$

where $\mathbf{q} = \{\frac{w}{b}, \alpha\}^T$ is the vector of the degrees of freedom, and the components of the matrix $\mathbf{A}$ are given as functions of the aeromechanical parameters and the reduced frequency k as

$$l_h = 1 - 2\frac{\imath}{k}C(k) \tag{II.30}$$

$$l_\alpha = -a_h - 2\left(\frac{1}{2}-a_h\right)\frac{\imath}{k}C(k) - \frac{\imath}{k} - 2\frac{1}{k^2}C(k) \tag{II.31}$$

$$m_h = -a_h + 2\left(a_h+\frac{1}{2}\right)\frac{\imath}{k}C(k) \tag{II.32}$$

$$\begin{aligned} m_\alpha = &\left(\frac{1}{8}+a_h\right)^2 - \left(\frac{1}{2}-a_h\right)\frac{\imath}{k} + 2\left(a_h+\frac{1}{2}\right)\left(\frac{1}{2}-a_h\right)\frac{\imath}{k}C(k) \\ &+2\left(a_h+\frac{1}{2}\right)\frac{1}{k^2}C(k)\end{aligned} \tag{II.33}$$

When the complete system of equations shall be resolved, this cannot be done directly by using the p method. The reason for this is that Theodorsen's function depends on the reduced frequency k, which is not given directly in the p method, but is one of the variables the system is solved for. The most simple approach to circumvent this problem is the k method [55] where instead of the airspeed V, the reduced frequency k is the given variable.

Assuming no damping, the equations (II.9) can then be given as

$$\lambda\left[(\mathbf{M}+\mathbf{A})\right]\mathbf{q} = \mathbf{K}^*\mathbf{q} \tag{II.34}$$

where $\mathbf{K}^*$ is the stiffness matrix obtained after dividing by ω_α^2. The eigenvalue λ can be defined as [55]

$$\lambda = (1+\imath g)\frac{\omega^2}{\omega_\alpha^2} \tag{II.35}$$

where g is an artificial damping coefficient. In practice, the flutter problem is thus solved by iterating over k (or its inverse $\frac{1}{k}$ to have linear results in velocity) and searching the root of g. As multiple roots of g can occur, it is useful to first just do iterations and then refine with a higher order method.

An example $V - g$ diagram is given in Figure II.4, where the example from [55] is solved using Theodorsen aerodynamics. Again, the stability limit of $g = 0$ is indicated by the red line. The unstable mode is the mode that is represented by the orange line, as the orange dotted line in Figure II.4 is the line to cross the instability limit at the lowest velocity. The critical flutter velocity at which that happens is $V_f^* = 2.2031$ in this example, which is indicated by the black arrow. This is significantly higher than the prediction of the Wright model.

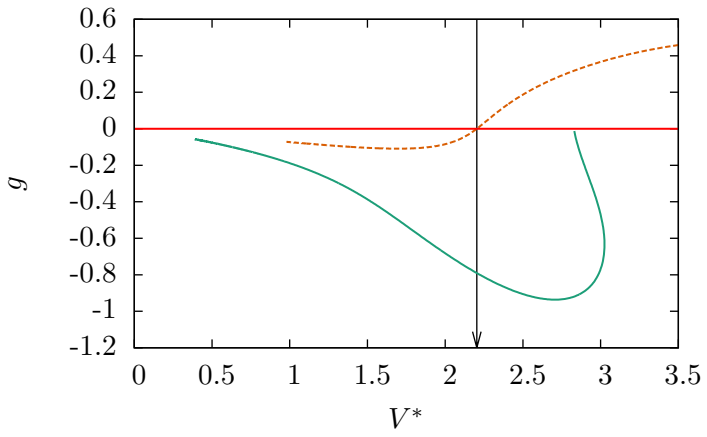

Fig. II.4 *$V - g$ diagram for the example from [55, p. 123] using k-method flutter solution with Theodorsen aerodynamics for a PAPA configuration with $\overline{\omega} = 0.4, r_\alpha^2 = \frac{6}{25}, x_\alpha = 0.1, \mu = 20, a_h = -0.2$. The orange line represents the fluttering mode. The nondimensional critical flutter velocity of $V_f^* = 2.2031$ is given by the black vertical arrow.*

The artificial damping coefficient g is often associated to structural damping.

If structural damping is present, the g term has to be adjusted to account for the positive structural damping present in the system. However, if classical structural damping terms are given, the conversion implies a known frequency, although it is present as an unknown in the above system. The problem can be solved by doing subsequent iterations, taking $g = 0$ as the starting point, determining the frequency and calculating a new candidate for g. This procedure must be repeated until an equilibrium is achieved [55].

II.2 Plate wings

In plate wings, bending and torsion are generally coupled and cannot be considered separately. Instead, the whole surface is in motion without a main axis specified. In addition

to that, where the PAPA aeroelastic models suppose an infinite wing, the plate wing model is finite.

Figure II.5 shows a model of a typical straight plate wing.

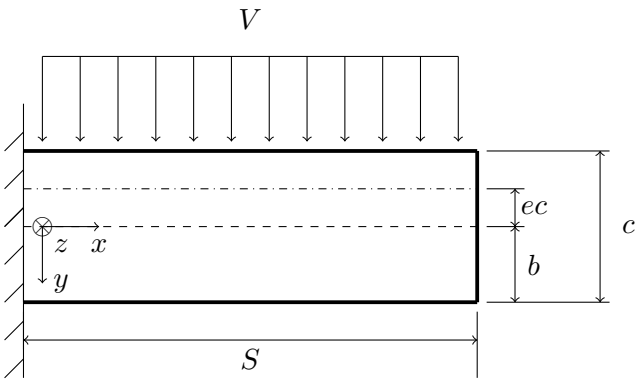

Fig. II.5 *Scheme of the rectangular plate wing model. The plate is clamped at $x = 0$ and subject to an incompressible flow in the y direction*

The excentricity of the lift is indicated by e. As it is assumed in this work that the wings are always flat plates, and potential flow theory is used, the excentricity factor is always $e = 0.25$, so $ec = \frac{1}{2}b$, with b the half chord. Finally, S is the half span of the wing[1]

In order to compute the model, it is assumed that the wing is of homogeneous density. Consequently, the centre of gravity is located at midchord. The midchord axis will be used as a reference axis (x axis represented by the dashed line in Figure II.5), which amounts to setting the parameter a_h to zero.

II.2.1 Rayleigh-Ritz approach

The wing structure is modelled as a Kirchhoff plate. In the following, the plate is considered to be made of a composite laminate, i.e. the stack of oriented orthotropic layers (a more detailed description and definition will be given in section III). In this case, the homogeneous equivalent behaviour of the plate is described by the Classical Laminated Plate Theory (CLPT). In this framework, the relation between the generalised forces and the displacements are given as [121]

$$\begin{bmatrix} \mathbf{n} \\ \mathbf{m} \end{bmatrix} = \begin{bmatrix} \mathbf{A} & \mathbf{B} \\ \mathbf{B} & \mathbf{D} \end{bmatrix} \begin{bmatrix} \boldsymbol{\varepsilon} \\ \boldsymbol{\kappa} \end{bmatrix} \tag{II.36}$$

where $\mathbf{n}$ are the membrane forces, and $\mathbf{m}$ are the bending moments. $\mathbf{A}$ is the in-plane stiffness tensor linking the membrane forces to the membrane strain, $\mathbf{D}$ is the bending stiffness linking the bending moment to the mid-planes' curvature $\boldsymbol{\kappa}$, and $\mathbf{B}$ is a coupling tensor, linking bending moments to membrane strain and membrane forces to curvature.

[1] The span is in aeronautic jargon defined in terms of an entire aircraft and is the measure from wingtip to wingtip. However, in this work, only one wing is considered.

The matrix which is composed of the **A**, **B** and **D** matrix is often referred to as the **ABD** matrix. The membrane strain $\boldsymbol{\epsilon}$ and the curvature $\boldsymbol{\kappa}$ are defined in Voigt's notation as [121, 114]

$$\boldsymbol{\epsilon} = \begin{bmatrix} \frac{\partial u}{\partial x} \\ \frac{\partial v}{\partial y} \\ \frac{\partial u}{\partial y} + \frac{\partial v}{\partial x} \end{bmatrix} \tag{II.37}$$

$$\boldsymbol{\kappa} = \begin{bmatrix} -\frac{\partial^2 w}{\partial x^2} \\ -\frac{\partial^2 w}{\partial y^2} \\ -2\frac{\partial^2 w}{\partial x \partial y} \end{bmatrix} \tag{II.38}$$

When there are no membrane loads ($\mathbf{n} = \mathbf{0}$), the **ABD** equation can be rewritten as [88]

$$\mathbf{m} = (\mathbf{D} - \mathbf{B}\mathbf{A}^{-1}\mathbf{B})\boldsymbol{\kappa} \tag{II.39}$$

which motivates a modified expression for the bending stiffness tensor

$$\tilde{\mathbf{D}} = \mathbf{D} - \mathbf{B}\mathbf{A}^{-1}\mathbf{B} \tag{II.40}$$

Using these expressions, the elastic potential energy can be calculated [4]

$$U = \frac{1}{2}\int\int \mathbf{m}^{\mathsf{T}}\kappa dxdy \tag{II.41}$$

which can be written using Equations (II.39) and (II.40) as

$$U = \frac{1}{2}\int\int \kappa^{\mathsf{T}}\tilde{\mathbf{D}}\kappa dxdy \tag{II.42}$$

The kinetic energy is given by

$$T = \frac{1}{2}\rho d\int\int \dot{w}^2 dxdy \tag{II.43}$$

where ρ is the density of the material and d is the total thickness of the plate.

In the framework of the Rayleigh-Ritz method, an approach is made for shapes of individual modes in the vertical displacement w. Although there are more precise methods like using orthogonal functions [102] , algebraic polynomials are used in this work for the sake of simplicity [107]

$$w(x,y,t) = \sum_{i=1}^{n_x}\sum_{j=1}^{n_y} \overline{w}_{ij}(t)\left(\frac{x}{S}\right)^{j+1}\left(\frac{y}{c}\right)^{j-1} \tag{II.44}$$

where the functions are chosen to respect the boundary conditions of the cantilevered plate (i.e. $w(x=0,y,t)=0$ and $\frac{\partial w}{\partial y}(x=0,y,t)=0$, see Figure II.5) . Finally, the vector of generalised coordinates $\mathbf{q}$ is made up from the time-dependent modal coefficients $\overline{w}_{ij}$. The coefficients themselves are

$$\overline{w}_{ij} = \hat{w}_{ij}\exp(\imath\omega t) \tag{II.45}$$

Inserting these terms into the Lagrange equations (II.1), the mass, stiffness and aerodynamic matrices can be derived using the expressions for kinetic energy, potential energy and the virtual work, and carrying out the derivatives by generalised coordinates, where the latter are the vectors of modal coefficients $\hat{w}_{(ij)}$ where (ij) is a combined index for the modes. The explicit expressions for the system matrices are given in appendix A.

The term of virtual work of the non-conservative forces in the Lagrange equations (II.1) corresponds to the contribution of the aerodynamic actions. It will leads to the aerodynamics matrixes, as it is explained in details in the following section.

II.2.2 Aerodynamic operators

To be able to use the potential flow-based aerodynamic operators already presented in the Pitch And Plunge Airfoil section, several assumptions are necessary.

First of all, the models assume a wing section and are not made for 3D structures like a plate. The most simple assumption is that the plate can be composed of infinitesimally small strips ("strip theory", [146]) to obtain the full lift. The potential flow models demonstrated actually assume that the wing is flat. This in turn means that the aerodynamic centre is located at a quarter of the chord measured from the leading edge. The absence of camber also means that the model does not take into account chord-wise modes and the mode shape assumptions (II.44) are cut off at $n_y = 2$.

Furthermore, the potential flow-based aerodynamic operators calculate the lift based on the angle of attack α, which is derived from the vertical displacement of the plate via a small deformation assumption [123]

$$\alpha \approx \sin(\alpha) = \frac{\partial w}{\partial y} \tag{II.46}$$

Other than PAPAs and beam wings, plate wings do not have a fixed reference axis. It is assumed here that the reference axis corresponds to midchord, which implies $a_h = 0$. Also, here is no common non-dimensionalisation for plate wings, which is why the dimensional expressions are used in this case.

The virtual work of the aerodynamic forces is then

$$\delta W = \int L dx \, (-\delta w) + \int M dx \delta\alpha \tag{II.47}$$

By inserting the expression into the Lagrange equation, the system matrices are recovered. This procedure is described in Appendix A along with their full expressions. The solution methods basically stay the same.

It must be noted that for simulating effects of a finite span, Stodieck et al. [123] multiplies the lift and moment expressions for the Wright operator by a factor of $\left[1 - \left(\frac{x}{S}\right)^3\right]$, except for the unsteady derivative expressions.

For demonstration purposes, the flutter diagram of a plate flutter example for a 1mm-thick steel plate is shown in Figure II.6. The Wright aerodynamic model is used in conjunction

with Stodieck's modification for finite span [123] and a p method solver. $n_x = 8$ modes are used along the span. As many of the dimensionless constants do not apply (for example, there is no ω_α), dimensional values are given.

Note that only a selection of modes is presented. In the upper part of the figure, the velocity-damping diagram is shown. The fluttering mode is depicted by a solid green line, which crosses the instability limit at $V_f = 68.41\,[m/s]$. It becomes stable again at higher velocities , when the green line passes the zero damping line again at values of V over 100 m/s (see Figure II.6.a). The associated frequency can be determined in the diagram of Figure II.6.b, following the solid green line. The flutter frequency is the frequency that occurs for the same mode as the fluttering mode determined in the first diagram, at the same velocity. The eigenvalues of the modes occur in complex conjugate pairs, which is why there is a counterpart of the frequency with a negative value.

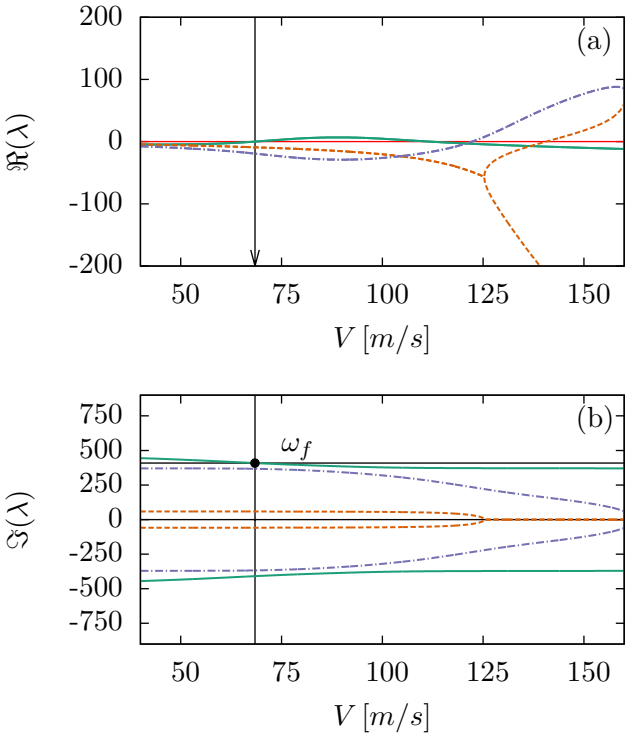

Fig. II.6 *Example $V - \lambda$ diagram for a 1mm-thick steel plate with a span of* $0.3048[m]$ *and a chord of* $0.0762[m]$ *using a p-method solver with Wright aerodynamics and a finite wing approximation [123]. The critical flutter velocity of* $68.41\,[m/s]$ *is indicated by the black vertical bar. In the lower part the flutter frequency of* $408.9\,[rad/s]$ *is given by the horizontal black bar and the black dot.*

Chapter III

Quantification of aleatory uncertainties: composite materials

The stiffness behaviour of aeronautic structures such as wings or stabilisers changes their aeroelastic response. In particular, anisotropic materials can have significant impacts on the critical flutter velocity [106]. Recent years have seen a surge in airframe constructions using composite materials, which are inherently anisotropic. These materials are primarily chosen for their advantageous stiffness- and strength-to-weight ratios, but also offer the possibility of steering the aeroelastic behaviour; a process that is referred to as aeroelastic tailoring [142]. These composite materials are mostly laminates, which means that they consist of layups of several oriented layers which are most commonly orthotropic. The manufacturing process of the final parts introduces many parameters, such as the ply angles and the ply thicknesses, and therefore sources of errors, which influence the anisotropic stiffness of the material and which can be regarded as uncertain.

In this chapter, the influence of deviations in the anisotropy will be examined. To this end, first a general representation method for anisotropic material parameters will be presented with the polar method [138], which will serve for analytical purposes, as well as for a reduction of the number of parameters to be examined. Using this approach, a preliminary deterministic study will be carried out, which will serve to investigate the influence of the anisotropy on the aeroelastic response. The primary focus will be set on the critical flutter velocity of which the concept was introduced in the previous chapter.

Following this analysis, points of interest will be identified in the domain of polar parameters for which layups will be reconstructed. A stochastic analysis of the effects of the manufacturing errors on the aeroelastic response will be performed on these laminates, where the ply angles and the ply thicknesses will serve as examples of manufacturing error.

While the study will be limited to the rather simple solution methods for the flutter problem, Monte Carlo simulation of the deviation still takes a lot of time, which would become a limiting factor for subsequent studies with more advanced aeroelastic solvers. Therefore, a surrogate model is developed to accelerate the stochastic analysis. The aforementioned

polar method will serve in this framework to reduce the number of uncertain variables to just six in order to keep the computational cost for the surrogate model at a reasonable level. The resulting polar parameters are correlated. Moreover, discontinuities are present in the aeroelastic response due to a mode switch. Both of these problems prompt for a special approach, based on arbitrary polynomial chaos and machine learning in this work.

An uncertainty quantification study on uncertain ply angles has already been conducted by [114]. A restriction in the underlying method limited the study to symmetric laminates, which implies neglecting the effects of membrane-bending coupling. As the polar method can be applied to the modified bending stiffness tensor $\tilde{\mathbf{D}}$, in this work, no restriction on the uncertainty such as an artificial symmetrisation of is performed, but the full uncertainty is respected. A study of the resulting differences was given in [96].

III.1 Dimension reduction and analysis: The polar method

In the framework of the plate wing, the stiffness of the material is expressed using the classical laminated plate theory (CLPT). In the CLPT, the membrane, bending and coupling stiffnesses are represented by the so-called ABD-matrix, of which $\mathbf{A}$ is the membrane stiffness, $\mathbf{D}$ the bending stiffness, and $\mathbf{B}$ is a coupling term. Starting form the stiffness tensor of one elementary layer $\mathbf{Q}$, the $\mathbf{A}$,$\mathbf{B}$ and $\mathbf{D}$ tensors are obtained as [121]

$$\mathbf{A} = \sum_k \mathbf{Q}_k (z_k - z_{k-1}) \tag{III.1}$$

$$\mathbf{B} = \frac{1}{2} \sum_k \mathbf{Q}_k (z_k^2 - z_{k-1}^2) \tag{III.2}$$

$$\mathbf{D} = \frac{1}{3} \sum_k \mathbf{Q}_k (z_k^3 - z_{k-1}^3) \tag{III.3}$$

The z_k represent are the positions of the ply limits. The stiffness tensor of the elementary layer has to be rotated appropriately to reflect the orientation of the corresponding layer in the stacking sequence.

In early analysis of anisotropy, the stacking sequence was used directly to analyse the properties of the layup. (e.g. [57, 62]). This is reasonable if the number of plies is limited. However, it becomes quite difficult if the number of plies is large. Tsai and Hahn [126] consequently proposed a representation of anisotropy which groups the cosines and sines of the ply angles, the so-called *lamination parameters*. In comparison to the stiffness tensor, these simplify handling of rotations of the reference frame. They provide more synthetic control over the anisotropy and have consequently been used in design and optimisation problems for laminates [53]. However, the lamination parameters suppose that the plies are identical in ply material and thickness, which limits their usability for the present problem. Moreover, they are defined with respect to the CLPT tensors $\mathbf{A}, \mathbf{B}$ and $\mathbf{D}$, so they cannot be applied directly to the modified bending stiffness $\tilde{\mathbf{D}}$ introduced in Equation (II.40).

For these reasons, the polar method [138, 66] is adopted in this work as a different representation of anisotropic plate behaviour. As it operates directly on 2D stiffness

tensors of any type and order, it is applicable to the modified bending stiffness $\tilde{\mathbf{D}}$ and does not need further hypotheses on the laminate stack such as identical plies. The use of $\tilde{\mathbf{D}}$ also enables it to treat non-symmetric stacks with the polar parameters of only one tensor. In the case of the lamination parameters, the representation of all three stiffness tensors is needed to achieve a full representation of the same material behaviour.

For an arbitrary symmetric positive-definite two-dimensional fourth-order tensor $\mathbb{L}$, the polar decomposition can be described as follows [133]

$$
\begin{aligned}
8T_0 &= L_{xx} - 2L_{xy} + 4L_{ss} + L_{yy} && \text{(III.4)}\\
8T_1 &= L_{xx} + 2L_{xy} + L_{yy} && \text{(III.5)}\\
8R_0 e^{\imath 4\Phi_0} &= L_{xx} + 4\imath L_{xs} - 2L_{xy} - 4L_{ss} - 4\imath L_{ys} + L_{yy} && \text{(III.6)}\\
8R_1 e^{\imath 2\Phi_1} &= L_{xx} + 2\imath L_{xs} + 2\imath L_{ys} - L_{yy} && \text{(III.7)}
\end{aligned}
$$

where $L_{\alpha\beta}$ are the Cartesian components of the Voigt notation $\mathbf{L}$ of tensor $\mathbb{L}$. The indices x and y refer to the axis coordinates, while s stands for *shear*.

The polar method decomposes the stiffness tensor into six polar components: two isotropic components T_0 and T_1, two anisotropic moduli R_0 and R_1 as well as two angles Φ_0 and Φ_1 giving the respective orientations of the anisotropic components [133]. The first four material constants are invariant to the orientation of the reference frame, as well as the difference between the polar angles. These five invariants are the minimum set of constants that represent elastic behaviour. However, the polar angles Φ_0 and Φ_1 individually depend on the orientation of the reference frame.

The cartesian representation of the tensor can be retrieved from the polar components using the following formulas [133]

$$
\begin{aligned}
L_{xx} &= T_0 + 2T_1 + R_0\cos(4\Phi_0) + 4R_1\cos(2\Phi_1) && \text{(III.8)}\\
L_{xy} &= -T_0 + 2T_1 - R_0\cos(4\Phi_0) && \text{(III.9)}\\
L_{xs} &= R_0\sin(4\Phi_0) + 2R_1\sin(2\Phi_1) && \text{(III.10)}\\
L_{yy} &= T_0 + 2T_1 + R_0\cos(4\Phi_0) - 4R_1\cos(2\Phi_1) && \text{(III.11)}\\
L_{ys} &= -R_0\sin(4\Phi_0) + 2R_1\sin(2\Phi_1) && \text{(III.12)}\\
L_{ss} &= T_0 - R_0\cos(4\Phi_0) && \text{(III.13)}
\end{aligned}
$$

An important feature of the polar method is its capacity to reveal material symmetries [133]. The easiest and most obvious case is isotropy, for which the anisotropic components R_0 and R_1 are zero, and consequently the polar angles Φ_0 and Φ_1 are not defined. Square symmetry can be identified in the case where R_1 is zero (which also renders the corresponding polar angle Φ_1 undefined) [133]. Orthotropy manifests in the difference of the polar angles being a multiple of $\frac{\pi}{4}$ [133]. As $\Phi_0 - \Phi_1$ is periodic with $\frac{\pi}{2}$, it is sufficient to distinguish the two cases $\Phi_0 - \Phi_1 = 0$ and $\Phi_0 - \Phi_1 = \frac{\pi}{4}$, so the condition can be summarised as $\Phi_0 - \Phi_1 = K\frac{\pi}{4}$. K is called *orthotropy shape parameter* and can take the values $K = \{0, 1\}$. Moreover, there is a special case of orthotropy in the case where R_0 is equal to zero, in which case the Φ_0 angle is not defined and thus the angular offset criterion does not make sense [132]. It mirrors the case of square symmetry. To reflect

that it is a special case, it is referred to as R_0-orthotropy [132, 133]. A summary of the symmetry conditions is given in Table III.1.

Elastic symmetry	Polar condition	Parameters for full description	Direction of the main orthotropy axis
Isotropy	$R_0 = R_1 = 0$	T_0, T_1	none
Square Symmetry	$R_1 = 0$	T_0, T_1, R_0, Φ_0	Φ_0
R_0-Orthotropy	$R_0 = 0$	T_0, T_1, R_1, Φ_1	Φ_1
Orthotropy	$\Phi_0 - \Phi_1 = K\frac{\pi}{4}, K \in \{0,1\}$	T_0, T_1, $R_K = (-1)^K R_0$, R_1, Φ_1	Φ_1

Table III.1 – Conditions for elastic symmetries in terms of polar invariants [133].

The polar constants cannot take arbitrary values, but are bound to thermodynamic limits (i. e. the stiffness tensor has to be positive-definite), as well as to geometric constraints when dealing with laminate layups. Considering orthotropic laminates made of an orthotropic base material layer, the bounds can be found in [89, 134] as

$$0 \leq R_1 \tag{III.14}$$

$$-R_K^{max} \leq R_K \leq R_K^{max} \tag{III.15}$$

$$2\left(\frac{R_1}{R_1^{max}}\right)^2 - 1 \leq \left(\frac{R_K}{R_K^{max}}\right) \tag{III.16}$$

correspond to the anisotropic polar parameter of a uni-directional laminate of overall thickness h made of the base material layer (for in-plane behaviour: $R_K^{max} = hR_K^{BM}$ and $R_1^{max} = hR_1^{BM}$, whilst for bending behaviour $R_K^{max} = \frac{1}{3}h^3R_K^{BM}$ and $R_1^{max} = \frac{1}{3}h^3R_1^{BM}$)

We remind that, for the case of laminates made of layers of the same base material, the isotropic polar parameters are nominally constant. Thus only anisotropic polar parameters R_K and R_1 can vary with respect to the laminate stacking sequence and their domain of definition is expressed by the thermodynamic and geometric bounds given by Equations (III.14)-(III.16). Thus, the domain in Figure III.1 describes the complete set of admissible orthotropic laminates. Given any possible stacking sequence corresponding to an orthotropic laminate of overall thickness h, its anisotropic polar parameters R_K and R_1 will belong to the domain of Figure III.1. Consequently, this is the domain of study for the analysis and optimisation of composite structures composed of orthotropic materials (see for instance [66]). Particularly, it is used here for the deterministic aeroelastic analysis of a composite plate wing.

The limits of the resulting domain are plotted in Figure III.1, for a given base layer with $K^{BM} = 0$ (which is the case for most common base materials). Assuming identical plies with the same base material and the same ply thickness, the isotropic constants do not depend on the layup. In order to be able to depict the whole orthotropic domain in one piece, the polar module R_0 and the orthotropy shape parameter K are combined in one single parameter $R_K = (-1)^K R_0$, which is now a signed parameter. With this measure, it is possible to describe the whole domain of orthotropic layups with just the parameters R_K and R_1.

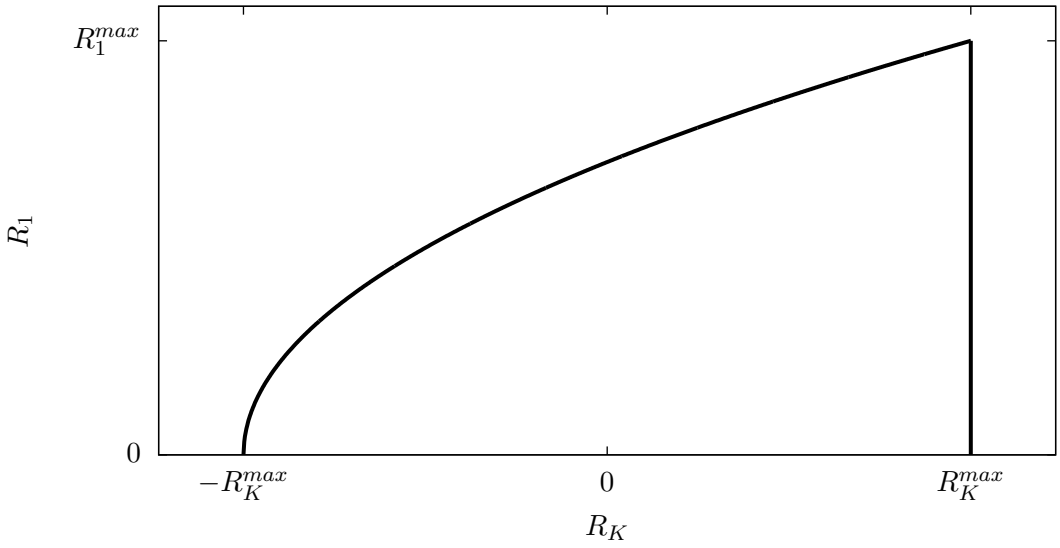

Fig. III.1 *Polar domain for orthotropic laminates in the plane of the anisotropic polar parameters R_K and R_1.*

In this domain, several special configurations of laminates can be directly identified. The right upper corner of the domain corresponds to the unidirectional laminate made of the underlying base material. The right edge of the domain corresponds to cross-ply laminates, while the upper, parabolic edge corresponds to angle-ply laminates. The left, lower edge finally corresponds to a stacking sequence with ply angles of $\pm 45°$.

III.2 Deterministic analysis

In this section, a preliminary deterministic study of the flutter response for a a composite rectangular plate wing will be carried out. This will serve to explore the aeroelastic behaviour of the wing. In particular, it is intended to identify physical phenomena occuring in the parameter space as well as provide information on cases where uncertainty is interesting to study. To this end, the plate wing model given in section II.2 (Figure II.5) is considered in conjunction with Wright aerodynamics (the unsteady derivative coefficient $M_{\dot{\alpha}}$ is set to $M_{\dot{\alpha}} = -1.2$ as in [123, 114]). As in these references, a sixteen-layer composite plate with a half-span of $S = 0.3048$ $[m]$ and a chord of $c = 0.0762$ $[m]$ will be used. In contrast to [114], the air density is adjusted to sea-level and the finite-wing approximation from [123] is used. A summary of the geometric and aeromechanical data is given in Table III.2.

Half-span $S[m]$	Chord $c[m]$	Air density $\rho_a[kg/m^3]$	Unsteady derivative $M_{\dot{\alpha}}$
0.3048	0.0762	1.225	-1.2

Table III.2 – Geometric and aeromechanical parameters for the plate wing depicted in Figure II.5.

All layups in this chapter are nominally uncoupled ($\mathbf{B} = \mathbf{0}$, i.e. $\tilde{\mathbf{D}} = \mathbf{D}$, see section II.2) employing AS4/3502 graphite/epoxy as base material [126, 128]. Table III.3 lists the engineering moduli of this material, along with the assumed ply thickness and density. The corresponding polar parameters, calculated by means of Equations (III.5)-(III.7), are given in Table III.4. It can be noted that this base material is highly anisotropic, as can be deduced from the highly different values of the engineering moduli, and even more clearly by the fact that the anisotropic polar moduli R_K^{BM} and R_1^{BM} are significantly different from zero. The base material is consequently suited to highlight the influence of the anisotropic behaviour of different layups.

$E_1[GPa]$	$E_2[GPa]$	$G_{12}[GPa]$	$\nu_{12}[-]$	$\rho[kg/m^3]$	Ply thickness $t[mm]$
138.0	8.96	7.1	0.3	1600	0.1

Table III.3 – Material properties and ply thickness for the AS4/3502 base layer used for the laminates analysed in this chapter.

$T_0^Q[GPa]$	$T_1^{BM}[GPa]$	$R_0^Q[GPa]$	$R_1^Q[GPa]$	$\Phi_0^Q[^\circ]$	$\Phi_1^Q[^\circ]$
21.35	19.15	14.25	16.23	0	0

Table III.4 – Polar constants for the stiffness tensor fo the AS4/3502 UD layer

As in the linear regime the plate wing is mainly subject to bending loads, the polar constants for a plate made of a sixteen-layer unidirectional layup with the fibres aligned to the half-span axis of the wing can be simply deduced by multiplying the polar constants of the base material given in Table III.4 by the geometric bending inertia of the plate, i.e. $\frac{h^3}{12}$ where $h = 16t$. The resulting unidirectional plate bending polar parameters are given in Table III.5. The anisotropic polar parameters represent the maximum admissible values R_K^{max} and R_1^{max} that appear in the geometric bounds (Equations (III.14)-(III.16)) and they define the admissible domain of all orthotropic sixteen-layer layups made of the AS4/3502 base material, that is depicted in Figure III.2.

$T_0^D[Nm]$	$T_1^D[Nm]$	$R_0^D[Nm]$	$R_1^D[Nm]$	$\Phi_0^D[°]$	$\Phi_1^D[°]$
7.29	6.54	4.86	5.54	0	0

Table III.5 – Bending stiffness polar constants for a unidirectional sixteen-layer laminate made of AS4/3502 base material.

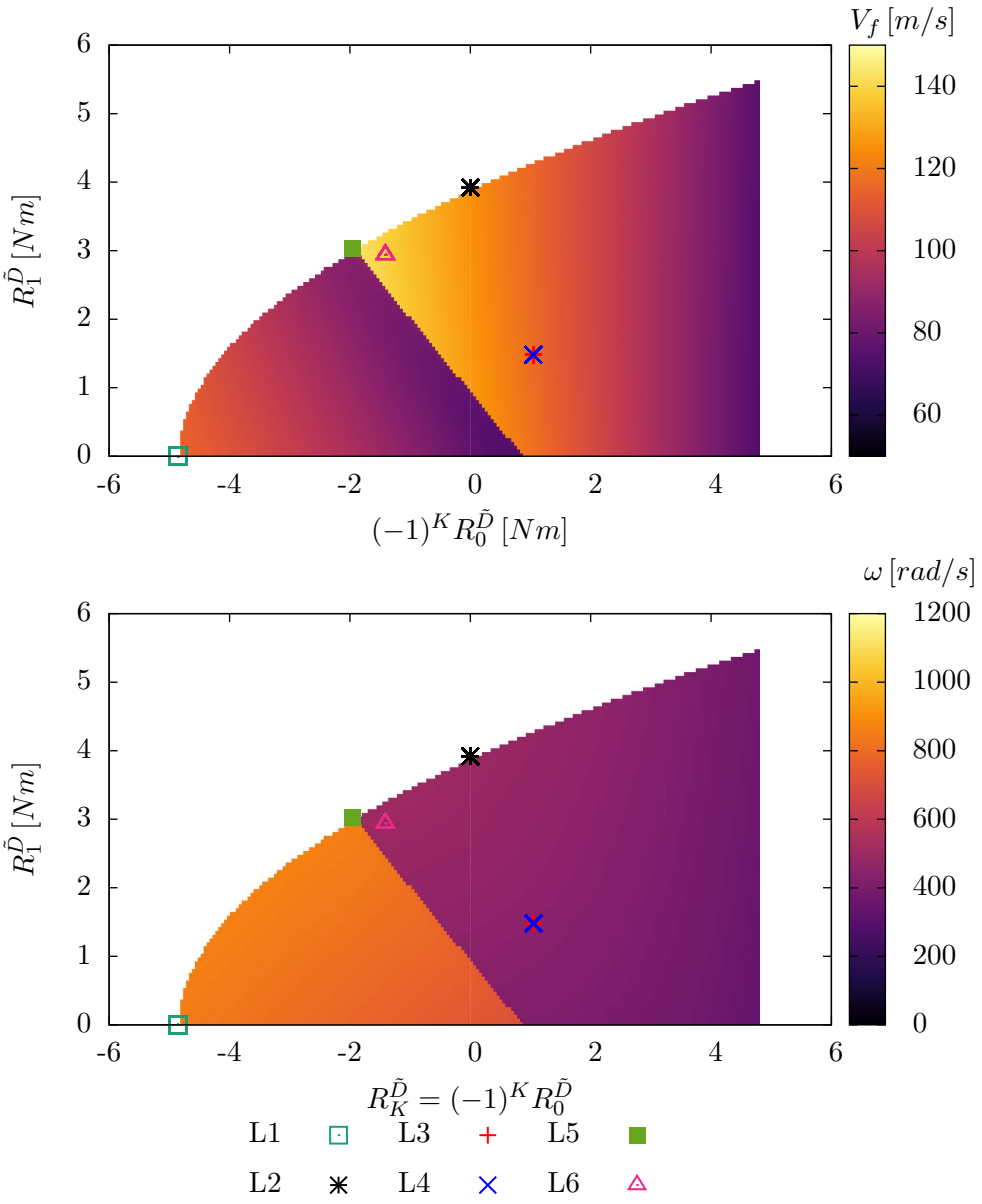

Fig. III.2 *Aeroelastic response surfaces of the critical flutter velocity V_f and the flutter frequency ω_f on the admissible domain for plate wings made of sixteen-layer uncoupled orthotropic laminates made from AS4/3502 (properties: Tables III.4,III.3) with geometry and aeromechanical parameters as in Table III.2*

As nominally uncoupled orthotropic laminates are considered, the isotropic polar constants T_0^D and T_1^D are independent from the layup (i.e. they are constant all over the domain of orthotropic sixteen-layer laminates of Figure III.2) and they are equal to the ones of the unidirectional sixteen-layer layup (see Table III.5). The angle Φ_1 is nominally fixed at zero, which means the principal axis of orthotropy is aligned with the spanwise mid-chord axis. Under these conditions, the parametric study can be limited to only R_K^D and R_1^D, with the geometry and the aeromechanical parameters kept fixed at the values defined in Table III.2. The corresponding response surfaces for the critical flutter velocity and flutter frequency on the resulting admissible domain for orthotropic laminates are given in Figure III.2.

The response surface clearly highlights that it is not sufficient to just maximise the anisotropic stiffness in order to also maximise the critical flutter velocity. Instead, the critical flutter velocity rises, moving from the right side of the domain (i.e. maximum value of R_K^D) towards lower values of R_K^D. The variation with R_1^D is less important, with a small increase in the critical flutter velocity when moving from $R_1^D = 0$ to the upper side of the domain. The maximum value of the critical flutter velocity $V_f^{max} = 148.43[m/s]$ is reached at point L5 (green square dot in Figure III.2.a), which is located on the upper bound of the domain (i.e. maximum admissible value for R_1^D). When moving further left from the maximum point along the upper bound of the domain, the critical flutter velocity drops abruptly to the minimum value over the domain $V_f^{min} = 76.3[m/s]$. When $(-1)^K R_0^D$ decreases further, V_f violently drops. This drop in the critical flutter velocity corresponds to a discontinuity of the response surface of V_f (see Figure III.2.a), which spans over a straight line, described by the equation

$$\begin{bmatrix} R_K^{D,switch} \\ R_1^{D,switch} \end{bmatrix} = \begin{bmatrix} 0.92 \\ 0 \end{bmatrix} + s \begin{bmatrix} -2.87 \\ 3.03 \end{bmatrix}, s \in [0,1] \tag{III.17}$$

On the left side of the discontinuity (i.e. decreasing values of R_K^D), the response surface for V_f is more skewed, with V_f increasing moving from the top to the bottom of the domain (i.e. decreasing values of R_1^D). It must be noticed that the same line of discontinuity is present in the frequency response surface (Figure III.2.b). This is indicating a regime change in the flutter behaviour. Right of the step, the flutter frequency is at about $500[rad/s]$, whereas the frequency rises to about $850[rad/s]$ on the left. Inside these two regimes, the flutter frequencies show much less variability than the critical flutter velocity. This again points to the fact that there are two flutter regimes, and the step is caused by a mode switch.

A number of significative points possesing interesting features are selected from the domain of nominally uncoupled orthotropic laminates of Figure III.2 In order to better explain the physical phenomena related to these aeroelastic response surfaces and to study the influence of uncertainties in a realistic way, the corresponding stacking sequences are reconstructed subsequently. The design rules for the corresponding layups are based on combinatorics and were demonstrated in [135, 136, 130]. The author of this thesis had access to the database resulting from that work.

The points chosen for further studies are indicated by markers in Figure III.2. Their full sets of polar parameters are given in Table III.6 together with the nominal values of the

critical flutter velocity V_f and flutter frequency ω_f. The corresponding stacking sequences are detailed in Table III.7.

Case	$T_0^{\tilde{D}}[Nm]$	$T_1^{\tilde{D}}[Nm]$	$R_K^{\tilde{D}}[Nm]$	$R_1^{\tilde{D}}[Nm]$	$\Phi_0^{\tilde{D}}[°]$	$\Phi_1^{\tilde{D}}[°]$	$V_f\,[m/s]$	$\omega_f\left[\frac{rad}{s}\right]$
L1	7.288	6.538	−4.865	0	0	0	115.46	847.14
L2	7.288	6.538	0	3.916	0	0	125.06	498.82
L3/L4	7.288	6.538	1.048	1.484	0	0	116.26	448.60
L5	7.288	6.538	−1.948	3.032	0	0	143.48	505.24
L6	7.288	6.538	−1.408	2.941	0	0	138.67	499.83

Table III.6 – Polar properties and flutter response of the six configurations chosen on the response surface of Figure III.2. Corresponding stacking sequences are given in Table III.7

Case	Stacking sequence	Property summary
L1	$[45_2, -45_4, 45_2, -45_2, 45_4, -45_2]$	nominally square symmetric ($R_1^{\tilde{D}} = 0$)
L2	$[22.5_2, -22.5_4, 22.5_2, -22.5_2, 22.5_4, -22.5_2]$	nominally R_0-orthotropic ($R_0^{\tilde{D}} = 0$)
L3	$[\pm 66.8, 0, -66.8, 0, 66.8_2, -66.8, 66.8, -66.8_2, 0, 66.8, 0, \pm 66.8]$	general orthotropic, shifted by 90°
L4	$[0, \pm 58.8, 0, -58.8, 0_2, 58.8, 58.8, 0_2, -58.8, 0, \mp 58.8, 0]$	same nominal properties as L3
L5	$[28.4_2, -28.4_4, 28.4_2, -28.4_2, 28.4_4, -28.4_2]$	general orthotropic, $V_{f_{max}}$
L6	$[34, 0, -34_2, \pm 34, 34, 0_2, -34, \pm 34, 34_2, 0, -34]$	general orthotropic

Table III.7 – List of laminates based on AS4/3502 corresponding to selected points on the response surface of Figure III.2

All of the stacking sequences are chosen to exactly correspond to the polar parameters given, that is, to be part of the domain described by the Figure III.2. This means that in their nominal configuration, they are all orthotropic with the main axis of orthotropy aligned with the span-wise mid-chord axis, and $\mathbf{D} = \tilde{\mathbf{D}}$, which means that they are uncoupled (i.e. $B = 0$). It can be noticed that, despite being uncoupled, these layups are not symmetric.

In the following, the choice of the particular points and layups will be motivated further.

- Layups L1 and L2 are chosen because they represent two special cases of elastic symmetries, of which it is expected to identify some effects on the flutter behaviour. It can be noticed that L1 is located at the extreme left corner of the domain (green square dot in Figure III.2) whilst L2 is on the upper bound of the domain (black asterisk in Figure III.2). By design, they both correspond to angle-ply sequences (i.e. two-orientation layups $\pm\alpha$, with $\alpha = 45$ and $\alpha = 22.5$, respectively).
  - Layup L1 is square symmetric, as its polar parameter $R_1^{\tilde{D}}$ is zero
  - Layup L2 is R_0-orthotropic, i. e. $R_K^{\tilde{D}} = 0$
- Layups L3 and L4 are general uncoupled orthotropic layups (3-orientation laminates,see Table III.7), but chosen for the study as they are two distinct layups sharing the same polar parameters and consequently corresponding to the same point (superposed red and blue crosses) in Figure III.2. They serve to identify influences of differences in the stacking sequence on the uncertainty.
- Layup L5 corresponds to the stacking sequence at the maximum value of the flutter velocity in the polar domain and also in direct vicinity of the mode switch (green

solid square dot in Figure III.2). By design, L5 is also an angle-ply configuration with $\eta = 28.4$.

- Layup L6 (pink triangle dot in L6 Figure III.2) is close to the maximum point, but not situated in direct vicinity of the mode switch. This will emulate a more realistic case for the uncertainty study, representing a situation where the mode switch is not directly hit, but "by accident". L6 is not on the upper border of the domain, thus it is not an angle-ply layup but a 3-orientation laminate ($\eta = 0$ and $\pm\xi = 34$) as written in Table III.7.

In order to graphically represent the different stiffnesses of the layups, circular diagrams of the engineering moduli are given in Figure III.3. They show their equivalent nominal bending Young's modulus E^D and torsional modulus G^D as function of the angular deviation δ from the material's principal orthotropy axis. Young's modulus E^D and the torsional modulus G^D are taken respectively as the reciprocal values of the $1,1$ and $6,6$ components of the normalised bending compliance tensor $d^* = \frac{h^3}{12}\tilde{D}^{-1}$ [89, 90]. The values for $\delta = 0$ correspond to the homogeneised bending moduli for each laminate in its main orthotropy axis.

By observing Figure III.3, the square symmetry of L1 can clearly be identified from the cross-shaped diagram of its bending modulus E^D as well as torsional modulus G^D. Moreover, compared to the other laminates, it has the highest possible value of the torsional modulus G^D in the orthotropy axes ($\delta = 0$ and $\delta = 90$, see Figure III.3.b), since it corresponds to the lowest possible value of R_K^D.

In contrast to that, the R_0-orthotropy of layup L2 is less clearly distinguishable by eye. It has an hourglass-shape in Young's modulus E^D (Figure III.3.a). The shear modulus G^D is cross-shaped and extends less than the laminates L1, L5 and L6 which also show a cross-shaped G^D outline (Figure III.3.b).

L3 and L4 are general orthotropic laminates. As both are designed to have the same polar parameters, then their homogenised elastic properties are the same and their curves coincide. The angular plot of Young's modulus for these layups is an oval of which the shape is closer to a circle than for the other examples (Figure III.3.a). This reflects the fact that the anisotropic polar parameters are closer to zero, so the materials can be looked upon as "more isotropic". This is also reflected in the shear modulus shape, which roughly resembles a square with rounded corners in contrast to the other layups, where the shear modulus always has a very pronounced cross shape (Figure III.3.b).

L5 and L6, despite representing different classes of layups and having even a different number of ply orientations, are close albeit not identical in polar parameters, which also is found again in the very similar angular modulus plots. As general orthotropic laminates, they expose the typical "butterfly" shape in the angular trace of Young's modulus E^D (Figure III.3.a). As for L1 and L2 their torsional modulus plot is cross-shaped, with the values being between the more extreme L1 and L2 (Figure III.3.b).

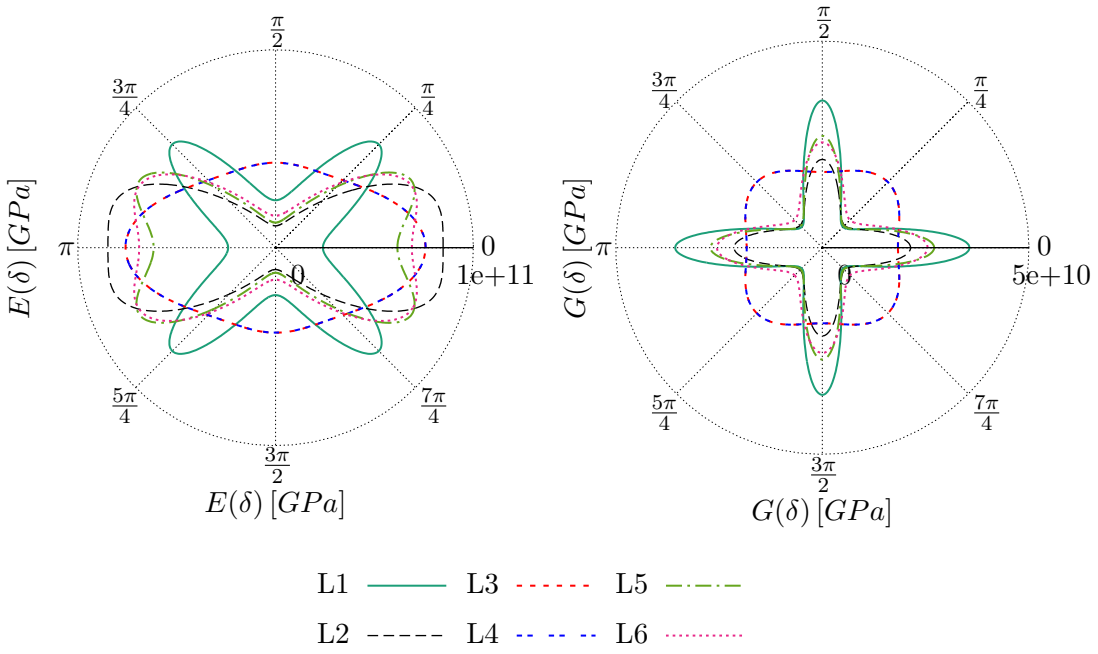

Fig. III.3 *Polar diagrams of nominal Young's modulus E and shear modulus G as a function of the angular deviation from the orthotropy axis δ for the selected layups given in Table III.7, for which the polar parameters are given in Table III.6*

In order to complete the deterministic aeroelastic analysis and to explain the shape of the response surface for V_f and ω_f, the $V-\lambda$ stability diagram as well as the corresponding aeroelastic mode shape are described in details for the selected laminate configurations given in Table III.7.

Figure III.4.a shows the $V-\lambda$ diagram, , i.e. the real part of the eigenvalues of the aeroelastic system plotted against the airspeed V, for a wing with specifications according to Table III.2 made up of the square symmetric layup L1. As explained in chapter II, any mode is stable as long as the real part of its corresponding eigenvalues is smaller than zero. The airspeed at which the real part of the eigenvalue becomes positive is the critical flutter velocity indicated by the black vertical bar, here at $V_f = 115.46[m/s]$. The unstable mode, represented in Figure III.4.a by the green solid line, has the shape shown in Figure III.4.b . The flutter mode is bending-dominated and resembles what in free vibration of a cantilevered beam would be called a second bending mode. Nevertheless, the mode also has small torsion components, which are less pronounced than the bending component. The modal bending behaviour can be guessed well by the material properties, as square-symmetric laminates are quite stiff against torsion, but less against bending (in Figure III.3 one can see that the bending modulus E^D of layup L1 in the orthotropy axis $\delta = 0$ is much smaller than for the other laminates in our set of study).

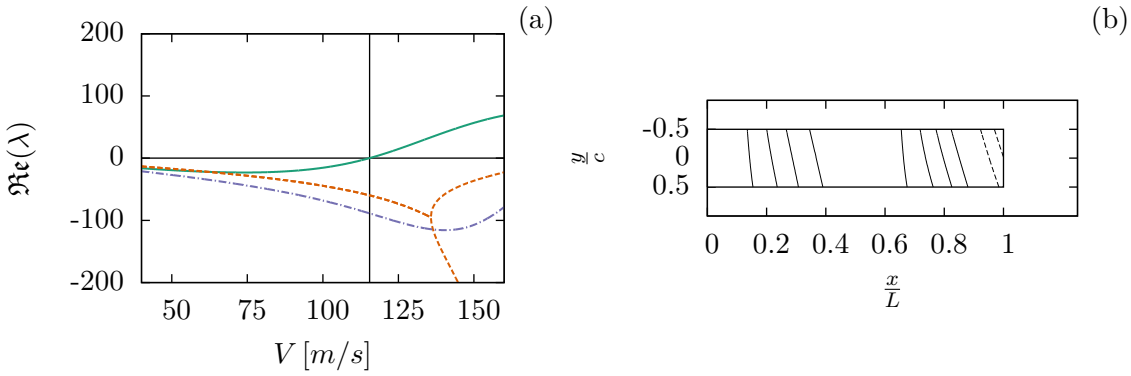

Fig. III.4 *$V-\lambda$ diagram and mode shape for layup L1 (Tables III.7,III.6)*

The fluttering mode for layup L2 becomes unstable at a higher velocity ($V_f = 125.06[m/s]$), but climbs up more abruptly than the previous example, as can be seen in Figure III.5(a). Being R_0-orthotropic, it has a much higher bending stiffness than L1, but a lower torsional stiffness. The mode shape is consequently torsion-dominated rather than bending-dominated, as shown in Figure III.5(b).

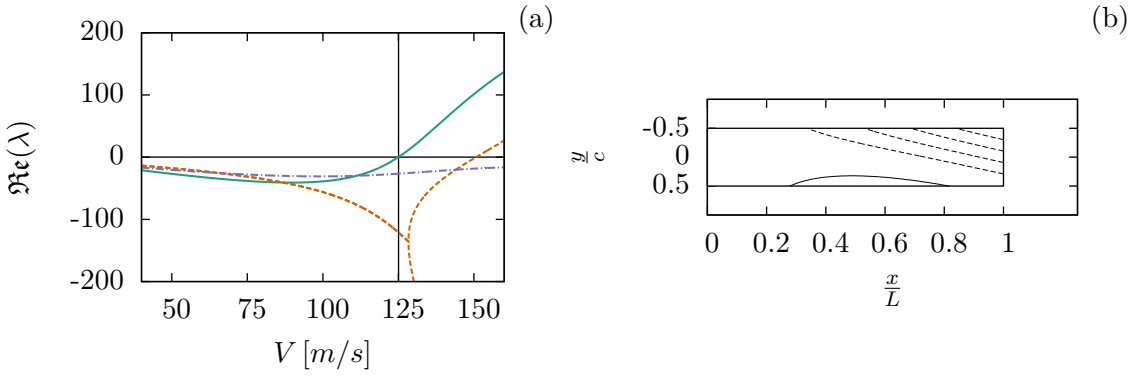

Fig. III.5 *$V-\lambda$ diagram and mode shape for layup L2 (Tables III.7,III.6)*

These two stacking sequences happen to represent two different modal regimes indicated by the response surface in the orthotropic plane depicted in Figure III.2. The response surface also suggests a rather violent transition between the two regimes in terms of flutter data. In order to deepen the investigation of the transition or "switch" between the modal regimes, L5 was picked. Because the transition is rather subtle in the flutter diagram, two laminates with a certain offset from L5 are generated in order to highlight the change of the mechanism. Advantage is taken from the fact that L5 is an angle-ply laminate with lamination angle $\eta = 28.4$ and sits on the border of the orthotropic domain. Further configurations that only move along the border of the orthotropic domain can be generated by just widening or narrowing the angles. For the following examples, laminates $L5^+$ and $L5^-$ are considered, with the lamination angle η respectively widened and narrowed by two degrees. Laminate $L5^+$ is consequently on the left side of the switch (i. e. its aeroelastic modal regime resembles that of layup L1), while Laminate $L5^-$ is

on the right side of the switch (i.e. it belongs to the same region and aeroelastic modal regime as layup L2).

The flutter diagram of the mode shape for $L5^+$ are shown in Figure III.6. The critical flutter velocity, in comparison with layup L1, has dropped to $89.54[m/s]$ (see vertical solid line in Figure III.6.a) . Nevertheless, its modal behaviour as depicted in Figure III.6.a) corresponds largely to the modal behaviour of L1, i.e., it resembles a second bending mode. However, the $V - \lambda$ diagram Figure III.6.a shows that the corresponding mode, represented by the violet dash-dotted line, barely becomes unstable. The real part of the eigenvalue does not pass the instability criterion by much. Moreover, it descends again below the instability limit at about $V = 130[m/s]$.

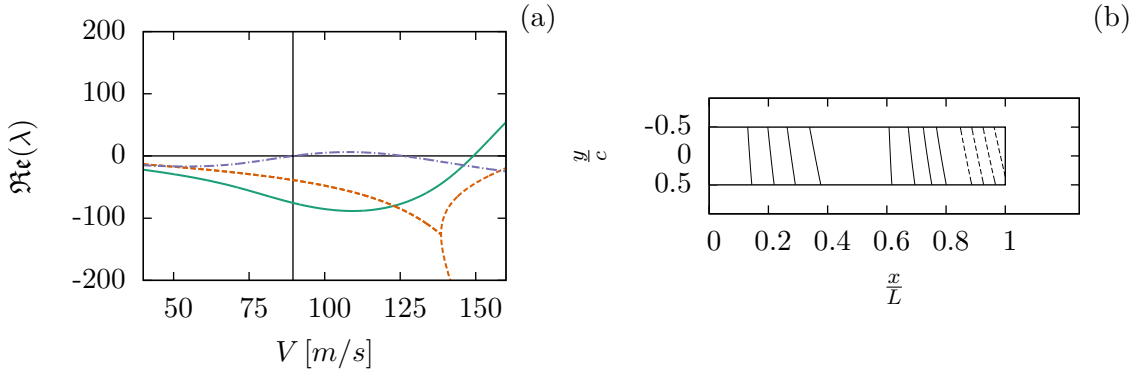

Fig. III.6 *$V - \lambda$ diagram and modal response of laminate $L5^+$.*

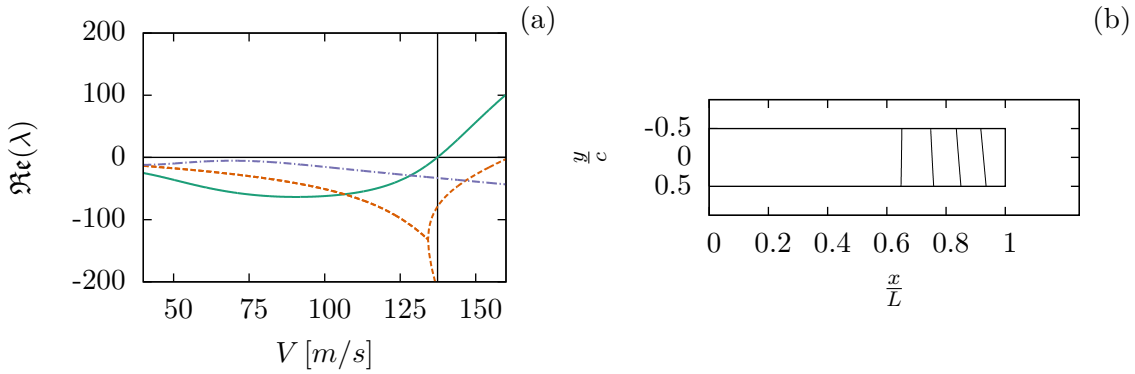

Fig. III.7 *$V - \lambda$ diagram and modal response of laminate $L5^-$.*

When considering laminate $L5^-$, thus moving the stiffness right from L5, the bending modulus increases whilst the torsional modulus decreases. The $V - \lambda$ diagram for layup $L5^-$ is given in Figure III.7.a. One can notice that the violet, the flutter mode of the previous example, again shown by the violet dash-dotted line is still recogniseable, as can be seen in Figure III.7.a. However, it does not pass the instability limit any more. Consequently, the first unstable mode becomes the mode indicated by the green solid line in both examples, which becomes unstable only at $V_f = 137.37[m/s]$ in the $L5^-$ case. The corresponding mode is now a "first bending" type mode, which with further shifts

transitions to torsion modes smoothly. This transition is consistent with the fact that the bending stiffness increases.

This deepened investigation confirms that the step in critical flutter velocity is caused by an abrupt switch in modal behaviour, which is the consequence of a change in the balance between bending and torsional stiffness. The change in balance leads to a shift in modal damping as a function of the freestream velocity, and thus changes the mode becoming unstable at the lowest velocity.

The investigation has shown that the critical flutter velocity is highly dependent on the material stiffness behaviour, especially in presence of mode switches, which lead to abrupt changes in the critical flutter velocity with very small changes in the material. This motivates the uncertainty quantification on manufacturing errors , such as on layers' thicknesses and orientation angles, affecting the stiffness properties of the laminate, which will be carried out in the next section.

III.3 Uncertainty propagation

In the previous section, it has been demonstrated by the example of orthotropic laminates how changes of the stiffness affect the critical flutter velocity of the composite plate wing example. In this section, typical uncertainties will be examined which alter the stiffness of the material using the laminates listed in Tables III.6,III.7. With the uncertainties added, the hypotheses made to construct the laminates for perfect orthotropy are no longer respected. Notably, they are no longer uncoupled; consequently, the full $\tilde{\mathbf{D}}$ tensor has to be taken into account.

Two of the most important uncertainties include uncertainty in ply angles and ply thicknesses [119]. This study will focus on those two examples. As these are supposed to be manufacturing errors and assuming that the manufacturer makes the best effort to fulfill the specifications, the errors are assumed Gaussian, where for the angular uncertainty, a standard deviation of 1° is assumed [127]. The author guesses the standard deviation of the ply thickness as 5% of the nominal value, which means that the standard deviation in this case is $0.005[mm]$. The standard deviations are summarised in Table III.8.

$\sigma_t[mm]$	0.005	$\sigma_\theta[^\circ]$	1.0

Table III.8 – Standard deviations of the uncertainties in ply thicknesses and angles

The uncertainties are in the following applied to the different laminates from Tables III.6,III.7, and the changes in critical flutter velocity are observed. The effects of the different uncertainties in the ply angles and the ply thicknesses will each be studied individually, as well as their combined effects. Special attention will be paid to the differences in the behaviours of the moduli and the uncertainty in the direction of the symmetry axes.

III.3.1 General orthotropic laminates and the influence of the stacking sequence

In the following, the two laminates out of the middle of the polar domain L3 and L4 will be examined. The laminates are general orthotropic laminates and are far from the limits of the domain, meaning that there are no special constraints on the stiffness.

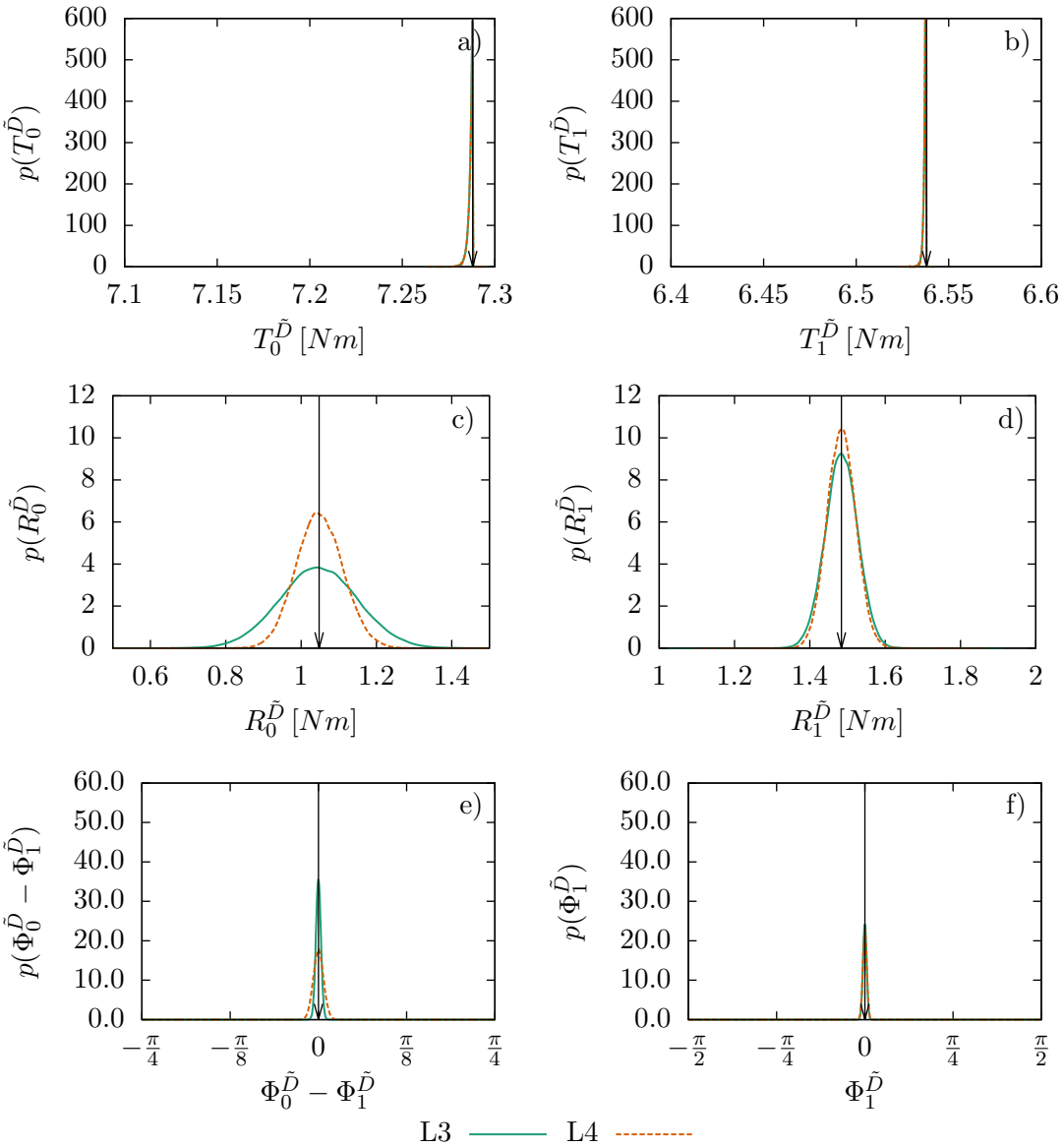

Fig. III.8 *Gaussian KDEs of layups L3 and L4 (Table III.7) with uncertain ply angles. Standard deviation on ply angles is* 1°*. The KDEs are obtained with Monte Carlo simulation using* 10^5 *samples*

First, the influence of the uncertainty in the ply angles on the material stiffnesses in form of the polar parameters is presented in Figure III.8. The histograms are obtained

using 10^5 samples. Despite the uncertainty concerning only rotation of plies, the isotropic parameters T_0 and T_1 are affected (Figure III.8.a,III.8.b). This is due to the incorporation of the membrane-bending coupling in the modified bending stiffness tensor. Nevertheless, this deviation is extremely small.

As both laminate layups are far from any constraints due to geometric or thermodynamic domain limits in terms of the anisotropic moduli, both R_0 and R_1 (Figure III.8.c,III.8.d) show bell-shaped curves for both of the laminates, which are roughly centered about the nominal values of the moduli. However, in the L3 case, the variance in $R_0^{\tilde{D}}$ is much higher, giving the curve a wider spread than in the L4 case. Also, the $R_1^{\tilde{D}}$ parameter has a greater variance in the L3 case but the difference in the distributions is much smaller. In contrast to this, the difference in the corresponding angles is inverted (Figure III.8.e,III.8.f), as these distributions have a higher spread in the L4 case.

The corresponding responses in critical flutter velocity are shown in Figure III.9. As before, both materials produce a bell-shaped curve roughly centered around the nominal value. The distribution for L4 however is slightly narrower and steeper than the curve for its L3 counterpart, indicating that the anisotropic moduli could play a bigger role in this case than the uncertainty in the polar angles.

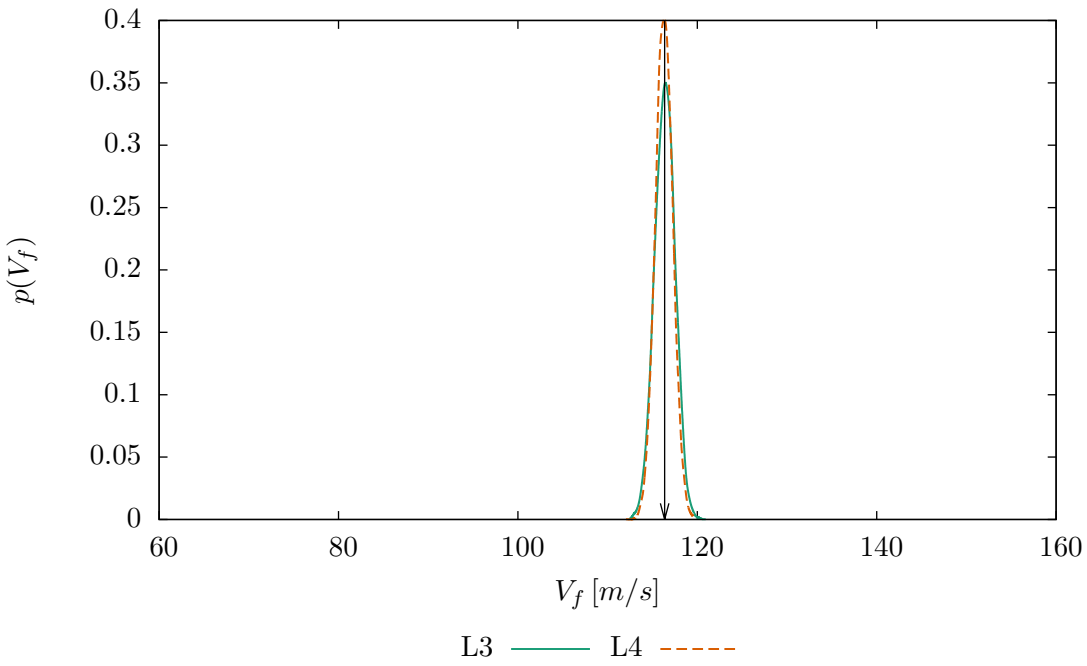

Fig. III.9 *Gaussian KDEs of critical flutter velocity (V_f) response for layups L3 and L4 (Table III.7) on uncertain ply angles with standard deviation of* 1°. *KDEs obtained by Monte Carlo simulation with* 10^5 *samples*

In the following example, the uncertainty in the ply thicknesses are studied. The thicknesses have two effects:

- Through the scaling of the whole stack, the plate can become more rigid or compliant
- The different scaling of the individual plies destroy the balance of the laminate. Via this mechanism, the uncertainty in the ply thicknesses also have an influence on the anisotropy and are able to alter it.

In this context, it is interesting to study the differences in behaviour in the two laminates sharing the same behaviour, as the influence of the stacking sequence can directly be revealed.

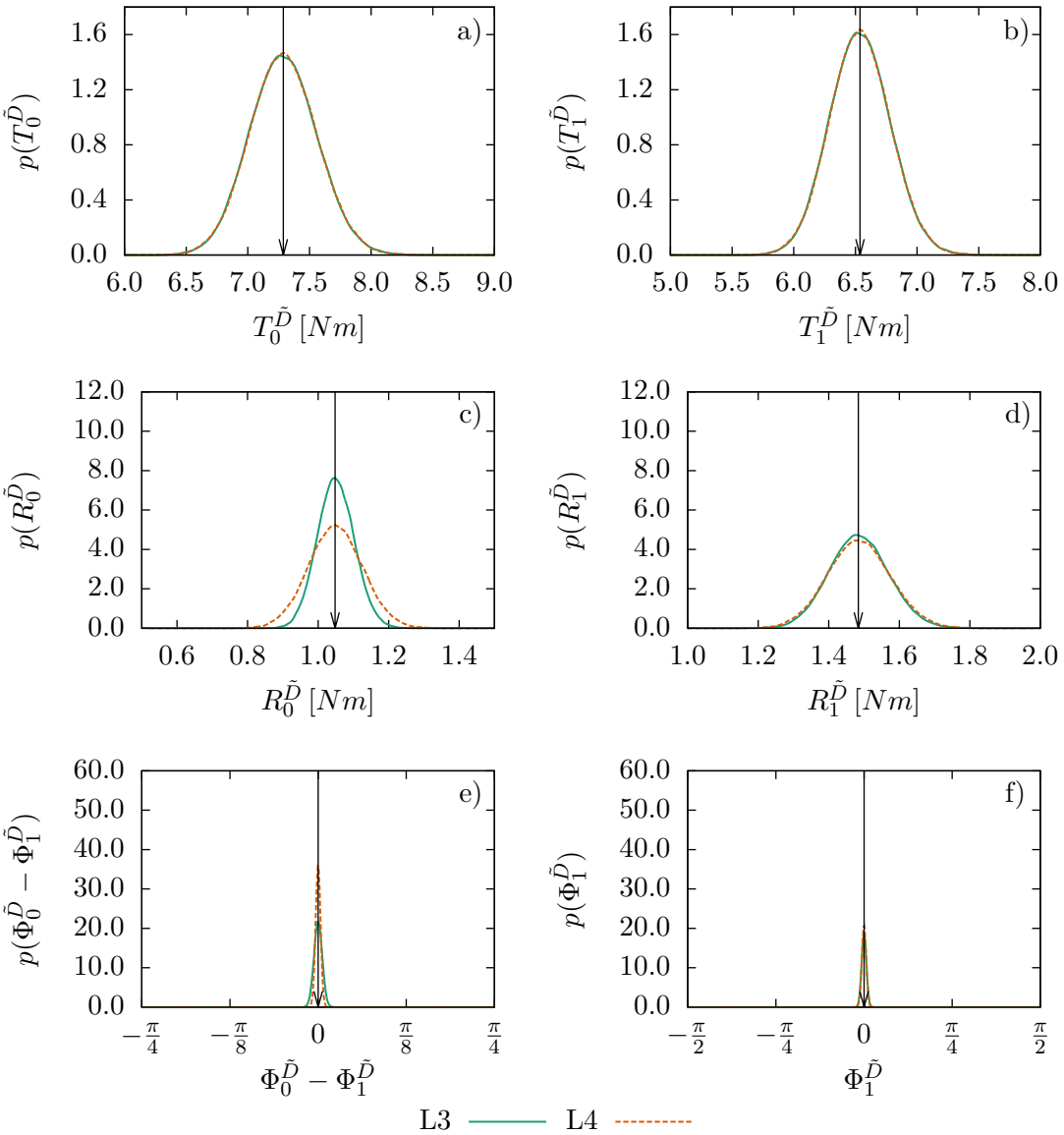

Fig. III.10 *Gaussian KDEs for layups L3 and L4 (Table III.7) with uncertain ply thicknesses. The CoV of the ply thickness is* 5%*. The KDEs are obtained with Monte Carlo simulation using* 10^5 *samples*

The results are shown in Figure III.10. Other than the angular uncertainty, the ply

thickness uncertainty has a big impact on the isotropic parameters $T_0^{\tilde{D}}$ and $T_1^{\tilde{D}}$, probably due to the aforementioned scaling effect. In contrast, there is a noticeable difference in the behaviour of the anisotropic moduli. The $R_0^{\tilde{D}}$ modulus shows significantly larger variation for the L4 laminate in comparison to L3. However, the associated angle $\Phi_0^{\tilde{D}}$ is less uncertain in the L4 case than in the L3 case.

As can be seen in Figure III.11, other than in the case of the angular uncertainty, the uncertainty in the ply thicknesses does not lead to any visible difference in the distribution of the critical flutter velocities in this case. Both examples show very similar bell-shaped curves distributed around the nominal critical flutter velocity. The reason might be that the differences in layup and the resulting differences in stiffness properties are too small to cause significant differences in the modal behaviour, which in turn leads to very similar behaviour in terms of critical flutter velocity.

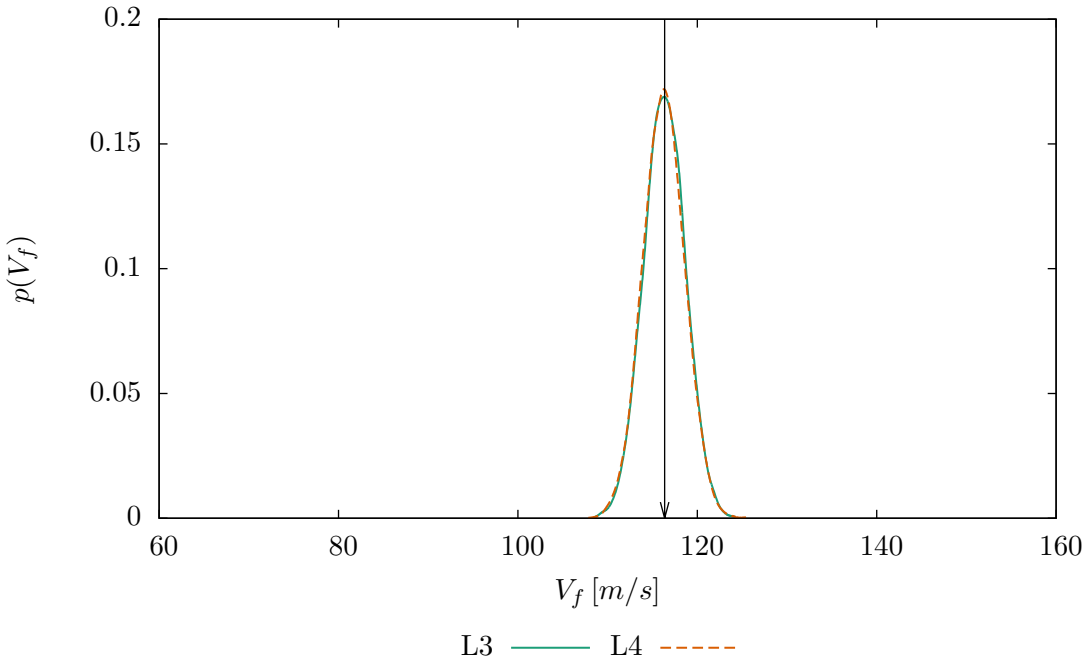

Fig. III.11 *Gaussian KDE of critical flutter velocity (V_f) response for layups L3 and L4 (Table III.7) on uncertain ply thickness with a CoV of* 5%*. The KDE is obtained by Monte Carlo simulation with* 10^5 *samples.*

Finally, the combined effect of the two uncertainty types is studied. The corresponding results are given in Figure III.12. In these cases, it is impossible to describe any of the two uncertainty types as dominant. Moreover, the differences between the two layups clearly appearing in the previous studies performing individual propagation of the uncertainties become much less important. There is, however, a small difference in the $R_0^{\tilde{D}}$, which means that the uncertainty in this parameter is less important for L4, which was the case, albeit to a way greater extent, in the angular uncertainty scenario.

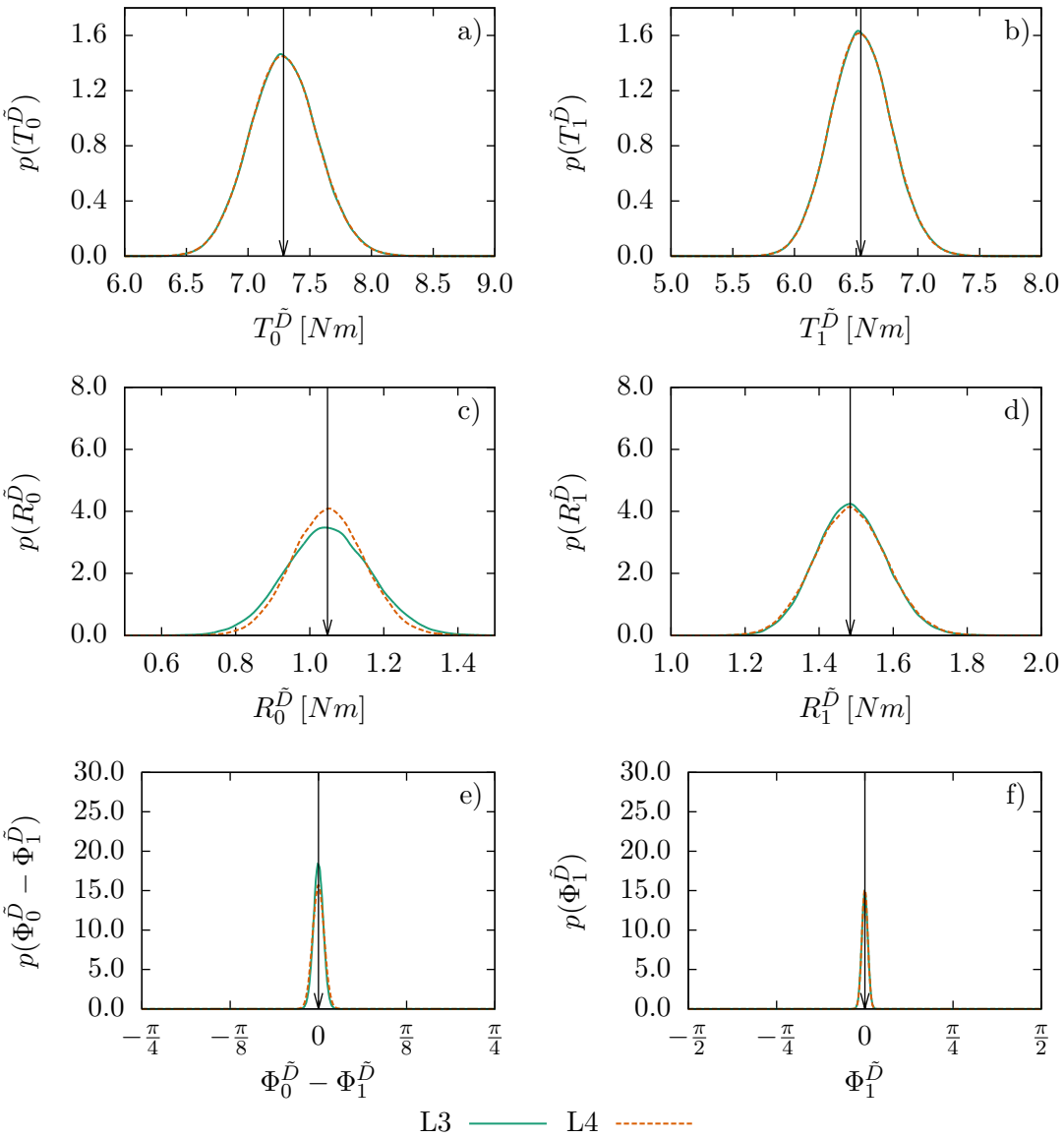

Fig. III.12 *KDEs of the polar parameters of layups L3 and L4 (Table III.7) with uncertain ply angles and uncertain ply thicknesses. The standard deviation of the ply angles is* 1° *and the CoV of the ply thicknesses is* 5%*. The histograms obtained with Monte Carlo simulation using* 10^5 *samples.*

The distribution of the critical flutter velocity, shown in Figure III.13, resembles more the thickness propagation case. The differences between the two layups present in the angular uncertainty propagation are almost completely equalised.

For giving a comparison with classical safety margins, the classical 15% margin on the predicted flutter onset is given along with an estimation for the 1% quantile. As the estimate for the quantile is significantly higher than the classical safety margin, a decent safety reserve can be assumed. This prompts the question after possibilities for optimisation.

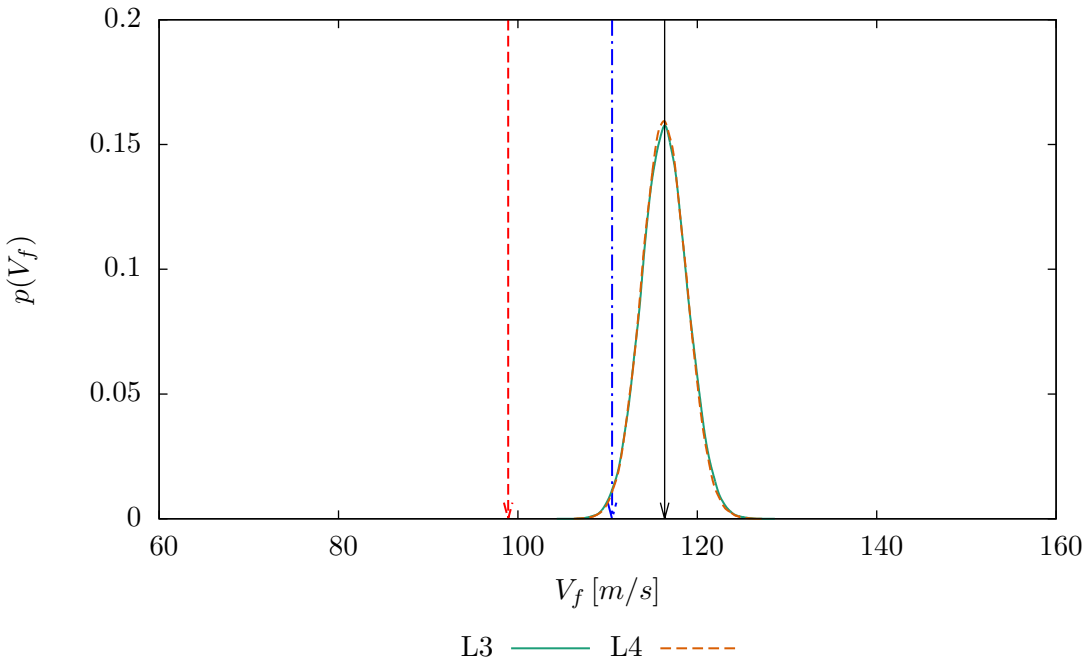

Fig. III.13 *Gaussian KDE of critical flutter velocity (V_f) response for layups L3 and L4 (Table III.7) on uncertain ply angles with a standard deviation of* 1° *and uncertain ply thicknesses with a CoV of* 5%*. The KDE is obtained by Monte Carlo simulation with* 10^5 *samples.*

III.3.2 Special material symmetries

Beyond ordinary orthotropy, with square symmetry and R_0-orthotropy, there are special cases of material symmetry implying additional constraints on the material behaviour. This section will be taking interest in the question if the restrictions implied by the symmetries have a stabilising effect or if, on the contrary, the loss of symmetry by the uncertainty causes a destabilisation of the stiffness, and consequently the aeroelastic behaviour of the plate wing. For this purpose, the effect of the uncertainties described previously (Table III.8) on laminate configurations with special symmetries, i. e. the square symmetric laminate L1 and the R_0-orthotropic laminate L2 (Tables III.6,III.7) will be examined.

a) Square symmetric layup L1

The analysis is started with the example layup L1, of which the polar parameter distributions for the angular uncertainty in the ply stack are given in Figure III.14. The isotropic parameters $T_0^{\tilde{D}}$ and $T_1^{\tilde{D}}$ are behaving much in the same way as in the previous example.

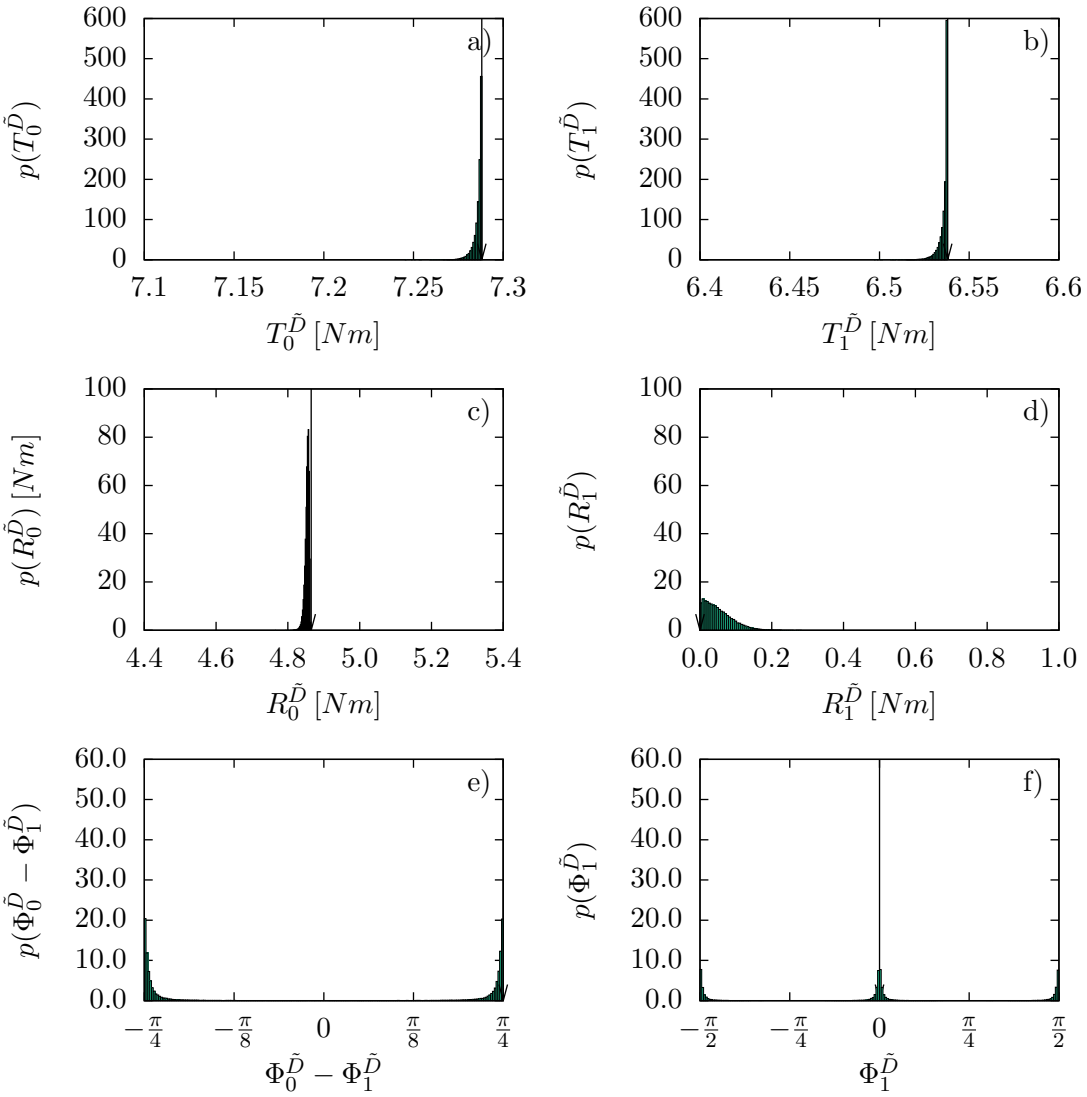

Fig. III.14 *Histograms of layup L1 (Table III.7) with uncertain ply angles. The standard deviation of the ply angles is* 1°. *The histograms are obtained with Monte Carlo simulation using* 10^5 *samples.*

The uncertainty leads to the loss of the symmetry type of the material. This can be observed in the polar parameters. In its nominal configuration, the L1 laminate layup is square symmetric, which means that its nominal $R_1^{\tilde{D}}$ is zero. With the uncertainty added, the parameter shifts up. The $R_0^{\tilde{D}}$ complements this behaviour by shifting down from its nominal value. As the material is on the border of the domain of existence, the nominal

value of $R_0^{\tilde{D}}$ represents a sharp upper limit.

The polar angle of the newly defined orthotropy axis, which was set to zero before, is now distributed at angles of zero and 90 degrees, which means that there is uncertainty of the direction of the material behaviour. This is logical in the context that the values of the corresponding $R_1^{\tilde{D}}$ modulus, despite now being different from zero, stay relatively low. This means that the associated anisotropic behaviour is not very strong, which is also expressed in the uncertain direction.

Figure III.15 shows the corresponding results for propagation of the uncertainty through the aeroelastic solver in terms of critical flutter velocity V_f. The angular uncertainty affects this flutter response surprisingly little. The distribution is a narrow spike around the value for the critical flutter velocity in nominal configuration of the composite material. This could be due to the response in critical flutter velocity being relatively flat in the region around the nominal configuration without any changes. This is at least true for the behaviour in the $R_0^{\tilde{D}}$ and $R_1^{\tilde{D}}$ with the nominal angles applied (Figure III.2). It could also be that the particular symmetry of the material adds to the stability of the material properties.

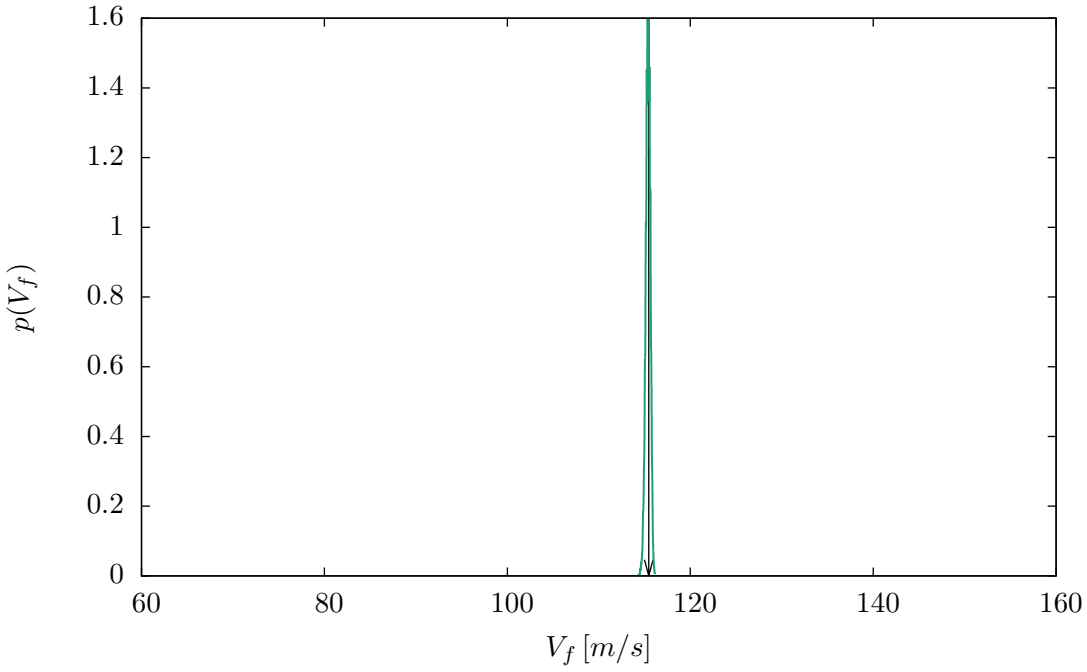

Fig. III.15 *Gaussian KDE of critical flutter velocity (V_f) response for layup L1 (Table III.7) on uncertain ply angles with a standard deviation of* 1°. *The KDE is obtained by Monte Carlo simulation with* 10^5 *samples*

Figure III.16 shows the effects of the uncertainty in the ply thickness on the polar properties laminate L1 (Tables III.7,III.6). The Gaussian nature of the thickness uncertainty translates to smooth bell-shaped curves in the isotropic material properties (Figure III.16.a and III.16.b). The more interesting effects are developing in the anisotropic

parts of the material behaviour. The $R_0^{\tilde{D}}$ modulus shows much of the same behaviour as the isotropic components, which is not very surprising considering that thickness information modulates all modulus information equally as seen in the introductory section of this chapter. An effect that goes beyond simple scaling through the thickness changes however is the loss of the material symmetry, which is indicated by the $R_1^{\tilde{D}}$ and angular values departing from their nominal values. $R_1^{\tilde{D}}$ becomes greater than its nominal value zero. This can only be explained by a shift in the relations between the individual plies, where the $R_1^{\tilde{D}}$ components do not eliminate each other any more. Consequently, the $R_1^{\tilde{D}}$ component becomes non zero. However, its values remain small.

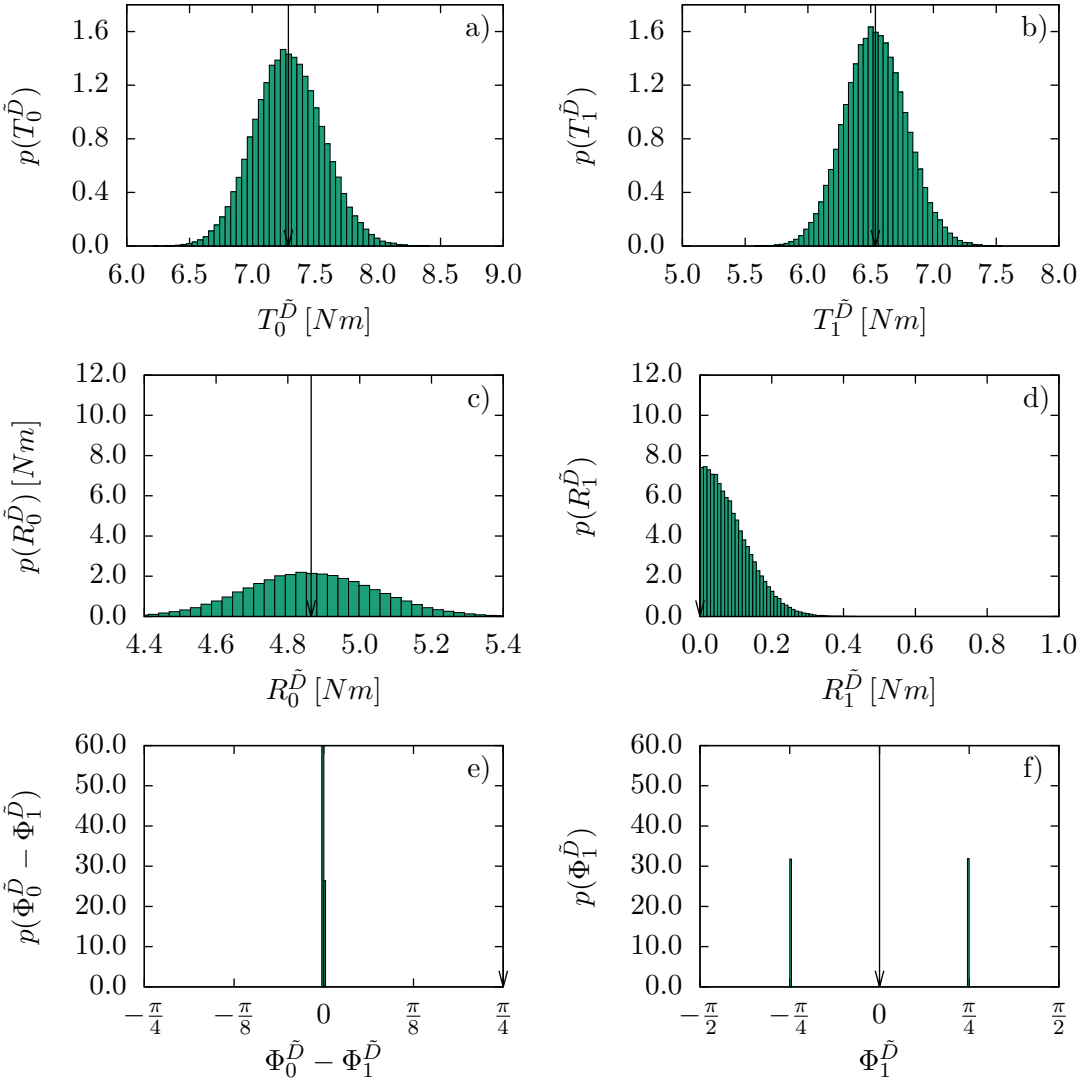

Fig. III.16 *Histograms of layup L1 (Table III.7) with uncertain ply thickness. The CoV of the ply thicknesses is* 5%*. The histograms are obtained with Monte Carlo simulation using* 10^5 *samples.*

The critical flutter velocity responds to the uncertainty much stronger than in the case

of the angular uncertainty, as can be seen in Figure III.17. Nevertheless, the curve stays relatively narrow and is centered at the nominal value for the critical flutter velocity. However, other than the response to the angular uncertainty which was clearly more stable, the response to the thickness uncertainty is comparable to other cases (e. g. the previous case, Figure III.11).

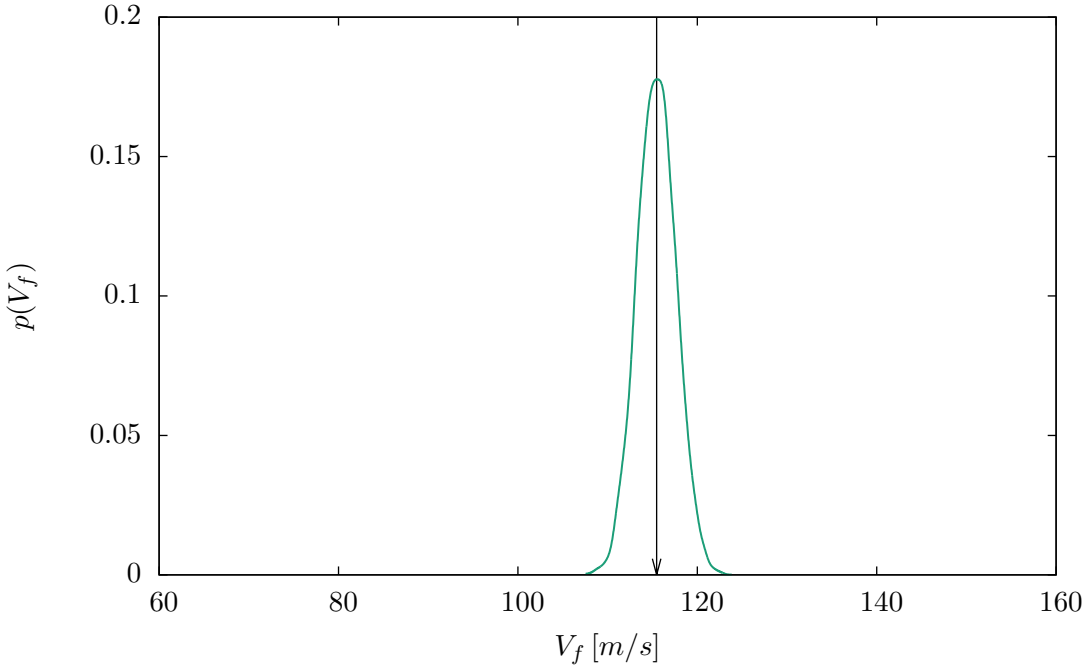

Fig. III.17 *Gaussian KDE of critical flutter velocity (V_f) response for layup L1 (Table III.7) on uncertain ply thicknesses with a CoV of* 5%. *The KDE is obtained by Monte Carlo simulation with* 10^5 *samples.*

The histograms of the polar parameters under influence of both of the uncertainties is shown in Figure III.18. As could be expected, the isotropic parameters take up mostly the behaviour of the uncertainty in the thickness, as the uncertainty in the angles only had a small effect. Consequently, the distributions of the polar parameters resemble the bell-shaped curves found for the thickness-only example.

The observation that the uncertainty in the thickness dominates the uncertainty in the polar parameters is confirmed in the parameter $R_0^{\tilde{D}}$, which is the parameter that is nominally non-zero. The limiting behaviour of the domain border in the propagation of the angular uncertainty is not found again. Instead, the distribution of the parameter takes again the form of a bell-shaped distribution roughly centered around the nominal value.

In contrast to the previous examples, the $R_1^{\tilde{D}}$ component, whose nominal value is zero, shows a behaviour that cannot be attributed to any of the two types of uncertainty individually. The parameter still shifts up from its nominal zero value as for the different uncertainties individually. Also, the distribution falls rapidly and ends in a very flat tail beyond values of 0.2, which could be observed for both types of uncertainty. However, in the previous example, the distribution started roughly at its maximum at the lower

bound of the parameter $R_1^{\tilde{D}} = 0.0$. In this case, it is zero at the lower bound and rises to its maximum at a value of about 0.05. The probability density for very low values of this parameter is thus significantly lowered. This effect can only be explained by a coupling of the two uncertainties, which makes it more unlikely to arrive at values of zero for the second parameter.

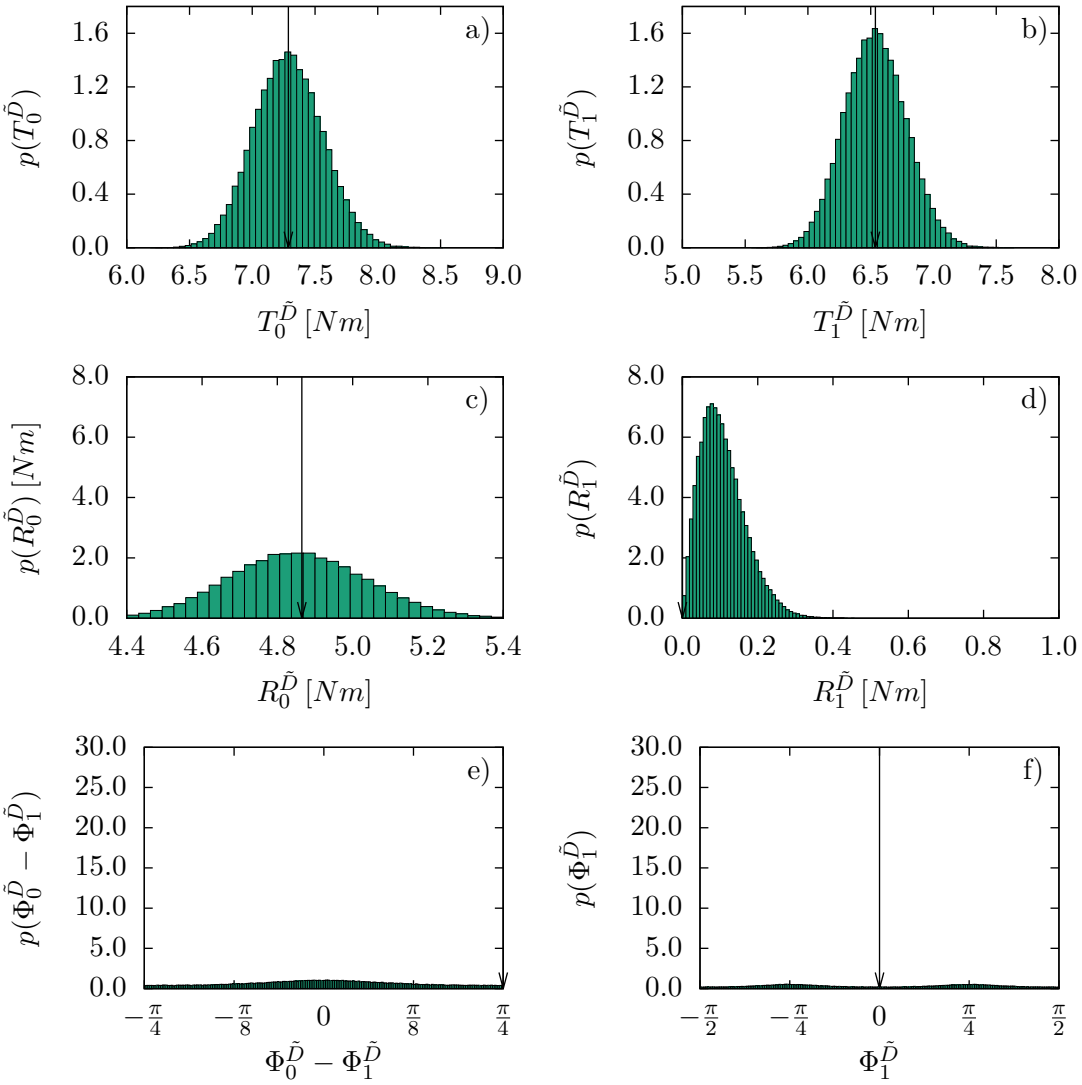

Fig. III.18 *Histograms of layup L1 (Table III.7) with uncertain ply angles and uncertain ply thicknesses. The standard deviation of the ply angles is* 1° *and the CoV of the ply thicknesses is* 5%*. The histograms are obtained with Monte Carlo simulation using* 10^5 *samples*

Another coupled effect can be observed in the polar angles. In the studies with the different uncertainties considered individually, the probability density functions were very narrow, with the axis of orthotropy distributed around $\Phi_1^{\tilde{D}} = \pm\frac{\pi}{4}$ in the thickness uncer-

tainty case and $\Phi_1^{\tilde{D}} = \{0, \pm\frac{\pi}{2}\}$ in the angular uncertainty, as well as the angular offset $\Phi_0^{\tilde{D}} - \Phi_1^{\tilde{D}}$ being distributed around $\pm\frac{\pi}{4}$ for both uncertainties. The highest probability density masses resemble more the thickness uncertainty case, the angles have become very uncertain, indicating another example of a coupled influence.

The stochastic response in critical flutter velocity is shown in Figure III.19. While the polar parameters show changes when the uncertainties are propagated together and not be explained by one dominating type of uncertainty, the distribution of the critical flutter velocity closely resembles the distribution in the thickness-only propagation. However, the propagation of the angles only did not have a big effect on the critical flutter velocity anyway. Again, the 15% criterion clearly is below any significant probability density mass.

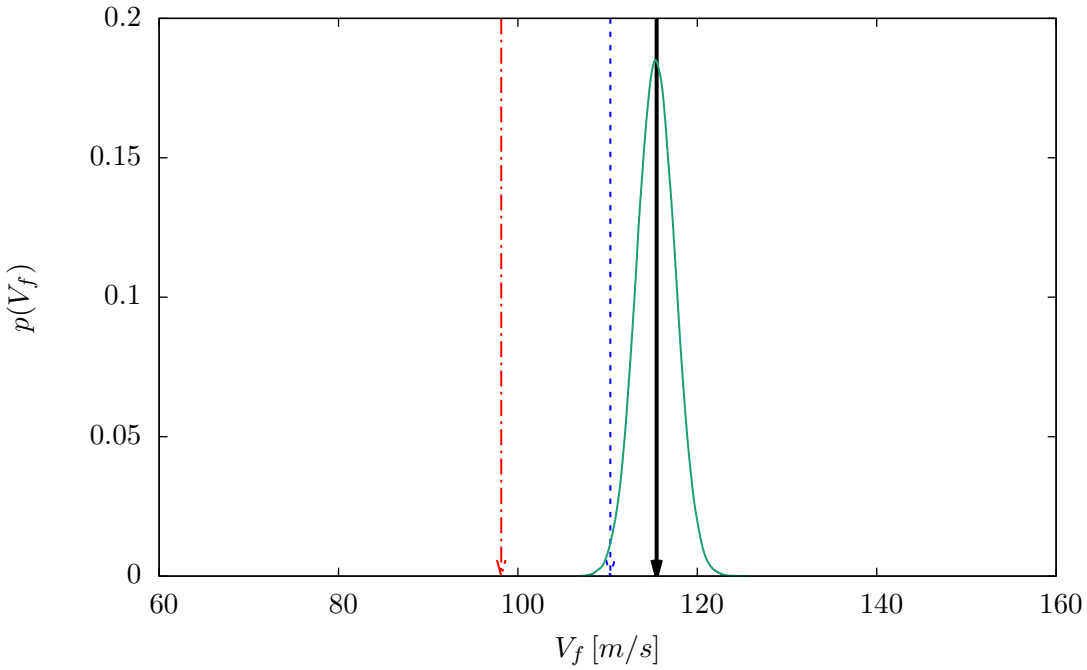

Fig. III.19 *Gaussian KDE of critical flutter velocity (V_f) response for layup L1 (Table III.7) on uncertain ply angles with a standard deviation of* 1° *and uncertain ply thicknesses with a CoV of* 5%*. The KDE is obtained by Monte Carlo simulation with* 10^5 *samples.*

b) R_0-orthotropic layup L2

Also the L2 layup possesses a special symmetry with one of the polar moduli being zero in the nominal configuration, which is $R_0^{\tilde{D}}$ in this case. The distribution of the polar parameters with applied ply angle uncertainty is shown in Figure III.20. As the isotropic parameters again behave in the same way as in the previous example, they will not receive any special comment in the following.

As in the previous example, the value of the anisotropic parameter that is nominally

zero, i. e. $R_0^{\tilde{D}}$, shifts up and the corresponding angular direction becomes uncertain ($R_0^{\tilde{D}}$ and $\Phi_0^{\tilde{D}}$). There are, however, some differences in the behaviour of the nominally non-zero polar parameter ($R_1^{\tilde{D}}$). Other than its counterpart in the square-symmetric case, it has a much greater variance, and the nominal value does not limit the deviations of the parameter in this case. Instead, the $R_1^{\tilde{D}}$ parameter shows a bell-shaped distribution centered around the value for the critical flutter velocity in the nominal configuration.

The isotropic moduli show the same behaviour as before. As this does not change significantly for the other layups, the distributions for the isotropic moduli will not be commented on any further.

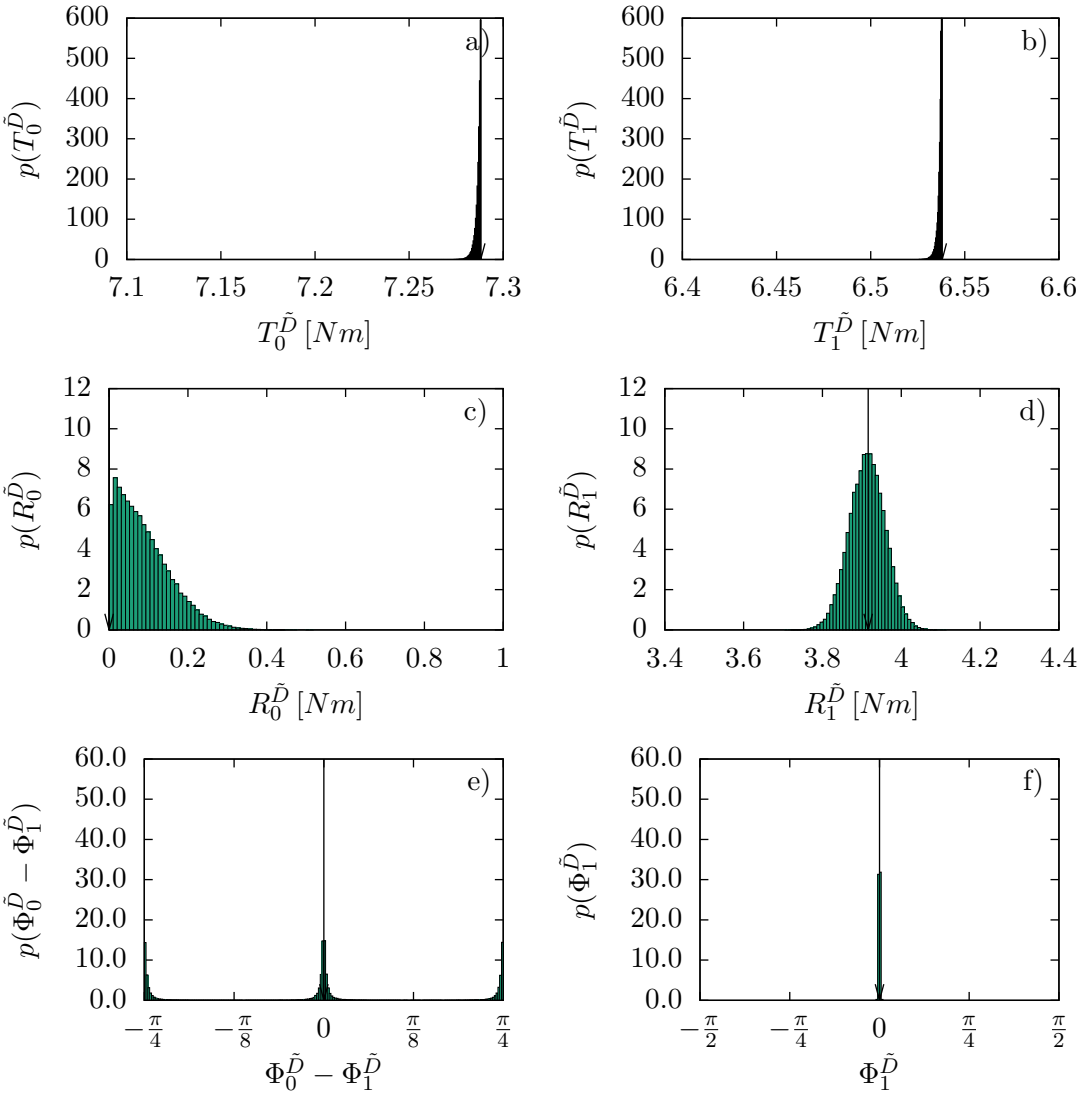

Fig. III.20 *Histograms of layup L2 (Table III.7) with uncertain ply angles. The standard deviation of the ply angles is* 1°. *The histograms are obtained with Monte Carlo simulation using* 10^5 *samples.*

The response in critical flutter velocity is shown in Figure III.21. The response is distributed closely around the V_f value obtained when calculating with the nominal configuration. However, this distribution is much wider than in the case of L1 (see Figure III.15. This could be the result of higher variance in the main anisotropic modulus compared to the previous case, or generally a steeper response surface in the region around the considered point.

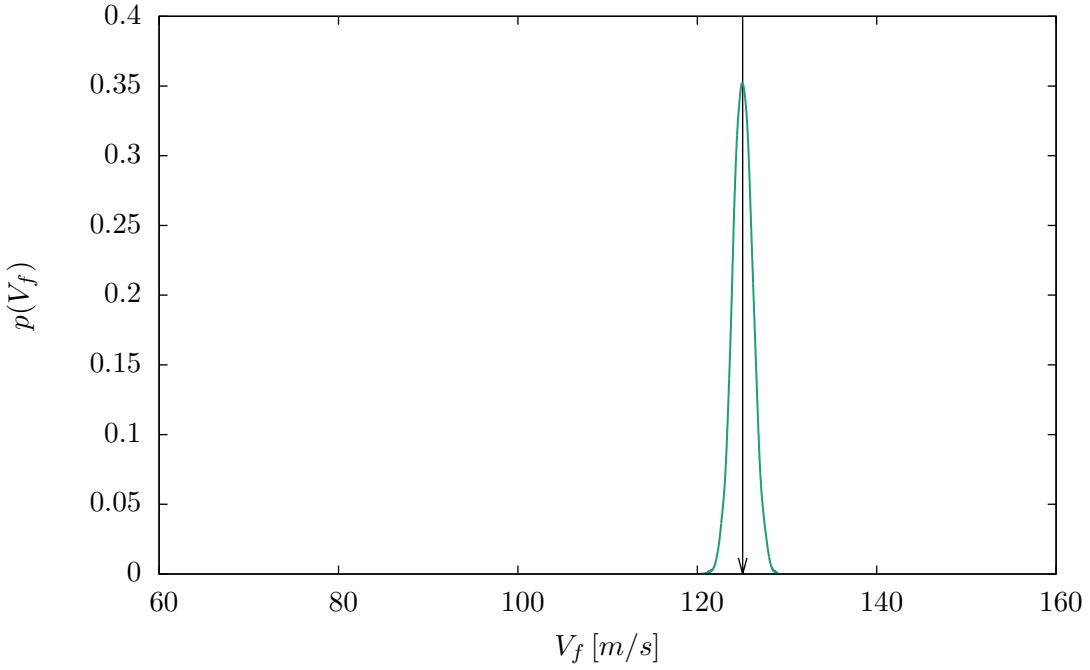

Fig. III.21 *Gaussian KDE of critical flutter velocity (V_f) response for layup L2 (Table III.7) on uncertain ply angles with a standard deviation of* $1°$*. The KDE is obtained by Monte Carlo simulation with* 10^5 *samples.*

As in the example on the ply angle uncertainty, the L2 layup mirrors the behaviour of L1 for an $R_0^{\tilde{D}}$-orthotropic setting. The nominally non-zero parameter (i. e. $R_1^{\tilde{D}}$) shows a bell-shaped curve, while the parameter that is zero in the nominal configuration (i. e. $R_0^{\tilde{D}}$) shifts up.

Other than before, the principal axis of orthotropy does not change position. This is due to the fact that the material, despite losing its special orthotropy, remains orthotropic and only deviates little from the orthotropic case, retaining a significant orthotropic characteristic dominated by $R_1^{\tilde{D}}$, which in the previous example suddenly built up. This is the case for this example with the $\Phi_0^{\tilde{D}}$ characteristic axis, where such an axis position change can be observed. This is a result from the axis deliberately being chosen as zero although it is not clearly defined if the value of the associated modulus is zero. It also has to be noticed that as before, the uncertainty in thickness does not affect the polar angles very much and the distribution of the angles cover only a very narrow range.

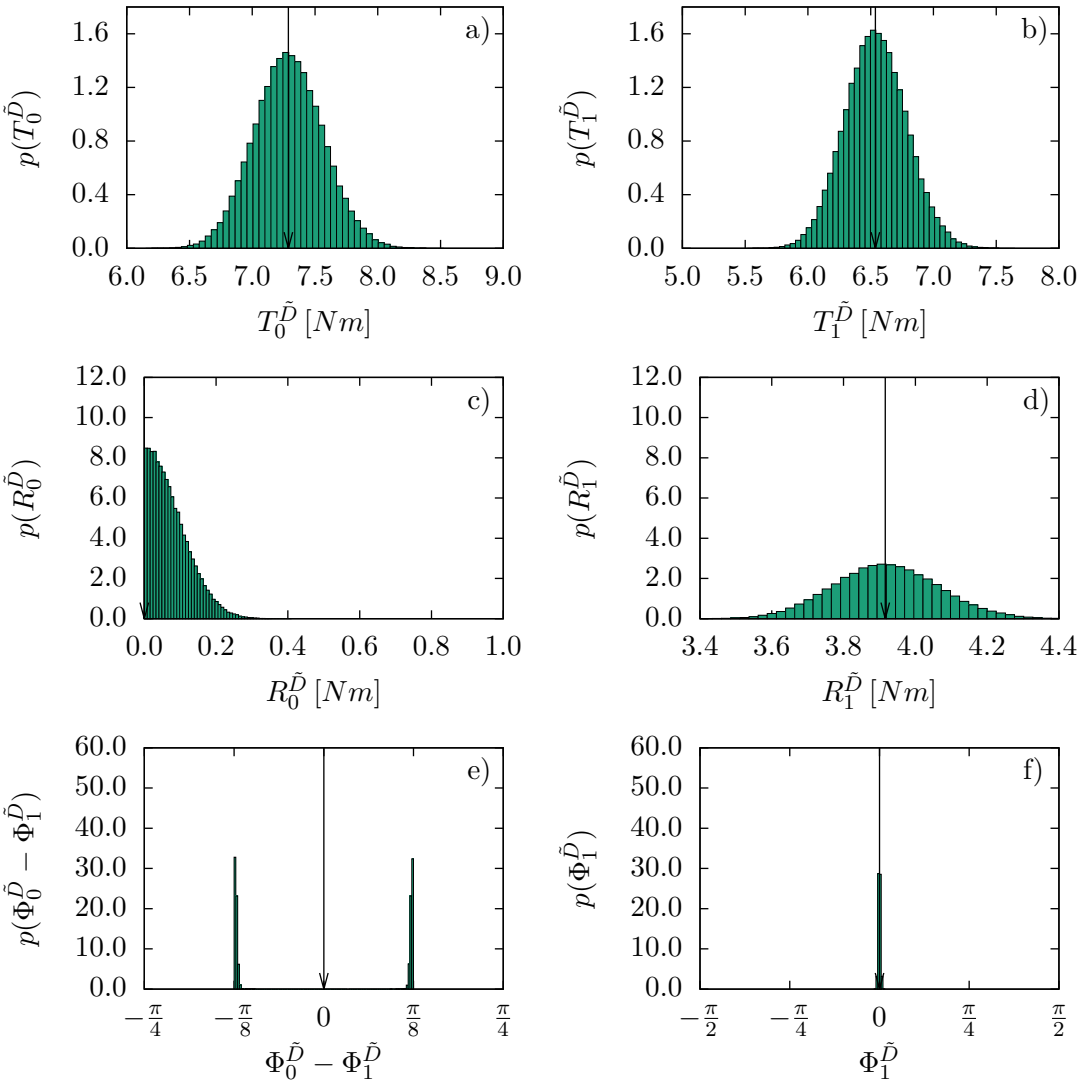

Fig. III.22 *Histograms of layup L1 (Table III.7) with uncertain ply thickness. The CoV of the ply thickness is* 5%. *The histograms are obtained with Monte Carlo simulation using* 10^5 *samples.*

The overall similar behaviour continues also in the critical flutter velocity, as shown in Figure III.23. Again, the critical flutter velocity shows a bell-shaped curve around the nominal value of the critical flutter velocity. Compared to the previous example, the nominal value is higher, which means that the curve shifts to higher values. Nevertheless, the higher nominal value does not mean that the variance would change significantly.

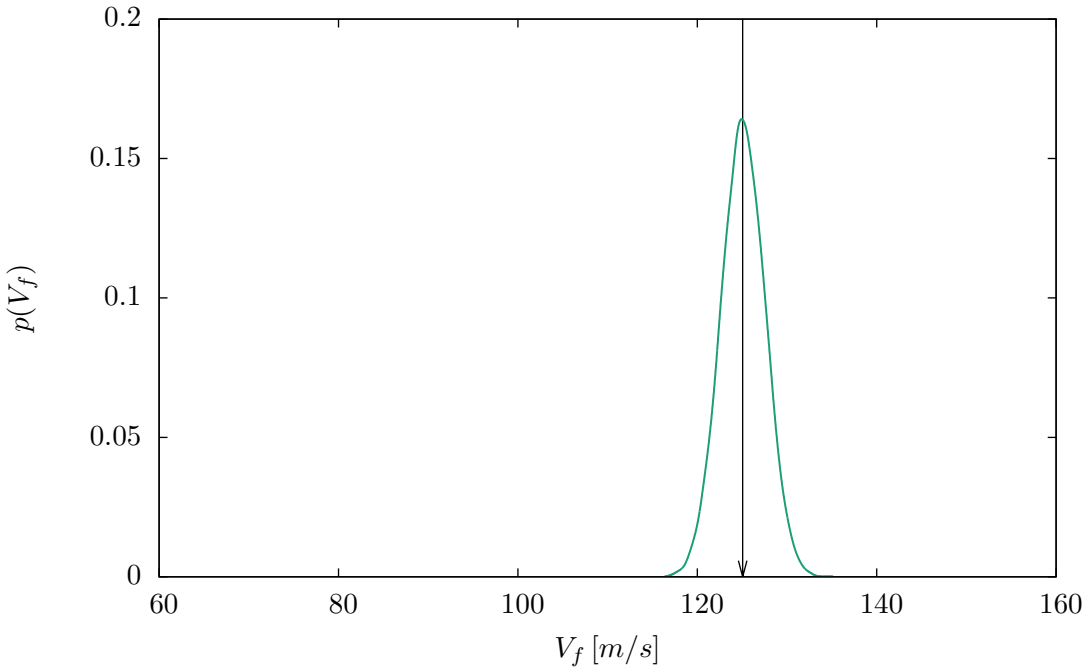

Fig. III.23 *Gaussian KDE of critical flutter velocity (V_f) response for layup L2 (Table III.7) on the uncertain ply thickness with a CoV of 5%. The KDE is obtained by Monte Carlo simulation with 10^5 samples.*

The results of the propagation of both the ply thickness and ply angle uncertainties for the polar parameters for laminate L2 are shown in Figure III.24. Again, the stochastic behaviour of the parameter that is nominally zero shows the coupling effect described earlier: other than in the individual propagation of uncertainties, the probability density is very low at very low values of the parameters, rises then to a maximum which is found at about 0.1 in this case and ends in a long tail. Meanwhile, the behaviour of the non-zero parameter takes again a bell-shaped form, which in this case cannot be clearly attributed to one of the two types of the uncertainties. However, the distribution does not seem to spread much further than in the thickness uncertainty case, which means that the uncertainties do not simply add up.

Moreover, the behaviour in the ply angles is different from what was observed in the previous case, with the distribution for the angle of the orthotropic axis $\Phi_1^{\tilde{D}}$ being narrowly distributed around its nominal value even with both uncertainties applied. This could be due to the fact that the main angles coincide for both uncertainty propagations. The axis offset $\Phi_0^{\tilde{D}} - \Phi_1^{\tilde{D}}$ however keeps the main features of its distribution under influence of only the angular uncertainty. Again, as the uncertainties do not coincide, the angle becomes

very uncertain and the distribution spreads all over the domain.

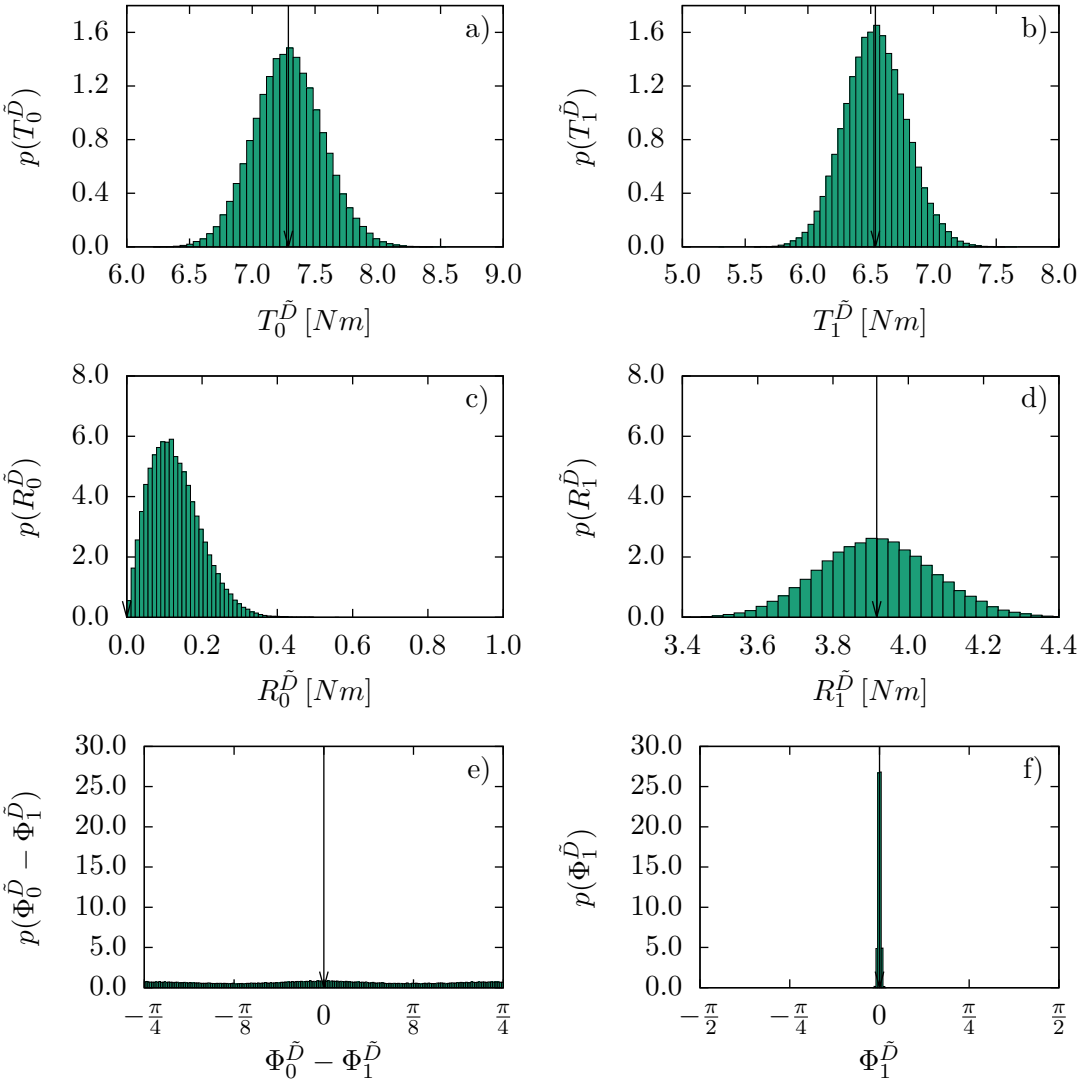

Fig. III.24 *Histograms of layup L2 (Table III.7) with uncertain ply angles and uncertain ply thicknesses. The standard deviation of the ply angles is* 1°*, and the CoV on ply thicknesses is* 5%*. The histograms are obtained with Monte Carlo simulation using* 10^5 *samples.*

The corresponding response in critical flutter velocity is given in Figure III.25. The response again resembles more the response to the thickness uncertainty, and any growth of the uncertainty over this response type is not noticeable. As before, the 15% offset seems very conservative with respect to the calculated uncertainty.

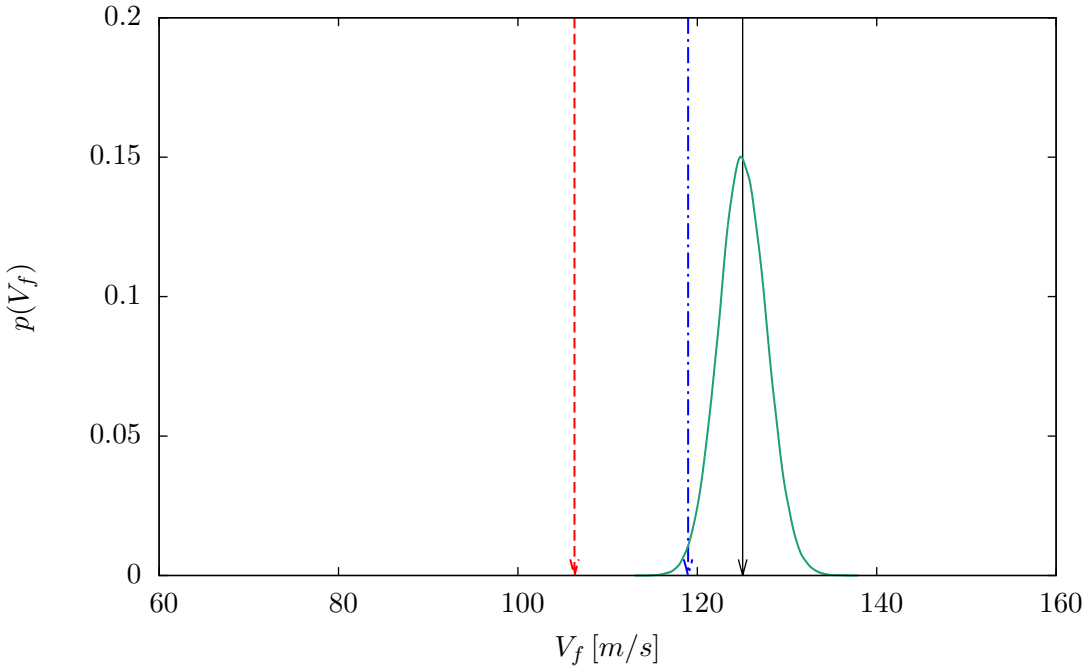

Fig. III.25 *Gaussian KDE of critical flutter velocity (V_f) response for layup L2 (Table III.7) on uncertain ply angles with a standard deviation of 1° and uncertain ply thicknesses with a CoV of 5%. The KDE is obtained by Monte Carlo simulation with 10^5 samples*

III.3.3 Configurations prone to mode switching

The previous examples showed configurations which are found in a smooth vicinity in terms of modal response and critical flutter velocity. The L5 and L6 layup sequences will be tested where mode switches are present in the region around the composite configurations. It will be observed if the uncertainties can provoke a discontinuity in behaviour.

a) Optimal configuration L5

Configuration L5 is especially critical, as it is located directly next to the mode switch in the orthotropic plane (Figure III.2). At the same time, it represents the optimal orthotropic configuration in terms of critical flutter velocity. Consequently, there is a double interest to study the effects of the uncertainties onthis particular layup.

The response of the polar parameters for configuration L5 to the uncertain ply angles is shown in Figure III.26. As it is a general orthotropic laminate, both anisotropic parameters are non-zero by default. Consequently, its behaviour is similar to the L3 and L4 examples, with bell-shaped curves around the nominal values of the polar parameters. The well-defined strong anisotropy also leads to the angular distributions being very narrow.

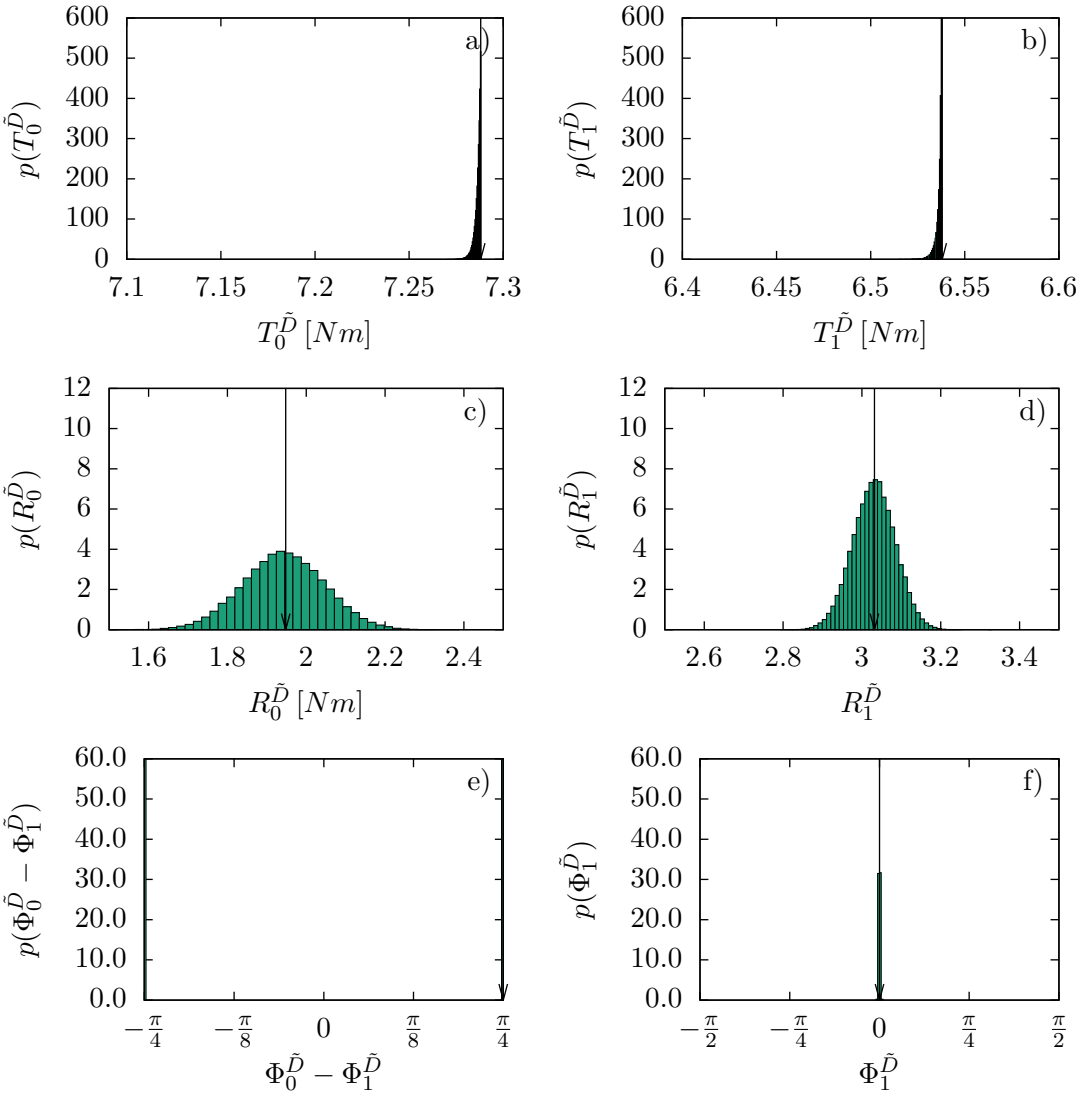

Fig. III.26 *Histogram of layup L5 (Table III.7) with uncertain ply angles. The standard deviation of the ply angles is* 1°. *The histograms are obtained with Monte Carlo simulation using* 10^5 *samples.*

The response of the critical flutter velocity to the uncertainty in the laminate is shown in Figure III.27. Clearly, the mode switch discovered in the deterministic response surface is trigerred, which is visible in the distribution because the curve is split into two "bumps". The more important one is close to the nominal value. However, its maximum probability density point does not coincide with the critical flutter velocity of the nominal configuration, but falls below. This is due to the nominal value being the maximum critical flutter velocity. The second probability density mass is found at values between about 85 and 90$[m/s]$. It is smaller than the main one. It is slightly skewed to the left.

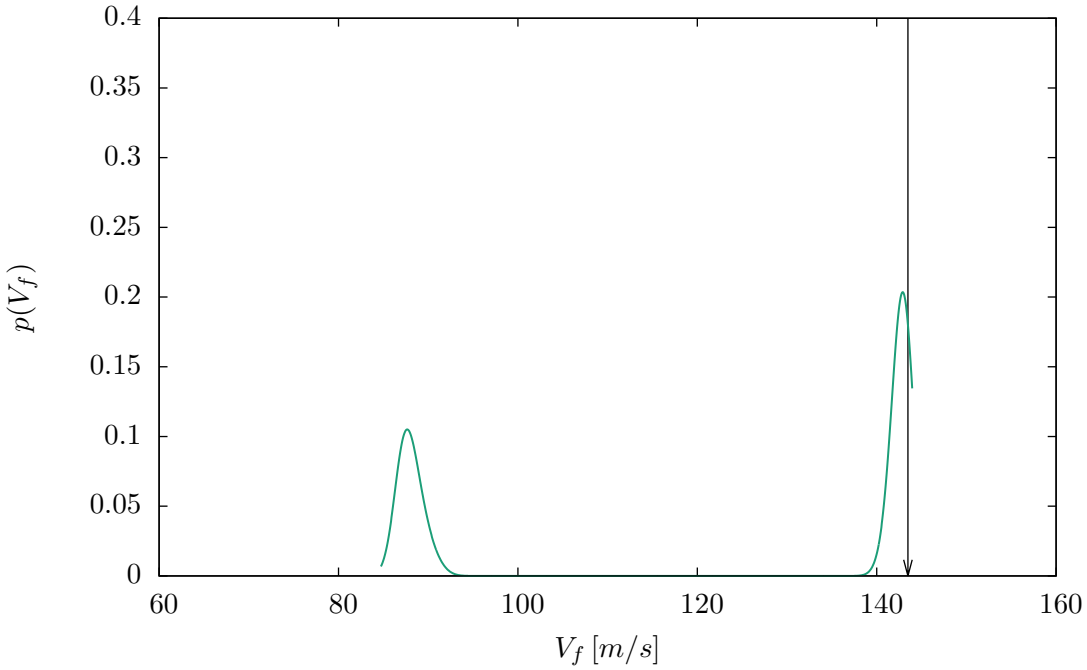

Fig. III.27 *Gaussian KDE of critical flutter velocity (V_f) response for layup L5 (Table III.7) on uncertain ply angles with a standard deviation of* 1°. *The KDE is obtained by Monte Carlo simulation with* 10^5 *samples*

Figure III.28 shows the propagation result from the thickness uncertainties to uncertainties in the polar parameters. As in the previous examples of the thickness uncertainties showing general orthotropic laminates (i. e. Figure III.10), the distributions of the anisotropic polar parameters $R_0^{\tilde{D}}$ and $R_1^{\tilde{D}}$ show bell-shaped curves. The fact that the nominal case is on the border of the orthotropic domain does not seem to impact the propagation of the uncertainties. Also, the polar angles $\Phi_0^{\tilde{D}}$ and $\Phi_1^{\tilde{D}}$ show a higher variance than in the previous examples.

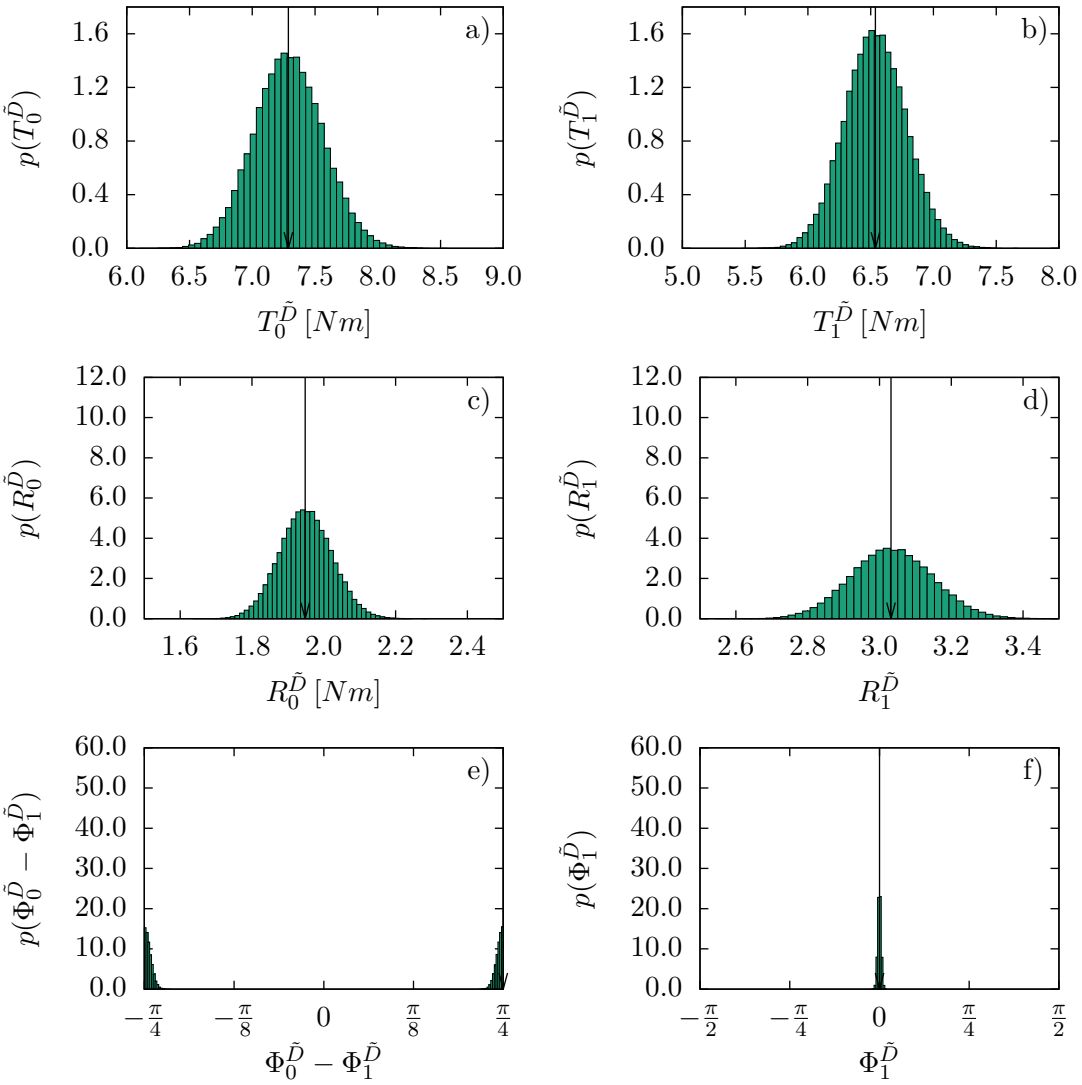

Fig. III.28 *Histograms of layup L5 (Table III.7) with uncertain ply thickness. The CoV of the ply thickness is* 5%. *The histograms are obtained with Monte Carlo simulation using* 10^5 *samples*

Figure III.29 shows the propagation results in terms of critical flutter velocity. As it can clearly be noticed, despite the fact that the uncertainty does not change the directions of the plies, it changes the stiffness properties sufficiently to push the flutter mode to a different modal behaviour, leading to the previously observed switching phenomenon. The second probability density mass, lying way below the nominal value, is even bigger than in the case of ply angle uncertainty only.

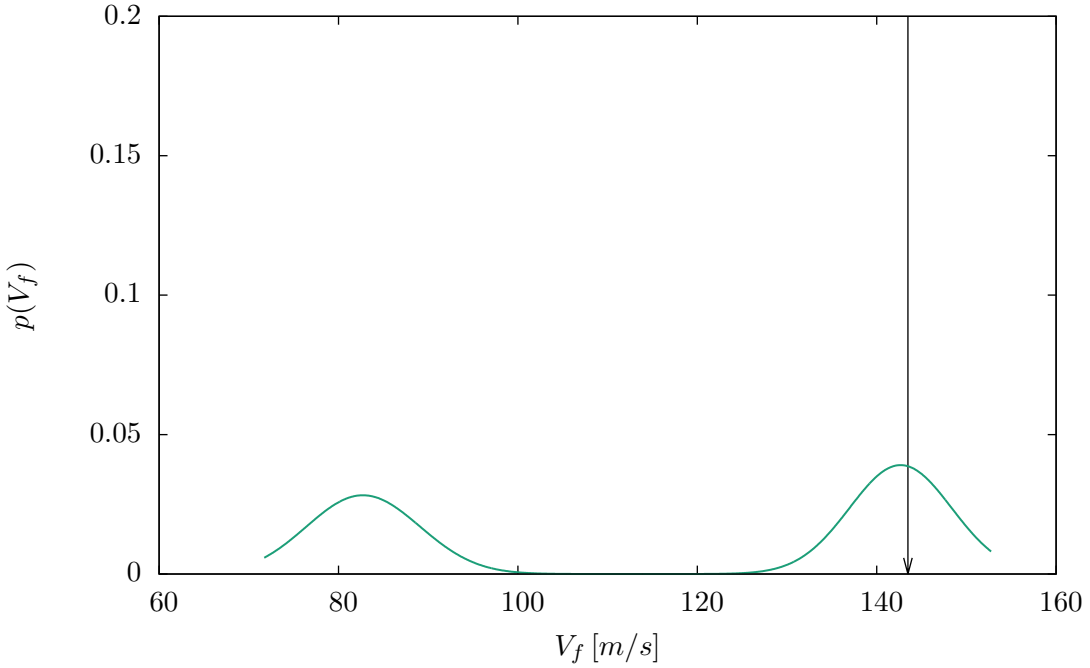

Fig. III.29 *Gaussian KDE of critical flutter velocity (V_f) response for layup L5 (Table III.7) on uncertain ply thickness with a CoV of 5%. The KDE is obtained by Monte Carlo simulation with 10^5 samples.*

In the following, it will be studied if the coupling of the two influences has consequences for the triggering of the mode switch. For the purpose of detecting changes in the material behaviour beforehand, the histograms for the polar parameters are given in Figure III.30. It can be observed that the behaviour of the anisotropic parameters is a mix of the behaviours observed under the individual uncertainties. While in the thickness-only case, $R_1^{\tilde{D}}$ is the more uncertain parameter, $R_0^{\tilde{D}}$ was in the case of the angular uncertainty. However, the distributions resemble each other more in the case of the combined uncertainty. The polar angles, however, take over their more uncertaint behaviour from the thickness uncertainty case.

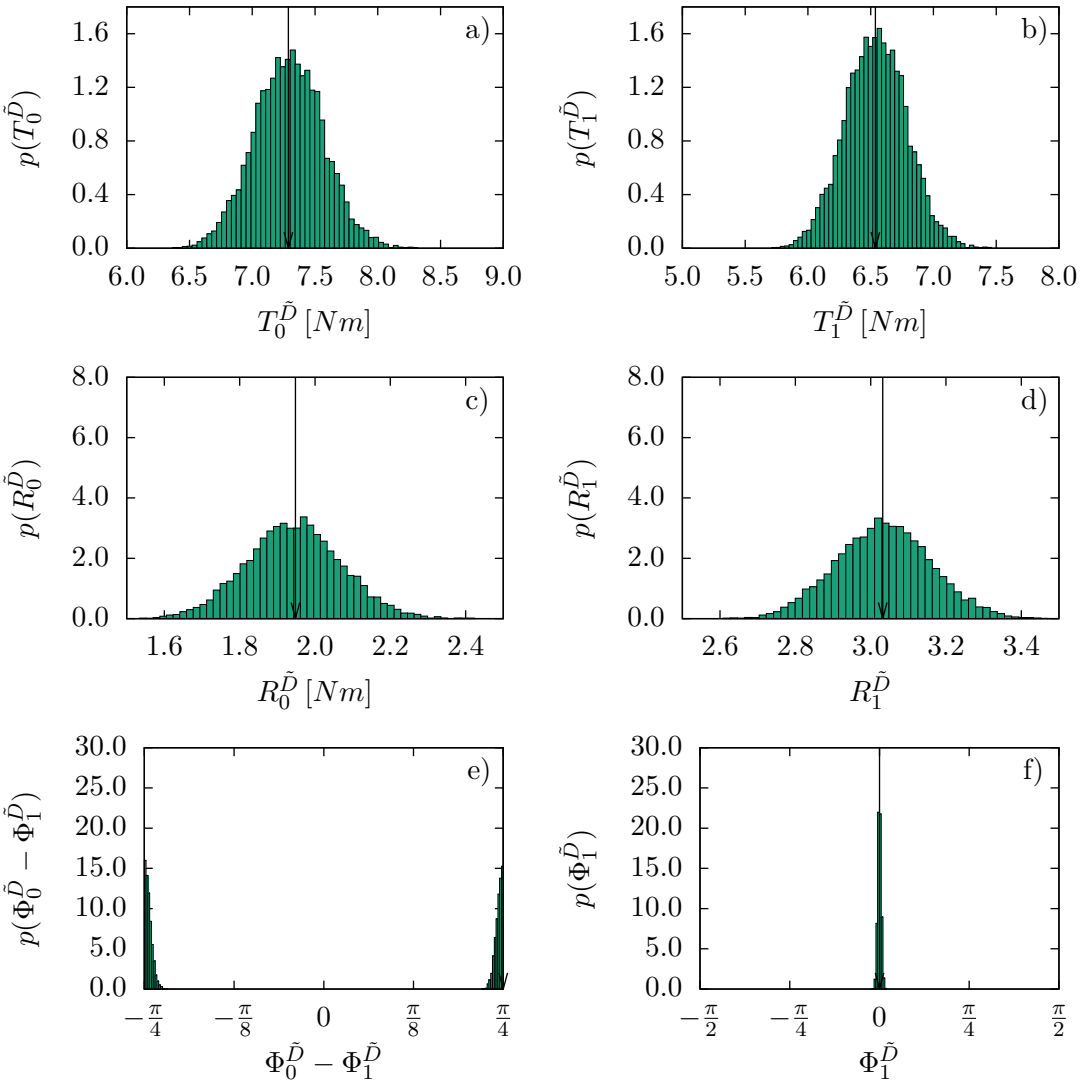

Fig. III.30 *Histograms of layup L5 (Table III.7) with uncertain ply angles and uncertain ply thicknesses. The standard deviation on ply angles is* 1°*, and the CoV on the ply thicknesses is* 5%*. The histograms are obtained with Monte Carlo simulation using* 10^5 *samples.*

The critical flutter velocity result is shown in Figure III.31. Again, the result resembles the thickness-only case more, but the "skewing" of the curves as in the angular uncertainty case is perceptible. It is also noticed that the variance of the different "bumps" of the distribution is reduced, but this could also be due to different values for the bandwidth parameter of the kernel density estimation. In this case, the uncertainty clearly leads to the usual 15% velocity offset security margin being undercut, which is highlighted by the fact that the estimate for the 1% quantile is found left of the security margin. Also, a significant probability density mass is found left of the classical margin. As the L5 layup represents the point of optimal critical flutter velocity, this means that there is a security risk of blindly optimising without checking for robustness. Moreover, in a case where mode switching and thus brutal changes of the critical flutter velocity occur as a consequence of manufacturing uncertainty, the classical flutter margin does not provide security against failures.

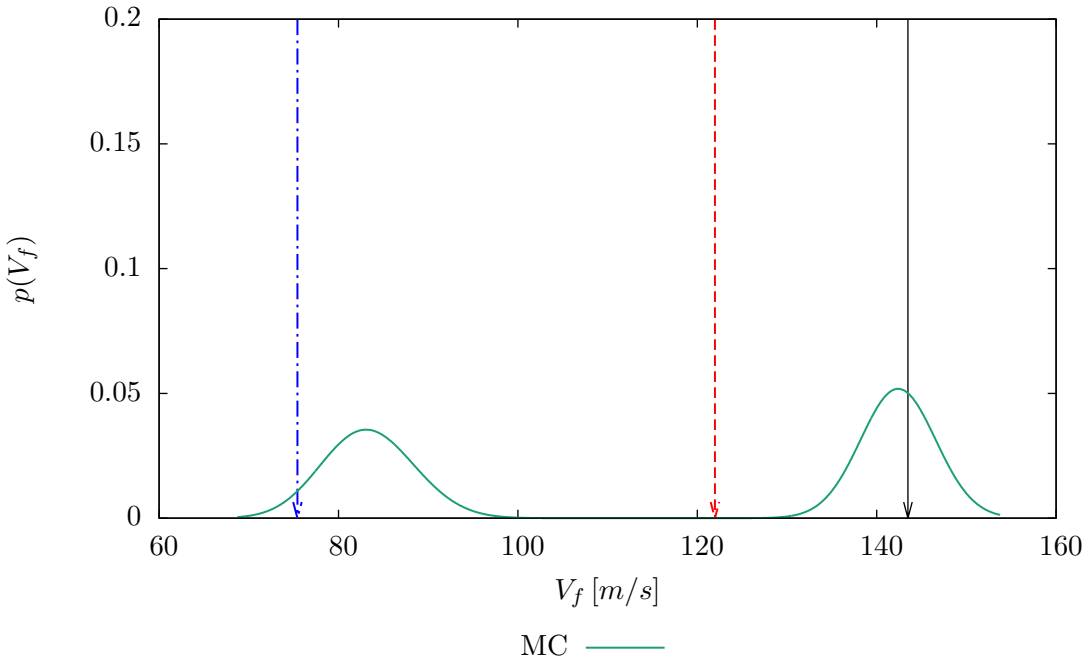

Fig. III.31 *Gaussian KDE of critical flutter velocity (V_f) response for layup L5 (Table III.7) on uncertain ply angles with a standard deviation of* 1° *and uncertain ply thicknesses with a CoV of* 5%*. The KDE is obtained by Monte Carlo simulation with* 10^5 *samples.*

b) Offset from the mode switch L6

The L6 example will be used to determine if the uncertainty in the ply thicknesses is also capable of triggering the mode switch in a more "accidental" scenario where the nominal configuration is not tightly placed in vicinity of the mode switch.

The uncertain polar properties of the final example laminate L6 are shown in Figure III.32. As a general orthotropic laminate of which the nominal polar properties are close to L5, its polar parameter distributions are very similar. However, the offset between the polar angles is more uncertain than in the previous case.

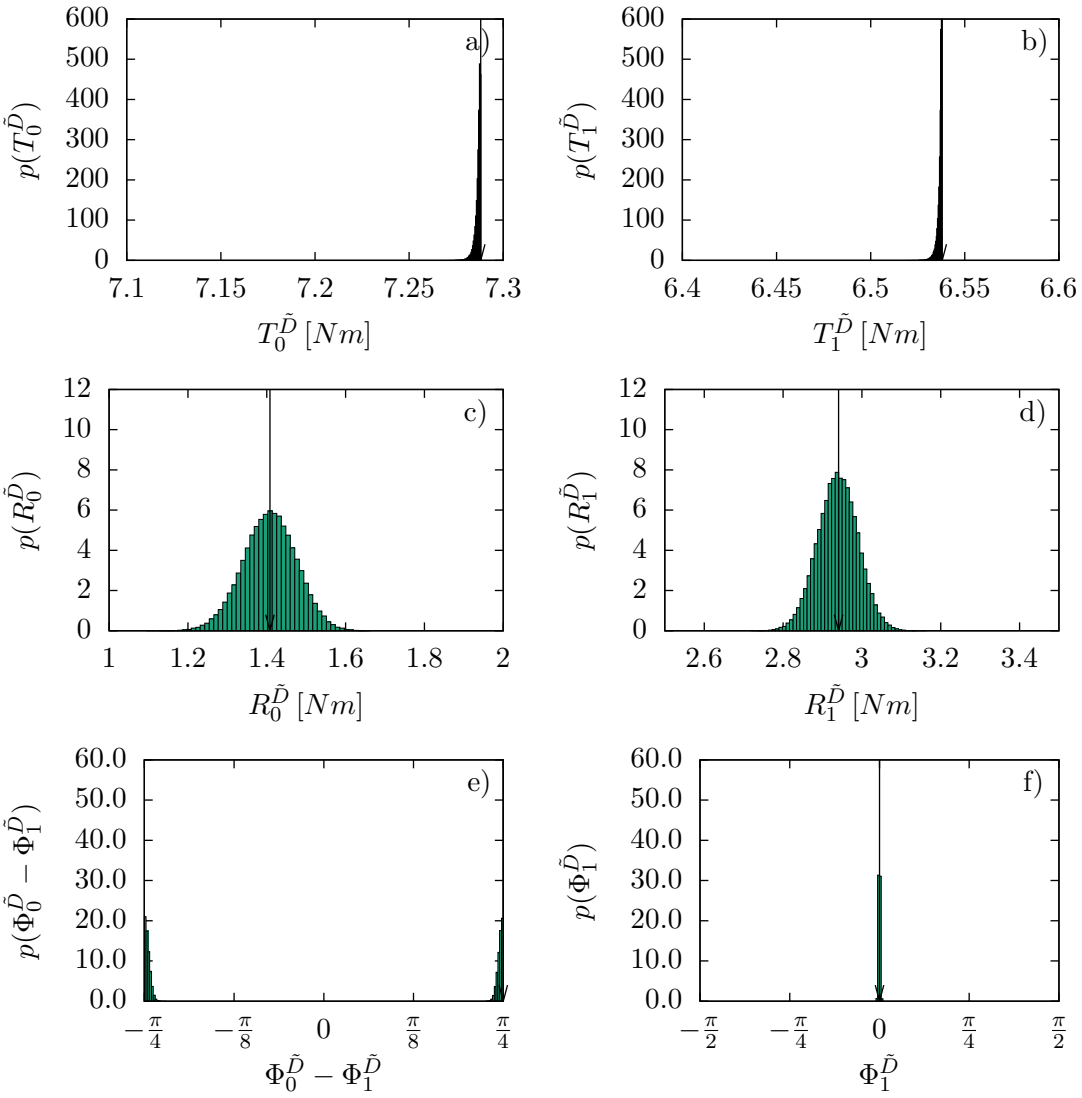

Fig. III.32 *Histogram of layup L6 (Table III.7) with uncertain ply angles. The standard deviation of the ply angles is* 1°. *The histograms are obtained with Monte Carlo simulation using* 10^5 *samples.*

The laminate L6 was deliberately chosen to have an offset from the mode switch. As can be seen in Figure III.33, this leads to the mode switch being barely passed. However, besides the main probability density mass distributed quite fairly around the critical flutter velocity of the nominal configuration, a much smaller probability density "bump" is present at around $80[m/s]$. This value is lower than the secondary probability density

mass in the previous example.

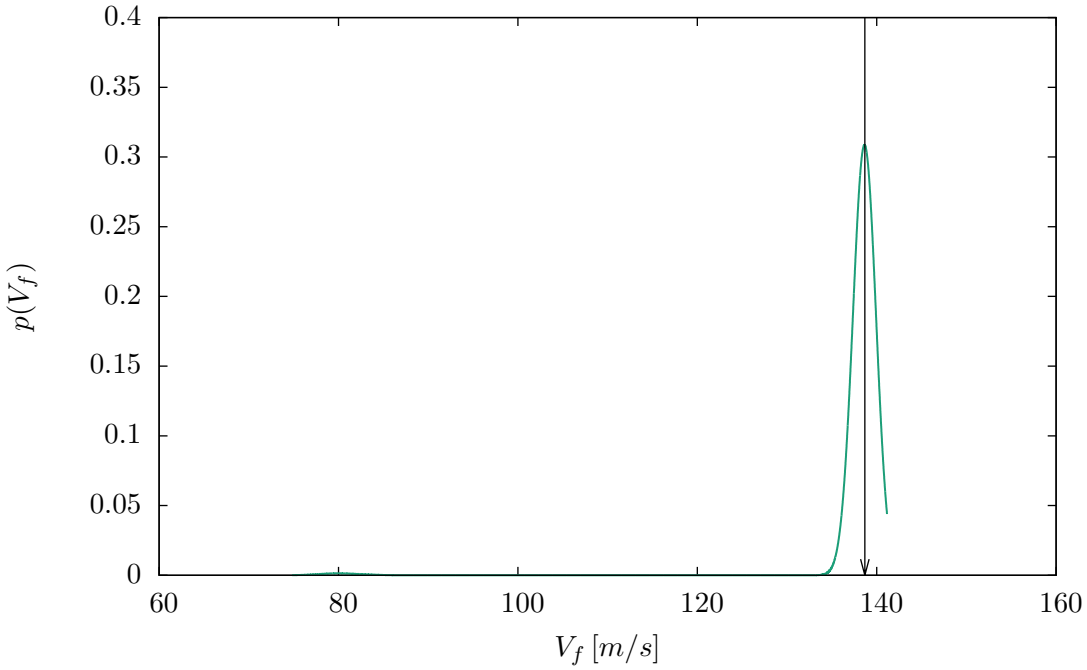

Fig. III.33 *Gaussian KDE of critical flutter velocity (V_f) response for layup L6 (Table III.7) on uncertain ply angles with a standard deviation of* 1°*. The KDE is obtained by Monte Carlo simulation with* 10^5 *samples.*

Figure III.34 shows the uncertainty in the polar parameters due to the uncertainties in the ply thicknesses of layup L6. As the layup is close in nominal polar parameters to the layup L5 that was examined in the last case, also the uncertainty is similar, apart from the slightly lower nominal values in the anisotropic polar parameters. The very different structure of the laminate does not affect the polar properties as much as in the comparison given between the laminates L3 and L4. Features like the higher uncertainty in the polar angles are also found in this case.

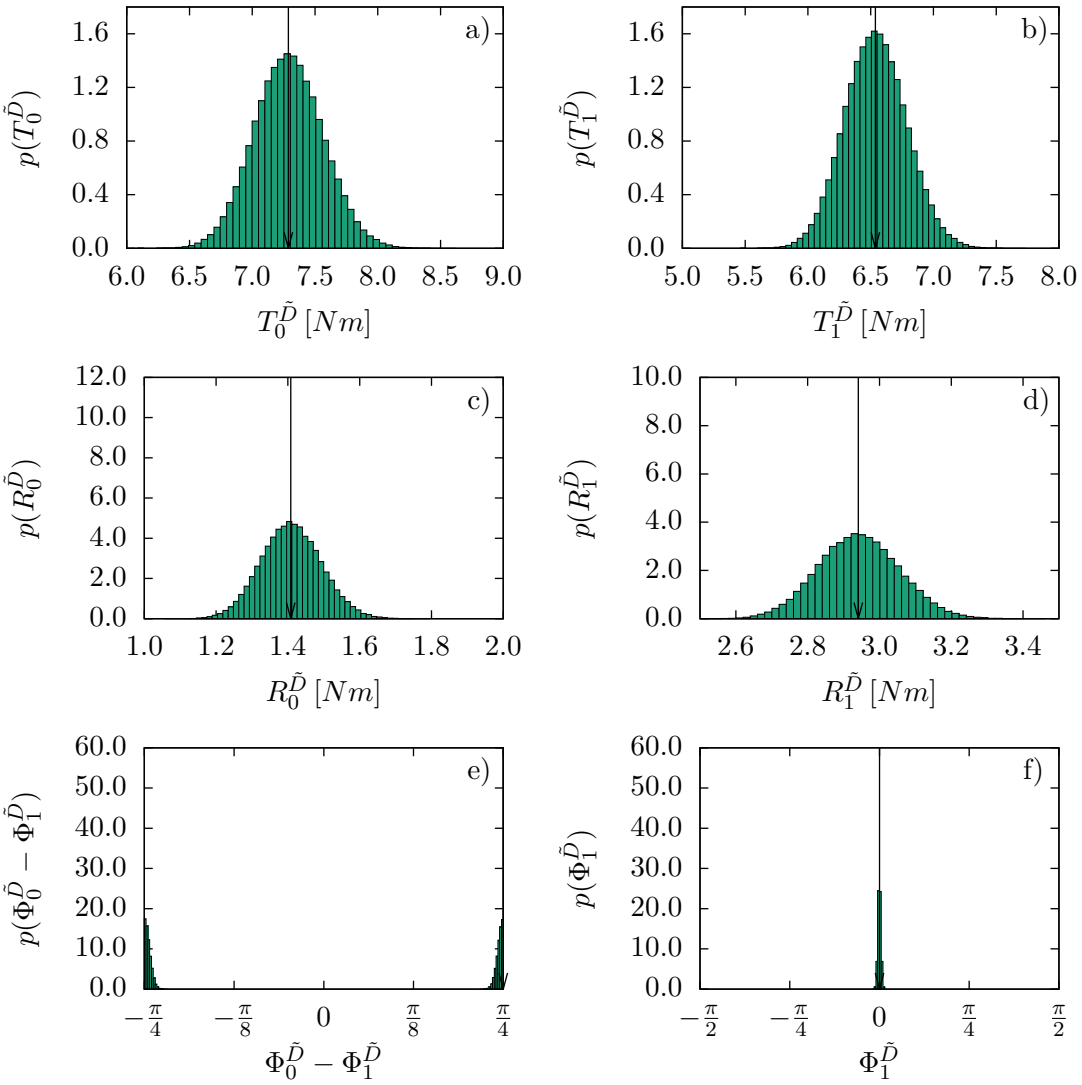

Fig. III.34 *Histograms of layup L5 (Table III.7) with uncertain ply thickness. CoV on ply thickness is* 5%*, histograms obtained with Monte Carlo simulation using* 10^5 *samples*

The propagation results for the critical flutter velocity are given in Figure III.35. Again, the uncertainty is sufficient to trigger the mode switch, as a second probability density mass can be identified at around $75[m/s]$. However, this second probability density mass is way smaller than in the previous example and also smaller than in the propagation of the angular uncertainty. Contrarily to the angular uncertainty example and also the L5 case, the main probability density mass gets a narrower distribution.

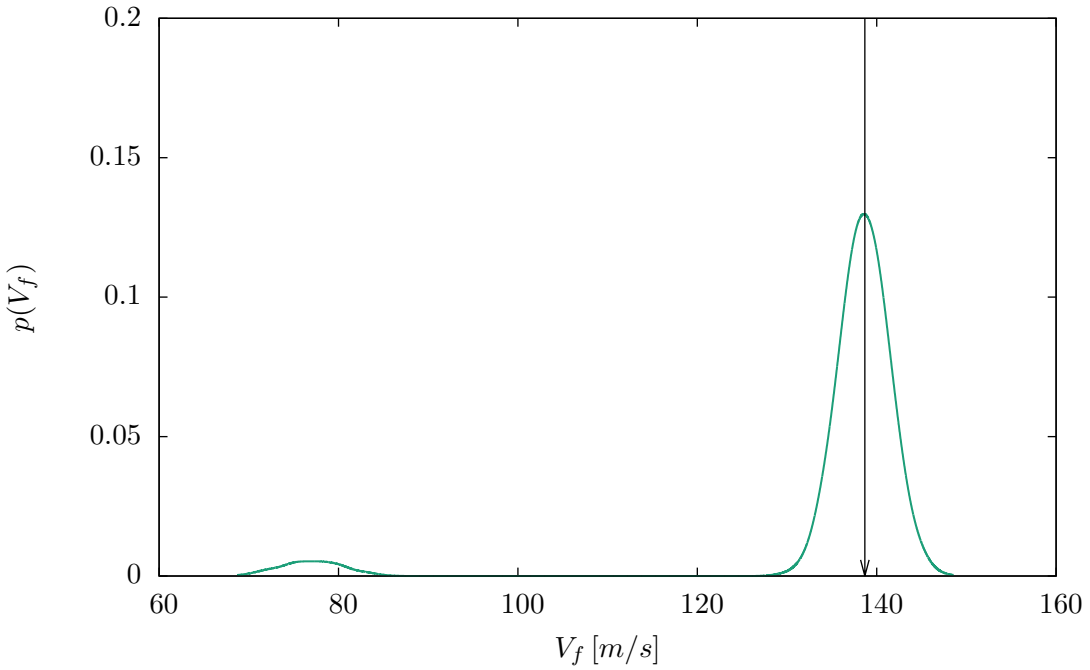

Fig. III.35 *Gaussian KDE of critical flutter velocity (V_f) response for layup L6 (Table III.7) on uncertain ply thickness with a CoV of* 5%. *The KDE is obtained by Monte Carlo simulation with* 10^5 *samples.*

The polar parameter distributions for L6 under the combined influences of the two types of uncertainty are shown in Figure III.36. As in the propagation examples of the individual uncertainties, the distributions are close to those of laminate L5 due to the polar parameters being close. The differences in the layup do not lead to significant differences in polar parameter distributions in this case. As in the L5 example, both of the anisotropic moduli are distributed following bell-shaped histograms roughly centered around the nominal value, with no noticeable difference in uncertainty. Again, the polar angles are narrowly distributed around their nominal values which means that the direction of the anisotropic behaviour stays well-defined despite the uncertainties.

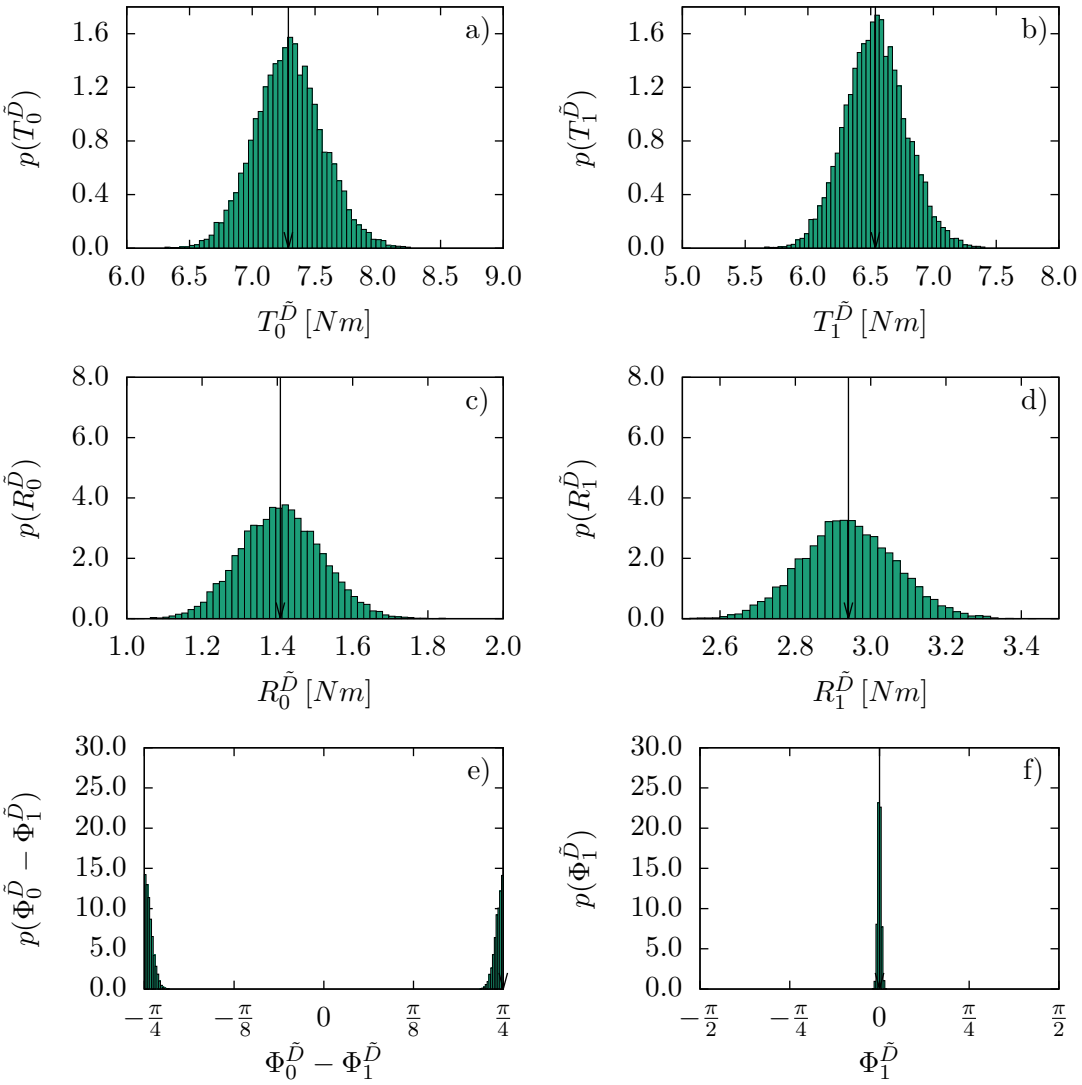

Fig. III.36 *Histograms of layup L6 (Table III.7) with uncertain ply angles and uncertain ply thicknesses. The standard deviation of the ply angles is* 1°, *and the CoV of the ply thicknesses is* 5%. *The histograms are obtained with Monte Carlo simulation using* 10^5 *samples.*

When looking at the results for V_f given in Figure III.37, the mode switch can be noticed again. The probability density mass on the lower-velocity side of the switch is clearly higher than in the angular uncertainty case and roughly equivalent to the thickness uncertainty case. The main probability density mass seems to be widened with respect to the thickness-uncertainty-only case.

Again, there is a significant probability density mass for critical flutter velocities below the 15% security margin. This shows that it is not necessary to have a configuration placed directly next to a mode switch to have a significant number of realisations fall into a range below the classical security margins, and consequently representing a great risk. This can be visualised by the estimate of the 1% quantile, which is way lower than the 15% security margin.

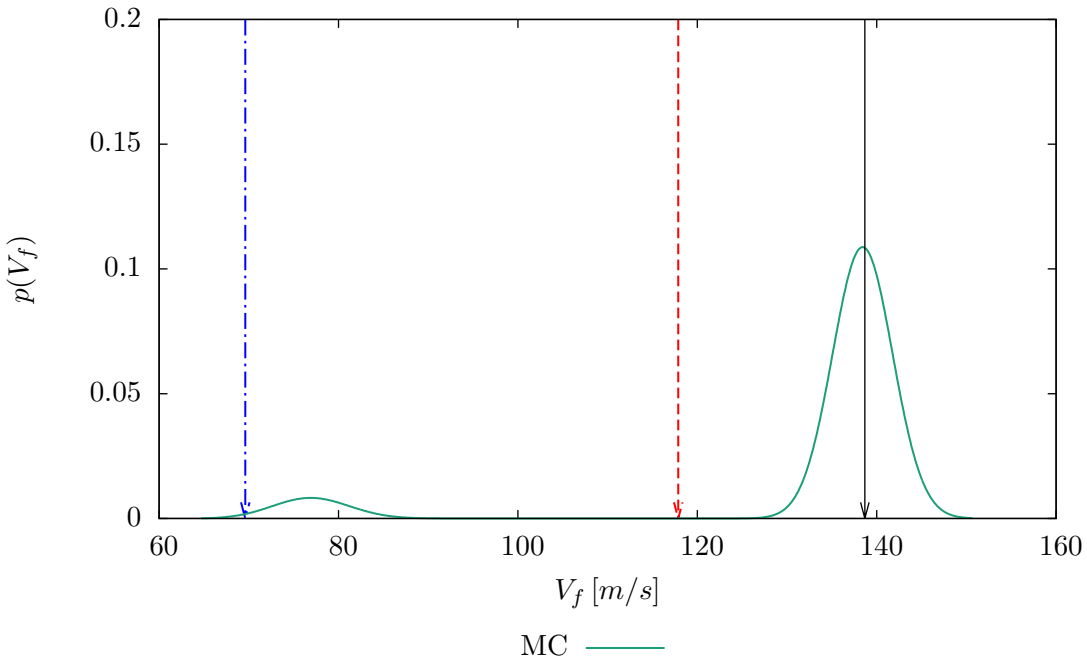

Fig. III.37 *Gaussian KDE of critical flutter velocity (V_f) response for layup L5 (Table III.7) on uncertain ply angles with a standard deviation of* 1° *and uncertain ply thicknesses with a CoV of* 5%*. The KDE is obtained by Monte Carlo simulation with* 10^5 *samples.*

III.4 Acceleration via polynomial chaos and the polar method

In the previous section, Monte Carlo simulation was used to investigate the uncertainties in ply thickness and ply angles in the composite plate wing case. However, due to the high number of solver runs necessary, Monte Carlo simulation becomes cost-prohibitive already for slightly more complex solvers than the one used in the present study. In the following, a method will be proposed in order to lower the number of direct runs of the

solver necessary for the uncertainty quantification. A popular method for acceleration in stochastic aeroelasticity is polynomial chaos. It is based on a spectral polynomial expansion in the stochastic space [82]

$$u(\boldsymbol{\theta}) = \sum_{i=1}^{M} \hat{u}_i \phi_i(\boldsymbol{\theta}) \tag{III.18}$$

where the Φ_i are orthogonal polynomials and the $\hat{u}_i$ are the so-called expansion coefficients by which the polynomial base functions are weighted. The response u corresponds here to the critical flutter velocity V_f, and the $\boldsymbol{\theta}$ denote the vector of uncertain parameters. The number of terms M is given by the following formula [75]

$$M = \frac{(P+N)!}{P!N!} - 1 \tag{III.19}$$

where P is the polynomial order, and N is the dimension of the parameter vector $\boldsymbol{\theta}$. In the case of interest of laminated composite structures, the number N of stochastic parameters is directly proportional to the number of constitutive layers in the stack. In the case of study here, the number of layers is set to sixteen, meaning sixteen uncertain orientation angles and sixteen uncertain ply thicknesses (i.e. $N = 32$). In the realistic case of more complex aeronautical structures, not only the number of constitutive layers can be higher, but there might also be several different layups to be considered. The dependence of the number on terms in the expansion expressed by formula (III.19) is the reason why polynomial chaos cannot be directly applied on the uncertanties on ply angles and thicknesses, as the computation of the expansion coefficients becomes expensive (a phenomenon referred to as "curse of dimensionality" [29]).

Alternatively, one can use homogenised elastic parameters in order to represent the uncertain behaviour of the laminate, such as the laminations parameters as it is done in [114]. In this work, the polar method is used to this purpose. As already explained in section III.1, the polar representation has several advantages with respect to the lamination parameters:

- It can be applied to any elastic tensor. Here the tensor of interest is the modified bending stiffness tensor $\tilde{\mathbf{D}}$.
- It provides general expressions of the laminate's homogenised tensors, so that it does not imply any simplifying hypothesis on the selected stacking sequences nor on the uncertainties:
  - Unsymmetrical and elastically coupled layups can be considered (general uncertainty on the ply angles),
  - as well as laminates with different layers (uncertainties on ply thicknesses).

However, the probability distribution of laminate's homogenised elastic parameters, such as polar parameters, is not Gaussian any more but arbitrary, and the polar parameters do not behave as independent stochastic variables, but they are correlated through the laminate's stacking sequence.

Soize and Ghanem [118] proposed an extension of the polynomial chaos method to arbitrary distributions, which was demonstrated to work with correlated distributions by [94]. This method is often referred to as "arbitrary polynomial chaos" (e. g. [101]). In the following, the method is presented in detail and applied to the problem of the composite plate wing.

III.4.1 Polynomial chaos for arbitrary distributions

The arbitrary polynomial chaos (aPC) approach uses Gram-Schmidt orthogonalisation to provide the necessary orthogonal polynomial basis for the expansion Equation III.18. Using this approach, polynomial chaos can be deployed on the composite plate wing problem with uncertain ply thicknesses and uncertain ply angles, where the vector θ of the stochastic parameters includes the six modified bending polar parameters $T_0^{\tilde{D}}$, etc.

In the framework of the Gram-Schmid algorithm, orthogonality of the polynomials ϕ_i is defined by a scalar product. The scalar product with respect to the joint probability density function $p(\boldsymbol{\theta})$ reads [94]

$$\langle \phi_i, \phi_j \rangle = \int_{\boldsymbol{\Theta}} \phi_i(\boldsymbol{\theta}) \phi_j(\boldsymbol{\theta}) p(\boldsymbol{\theta}) d\boldsymbol{\theta} = \mathbb{E}\{\phi_i(\boldsymbol{\theta})^2\} \delta_{ij} \tag{III.20}$$

The orthogonalisation is carried out by performing a series of subtractions of newly added monomials $e_j = \{1, \theta_1, \theta_2, \ldots, \theta_6, \theta_1^2, \theta_1\theta_2, \theta_1\theta_3, \ldots\}$ to ensure orthogonality with the polynomials created in the previous steps. The steps are as follows [94]

$$\phi_0(\boldsymbol{\theta}) = 1 \tag{III.21}$$

$$\phi_j(\boldsymbol{\theta}) = e_j(\boldsymbol{\theta}) - \sum_{k=0}^{j-1} c_{jk} \phi_k(\boldsymbol{\theta}) \tag{III.22}$$

The coefficients c_{jk} are again calculated using the scalar product Equation (III.20) [94]

$$c_{jk} = \frac{\langle e_j(\boldsymbol{\theta}), \phi_k(\boldsymbol{\theta}) \rangle}{\langle \phi_k(\boldsymbol{\theta}), \phi_k(\boldsymbol{\theta}) \rangle} \tag{III.23}$$

The integrals can be evaluated using different methods. While quadratures are an option, Navarro Jimenez, M.I. et al. [94] use moment-generating functions. However, in the present case, neither moment-generating functions nor an analytical form of the distribution function is available for the distribution of the polar parameters. The integrals are thus computed using the Monte Carlo method. This is computationally cheap since only polynomial evaluations need to be carried out and no calls to solvers are involved. However, this method limits the precision of the approach. Several tests highlighting this problem are shown in Appendix B.

Beside the orthogonal polynomials, the weighting coefficients $\hat{u}_j$ need to be computed in order to obtain an approximation of the stochastic response surface. Normally, this is done again by use of the orthogonality relation Equation (III.20) as [75]

$$\hat{u}_i = \frac{\langle u(\boldsymbol{\theta}), \phi_i(\boldsymbol{\theta}) \rangle}{\langle \phi_i(\boldsymbol{\theta}), \phi_i(\boldsymbol{\theta}) \rangle} \tag{III.24}$$

In generalised polynomial chaos, these coefficients are computed using quadratures which are adapted to the distribution. However, as the distribution is not known in this case, again, quadratures are not available. Instead, a least-squares fit on a set of random points in the polar parameter space following their distribution is performed [114].

A summary of the complete arbitrary polynomial chaos expansion for the response surface in V_f is given in Figure III.38.

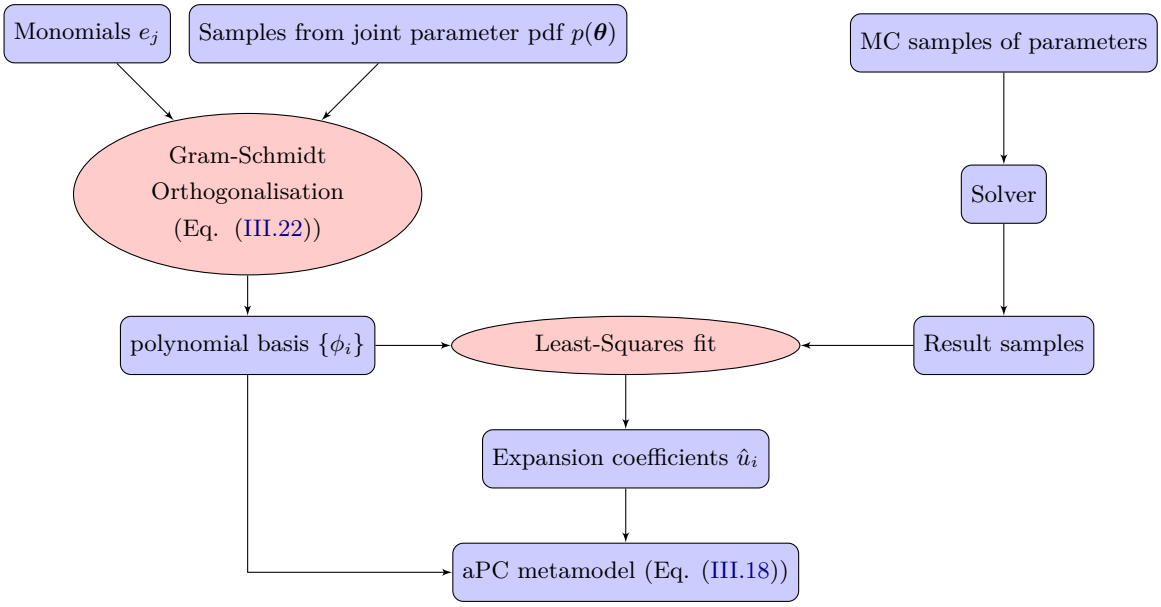

Fig. III.38 *Flowchart of the response surface construction using arbitrary polynomial chaos with Monte Carlo integration and least squares fitting of the expansion coefficients*

III.4.2 Dealing with discontinuous response surfaces

While global polynomial chaos approaches like the one given in the previous section work well for smooth response surfaces, they have difficulties when discontinuities in the response surface occur [114]. For demonstration purposes, Figure III.39 shows the above approach applied without any further measures in the case of laminate L5, where a mode switch due to the uncertain material caused a discontinuity in velocity response. It is clear that the approximation provided by global arbitrary polynomial chaos (dashed orangle

line in Figure III.39) does not properly capture the two peaks of probability for V_f due to the presence of the discontinuity in the random space.

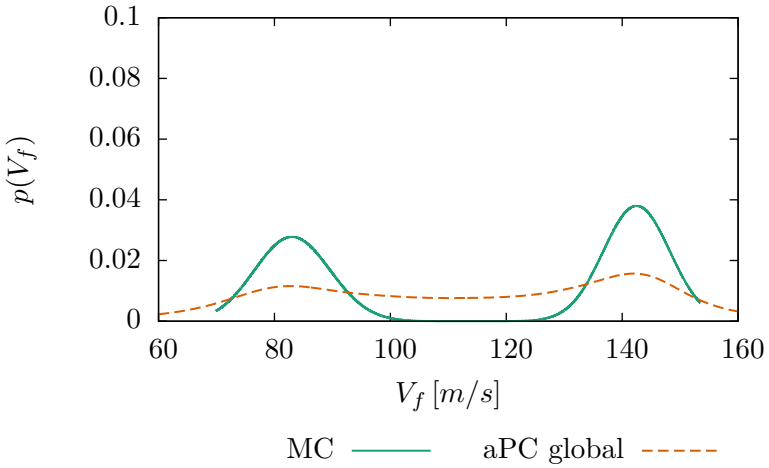

Fig. III.39 *Global aPC of polynomial order three with* 10^5 *samples for orthogonalisation of the polynomials and 200 samples for least squares fitting vs Monte Carlo simulation with* 10^5 *samples*

In [114], it has been proposed to split the response surface along the discontinuity using a convex-hull approach, in order to prevent the problems associated with the global response surface approximation. In this work, an approach based on machine-learning algorithms is developed, which is easier to automate and avoids the problem of samples falling outside the regions identified by a convex hull approach after a preliminary sampling.

The machine learning approach used in this work has two main steps.

- In the first step, samples from a preliminary Monte Carlo simulation with only few samples are used to identify the modal regimes using a clustering algorithm. These samples are reused in the fitting of the final aPC model in order to avoid additional calls to the solver.
- In a second step, the information from the clustering step will be used to classify samples and attribute them to one of the modal regimes identified in the first step. The classified samples are then fed into the aPC method by modal regime.

In order to identify the different modal regimes, the method is fed with both values of the critical flutter velocity V_f and the corresponding flutter frequency ω_f, which is a strong indicator of the change in modal regime. An example of the point cloud received in a propagation of the ply angle and ply thickness uncertainty is given in Figure III.40, where the uncertainty quantification example on laminate L5 is used for demonstration.

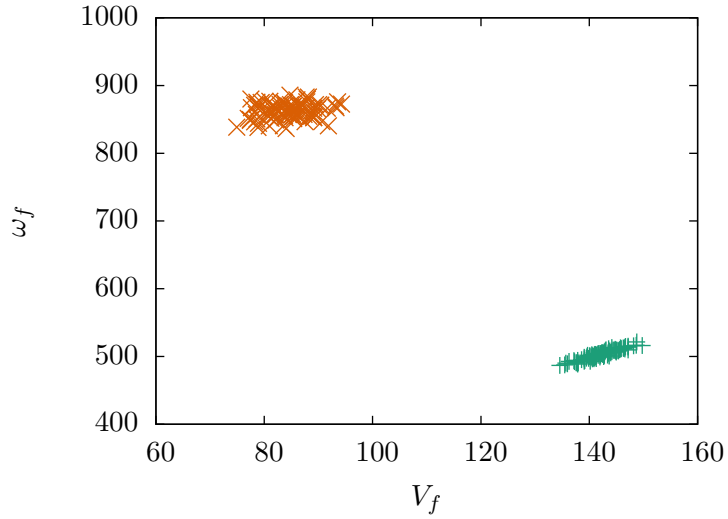

Fig. III.40 *Clouds of example points showing V_f plotted against ω_f for layup L5 (Table III.7). The colors indicate the results of the DBSCAN clustering.*

As it is the case in Figure III.2, when a mode switch occurs, most of the time either the critical flutter velocity V_f or the flutter fequency ω_f change drastically (Figure III.40) . Most of the time, even both V_f and ω_f change at the same time. This leads to the points of different modal regimes being separated by regions where practically no points occur. This is the scenario for which the DBSCAN algorithm was designed [40]. Consequently, it is the algorithm of choice for the clustering step in this work, where the implementation in *scikit-learn*[104] in version 0.19.0 is used. Moreover, it has the advantage of not taking the number of clusters as parameter, which is desired because generally, the number of modal regimes cannot be guessed in advance with absolute certainty. In order to prevent the algorithm from performing too many splits, the critical core point distance ϵ is adjusted with respect to the typical spread of the cluster and the minimum cluster size is set to ten samples.

The clustering assigns labels to the samples of V_f and ω_f, which each correspond to a set of polar parameters, representing the material properties that led to the result in V_f and ω_f. The labels, along with the polar parameters of the samples, but without the information on V_f and ω_f are then used to train a classification algorithm. Three different algorithms from *scikit-learn* were tested and classification accuracy was evaluated by comparison with a clustering result from a full Monte Carlo simulation providing values of V_f and ω_f on the samples in question. A normalisation of the data is performed before training/classification. The results are shown in Table III.9. As the Multi Layer Perceptron (MLP) Classifier produces the best results, it is retained for the remainder of the study. A summary of how the algorithms are chained in this work is given in Figure III.41. It is interesting to notice that this approach is very general, since it can independently recognise how many clusters/discontinuities happen in the vicinity of the point of interest. In partcular, when the response surface is smooth, one single cluster is automatically detected.

Algorithm	Correctly identified samples (%)
k Nearest Neighbours	92.9%
Support Vector Machine	96.1%
Multi Layer Perceptron Classifier	98.4%

Table III.9 – Percentage of correctly identified samples in a set of 10^5 Monte Carlo samples for configuration L5 (Table III.7).

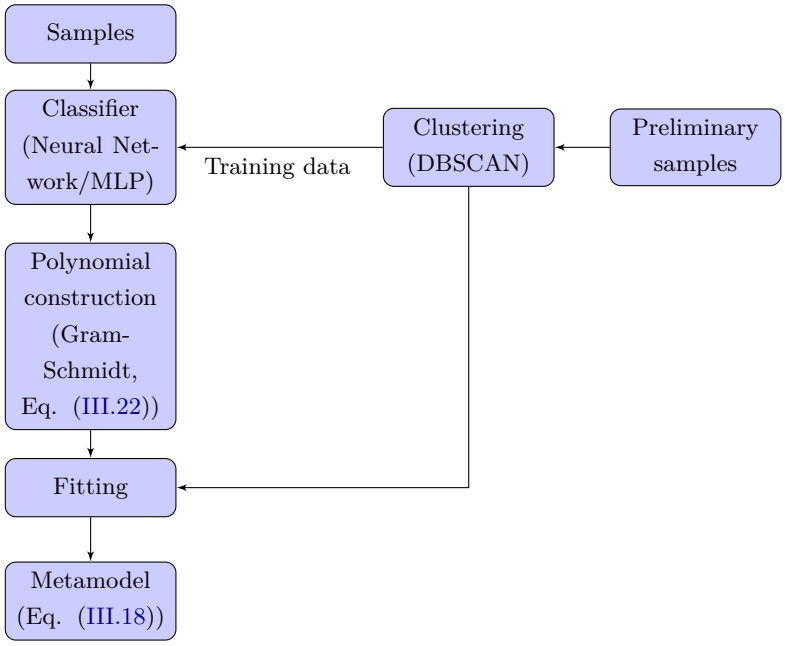

Fig. III.41 *Intervention points of the machine learning approach employed in the aPC framework*

III.4.3 Results of the machine-learning-augmented aPC on the discontinuty

The method introduced above is deployed on the cases L5 and L6, which showed mode switches in their uncertain response. A preliminary sampling is performed with 1000 samples, which serves for the clustering and the fitting of the different response surfaces. The final evaluation is performed with 10^5 samples.

The result for the L5 case is given in Figure III.42. The curves obtained using the machine-learning-augmented aPC method and a comparison KDE obtained using plain Monte Carlo simulation are in satisfactory agreement. Also the mode switch is captured well, as the parts of the distribution are in correct proportion.

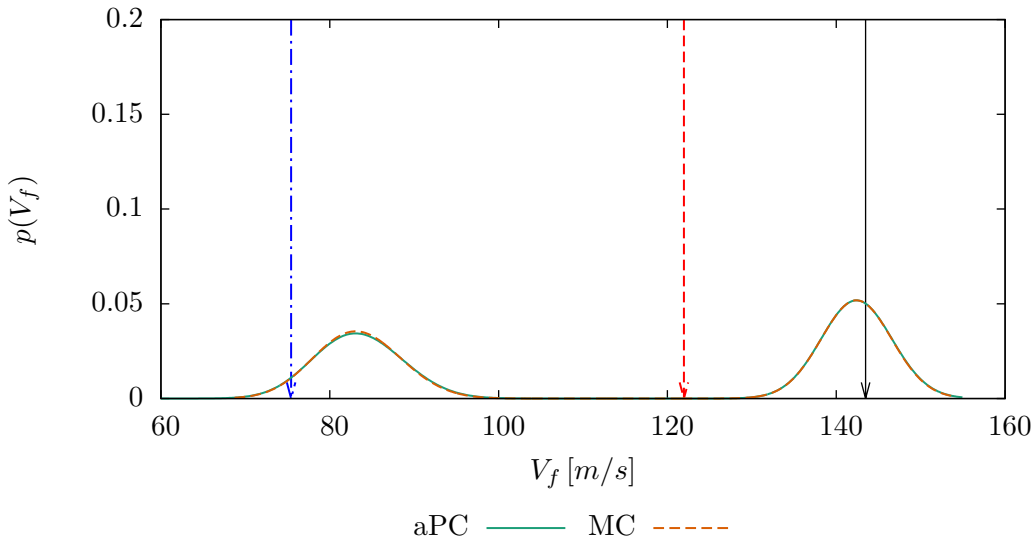

Fig. III.42 *Gaussian KDE of critical flutter velocity (V_f) response for layup L5 (Table III.7) on uncertain ply angles with standard deviation of 1° and uncertain ply thicknesses with a CoV of 5%, obtained by aPC with 10^3 preliminary samples and 10^5 samples on the final response surface. Comparison Monte Carlo simulation has 10^5 samples*

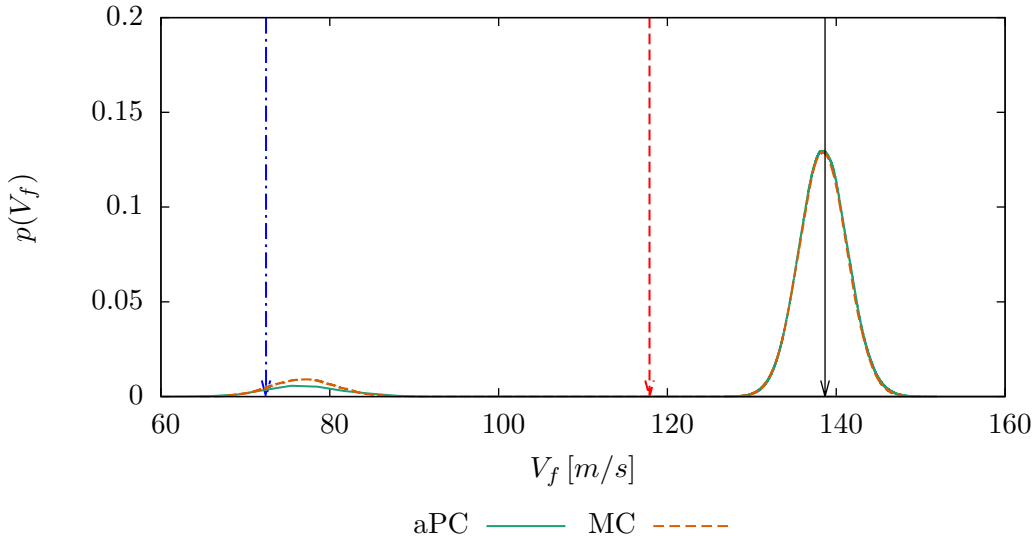

Fig. III.43 *Gaussian KDE of critical flutter velocity (V_f) response for layup L6 (Table III.7) on uncertain ply angles with standard deviation of 1° and uncertain ply thicknesses with a CoV of 5%, obtained by aPC with 10^3 preliminary samples and 10^5 samples on the final response surface. Comparison Monte Carlo simulation has 10^5 samples*

In Figure III.43, the result for the L6 example is shown. This example is more challenging, as few samples fall on the other side of the mode switch, which is difficult to capture by the low-resolution preliminary sampling used for mode identification and the fitting. This impacts the results. Effectively, while the main probability density mass close to the value of V_f obtained with the nominal configuration still is well-resolved, the smaller probability density mass at lower values of V_f shows visible deviation from the comparison obtained with plain Monte Carlo simulation.

In cases where no mode switch occurs, the machine learning aPC method falls back to standard global aPC. This is ensured by the clustering algorithm, which will only identify one unique cluster in that case. The clusters are counted after this process, and when only one cluster is found, the classification step is switched off and only one response surface constructed. An example for that case is given in Figure III.44, where the results are shown for layup L1. Again, the curves are in satisfactory agreement, confirming the performance of the method and demonstrating the fallback after machine learning has only identified one modal regime.

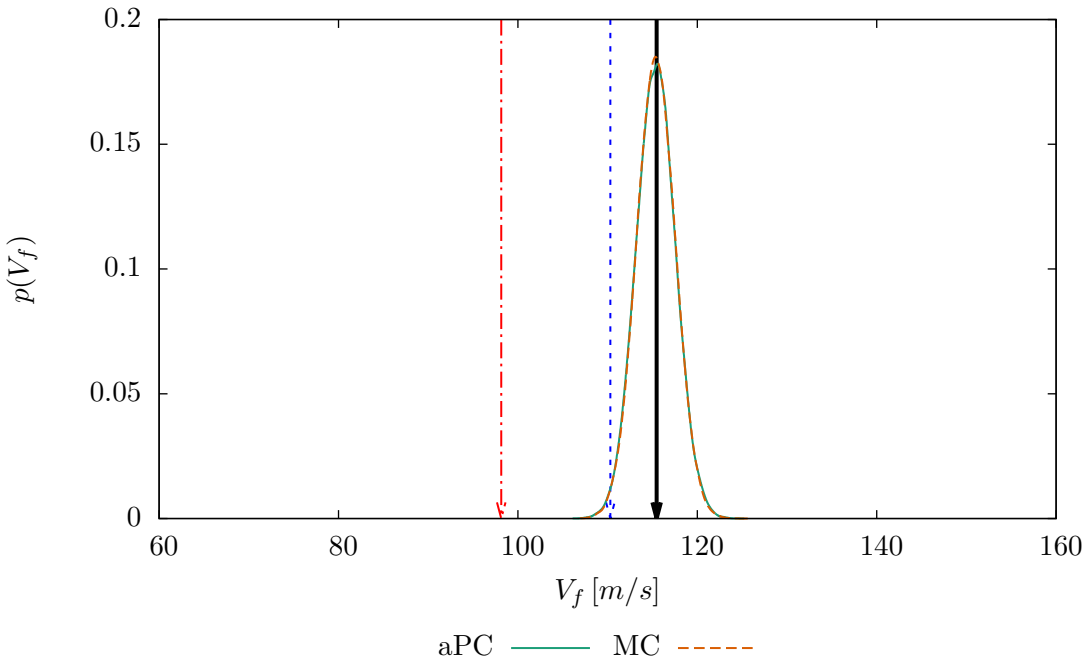

Fig. III.44 *Gaussian KDE of critical flutter velocity (V_f) response for layup L1 (Table III.7) on uncertain ply angles with standard deviation of 1° and uncertain ply thicknesses with a CoV of 5%, obtained by aPC with 1000 preliminary samples and 10^5 samples on the final response surface. Comparison Monte Carlo simulation has 10^5 samples*

III.5 Conclusion

As example problem, the case of a straight rectangular composite plate wing was considered for its relative simplicity, but richness in dynamic behaviour, being capable of producing modal behaviours which also would occur in more complex structures. It was modelled as a Kirchhoff plate model using a Rayleigh-Ritz approach to solve the dynamic problem.

On this aeroelastic problem, an uncertainty quantification study on the ply angles and ply thicknesses of the composite plate was performed, where the impact of the uncertainties on the critical flutter velocity was evaluated. For purposes of analysis, the impact of the uncertainties was first examined individually, before a combined study was carried out.

A preliminary deterministic study was performed on the composite cantilevered plate wing problem. The polar method was employed to reduce the number of parameters to observe as well as giving a convenient way to identify or construct special material symmetry. This way, the preliminary study could be limited to the domain of orthotropic materials, which thanks to the polar method could be visualised with only two parameters representing the anisotropic part of the material behaviour. The study revealed a complex dependence of the critical flutter velocity on the elastic properties of the material. This dependence was shown to have its origin in the modal behaviour of the wing. Most importantly, an abrupt change in modal behaviour was detected, which in turn leads to an equally abrupt change in critical flutter velocity. With the modal regime changes the dependence of the critical flutter velocity on the elastic parameters. In the examined plane of orthotropic materials, five points were picked for uncertainty quantification, from which six laminate layup stacking sequences were reverse-engineered.

When the uncertainties in ply angles and ply thicknesses were propagated through the solver using Monte Carlo simulation, important deviations in the critical flutter velocity were observed. In these deviations, both uncertainties were found to play a role, although the uncertainty in the thickness dominates. Most importantly, the mode switch observed in the deterministic study was triggered. The resulting discontinuity in the critical flutter velocity clearly undercuts the classical 15% margin on the nominal flutter speed, normally taken as security measure. This means that mode switches due to manufacturing error are a significant threat for aeroelastic safety, especially as the most heavily affected configuration in this study represents the optimum in critical flutter velocity. Another interesting finding was that the square-symmetric layup proved very stable against uncertainties in the ply angles. Further studies have to be taken to see if this finding can be generalised.

Although the solving methods used in this work are simple and computationally cheap, doing the stochastic studies by Monte Carlo simulation is computationally costly. For this reason, the author deployed a polynomial chaos surrogate model in order to accelerate the computations. The polar method with its significantly reduced number of parameters helped avoid the “curse of dimensionality”. Other than in previous studies using lamination parameters [114], the uncertainty in the ply thicknesses could be treated, and no restriction on the ply angle uncertainties such as an artificial symmetrisation had to be imposed. The correlation occuring in the polar parameters was treated by using a custom

polynomial basis constructed using the Gram-Schmidt algorithm. The discontinuities in the response surface due to mode switching were dealt with by splitting the response surface and modelling the different parts of the response surface individually, where the splitting was carried out by a machine learning algorithm. This way, a more efficient, fully automatic technique to compute the stochastic response was constructed. The number of calls to the solver could be cut from 10^5 for a plain Monte Carlo simulation to 1000 needed for the training of the machine learning algorithms and the fitting of the response surface surrogate models.

Chapter IV

Bayesian uncertainty quantification: aerodynamic modelling

Because of the coupled nature of the problem, simulation results for the aeroelastic response depend very much on the aerodynamic model that is used. The choice of aerodynamic operators will change the characteristics of the coupled system such as restoring forces, inertia via added-mass effects and damping. These effects lead to significant changes in the predictions of the critical flutter velocity, the flutter frequency and the modal behaviour.

The differences in results between the different aeroelastic models or even different choices in their parameters give rise to the question which model to choose. As results vary between scenarios, even with classical comparison with experimental results, an answer is difficult to give. Bayesian uncertainty quantification regards this open question as another kind of uncertainty, called epistemic uncertainty, and tries to express it in form of probabilities and distribution.

In this chapter, this technique will be applied to the question of the choice of the aerodynamic model and the right values of the corresponding parameters. First, the mathematic framework will be given. During the presentation of the framework, it will be shown that a prior belief for the distributions and probabilities is required, which will be defined for the present models afterwards. Then, a calibration study is conducted, before assessing different aspects of the model uncertainty.

IV.1 Mathematic framework

In order to be able to attribute distributions, the Bayesian approach defines an error term $\boldsymbol{\epsilon}$ which is used to describe the discrepancy between the simulation results $\mathbf{y}$ and the real value of the quantity of interest $\mathbf{q}$ [23]

$$\mathbf{q} = \mathbf{y}(\mathbf{x}, \boldsymbol{\theta}, \mathcal{M}) + \boldsymbol{\epsilon}(\mathcal{M}) \tag{IV.1}$$

where the $\boldsymbol{\theta}$ are the aerodynamic parameters of the model, itself denoted as $\mathcal{M}$, that are regarded as uncertain. The $\mathbf{x}$ are deterministic explanatory parameters, describing the setup used to determine the configuration that is used to obtain the data. The output of the model is denoted $\mathbf{y}$, and $\boldsymbol{\epsilon}$ is the model error.

Interpretations of this error term vary. While some attribute the error to model inadequacy [110, 35], it is more common to regard this error term as an expression for measurement error [9, 23]. The two interpretations can be reconciled by acknowledging that "measurement error" includes the possibility that the data does not reflect assumptions behind the model. At the same time, this interpretation allows for the inclusion of actual measurement errors by including multiple points into the set of experimental data that share the same set of explanatory parameters.

There also is an approach by Butler et al. [21] based on measure theory that does not possess an error term, but rather directly models the distribution of the data. Technically, through use of Gaussian kernel density approximations, the latter approach works similarly, but offers an interpretation of Bayesian statistics that can be properly explained using a theory of sets. However, this work will stay with the classical approach.

Practically, the error term is often assumed Gaussian, which also is a common description for measurement error. This will also be adopted in the following. Then, data is introduced as realisations of the quantity of interest. Using the distribution of the error term, the relation between the model and the data can then be inverted and the likelihood of a simulation result corresponding to a data point can be computed as [23]

$$f_L(\mathcal{D}|\boldsymbol{\theta}, \mathcal{M}) = \frac{1}{\sqrt{(2\pi)^n \det(\boldsymbol{\Sigma})}} \exp\left(-\frac{1}{2}\left[\mathbf{d} - \mathbf{y}(\boldsymbol{\theta}, \mathcal{M})\right]^\mathsf{T} \boldsymbol{\Sigma}^{-1} \left[\mathbf{d} - \mathbf{y}(\boldsymbol{\theta}, \mathcal{M})\right]\right) \tag{IV.2}$$

where $\mathbf{d}$ is the vector of data points, and $\boldsymbol{\Sigma}$ is the covariance matrix of the data points, which allows for including error informations on observables that are functionally linked.

Using this expression, multiple quantities can be derived. In particular,

$$p(\boldsymbol{\theta}|\mathcal{D}, \mathcal{M}) = \frac{1}{C_n} f_L(\mathcal{D}|\boldsymbol{\theta}, \mathcal{M}) p(\boldsymbol{\theta}|\mathcal{M}) \tag{IV.3}$$

is the posterior distribution for the uncertain parameters $\boldsymbol{\theta}$ and C_n is a normalisation constant, which normally is not given because it is not crucial to the inference process and thus avoided by giving a proportionality sign [56]. Note that the structure of the expression resembles Bayes' theorem.

In case of multiple different models, the model can also be regarded as a parameter. The distribution between the models is then discrete. To compute the probability of the individual models, an integration over the model parameters is performed. The individual model probabilities are then [56]

$$P(\mathcal{M}_i|\mathcal{D}) = \frac{P(\mathcal{D}|\mathcal{M}_i)P(\mathcal{M}_i)}{\sum_{j=1}^{N_m} P(\mathcal{D}|\mathcal{M}_j)P(\mathcal{M}_j)} \tag{IV.4}$$

where

$$P(\mathcal{D}|\mathcal{M}_i) = \int_{\boldsymbol{\Theta}} f_L(\mathcal{D}|\boldsymbol{\theta}, \mathcal{M}_i)p(\boldsymbol{\theta}|\mathcal{M}_i)d\boldsymbol{\theta} \tag{IV.5}$$

is the marginal likelihood describing the global likelihood of one individual model with the uncertain parameters marginalised out. $P(\mathcal{M}_i)$ is the prior probability for one individual model $\mathcal{M}_i$, which is usually assumed flat [56].

In order to accurately make predictions that include the aforementioned errors, there is an expression which adds the error back onto the simulation results in order to give the distribution of the quantity of interest [23]

$$p(\mathbf{q}|\mathcal{D}, \mathcal{M}_i) = \int_{\boldsymbol{\Theta}} p(\mathbf{q}|\theta, \mathcal{M}_i)p(\boldsymbol{\theta}|\mathcal{D}, \mathcal{M}_i)d\boldsymbol{\theta} \tag{IV.6}$$

where

$$p(\mathbf{q}|\theta, \mathcal{M}_i) = \frac{1}{\sqrt{(2\pi)^n \det(\boldsymbol{\Sigma})}} \exp\left(-\frac{1}{2}\left[\mathbf{q} - \mathbf{y}(\boldsymbol{\theta}, \mathcal{M})\right]^{\mathsf{T}} \boldsymbol{\Sigma}^{-1} \left[\mathbf{d} - \mathbf{y}(\boldsymbol{\theta}, \mathcal{M})\right]\right) \tag{IV.7}$$

is the distribution of the quantity of interest as a function of the simulation results [9].

In case of multiple models, the predictive distributions can be combined as a sum of the individual predictive distributions weighted by their model probability, in order to take profit from different models making different physical assumptions [23]

$$p(\mathbf{q}|\mathcal{D}) = \sum_{i=1}^{N_m} p(\mathbf{q}|\mathcal{D}, \mathcal{M}_i)P(\mathcal{M}_i|\mathcal{D}) \tag{IV.8}$$

The process is called Bayesian model averaging [56].

IV.2 Uncertainty in aerodynamic modeling

The presence of different aerodynamic models generates an uncertainty of choice. In this work, this uncertainty will be illustrated by using the Wright model [146], as presented in chapter II and used for plate wing modelling in chapter II.2 and the more common Theodorsen aerodynamic model [124] as used by Hodges and Pierce [55].

Specifically, the epistemic uncertainty in the choice of parameters is pointed out in the following.

IV.2.1 Approximations of Theodorsen's function

The centerpiece of the unsteady aerodynamic theory by Theodorsen [124] is a function that models the influence of a model of the wake on the aerodynamic lift and moment. In said work, Theodorsen derived an analytical expression for the function which depends on the reduced frequency. However, this function is often described as complicated to implement [55, 57]. Consequently, a number of approximations have been proposed in the literature. As first noticed by [43], it is linked to Wagner's function by inverse Laplace transform [55, 42], which may have been an additional motivation to recover approximations. Most examples are aimed at the domain of control theory [63, 64] and are often directly derived from Theodorsen's function, either by Padé approximation [137] or balanced truncation development of state-space realisations of the flutter system [20]. Brunton and Rowley [20] and Riley [109] provide lists of common approximations in use, of which a selection sorted by their number of states is presented in Table IV.1 in the form in which they are found in the respective source.

Nb. of states	Reference	Function definition
Two states	Jones R.T [63]	$C(k) \approx 1.0 - \frac{0.165k}{k-0.0455\imath} - \frac{0.335k}{k-0.3\imath}$
	Jones W.P [64]	$C(k) \approx 1.0 - \frac{0.165k}{k-0.041\imath} - \frac{0.335k}{k-0.32\imath}$
	Riley [109]	$C(k) \approx \frac{(1.0+10.61\imath k)(1.0+1.774\imath k)}{(1.0+13.51\imath k)(1.0+2.745\imath k)}$
	Jones rounded [109]	$C(k) \approx \frac{0.015+0.3\imath k-0.5k^2}{0.015+0.35\imath k-k^2}$
Four states	Brunton [20]	$C(k) \approx \frac{0.5k^4-0.703\imath k^3-0.2393k^2+0.01894\imath k+2.32510^{-4}}{k^4-1.158\imath k^3-0.3052k^2+0.02028\imath k+2.32510^{-4}}$
	Vepa [137]	$C(k) \approx \frac{k^4-0.761\imath k^3-0.1021k^2+2.551\imath 10^{-3}k+9.55710^{-6}}{2k^4-1.064\imath k^3-0.1134k^2+2.617\imath 10^{-3}k+9.55710^{-6}}$

Table IV.1 – Approximations of Theodorsen's function used to construct the stochastic lift functions [20, 109]

a) Variability in the function values and flutter results

As shown in IV.1, the different approximations deviate from the original function described by Theodorsen. A range of k from 0 to one is examined, as this is the most realistic range of reduced frequency [55, p. 137]. The original function takes a value of one with no imaginary part at a reduced frequency of zero. At higher reduced frequencies, the real part decreases until tending asymptotically to $\frac{1}{2}$. At the same time, the imaginary part becomes negative, with the minimum value reached at about $k = 0.15$, but returns to zero.

The real parts of the different approximations are relatively close to the original function, with the exception of the rounded Jones' 1938 model proposed by [109] of which the real part decreases noticeably more slowly. The model described in [20] matches the function the most closely in the examined range. The more clear deviations occur in the imaginary part of the function approximations. Again, the four-states approximations generally match better, with the model proposed in [20] matching best. The two-states approximations tend to overestimate the magnitude of the imaginary part, again with the rounded Jones' model as the most visible outlier.

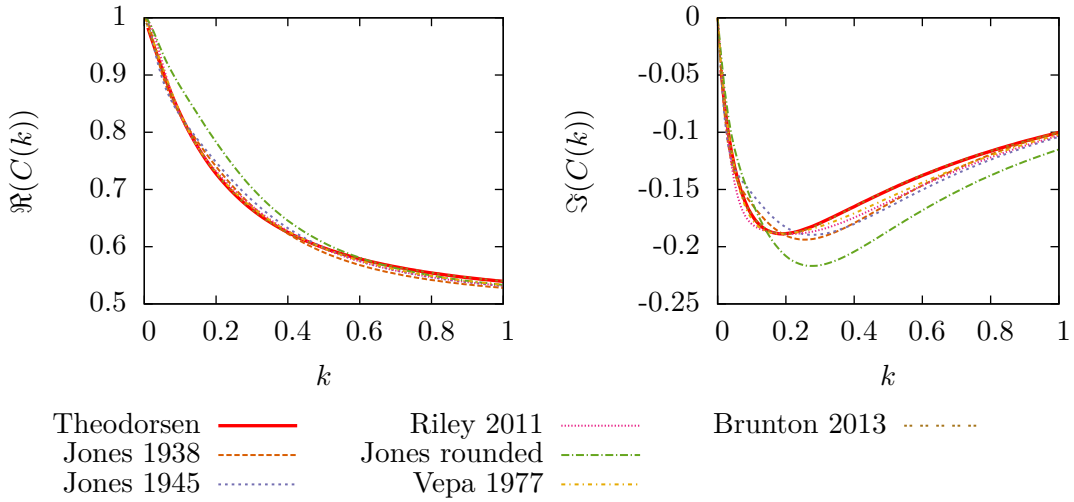

Fig. IV.1 *Real and imaginary part of the different approximations of Theodorsen's function listed in IV.1 as a function of the reduced frequency k, compared to the analytical function representation*

Obviously, the differences in the function values will affect the prediction of the critical flutter velocity as shown in chapter II. As example, the values obtained with the different models in the original validation case of Theodorsen are shown in Figure IV.2.

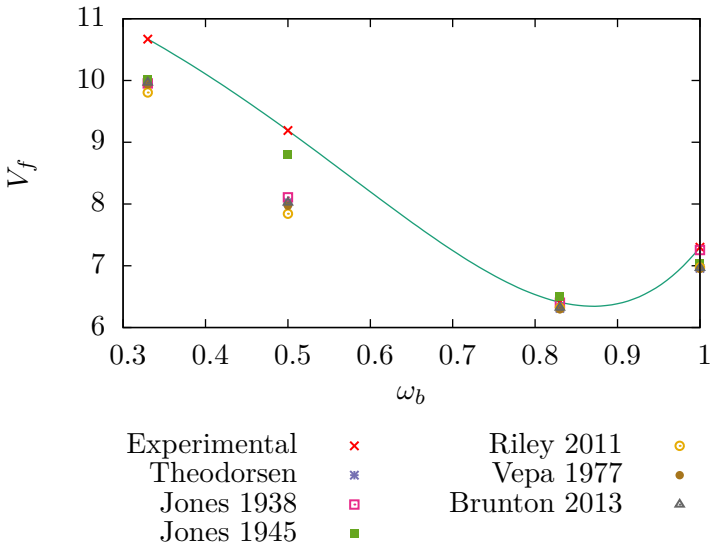

Fig. IV.2 *Flutter results of the different approximations of Theodorsen's function listed in Table IV.1 as a function of the ratio of the natural frequencies in pitch and plunge without coupling for the reference points given in [124, Fig. 11]*

$\overline{\omega}$	Exp.	Theodorsen [124]	Jones 1938 [63]	Jones 1945 [64]	Riley [109]	Jones rounded [109]	Vepa [137]	Brunton [20]
0.33	10.67	9.967	9.952	10.018	9.805	9.943	9.937	9.965
0.5	9.19	8.029	8.107	8.797	7.843	8.171	7.973	8.024
0.83	6.41	6.312	6.402	6.499	6.317	6.261	6.293	6.321
1.0	7.30	6.960	7.255	7.044	6.973	6.805	6.949	6.966

Table IV.2 – Results for critical flutter velocity V_f^* with the different lift function models presented in Table IV.1 as depicted in Fig. IV.2.

It can be noted that the models tend to underestimate the critical flutter velocity in the shown cases, as does Theodorsen's original function. Most approximations are closest at point C, where the approximations give results distributed around the experimental value. In point B, the Jones 1945 [64] model acts as an outlier and provides a prediction significantly closer to the experimental value than the other models.

The differences highlight the influence of different choices for the parameters on the predictions. Therefore, a stochastic calibration model will be established in the following. As the Bayesian approach needs a formulation for the prior belief, prior distributions for the parameters will be determined first, before adding the data and performing the actual calibration.

b) Construction of the priors

As the Bayesian uncertainty quantification method is based on Bayes' theorem, a prior distribution is necessary to build the stochastic model. The challenge is to specify a prior distribution that does not include more information than necessary or even available, as the prior distribution chosen too tight would result in conclusions that are false [21]. A good indicator can be the information entropy, which assesses the amount of information contained in a distribution [9].

Observing the approximations from Table IV.1, it is noticed that they can be casted in a common form [97]

$$C(k) \approx 1 - \sum_{j=1}^{N} \frac{\alpha_j k}{k - \beta_j i} \tag{IV.9}$$

where N is the number of states of the model. The values for the coefficients α_j and β_j are given in Table IV.3.

	α_1	α_2	α_3	α_4	β_1	β_2	β_3	β_4
Jones R.T (1938) [63]	0.165	0.335			0.0455	0.3		
Jones W.P (1945) [64]	0.165	0.335			0.041	0.32		
Riley (2011) [109]	0.2346	0.2664			0.074	0.3643		
Jones rounded [109]	0.1	0.4			0.05	0.3		
Brunton (2013) [20]	0.0396	0.1555	0.2438	0.0612	0.0144	0.0786	0.2522	0.8128
Vepa (1977) [137]	0.0128	0.0333	0.2279	0.2259	0.0045	0.0257	0.1042	0.3976

Table IV.3 – Coefficients of the approximations of $C(k)$ according to Eq. (IV.9).

In order to highlight the physical meaning of the parameters, the inverse Laplace transform of the functions is examined, which can be used to calculate the response of a wing profile to a gust and relates the function to the time domain [43, 64, 20]

$$\mathcal{L}^{-1}\{C\} = 1 - \sum_{j=1}^{N} \alpha_j \exp(-\beta_j \tau) \tag{IV.10}$$

In this form parametrised using the non-dimensional time $\tau = Vt/b$, the coefficients β_j can be identified as time scale parameters, whereas the coefficients α_j take the role as weights.

Based on these considerations, a prior belief on their value range can be established by making the following assumptions:

1. When the wing does not move, thus when the frequency is zero, the lift and moment are required to be the same as for the stationary solution. Consequently, the real value of the function at $k = 0$ has to be one and the imaginary value, which corresponds to a phase shift, has to be zero. $\lim_{k\to 0} \Re(C(k)) \to 1$, $\lim_{k\to 0} \Im(C(k)) \to 0$
2. Corresponding to the original function, it is also required that for infinite frequencies, the aerodynamic lift and moment are half of the stationary solution $\lim_{k\to\infty} \Re(C(k)) \to \frac{1}{2}$, $\lim_{k\to\infty} \Im(C(k)) \to 0$.
3. The real part of the function has to monotonically decrease between its limit values.
4. The imaginary part of the function must always be smaller than or equal to zero $\Im(C(k)) \leq 0$, which means that there is a positive phase shift between the flow motion and the displacmeent of the wing. This is explained by the fact that the flow cannot anticipate wing movements, but reacts to its changes in position.

For assumptions 1, 3 and 4 to be met, the parameter values have to be positive, which is also the sufficient condition. However, for assumption number 2 to be true, the sum of the α_j parameters has to be $\sum_{j=1}^{N} \alpha_j = \frac{1}{2}$. As only two-states models will be treated, this is ensured by setting $\alpha_2 = \frac{1}{2} - \alpha_1$.

According to these constraints, the bounds of the domains for the α_j parameters are clearly defined. For given bounds, the maximum entropy distribution is the uniform distribution [81]. Consequently, the distribution of α_1 is set to $\mathcal{U}\left[0, \frac{1}{2}\right]$ The marginal distribution of α_2 can be easily calculated to be the same. It has to be noted that because of its functional dependence on α_1, there is correlation. The same approach is also adopted by Sandhu et al. [113].

For the β_j parameters, only the lower bound is given by the above assumptions with $\beta_j = 0$. For the upper bound, the limit is less clear. For the constraint of positivity, an exponential distribution, which has no upper bound, could be adopted. Sandhu et al. [113] employs a lognormal prior, which does not exclude infinite values, but disencourages low values, which are observed in almost all models in Table IV.3. However, in the models listed in Table IV.3, no model has values of $\beta_j > 0.813$. For this reason, in this work, a

practical limit of $\beta_j = 0.9$ is supposed, which is about 10% higher and should cover any value relevant in practice. This leads to a uniform prior with $\beta_j \sim \mathcal{U}[0, 0.9]$.

The distributions for the parameters α_j and β_j can thus be summarised as

$$\alpha_j \sim \mathcal{U}\left[0, \frac{1}{2}\right] \tag{IV.11}$$

$$\beta_j \sim \mathcal{U}[0, 0.9] \tag{IV.12}$$

IV.2.2 Bayesian calibration of Wright's aerodynamic model

Wright's model is based on quasi-steady potential flow with an aerodynamic unsteady moment derivative $M_{\dot{\alpha}}$. Although Wright and Cooper [146, p. 168] states that the derivative depends on the flutter frequency, the value of $M_{\dot{\alpha}}$ value is set to $M_{\dot{\alpha}} = -1.2$ for a number of different problems and very different frequency regimes, which suggests that this can be used as a universal value.

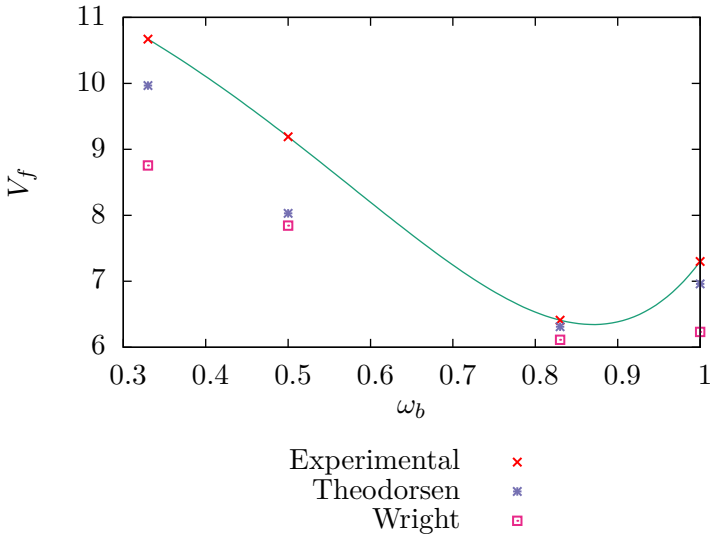

Fig. IV.3 *Flutter results using the Wright model with $M_{\dot{\alpha}} = -1.2$, as a function of the ratio of the natural frequencies in pitch and plunge without coupling for the reference points given in [124, Fig. 11].*

Results for the flutter cases shown before using this model with $M_{\dot{\alpha}} = -1.2$ are given in Figure IV.3. While the results match the experimental results quite well for $\overline{\omega} = 0.5$ and $\overline{\omega} = 0.83$ and are close to the results obtained with Theodorsen's function, the discrepancy is even larger for natural frequency ratios of $\overline{\omega} = 0.33$ and $\overline{\omega} = 1.0$. As the negative of $M_{\dot{\alpha}}$ is a damping term and adding damping usually raises the flutter velocity, this suggests that the value of $M_{\dot{\alpha}}$ might actually be lower. It can also be remarked that the Wright model systematically estimates lower values for the critical flutter velocity

than the Theodorsen fully unsteady model. Other than the approximated Theodorsen-type models, it also systematically estimates the critical flutter velocity to be below the experimental values.

In this work, the Bayesian framework is used to verify the choice of the model parameter $M_{\dot{\alpha}}$ by performing a Bayesian calibration. Afterwards, the pertinence of this model will be evaluated by setting it up in Bayesian Model Averaging/ Bayesian Model Selection against the approximations of Theodorsen's more complex approach.

Again, a reasonable prior has to be established using the available knowledge. Wright and Cooper [146, p. 168] states that the $M_{\dot{\alpha}}$ value is negative, which is also suggested by Hancock [54]. Finally, the universal use of $M_{\dot{\alpha}} = -1.2$ suggests it to be a kind of mean value. For $-M_{\dot{\alpha}}$ which would be positive, the maximum entropy distribution is an exponential distribution [81]. The distribution for $M_{\dot{\alpha}}$ can thus be given as

$$p(M_{\dot{\alpha}}) = \begin{cases} \frac{1}{\beta} \exp\left(\frac{1}{\beta} M_{\dot{\alpha}}\right) & \forall M_{\dot{\alpha}} < 0 \\ 0 & \text{otherwise} \end{cases} \tag{IV.13}$$

and $\beta = 1.2$.

IV.3 Parameter calibration

The prior distributions have been set to the minimum of prior knowledge. In the following, the parameters of the two models are updated using the experimental data from [124] first shown in this work in Table IV.2. A forward propagation of the prior distribution is performed. Then, the calibration is performed and its results are analysed with respect to the propagation of the prior distribution as well as the experimental results.

The calibration is carried out using importance sampling [6], which consists in this case of a forward propagation of the distribution and an assignment of weights to the samples. No re-sampling is performed. As sampling distribution, the prior distribution is used.

In order to be able to perform the calibration, the parameters of the error term $\boldsymbol{\epsilon}$ and consequently, the likelihood function Eq. (IV.2), have to be determined. In this case, starting from the assumption that the error is Gaussian and has zero mean, the only parameter to be estimated is the error standard deviation σ. This parameter is determined using the evidence method [6], which means optimising the integrated likelihood. The curves of the log of the integrated likelihoods are shown in Figure IV.4.

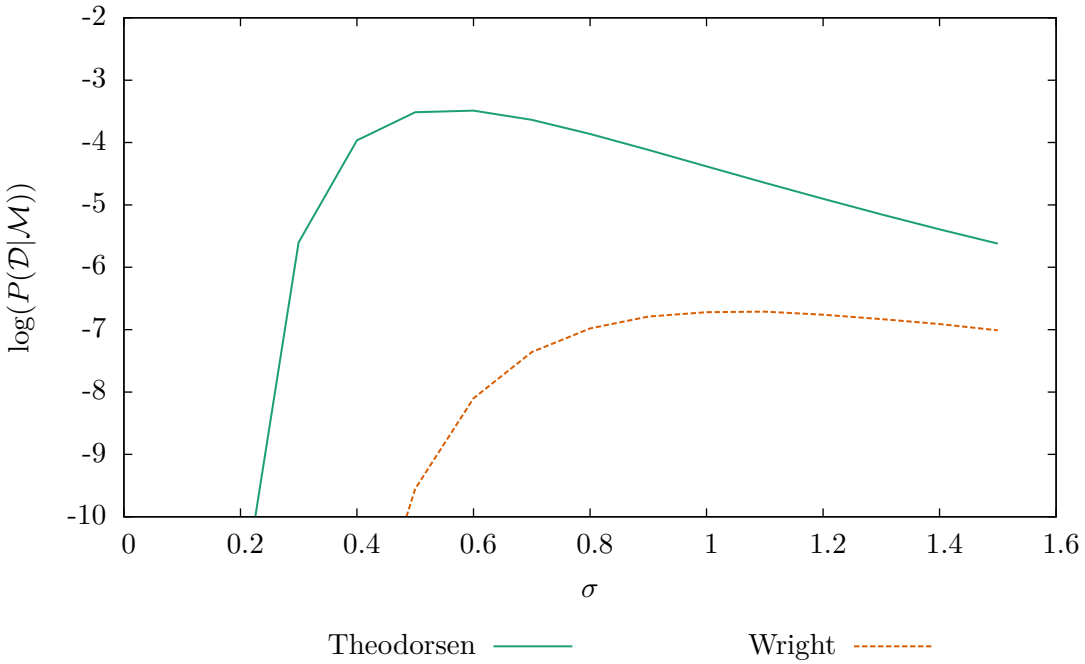

Fig. IV.4 *Log likelihoods* $\log P(\mathcal{D}|\mathcal{M})$ *as a function of the error standard deviation for the Wright aerodynamic model and the Theodorsen type approximated model. Optimal points at* $\sigma = 0.6$ *for the Theodorsen type aerodynamic model and* $\sigma = 1.1$ *for the Wright type model.*

While the standard deviation of the error for the Theodorsen model can be found according to the Figure IV.4 to be $\sigma = 0.6$, the offset for the Wright model can be found to be at $\sigma = 1.1$. Already, the values are relatively high, given that the nondimensional experimental values for the critical flutter velocities are between $V_f^* = 6.41$ and $V_f^* = 10.67$ (Table IV.2). Although critical flutter velocities are hard to determine experimentally, an error of 10% would be unusual. The difference between the two values suggests that at least a part of the discrepancy between the experimental values and the computational results can be attributed to model error. Therefore, setting the term for σ just to the experimental error could be problematic in that case.

IV.3.1 Bayesian calibration of approximations to Theodorsen's aerodynamic model

a) Propagation of the prior

Starting from the definitions of the prior distributions defined in Equations (IV.11),(IV.12), samples are generated from said distributions and propagated through a k-method solver for the PAPA problem as given in section II.1.2. The results are given in Figure IV.5[1].

[1] If the distributions are cut off, this is due to a faulty automatic estimation of their support

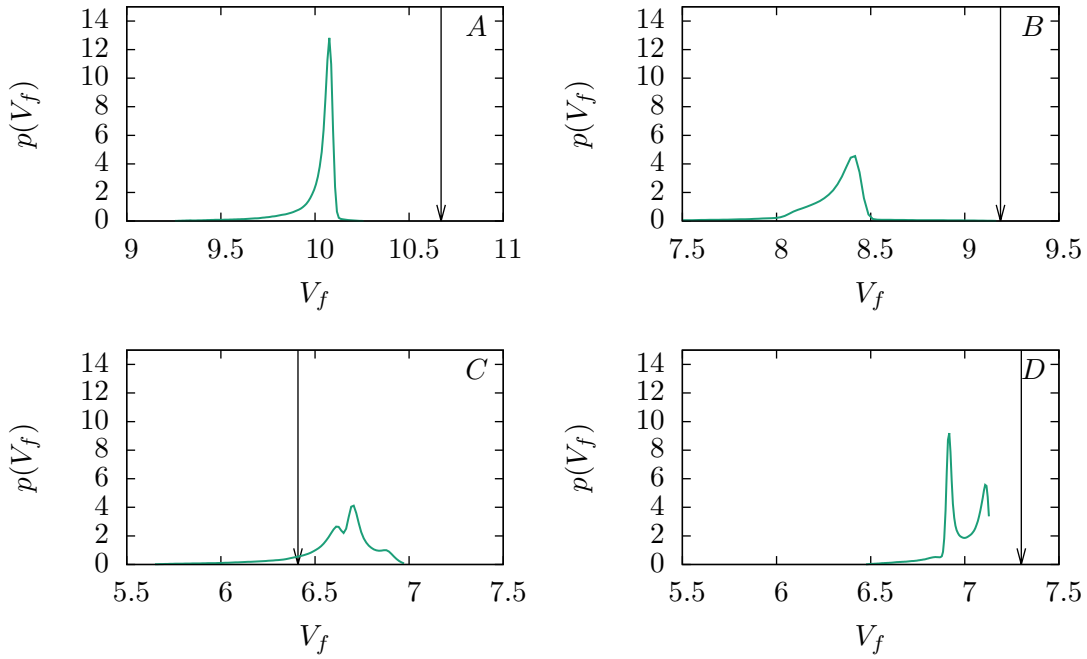

Fig. IV.5 *Kernel density estimations for Monte Carlo propagation of prior distributions through the data points defined in Table IV.2, with* 10^5 *samples. The experimental results are given by the black arrows.*

In all of the cases, a significant offset of the maximum probability density from the experimental value can be found. Only in scenario C, the distribution actually covers the experimental result with a non-negligible probability density. In scenarios A, B and D, spikes in probability density can be found where the majority of results of the initial models fall, too (see Table IV.2).

b) Calibration

Model calibrated	Theodorsen-type
Hyperparameters	$\sigma = 0.6$
Calibrated parameters	α_1, α_2, β_1, β_2 (aerodynamics)
Data used	Scenarios A,B,C,D (Table IV.2)[124]

Table IV.4 – Summary of parameters and data for calibration.

In order to improve the results from Figure IV.5, calibration is performed using the framework used before on all the four data points from [124] which were given in Table IV.2. The results of this process are given in Figure IV.6. The weighting parameters α can be found to remain almost flat, meaning they do not change in a meaningful way from the prior and that no possible value is preferred from another. This is substantially different from the value for the β type parameters, where the model shows a clear preference

for values on the upper end of the given spectrum. Below values of 0.3, the probability density drops rapidly. However, a small spike remains at values below values of 0.1. This is consistent with the models shown in Table IV.3, which all have at least one β type parameter at values between 0.0 and 0.1. However, the results given here do not reflect that in the literature, there is a cumulation of parameters between about 0.25 and 0.4 (Table IV.3). This could be explained by the frequency range of the experimental results being limited and thus searching for higher accuracy in low frequency regions, cumulating parameters at high values.

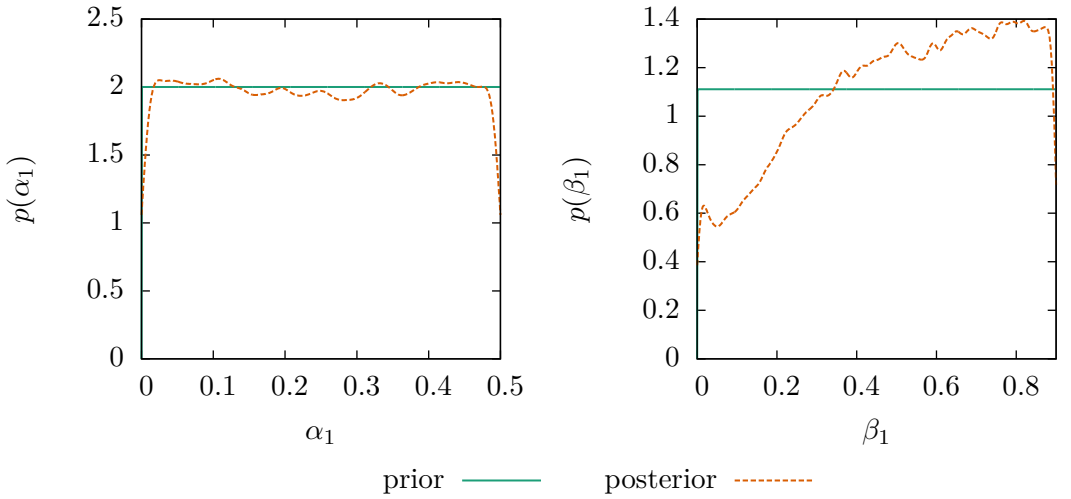

Fig. IV.6 *Posterior distributions for the two parameter types for the Theodorsen model using the four data points from [124] given in Table IV.2.*

In the previous figure, only marginal distributions for individual parameters were shown. However, the parameter values are linked via the common model, so correlations are possible. Figure IV.7 shows pairs of parameters. As the parameters are organised by α, β pairs in the model, on the left, the marginal distribution of such a pair is shown.

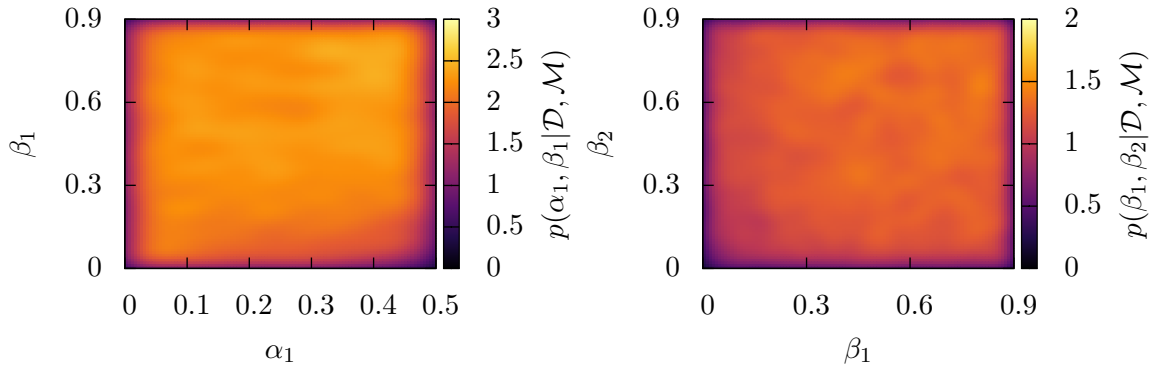

Fig. IV.7 *Posterior distributions for pairs of the parameters for the Theodorsen model using the four data points from [124] given in Table IV.2.*

Unfortunately, due to the small degree of information obtained during the calibration, little information about the correlation between the parameters is gained. However, a drop in probability density on the right lower corner of the figure can be noticed, meaning that it is more unlikeliy to encounter low values of the β parameters at high values of α parameters. This is consistent with the models in the literature (see Table IV.3).

While the relation between the α parameters is fixed due to the requirement that their sum has to give 0.5, no such condition for the β parameters exist. Therefore, the common marginal distribution for the two betas is shown on the right of Figure IV.7. Again, the information gain is not high. A drop in probability density can be noticed towards the lower left corner, which means that is less probable to encounter two β parameters in the same model that have low values.

The simulation results for the updated parameter distributions are shown in Figure IV.8. The improvements that are obtained are relatively small. Generally, the probability density peaks closest to the experimental results get stronger than in the prior distribution, while the distributions retreat from the end far from the experimental values. However, despite the probability density mass getting closer to the experimental result, there seems to be a limit of adaption of the model, beyond which the distributions fail to extend. This means that the prediction capacities of the model are quite limited for the present data.

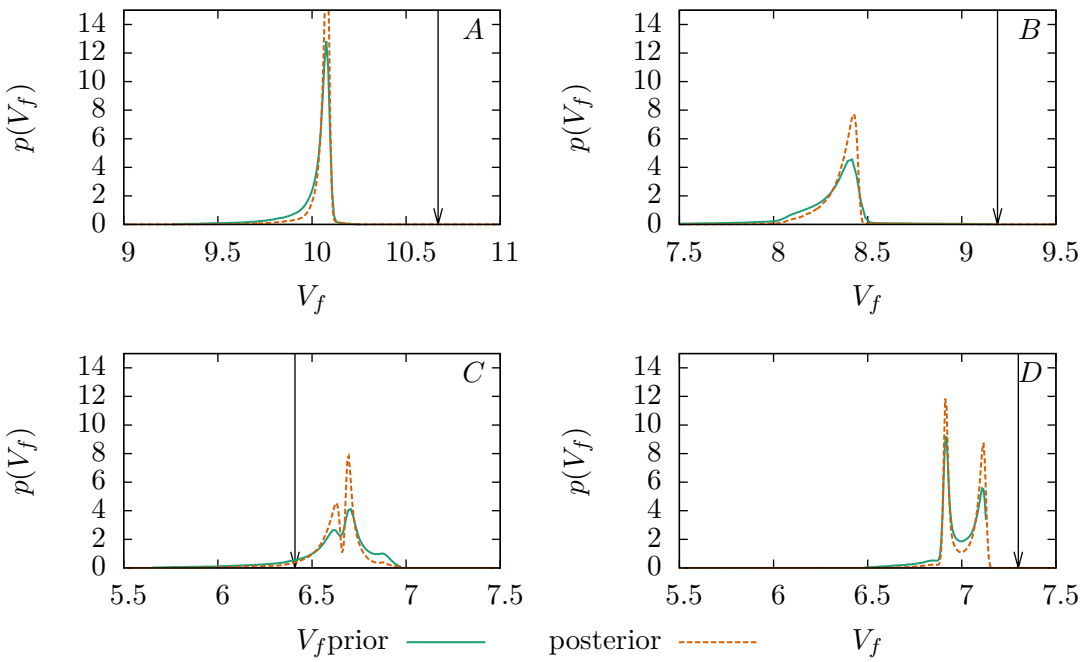

Fig. IV.8 *Posterior critical flutter velocity simulation results for the Theodorsen mdoel using the four data points from [124] given in Table IV.2.*

c) Prediction

Model calibrated	Theodorsen-type
Hyperparameters	$\sigma = 0.6$ (attention: found with 4 datapoints evaluated)
Calibrated parameters	α_1, α_2, β_1, β_2 (aerodynamics)
Data used	Scenarios A,C,D (Table IV.2) [124]
Predicted	V_f^*, scenario B (Table IV.2) [124]

Table IV.5 – Summary of parameters and data for calibration.

In order to give an example for the prediction capabilities of the Bayesian approach, another calibration will be performed on the three scenarios A,C and D, and the calibrated model will be used to perform a prediction on scenario B, as it was performed in [97].The predictive distribution is the forward propagation of the posterior samples with the error term added. In case of a Gaussian error, this will result in a smoothing effect on the results.

The example for the predictive distribution is given in Figure IV.9. It has to be noted that as when calibrating with the three scenarios mentioned, the distribution does not get informed any better than with four points. Consequently, the predictive distribution changes only very little when compared to forward propagation with the error added ("prior predictive distribution").

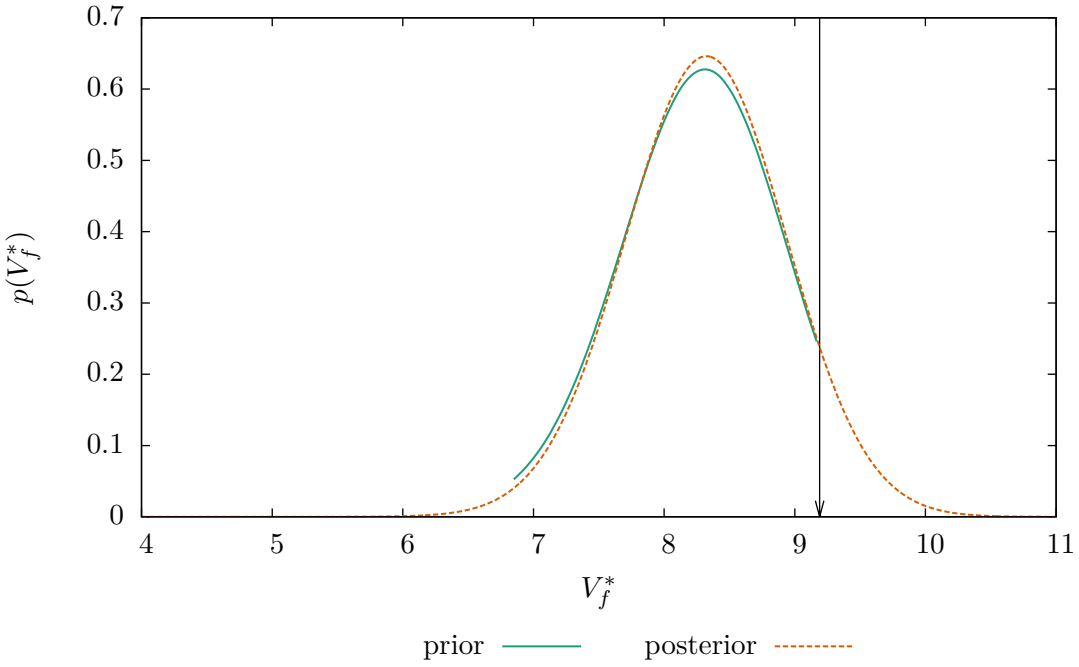

Fig. IV.9 *Predictive distribution before and after calibration using scenarios A,C and D (Table IV.2) with the Theodorsen-type model, setting* $\sigma = 0.6$*, obtained using importance sampling with* 10^5 *samples.*

IV.3.2 Bayesian calibration of Wright's model

a) Propagation of the prior

As before, the prior distribution is propagated through the model for analysis purposes. Samples are generated from the exponential prior distribution on $M_{\dot{\alpha}}$ Equation (IV.13) and propagated through the solver, which is a p-method solver in this case (see section II.1.1). The corresponding pdf of V_f^* is given in Figure IV.10.

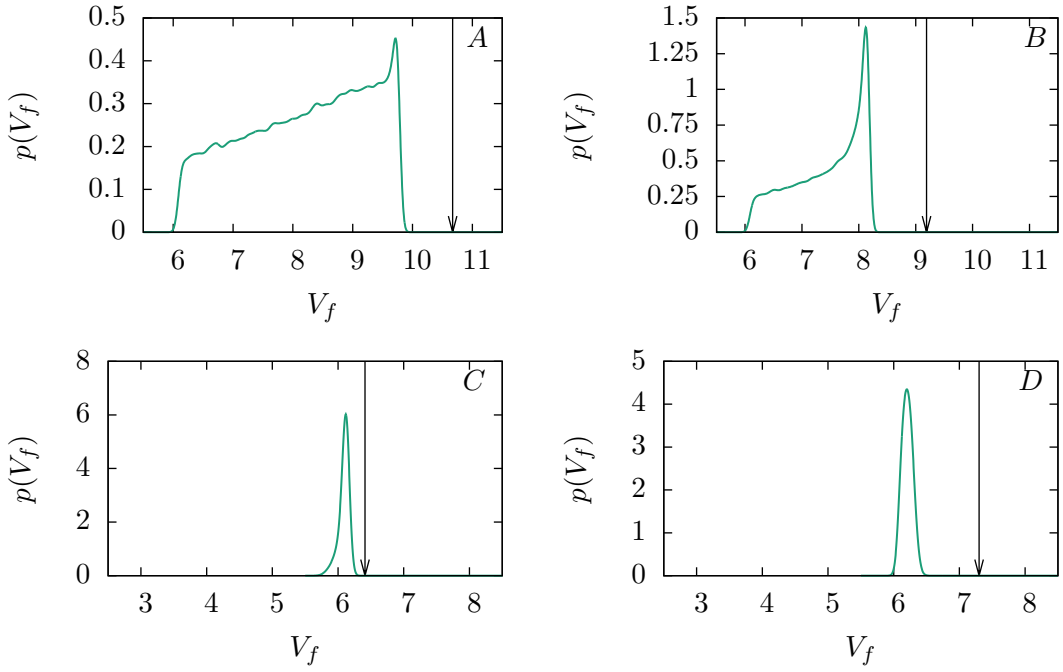

Fig. IV.10 *Kernel density estimations for Monte Carlo propagation of prior distributions through the data points defined in Table IV.2, with* 10^5 *samples. The experimental results are given by the black arrows.*

Results show that the critical flutter velocity is systematically underestimated by this model, even when its principal parameter is considered uncertain. The distributions peak at the side where they are closest to the experimental result, and the probability density values fall off more or less quickly at velocity values below the peak. The biggest variations, i. e. higher critical flutter velocity, can be observed in scenarios A and B, whereas for scenario C, there is only a small variation.

Other than in case of the Theodorsen model, the result of the propagation of the prior reveals that in no case, the model is actually able to reproduce the experimental value with $M_{\dot{\alpha}}$ within the range of the prior.

b) Calibration

Model calibrated	Wright-type
Calibrated parameters	$M_{\dot{\alpha}}$ (aerodynamics)
Hyperparameters	$\sigma = 1.1$
Data used	[124], scenarios A,B,C,D (Table IV.2)

Table IV.6 – Summary of parameters and data for calibration.

As on the Theodorsen type model, a calibration is performed on the parameters of the model, which are here limited to $M_{\dot{\alpha}}$. Figure IV.11 shows the calibration results in comparison to the prior distribution. The distribution for the $M_{\dot{\alpha}}$ parameter clearly shifts to lower values. Below a value of -2, the probability density is zero or almost zero, also ruling out the value of -1.2 given to the parameter in [146, 123, 114]. Actually, the probability maximum for $M_{\dot{\alpha}}$ can be found at about $M_{\dot{\alpha}} = -3$. Considering that the $M_{\dot{\alpha}}$ parameter adds damping to the system, this means that there is much more damping in the system, which could be of aerodynamic origin. However, the distribution having non-negligible probability density values between -2 and -6, considerable uncertainty concerning the value is still present. Moreover, as the right flank of the curve descends smoothly and has higher values than the prior everywhere, it is possible that the posterior is not independent from the prior in this case either.

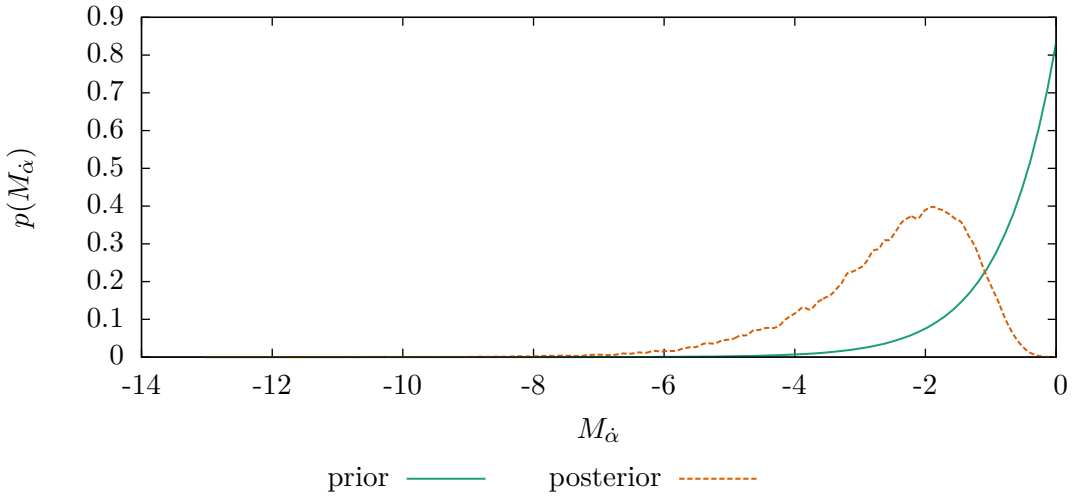

Fig. IV.11 *Posteriors for the $M_{\dot{\alpha}}$ parameter of the Wright model using the four data points from [124] given in Table IV.2.*

Figure IV.12 shows the posterior pdf for the non-dimensional critical flutter velocity V_f^*. It can be seen that the velocity distributions after calibration are, for cases A, B and D, much more peaked. Their "tail" on the side off the experimental results is very much reduced. Although the probability density maximum was already on the side of the experimental result, the maxima get much higher and in most cases closer to the experimental value.

The C case, in which the distribution was very peaked and close to the experimental

result before, actually does show the contrary. The distribution gets flatter, attributing significant probability density to a much wider range of values. The maximum of probability density even shifts away from the experimental result. This could be a result of different effects working on the C case as in the other three scenarios.

Similarly to Theodorsen's model, it is observed that the models reach a kind of barrier, beyond which it cannot be improved. Contrarily to the Theodorsen-type models, this is also the case for case C. While the difference in scenario C is probably due to the ability of the Theodorsen type models of modelling unsteady effects more correctly, this could indicate phenomena present in the real-world experiences that are not taken into account by the models.

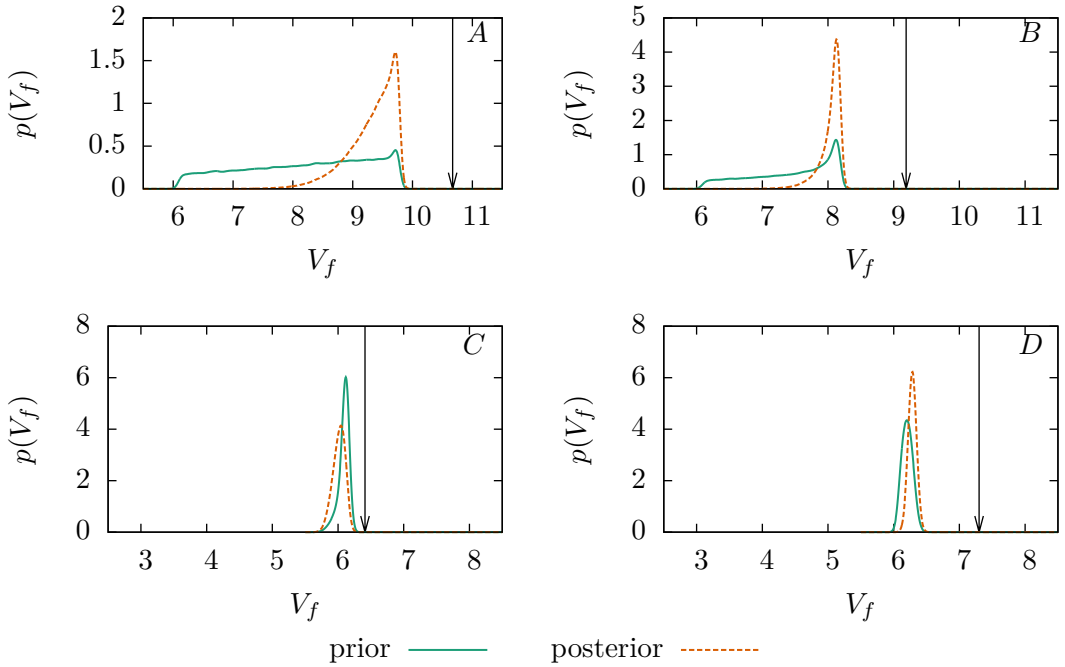

Fig. IV.12 *Posterior critical flutter velocity simulation results for the Hancock model using the four data points from [124] given in Table IV.2.*

c) Prediction

Model calibrated	Wright-type
Calibrated parameters	$M_{\dot{\alpha}}$ (aerodynamics)
Hyperparameters	$\sigma = 1.1$ (attention: found with 4 datapoints evaluated)
Data used	[124], scenarios A,C,D (Table IV.2)
Predicted	V_f^*, [124], scenario B

Table IV.7 – Summary of parameters and data for calibration

Again, the calibration is used to perform a prediction for the quantity of interest $\mathbf{q}$, thus

here values of the normalised critical flutter velocity V_f^*. The scenarios used for calibration remain A, C and D, while B is again the scenario for which the critical flutter velocity is predicted.

Other than in the Theodorsen model case Figure IV.9, the predictive distribution of V_f^* for the Wright model changes significantly after calibration as shown in Figure IV.13. A shift towards the experimental value, which is indicated by the black vertial arrow, is observed in the distribution. However, the very large standard deviation for the error term makes that the distribution is very widely spread and heavily smoothed.

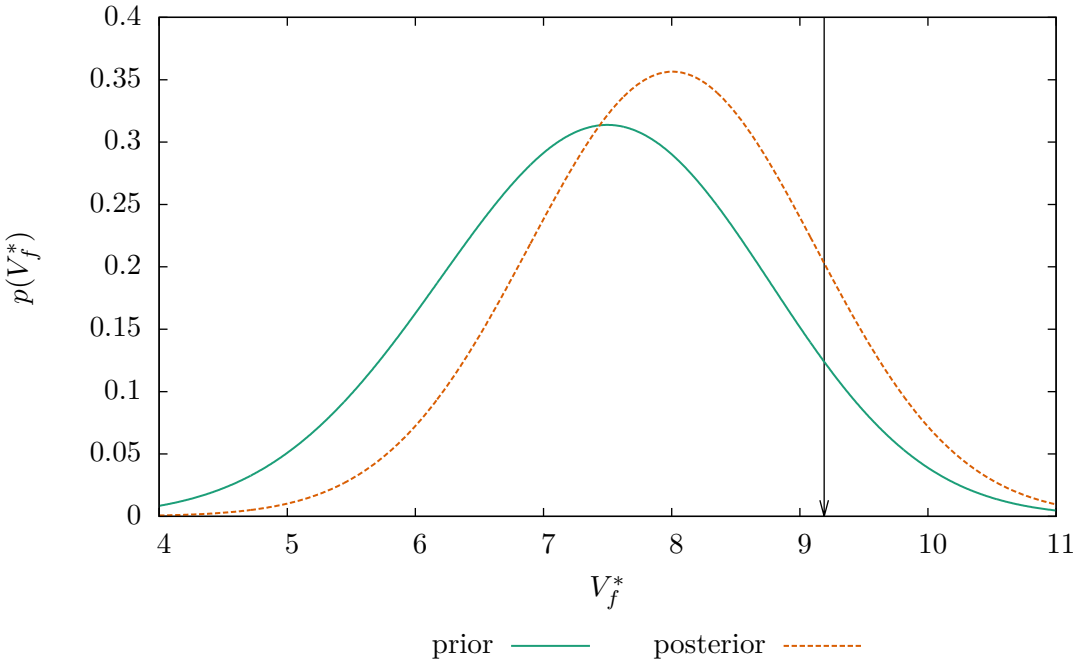

Fig. IV.13 *Predictive distribution before and after calibration using scenarios A,C and D (Table IV.2) with the Wright-type model, setting* $\sigma = 1.1$*, obtained using importance sampling with* 100000 *samples.*

IV.4 Model uncertainty

As the two models represent different approaches for the aerodynamic forces, and both are applied to similar use cases, there is the question of which model to choose. This difficulty leads to a kind of epistemic uncertainty that is an uncertainty of choice, the model or model-form uncertainty [109]. In this work, this source of uncertainty is addressed by Bayesian Model Averaging, which calculates model probabilities in order to calculate a weighted average of the different models [56]. The model probabilities have also been used to perform model selection [112].

In order to determine the model probabilities for the present case, Equation (IV.4) is used with the integrated likelihoods of the two models. In both cases, the error standard

deviation σ is set to the value producing the maximum integrated likelihood, respectively. The prior model probabilities are supposed to be discrete uniform. As two models are studied, this corresponds to equal prior model probabilities of 0.5 each. The results for the posterior model probabilities are given in Table IV.8.

	Theodorsen	Wright
$P(\mathcal{M}\|\mathcal{D})$	0.956	0.044

Table IV.8 – Posterior model probabilities for the Wright and Theodorsen models using Equation (IV.4). Integrated likelihoods found using $\sigma = 0.6$ for the Theodorsen model and $\sigma = 1.1$ for the Wright model (see Figure IV.4), scenarios A,C and D and 10^5 Monte Carlo samples for integration.

The Theodorsen aerodynamic approximation has a much higher model probability than the Wright model. The two models take very different approaches, produce very different results and would be interesting to average, but the averaging degenerates to a model selection. Consequently, the Wright model has virtually no influence in the total distribution. This is illustrated in Figure IV.14. The total distribution is very close to the predictive distribution generated using the Theodorsen-type model alone.

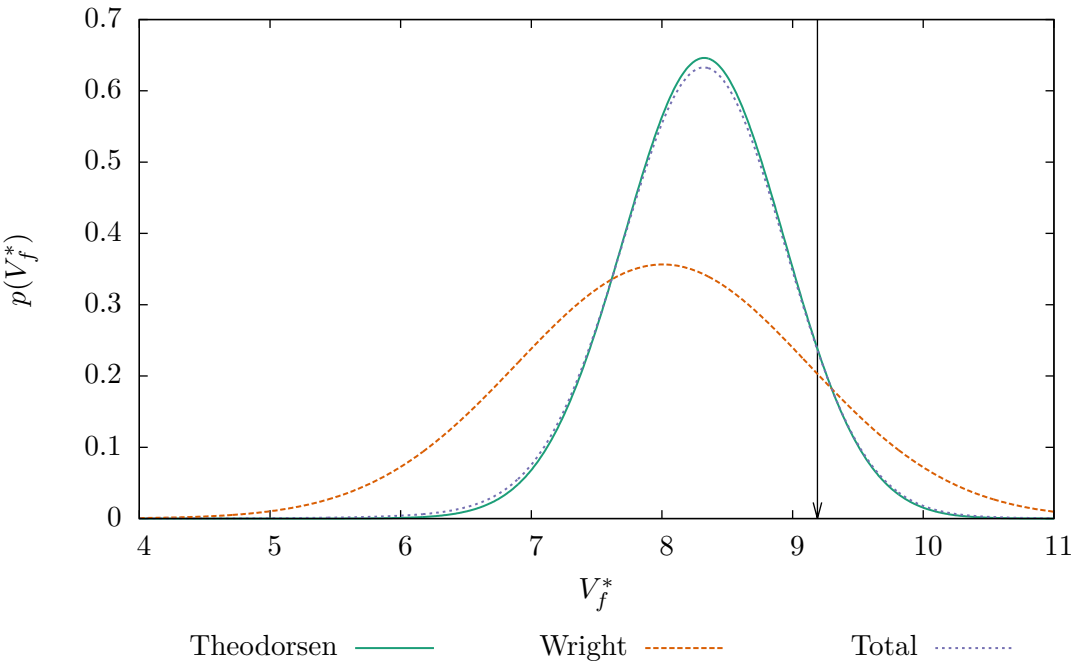

Fig. IV.14 *Individual and total predictive distributions, obtained after calibration using A,C and D (Table IV.2) and the respective hyperparameter settings and importance sampling with* 10^5 *samples.*

This means that probably, the Theodorsen model models the aerodynamics a lot more accurately. This might come from the fact that the Theodorsen model is designed to better account for unsteady effects.

IV.5 Considerations on the choice of the hyperparameters

The choice of the hyperparameters is crucial for the calibration problem. Often they are chosen as the parameters of the distribution of the experimental error [23]. In the context of the present work, this approach has, however, two important shortcomings. First, the experiments furnishing the data were not conducted in the facility where the author works and information about the experimental error was not provided in the literature. The author would have to resort to an educated guess, which, due to the complex nature of the experiments and the dependence on the experimental facilities is difficult to make. Second, the error starts often from the notion that it can be determined by solely knowing a number of outputs from the experiments, but without knowing the model, and that the mean of the experiments and the model output should correspond more or less. However, when a large discrepancy is present which has its origin in the model, taking solely the experimental measures as a basis for the definition of the error term is problematic.

As it was demonstrated in [97], the hyperparameters, and most importantly the standard deviation of the error, determine how well the parameters are informed. For illustration purposes, Figure IV.15 is reproduced from [97].

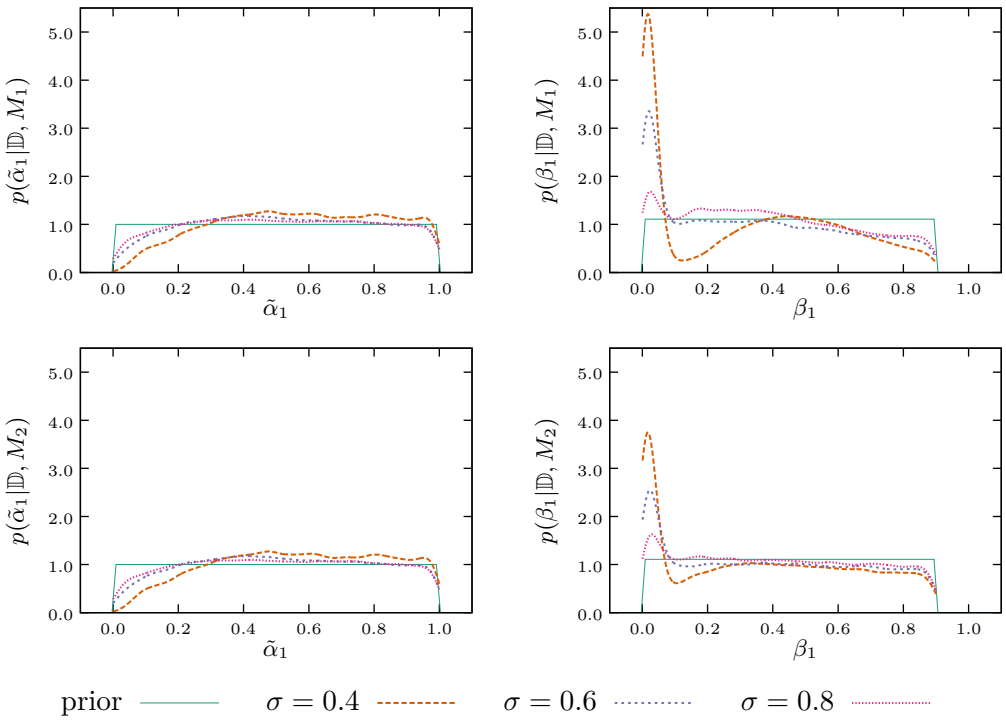

Fig. IV.15 *Demonstration of the dependence of the Theodorsen model parameters on the error term standard deviation σ from [97]. Differences to the distributions found in this work come from a different definition of the priors.*

Different methods for determining the hyperparameters exist. The evidence method was used in this work, which relies on an optimisation of the integrated likelihood. This is

equivalent to [97], where it was used under a form commonly known in the context of model selection as the BIC. However, as the BIC normally implies a number of approximations not applied in this work [77], it is simply referred to the log-likelihood as parameter to be optimised.

The other possibility is to calibrate the hyperparameters together with the uncertain model parameters [76, 34] and was also used in [97]. This is referred to as hyper parameter inference (HPI). To highlight the difference between the two methods, the comparison between a calibrated pdf with hpi and a pdf obtained using a fixed value for the hyperparameter obtained using the evidence method is shown in Figure IV.16.

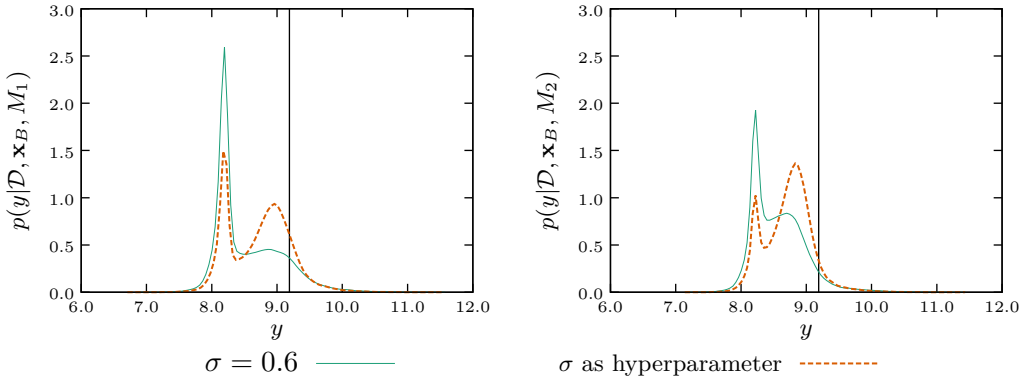

Fig. IV.16 *Demonstration of the difference between critical velocity distributions after calibration of the corresponding parameters, conducted with hyperparameter inference (HPI) and a fixed hyperparameter value obtained using the evidence method, taken from [97].*

While the hpi procedure calibrates the distributions more easily, it adds some ambiguity to the calibration result, because the error does not necessarily have to be optimal for all points of data at all times, but can adapt when one set of parameters produces results close to one of the datapoints. With respect to a fixed value obtained by the evidence method, this can lead to certain parameter values being "overpronounced" in probability density. Obviously, this ambiguity disappears in the context of a maximum a posteriori (MAP) estimate of parameters, as only one optimal value of the hyperparameter is picked. To avoid the ambiguity, this work used the evidence method.

IV.6 Introducing a bias

The fact that the prediction show high error standard deviations even after calibration indicates that there is considerable model inadequacy in the present aeroelastic calibration analysis. The deterministic results as well as the propagations of the prior and posterior distributions systematically underestimate the critical flutter velocity. In this subsection, the error term will be modified, as was already demonstrated in [97] in order to account for this offset and better model the model inadequacy. Specifically, in order to model the discrepancy, a constant, positive offset will be introduced into the error term of Equation

(IV.1), which is repeated below as a reminder.

$$\mathbf{q} = \mathbf{y}(\mathbf{x}, \boldsymbol{\theta}) + \boldsymbol{\epsilon} \tag{IV.14}$$

The introduction of the discrepancy term into the error represents a deviation from the common assumption of a Gaussian zero-mean error; in this case, the error will have a mean. In the following, instead of being distributed $\boldsymbol{\epsilon} \sim \mathcal{N}(0, \sigma)$, the error will be modelled as

$$\boldsymbol{\epsilon} \sim \mathcal{N}(\mu, \sigma) \tag{IV.15}$$

The mean μ of the error term on the critical flutter velocity V_f^* is an additional hyperparameter. It is determined together with σ as before by using the integrated likelihood obtained from integration using the likelihood involving the full dataset. The optimal set of hyperparameters is presented in Table IV.9.

	Wright	Theodorsen
μ	0.9	0.4
σ	0.3	0.4

Table IV.9 – Optimal hyperparameters for the different aerodynamic models obtained by optimising the integrated likelihood. The likelihood is calculated on full dataset (Table IV.2). The integration is performed using Monte Carlo integration with 10^5 samples.

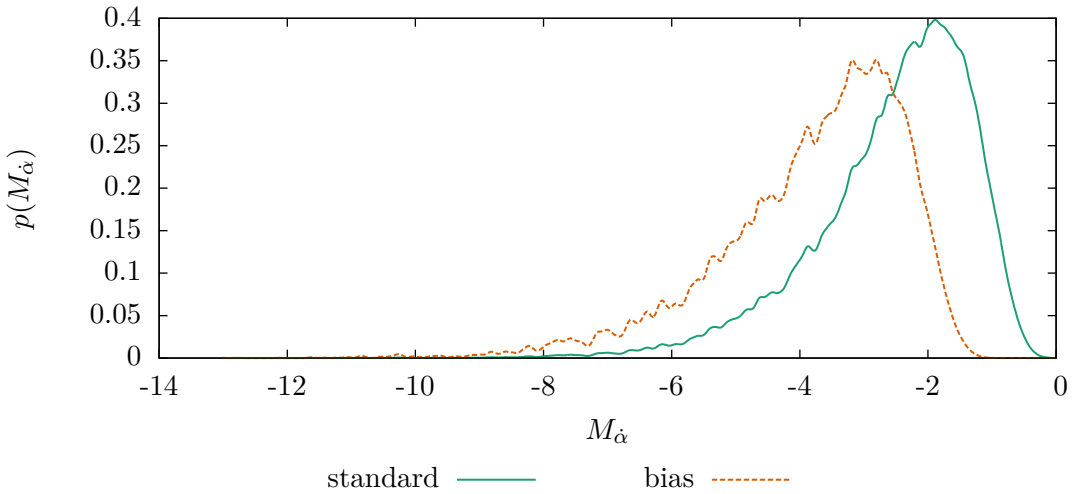

Fig. IV.17 *Posterior distribution for Wright model parameter $M_{\dot{\alpha}}$ obtained by calibration on scenarios A, C and D from [124] and the hyperparameters for the non-zero mean error given in Table IV.9. Posterior distribution obtained using importance sampling with 10^5 samples.*

Of course, the parameter calibration is affected by the use of the bias. The posterior distribution for the parameter $M_{\dot{\alpha}}$ corresponding to the prediction result in Figure IV.18

is shown in Figure IV.17. The distribution is shifted to the left with respect to the result of the ordinary calibration. In addition to that, it only starts to show significant probability density values at parameter values of below $M_{\dot{\alpha}} < -2$. The tail of the distribution also extends to lower values of the parameter.

The corresponding predictive distribution in V_f^* is shown in Figure IV.18. A clear improvement can be noticed. The standard deviation of the predictive distribution is significantly reduced, and the main probability density mass moves towards the experimental value.

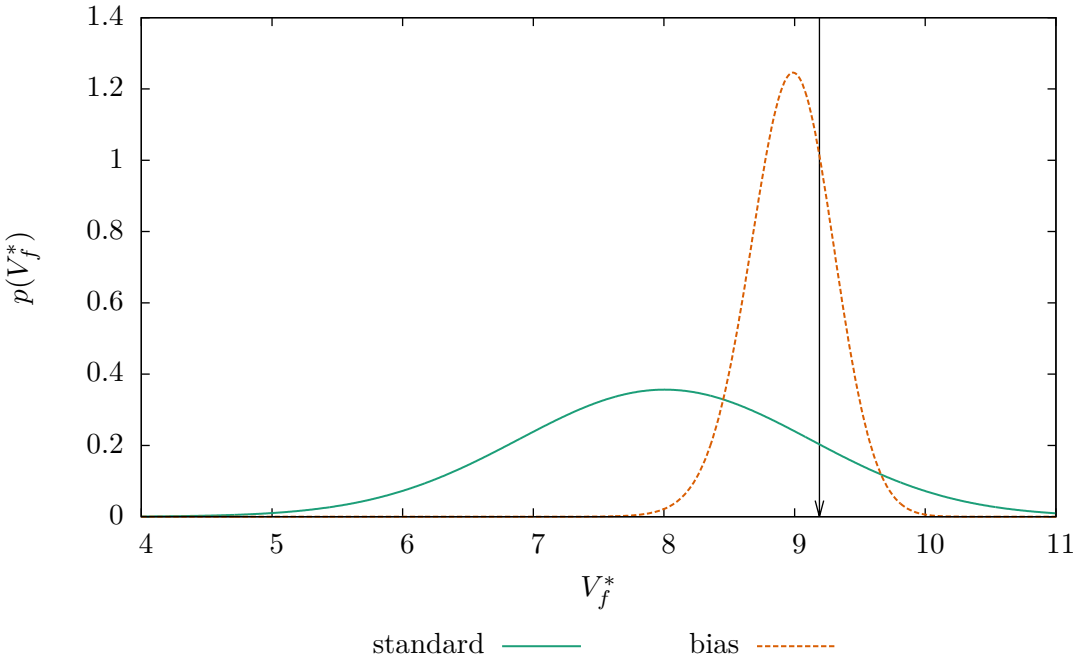

Fig. IV.18 *Predictive distribution for scenario B obtained using the Wright model calibrated on scenarios A, C and D from [124] and the hyperparameters for the non-zero mean error given in Table IV.9. Predictive distribution obtained using importance sampling with* 10^5 *samples.*

The predictive distribution for the Theodorsen type model is shown in Figure IV.19. As in the case of the Wright model, the distribution shifts towards the experimental value that is tried to predict, and the standard deviation of the distribution is significantly reduced, albeit the difference is not as pronounced as in the Wright aerodynamic model.

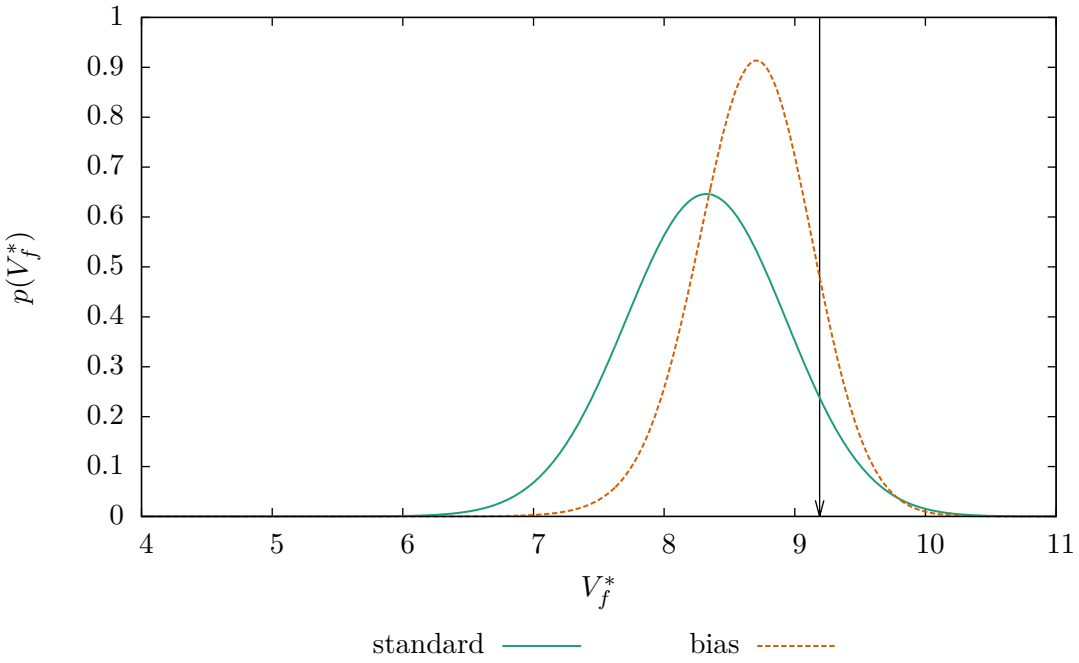

Fig. IV.19 *Predictive distribution for scenario B obtained using the Theodorsen model calibrated on scenarios A, C and D from [124] and the hyperparameters for the non-zero mean error given in Table IV.9. Predictive distribution obtained using importance sampling with* 10^5 *samples.*

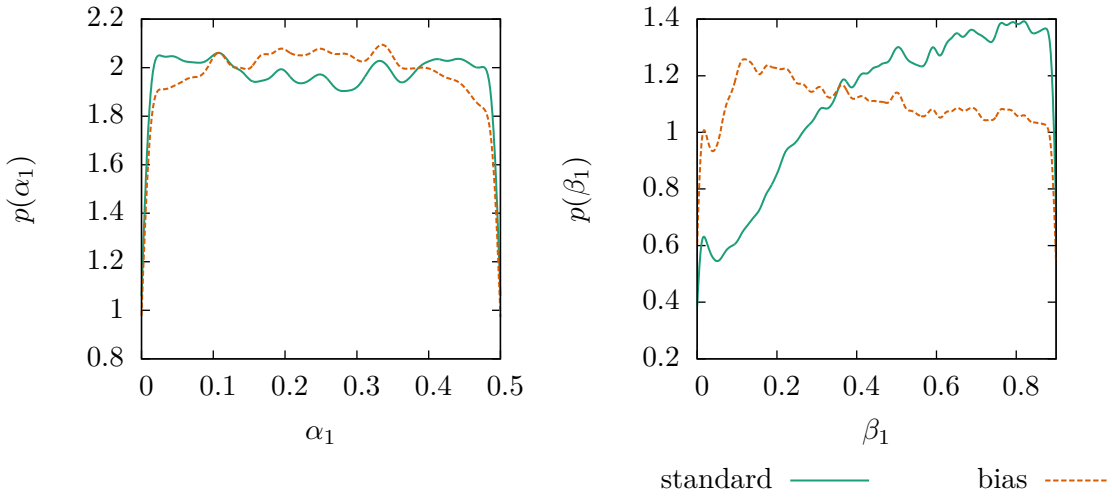

Fig. IV.20 *Posterior distribution for Theodorsen model parameters* α *and* β *obtained by calibration on scenarios A, C and D from [124] and the hyperparameters for the non-zero mean error given in Table IV.9. Posterior distribution obtained using importance sampling with* 100000 *samples.*

As in the Wright example, the posterior parameter distributions are also influenced by the bias in the likelihood used for the calibration, as shown in Figure IV.20. The α weight parameter values now tend more towards moderate values at the center of the priors instead of the extremes. The maximum probability density of the β time scale parameter values, before to be found at values between 0.3 and 0.4 can now be found at values significantly lower, between 0.1 and 0.2.

In conclusion, the adaptation of the error term can improve the prediction. However, it influences the calibration. It is thus preferable to put more intelligence in the models in order to suppress eventual errors. However, in this process, a well-adapted error term can give additional clues about the nature of the error.

IV.7 Critical discussion

In this chapter, a calibration study was performed on two different aeroelastic models in order to improve the prediction results. While in some cases, an improvement could actually be achieved, this was not the case for all the scenarios taken into account, and propagation results were systematically off in many scenarios despite calibration.

The remaining discrepancies point to inadequacies in the models that cannot be fixed by a calibration of the model parameters as done in the framework of this thesis. Possible sources of these model errors are listed in the following.

- Friction in the apparatus was not taken into account by the calculation. Adding friction probably would rise the critical flutter velocity [124], which could be an explanation why the model so heavily underestimates it.
- The wing used in the PAPA case has a profile [124], while the aerodynamic model is made for a flat plate. The profile could alter the behaviour of the aerodynamic lift and moment as a function of the degrees of freedom, as well as make their behaviour in time more complicated. However, it is difficult to estimate how this would change the prediction of the flutter response.

The usefulness of the calibrations is further limited by the fact that the aerodynamic models used in this work, especially the approximations of Theodorsen's function, are difficult to calibrate. This comes from the fact that almost any parameter in the models is frequency-related and will deliver different performances for each scenario. Moreover, the mapping of parameter values to velocity values is not unique in the case of Theodorsen's function's approximation, which makes calibration harder. Sandhu et al. [113] apparently tried to solve that problem by a partitioning of the prior parameter space, which would explain the choice of priors. The approach adopted in this work tried to let the Bayesian techniques do the work, which led to the posteriors being very ambiguous, and providing little scientific benefit.

Bayesian model uncertainty quantification methods quickly come to a limit in cases where the discrepancy between model and experiment is big. The controversy if the error term in the classical Bayesian framework is a "modelling error" or a "measurement error"

points to this problematic. Most of the time, it is supposed that the model is perfect and any error comes from the experiment having deviances (e. g. [50]). In this case, this means in the case of the Wright model that the experiment would actually create a quasi-steady potential flow plus some airstream velocity-dependent damping term. In the case of the Theodorsen model, it would mean that it would have to be some modulated vortex sheet that is transported in a potential flow. Of course, any experiment can not even come close to that. The set-theory based Bayesian framework by [21] would not even allow any deviation, because it assumes that for any point in the data space, there is a parameter value that accurately predicts the data. In this work, this issue is adressed by demonstrating the use of a bias term in the PAPA case. This has the inconvenient that the bias term is not physically motivated, but just describes the error. In this work, the bias term does not shift the calibration results to values that would be completely contradicted by different experiments, but nevertheless, the bias term has to be regarded as a band aid. The author recommends to use more complex physical models that is able to reproduce the data with its parameters.

A last but considerable weakness is the number of available data points. In this study, four datapoints with only one feature were available. In the data science domain, this is considered too small a number in order to reproduce reliable results [69], nor do they cover enough scenarios to give a universal stochastic model as an output. Moreover, the aim of any Bayesian study is to get the posteriors independent from the choice of the priors, but this is clearly not achieved here: in limits and shape of the distributions, the posteriors clearly remain influenced by the shape and scale of the prior distributions. As physical considerations were incorporated into the priors and great attention was paid to pick priors with the biggest entropy possible, the conclusions are prevented from getting unphysical. Combining data from different experiments may have helped the calibration. Still, the reader should be clearly warned that any conclusion is tied to the datasets used in this work and may not be generalisable. In [97] which relied on the same data points and consequently suffered from the same problem, a study was conducted using interpolated data to demonstrate that the distributions change from the state that is achieved by the calibration using the four points "naturally" present. In this work, it will be tried to solve the problem by adding data from different types of experiments that can contribute information on the parameters. This will be, together with the problem of calibration in presence of aleatory uncertainties, the subject of the next chapter.

IV.8 Conclusions

In this chapter, Bayesian calibration was performed in order to obtain stochastic estimates for the aerodynamic models by Wright and Cooper [146] and approximated versions of the model by Theodorsen [124]. The calibration was performed using flutter velocity data from PAPA experiments from Theodorsen [124].

Prior distributions were defined based on information entropy considerations, where physical constraints and indications on the values of the model parameters given in the literature were taken into account. As no indications on the experimental error was given in

the reference, the hyperparameter, namely the standard deviation of the critical flutter velocity in the likelihood function, was determined using the evidence method.

Using this setup, calibration of the two models was performed. Wright's model was very responsive to the calibration, while Theodorsen's model reacted less clearly. In both cases, considerable uncertainty was left in the model parameters. The results of the calibrated models in critical flutter velocity were improved in both models. However, neither of the models could reproduce the data exactly and in many examples, calibration seemed to be limited by a barrier.

Model probabilities were calculated for both models using Bayesian Model Averaging. However, the model probability of the Theodorsen-type models were at 95%, effectively dismissing Wright's model. This confirms the expectation that the Theodorsen-type models due to their unsteady nature are much more effective at predicting the critical flutter velocities. Consequently, the total predictive distribution was very close to a prediction using the Theodorsen model alone.

As the models were observed to underestimate the critical flutter velocity even after calibration, a bias term in form of a mean in the error was introduced to improve predictions. While this approach succeeded in reducing the variance of the predictive distributions and more accurately predicting the flutter velocity, it had repercussions on the calibration of the parameters, which could lead to unphysical results.

Finally, several weaknesses of the study were pointed out, the most important of them being the limited accuracy of the models and the lack of data. In the last part of the following chapter, this issue will be adressed by incorporating multiple data sources from different experiment types.

Chapter V

Application to a composite plate wing

The examples in the previous chapter relied on a rather simple test case, which was a pitch and plunge airfoil. A number of experimental data were used to calibrate the aerodynamic model parameters of selected models. Any additional parameters further defining the problem were assumed to be deterministic. While this focus on the non-accessible model parameters is common in Bayesian calibration studies, the assumption that the other, more accessible parameters in the model are deterministic is not always a reasonable choice. Uncertainties in other parameters can significantly affect the prediction and also influence the calibration.

In the following, such a case will be considered by performing the Bayesian calibration, which was introduced in the previous chapter, on the aerodynamic model parameters of the composite plate wing problem discussed in chapter III. First, the calibration will be performed assuming that the composite material is deterministic. Afterwards, the uncertainty in the composite material as given in chapter III will be inserted into the problem. Finally, further steps will be taken to refine the uncertainty definitions, separate the different effects and optimally exploit all given data. In particular, the calibration procedure will use data from the different kinds of experiments.

V.1 Reference data

In this chapter, the reference data are taken from Hollowell and Dugundji [58], who performed wind tunnel experiments for flutter on composite plates. The composite plates used were six-layer layups made of AS1-3501 graphite-epoxy composite material. Its basic properties are repeated in Table V.1 for convenience.

$E_1[GPa]$	$E_2[GPa]$	$G_{12}[GPa]$	ν_{12}	$\rho[kg/m^3]$	$t_p[m]$
98	7.9	5.6	0.28	1520	$0.134 \cdot 10^{-3}$

Table V.1 – Engineering moduli and other basic properties for the base layer AS1 3501 composite graphite-epoxy material used in [58].

The layup sequences are given in Table V.2 alongside with the nominal values of the polar parameters. It must be noted that with respect to [58], the signs of the angles are inverted because a different sign and axis convention is used. It has to be noted that except for layup A, none of the layups possesses any particular elastic symmetries, as R_0 and R_1 are non-zero and the angular difference $\Phi_0 - \Phi_1$ is not a multiple of $\frac{\pi}{4}$ (see Table III.1). Also, all layups have a strong directional character.

Scenario	Layup	$\tilde{T_0^D}[Nm]$	$\tilde{T_1^D}[Nm]$	$\tilde{R_0^D}[Nm]$	$\tilde{R_1^D}[Nm]$	$\tilde{\Phi_0^D}$	$\tilde{\Phi_1^D}$
A	$[0_2/90]_S$	0.674	0.601	0.432	0.455	0	0
B	$[\mp 45/0]_S$	0.674	0.601	0.400	0.219	$-\frac{\pi}{4}$	-0.744
C	$[-45_2/0]_S$	0.674	0.601	0.400	0.473	$-\frac{\pi}{4}$	-0.766
D	$[+45_2/0]_S$	0.674	0.601	0.400	0.473	$\frac{\pi}{4}$	0.766
E	$[-30_2/0]_S$	0.674	0.601	0.408	0.482	-0.515	-0.507
F	$[+30_2/0]_S$	0.674	0.601	0.408	0.482	0.515	0.507

Table V.2 – Layups of [58] and the corresponding polar parameters.

In the following, the data from Hollowell's [58] experiments will be given for free vibration as well as for the aeroelasticity problem, and compared to the original numeric results as well as the deterministic results from the solvers presented in Chapter II .

V.1.1 Free vibration data

Scenario	Layup	$\omega_1[rad/s]$	$\omega_2[rad/s]$	$\omega_3[rad/s]$
A	$[0_2/90]_S$	69.74 (69.54)	263.89 (248.76)	433.54 (435.80)
B	$[\mp 45/0]_S$	38.33 (40.48)	238.76 (252.44)	483.81 (461.54)
C	$[-45_2/0]_S$	30.16 (30.88)	188.50 (190.77)	320.44 (463.15)
D	$[+45_2/0]_S$	30.16 (30.88)	188.50 (190.77)	320.44 (463.15)
E	$[-30_2/0]_S$	37.70 (39.90)	226.19 (238.34)	364.42 (441.06)
F	$[+30_2/0]_S$	37.70 (39.90)	226.19 (238.34)	364.42 (441.06)

Table V.3 – Free vibration experimental results from Hollowell and Dugundji [58]. Numerical results using eight modes in span-wise and two modes in chord-wise direction given in parentheses. Note the changed signs, which are due to the z axis pointing downwards in the framework of this work.

Table V.3 shows the results from the free vibration experiments from [58]. Note that configurations C and D as well as E and F are identical with respect to free vibration, as they are just flipped. However, in flutter experiments, this will make a difference.

It must be noted that the frequencies for the third mode are estimated too high for the cases C-F, which is due to the number of modes in chord-wise direction being limited to two. As this shortcoming would affect the estimation of the material properties, modes above the second mode are left out of the analysis. However, the limitation of chord-wise modes is necessary for the flutter models which assume the plate to be rigid in direction of the chord. Nevertheless, this is not expected to affect the flutter prediction by much, as flutter modes are often of low-order kind [28].

V.1.2 Flutter experimental data

In fact, only the flutter points from cases A, C and E are fully usable for the Bayesian study (see [58]). Case B's flutter limit exceeded the maximum speed of the wind tunnel, so no experimental data had been obtained. Cases D and F are subject to aeroelastic divergence before they start to flutter. Aside from the fact that the k-type aeroelastic solver used in this work cannot predict divergence, only the quasi-stationary part of the aerodynamic model contributes to the limit speed. Consequently, these scenarios are useless for calibrating the model parameters identified as epistemically uncertain, because these are all related to unstationary effects.

The original results from [58] are given in Table V.4, along with the numerical results of the original article, which are given in parentheses. Hollowell and Dugundji [58] article uses beam functions and a camber correction as the mode shapes, and Theodorsen aerodynamics with Jones' 1938 approximation to Theodorsen's function [57]. In case A, both the flutter velocity and the flutter frequency are significantly lower than the values found by experiment. In contrast, the flutter velocity calculated for the C and E cases is very close to the experimental results, while the calculated flutter frequencies are considerably higher than their equivalents found experimentally.

Case	Flutter speed $V_f[m/s]$	Flutter circular frequency $\omega_f[rad/s]$
A	25 (21.0)	182.21 (157.08)
C	28 (27.8)	150.80 (175.93)
E	27 (27.8)	175.93 (194.78)

Table V.4 – Flutter data from [58], obtained for the wings with geometric specification given in Table III.2 and material configurations given in Tables V.1 and V.2. Only usable points with experimental data for flutter are given. The numerical results from the original article are given in parentheses

The numerical flutter results obtained by applying the two aerodynamic models previously introduced in this work, namely the Wright model and the implementation of Theodorsen's model as described in Chapter II, are shown in Table V.5.

Case	Flutter speed $V_f[m/s]$	Flutter circular frequency $\omega_f[rad/s]$
Wright		
A	13.49	201.30
C	28.64	176.25
E	22.68	193.84
Theodorsen		
A	21.00	159.00
C	30.89	161.03
E	27.02	176.25

Table V.5 – Deterministic numerical results using Wright's original model with $M_{\dot{\alpha}} = -1.2$ and Theodorsen's model with the original function from [124]. Geometric specifications for the plate wings are given in Table III.2 and material configurations given in Tables V.1 and V.2

The Wright model delivers mixed results for the choice of the instationary parameter $M_{\dot{\alpha}} = -1.2$. In scenario A, the frequency is overestimated, while the result for the critical flutter velocity lies considerably below the experimental or original numerical results. The results for scenario C are much closer, with the critical flutter velocity predicted to within below $1[m/s]$, and the flutter frequency predicted to within $20[rad/s]$. The E scenario lies in between the two extremes, with the critical flutter velocity considerably underestimated, albeit not by as much as in the A scenario, and the flutter frequency is once again overestimated by $\approx 20[rad/s]$.

The Theodorsen model delivers much more consistent results with respect to the experiments, with the predicted critical flutter velocity being much closer to the experimental values than the Wright model. Again, the prediction for scenario A is the worst. The model does worse for the C scenario than its Wright counterpart, but better for the E scenario, where the velocity matches the experimental result very closely. The frequency estimates are also closer, but consistently underestimated except for the E scenario, where the frequency calculation is remarkably close. It is to be noted that these results are different from the original numerical results from [57, 58], which is partly due to the different assumed mode shapes, but also to the use of Theodorsen's function instead of Jones' approximation.

V.2 Bayesian study on the aerodynamic models with deterministic material

In this section, the data presented in the beginning of this chapter will be used to perform a calibration of the aerodynamic parameters, as it was done in Section IV.3 for the PAPA case from [124]. However, for the plate wing, frequency data is available, which is expected to alter the results. Moreover, the modal shapes play a more fine-grained role in the ratio between the pitch and plunge movements that the two models depend on, which could provide additional information. Nevertheless, the physical assumptions made to

construct the priors remain valid. Therefore, the same priors as in the previous chapters are employed.

The hyperparameters are identified using the evidence method introduced in section IV.3, where different σ values for frequency σ_ω and velocity σ_V are searched for. As before, the experiments are supposed independent. Moreover, it is assumed that the flutter frequency and the flutter velocity are not correlated. This gives the covariance matrix a diagonal structure. Each of the two hyperparameters is supposed to have the same value for each experiment in this case. Consequently, only two values have to be calibrated. Hollowell and Dugundji [58] gives the frequency results in steps of $1[Hz] = 2\pi[rad/s]$ and the velocity results in steps of $1[m/s]$. Consequently, the optimisation of the hyperparameter values is performed in the same way.

Results are given in Table V.6, where the lines are a function of the standard deviation in critical flutter velocity, while the columns represent the flutter frequency. The maximum value of the integrated likelihood is found for the Wright model at $\sigma_V = 5[m/s]$ and $\sigma_\omega = 2[Hz]$, while for the Theodorsen model, the maximum value is obtained for $\sigma_V = 4[m/s]$ and $\sigma_\omega = 2[Hz]$. The method thus claims the Theodorsen model to be slightly more precise.

Wright						
$\sigma_V[m/s]/\sigma_\omega[Hz]$	1	2	3	4	5	6
1	-45.89	-33.02	-30.76	-30.38	-30.47	-30.70
2	-30.83	-25.95	-25.09	-25.08	-25.32	-25.63
3	-27.46	-23.74	-23.56	-23.84	-24.22	-24.60
4	-26.56	-23.03	-23.01	-23.38	-23.81	-24.22
5	-26.39	-22.88	-22.89	-23.29	-23.72	-24.15
6	-26.47	-22.98	-22.97	-23.36	-23.80	-24.22
Theodorsen						
$\sigma_V[m/s]/\sigma_\omega[Hz]$	1	2	3	4	5	6
1	-34.81	-28.89	-28.13	-28.11	-28.28	-28.53
2	-26.04	-22.37	-22.19	-22.50	-22.88	-23.26
3	-24.68	-21.28	-21.26	-21.66	-22.09	-22.50
4	-24.54	-21.14	-21.16	-21.66	-22.09	-22.50
5	-24.72	-21.29	-21.32	-21.73	-22.19	-22.61
6	-24.99	-21.54	-21.56	-21.97	-22.44	-22.86

Table V.6 – $\log(P(D|M))$ for the aerodynamic models in the plate flutter problem, using the nominal values of the composite stiffnesses as deterministic explanatory parameters. The maximum value is best. Integrated likelihood obtaines using Monte Carlo simulation with 10^5 samples.

As before, the calibration study will start with the Wright model. In Table V.7, the calibrated parameters, and the choices for the datapoints used for calibration and the hyperparameters are summarised.

Model calibrated $\mathcal{D}$	Wright-type
Calibrated parameters $\boldsymbol{\theta}$	$M_{\dot{\alpha}}$ (aerodynamics)
Hyperparameters	$\sigma_{V_f} = 5, \sigma_\omega = 4\pi$
Data used $\mathcal{D}$	[58], scenarios A,C,E (flutter data) (Table V.4)

Table V.7 – Summary of calibrated parameters, settings and data for calibration of the Wright model supposing deterministic material stiffnesses

Figure V.1 shows the calibration results for the Wright model obtained using the plate flutter dataset from [58] in comparison to the calibration results obtained using the PAPA dataset, which were presented in Chapter IV.3. While the shape of the posterior is confirmed, the distribution curve gets steeper and narrower, which means that more information is drawn from the plate flutter dataset. This could be due to the fact that contrarily to the PAPA dataset, the plate flutter dataset also contains information on the flutter frequency. Moreover, the curve shifts more to the left, with the maximum probability density now at about $M_{\dot{\alpha}} = -3$. This could be due to the fact that the two datasets map computationally to different frequency ranges and would support the claim by [146] that the value of the parameter could be frequency-dependent. Another possible reason for the difference could be the presence of structural damping in the PAPA used by [124], which the model does not account for. As $M_{\dot{\alpha}}$ adds to the global damping in the model, information about damping could instead go into the parameter originally intended for aerodynamic modelling.

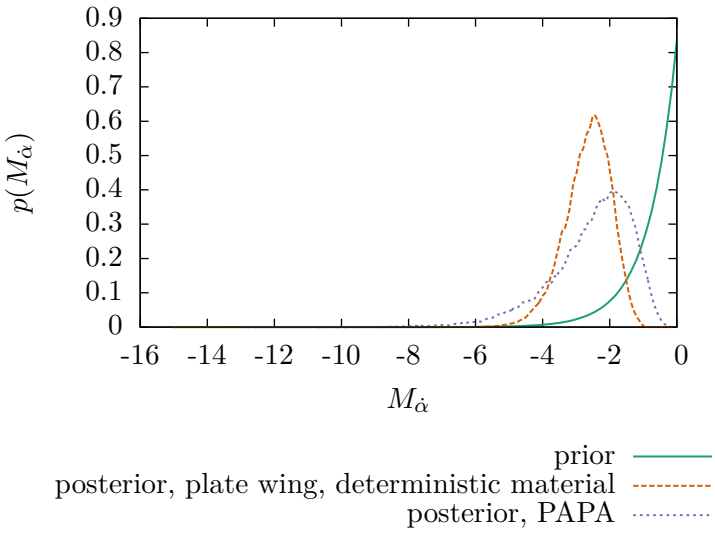

Fig. V.1 *Posterior for the Wright model aerodynamic parameter obtained using the plate flutter data from [58] compared to posterior obtained using the PAPA data from [124]. Distribution obtained using importance sampling with* 10^5 *samples.*

The corresponding frequency and velocity distributions are shown in Figure V.2. While

the propagations of the priors often are relatively widely spread, the model response approaches the experimental value in all cases. The most clear case is scenario C, where the model had a split in the frequency range and thus considered two modal regimes. The final distribution has only one modal regime. However, this restricts the modeling capacity in a way that in comparison to the prior, less samples fall on the experimental result for the velocity. Generally, the model does not cover all experimental results with significant probability density, meaning that it is not capable of simulating all experimental results with one set of parameters.

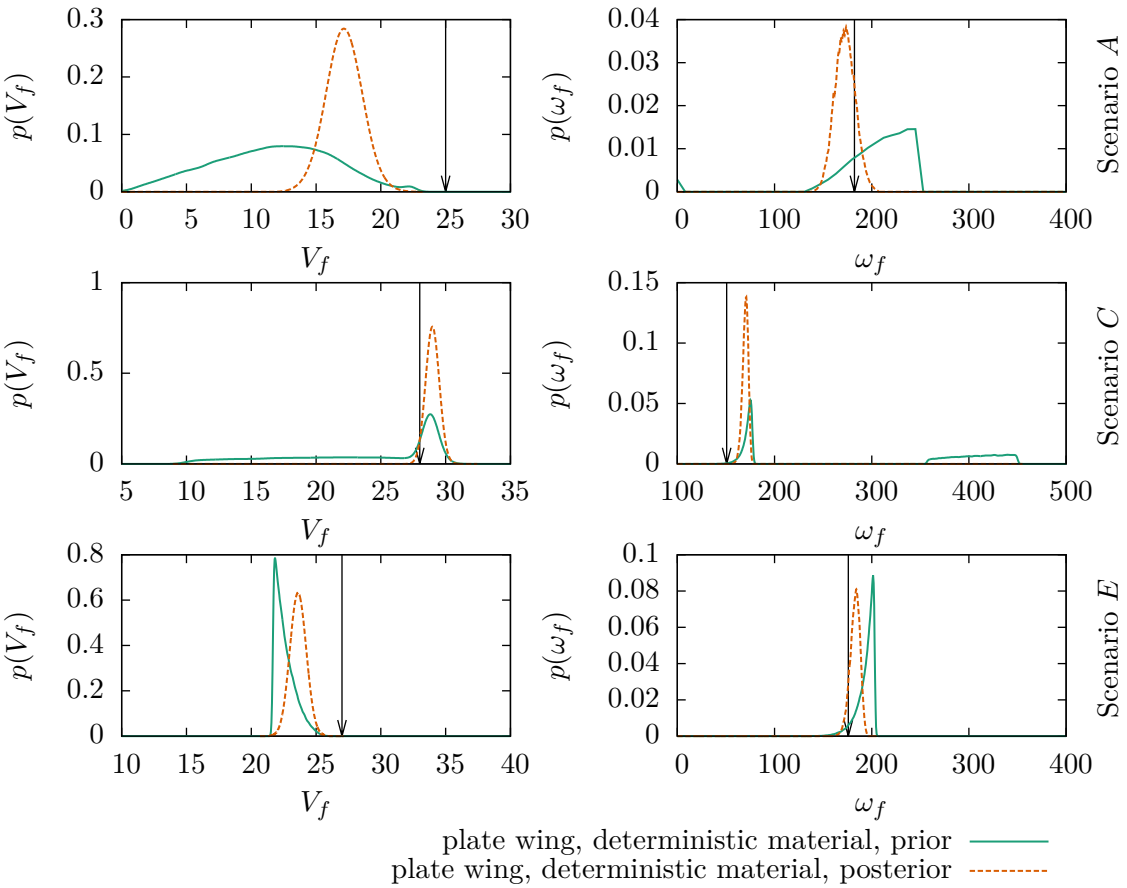

Fig. V.2 *Posterior velocity and frequency results of the Wright aerodynamic model with the nominal material properties used and using only the flutter data from [58] (Table V.4). Distribution obtained using importance sampling with* 10^5 *samples.*

.

Model calibrated $\mathcal{M}$	Theodorsen-type
Calibrated parameters $\boldsymbol{\theta}$	α_1, α_2, β_1, β_2 (aerodynamics)
Hyperparameters	$\sigma_{V_f} = 4, \sigma_\omega = 4\pi$
Data used $\mathcal{D}$	[58], scenarios A,C,E (flutter problem) (Table V.4)

Table V.8 – Summary of calibrated parameters, settings and data for the Theodorsen model on the plate wing case from [58], supposing deterministic material stiffnesses.

The calibration results for the Theodorsen model are shown in Figure V.3 and compared to the previous calibration results using the data from Theodorsen's experiments, which were given in Figure IV.6. Generally, it can be stated that the parameters are better informed. The distributions for the weighting parameters α_j that were previously stated flat have become more accentuated, with the maximum between 0.1 and about 0.35, which corresponds to the model in use. The time scale parameters β_j generally shift to the left, and a new local maximum at values between 0.3 and 0.4 develops. The small local peak at values below 0.1 is confirmed and considerably strenghtened.

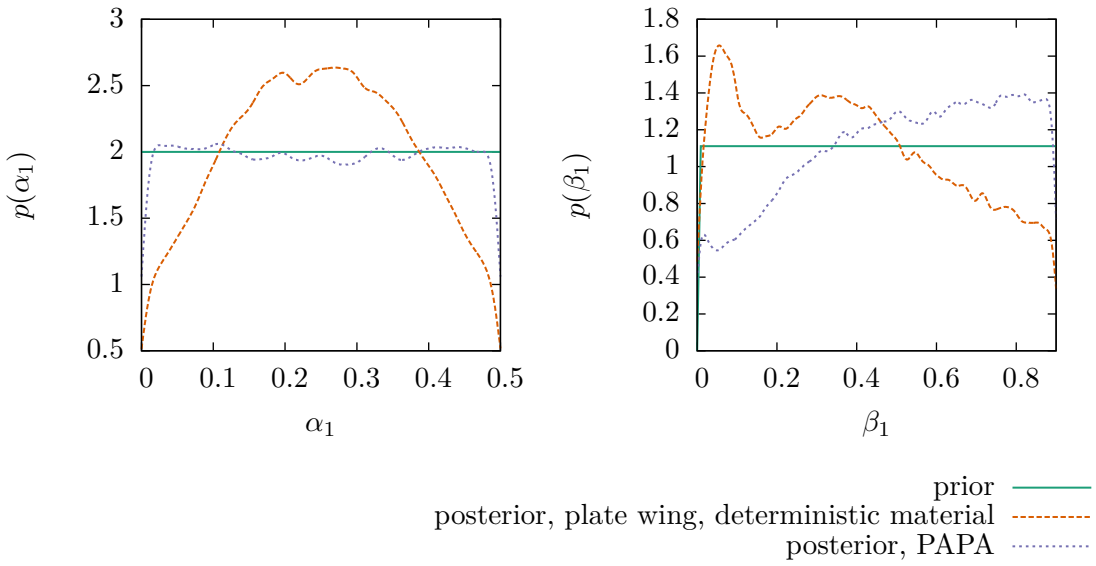

Fig. V.3 *Posteriors for the Theodorsen model aerodynamic parameters obtained using the PAPA flutter data from [124] compared to posteriors obtained using plate flutter data from [58] (Table V.4). Distribution obtained using importance sampling with* 10^5 *samples.*

Figure V.4 shows the corresponding results in critical flutter velocity V_f and flutter frequency ω_f. The improvements in V_f remain relatively small, but the maximum of probability density moves nevertheless towards the experimental result. In contrast, the reduction of uncertainty for the critical flutter velocity is visible more clearly.

However, the model takes less profit from the data than the Wright model. This might come from the fact that in comparison to the latter, already the prior propagation results

were quite close to the experimental results. Again, coverage of the experimental results with samples is not ideal, and during calibration, often the probability density for the individual experimental value is even lowered, as for the velocity and the frequency in scenario A and C. This means that this model is not capable of perfectly simulating all results at once, either.

The gain in information in both scenarios may come from the fact that in the Hollowell and Dugundji [58] dataset, frequency data is available, which was not the case in the [124] dataset. Moreover, in the Hollowell and Dugundji [58] scenarios, the modal behaviour is more complex than in the two-degree-of-freedom configuration in the PAPA scenarios, which might also contribute to the fact that more information is obtained.

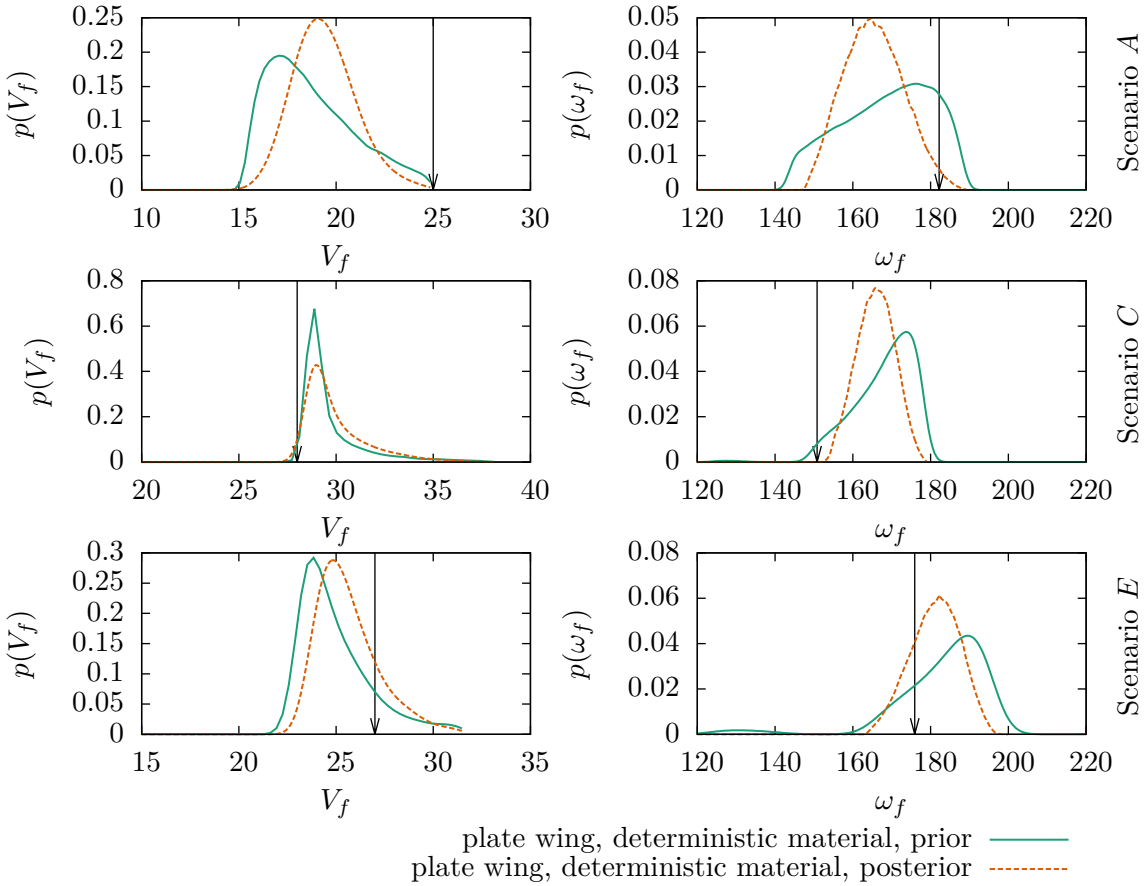

Fig. V.4 *Posterior velocity and frequency results for the Theodorsen aerodynamic model with the nominal material properties used and using only the flutter data from [58] (Table V.4). Distribution obtained using importance sampling with* 10^5 *samples.*

.

The differences in the distributions can have multiple sources. It is possible that the availability of frequency information in the composite plate wing scenarios also contributed to the shift in value, as the Bayesian technique just shifts the values of the parameters to the

combination that is "easiest" to obtain, meaning different results can be obtained when the model just has to predict the velocity data as when it has to respect both velocity and frequency constraints. Another probable reason for the shift could be that the two sets of scenarios cover different frequency ranges, which could provoke a difference notably in any parameter linked to time scales. This would also explain the big differences in calibrations for the β parameters of the Theodorsen models.

Finally, the model probabilities for the two models are evaluated as in the previous chapter. The results are given in Table V.9.

	Wright	Theodorsen
$P(\mathcal{M}\|\mathcal{D})$	0.15	0.85

Table V.9 – Model probabilities for the plate wing problem with deterministic material parameters, calculated using Monte Carlo simulation with 10^5 samples.

Again, the Theodorsen model has a much higher model probability. However, compared with the PAPA problem (see Table IV.8), the model probabilities are more favourable for the Wright model. This could possibly indicate that the role of the unsteady modeling provided by the Theodorsen model is less important in this case, making the decision between the two models less clear. Another possibility is that the Wright model is more suited for the frequency range of the plate wing experiments [58] used as data than for the frequency range of the PAPA data. However, as no explicit information on the frequency in the PAPA data was given, this remains speculation.

V.3 Bayesian study including uncertainty in the composite material

The aerodynamic models benefit from stochastic calibration, as demonstrated by the results shown for a PAPA model in section IV.3 and for a composite plate wing model in the previous section V.2. However, in the latter case, the material can be a considerable source of uncertainty. As this uncertainty originates in the manufacturing process and in measurement errors, it is assumed to be aleatory in nature, as discussed in chapter I. The consequences of such an uncertainty on the critical flutter velocity have been demonstrated in chapter III. Not taking this uncertainty into account could obviously distort the calibration results. In this section, an attempt is made to calibrate the aerodynamic model while taking into account an aleatory uncertainty in the material in the prediction of the flutter onset for the composite plate wing.

Two approaches are possible. Jakeman et al. [61] proposes to sample the aleatory uncertainty and for each sample of the aleatory uncertainty choice, sample the conditional posterior pdf for the given sample. In the end, the results for the different samples of the aleatory uncertainty are combined. In this work, another approach is taken such that the aleatory uncertainty is treated as epistemic uncertainty and added to the parameters $\boldsymbol{\theta}$. If the uncertainty is aleatory, i.e. irreducible, its distribution will not change and the

result should be the same for both methods. Otherwise, this approach will show that the distribution selected for the uncertainty is not actually represented by the data.

Technically, the calibration of the material will be performed supposing the error in the stacking sequence being the same. Consequently, common error terms are sampled, which are then added to the nominal stacking sequences in order to obtain the disturbed sequences. These realisations are then used to calculate the polar parameters which are presented. I will nevertheless refer to the polar parameters as the uncertain parameters.

Model calibrated $\mathcal{M}$	Wright-type
Calibrated parameters $\boldsymbol{\theta}$	$M_{\dot{\alpha}}$ (aerodynamics), $T_0^{\tilde{D}}, T_1^{\tilde{D}}, R_0^{\tilde{D}}, R_1^{\tilde{D}}, \Phi_0^{\tilde{D}}, \Phi_1^{\tilde{D}}$
Hyperparameters	$\sigma_{V_f} = 5, \sigma_\omega = 4\pi$
Data used $\mathcal{D}$	[58], scenarios A,C,E (flutter problem) (Table V.4)

Table V.10 – Summary of calibrated parameters, settings and data for the Wright model on the plate wing case from [58], with uncertain material stiffnesses.

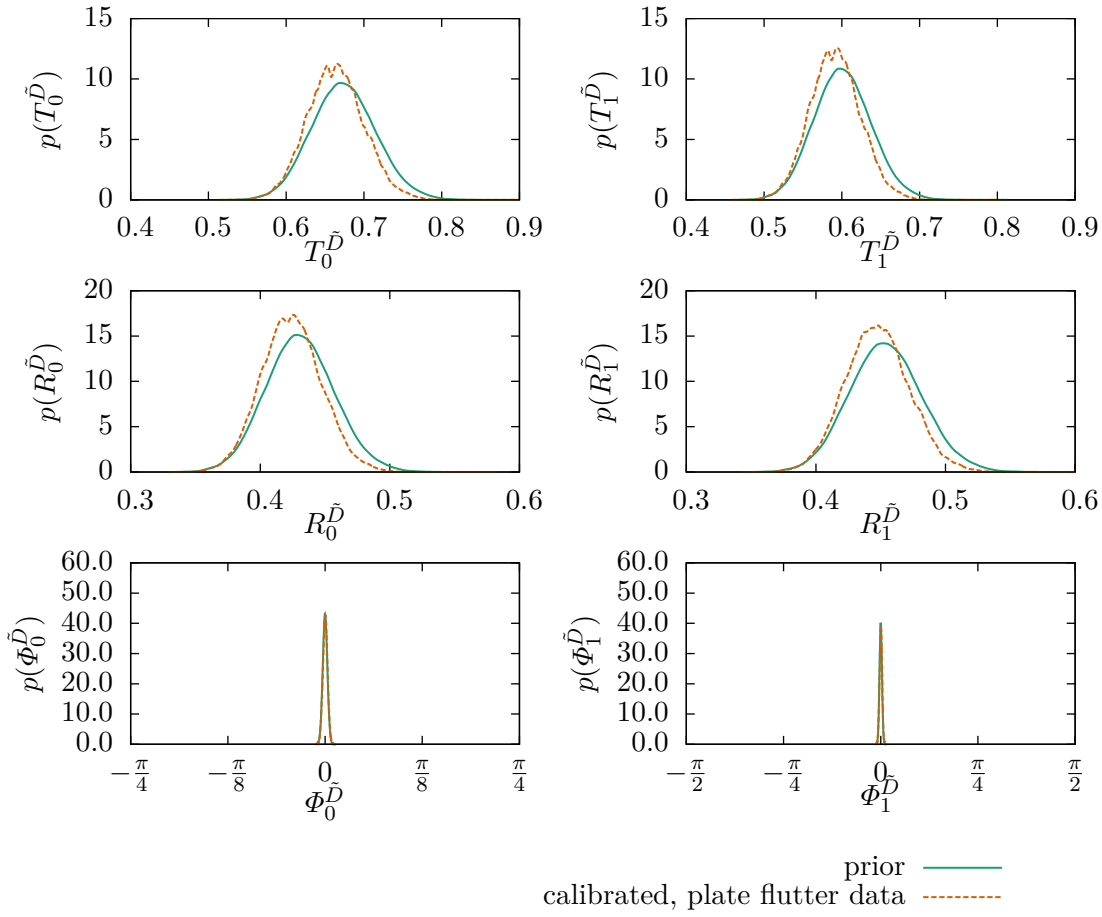

Fig. V.5 *Posterior distributions for the polar parameters for scenario A from [58], calibrated together with the Wright model on scenarios A, C and E, in comparison to the assumed distribution, used here as a prior. Distribution obtained using importance sampling with* 10^5 *samples.*

The marginal posterior distributions for the polar parameters when calibrated together with the Wright model on the three flutter scenarios from Table V.4 are shown in Figure V.5. While the distributions for the module parameters remain relatively close to the assumed distribution, they still are informed by the added data, which leads to a slight change, which can nevertheless be noticed.

The probability density functions for the parameters T_0, T_1, R_0, R_1 all show a shift to lower values, which could indicate that the stiffness is lower than initially assumed. At the same time, as all the parameter distributions shift in the same way, the material symmetry behaviour is not assumed to be altered with respect to the assumption underlying the prior distribution. One possible reason for the lower parameter values could be that the plies tend to be thinner than initially assumed. An alternative explanation would be lower elastic properties of the base material, even if those were not initially considered to be uncertain. However, the two effects are indistinguishable in the homogenised polar parameters, so neither of the two reasons can be ruled out.

The small changes in distribution of the stiffness properties could have multiple meanings. One interpretation could be that the supposed distribution used as a prior is close to the actual aleatory distribution, which would be the most favorable outcome. In that case, it could be used as a reasonable guess for the aleatory uncertainty. Another possible interpretation is that the experiments do not provide much information on the material, or that the other uncertainties present in the problem "drown" the material uncertainty, which cannot be determined further. In that case, this would mean that the supposed distribution does not picture the uncertainty in the material parameters correctly. In that case, an epistemic uncertainty about the true distribution of the material parameters arises.

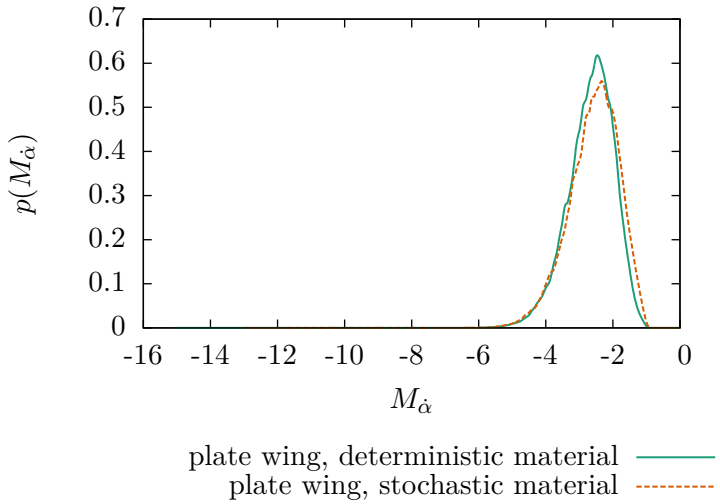

Fig. V.6 *Posterior distributions for the aerodynamic parameters of the Wright-type model, calibrated on scenarios A, C and E with uncertain material parameters, in comparison to the posterior distributions obtained by calibration on the same dataset assuming the nominal values of the polar parameters to be deterministic. Distribution obtained using importance sampling with* 10^5 *samples.*

The inclusion of the uncertainty in the stiffness of the composite material has almost

no effect on the calibration of the aerodynamic unsteady angular moment derivative $M_{\dot{\alpha}}$ in this case, as shown in Figure V.6. The maximum of probability density is slightly lower, and the maximum moves towards higher values by a small amount. However, these changes are not significant.

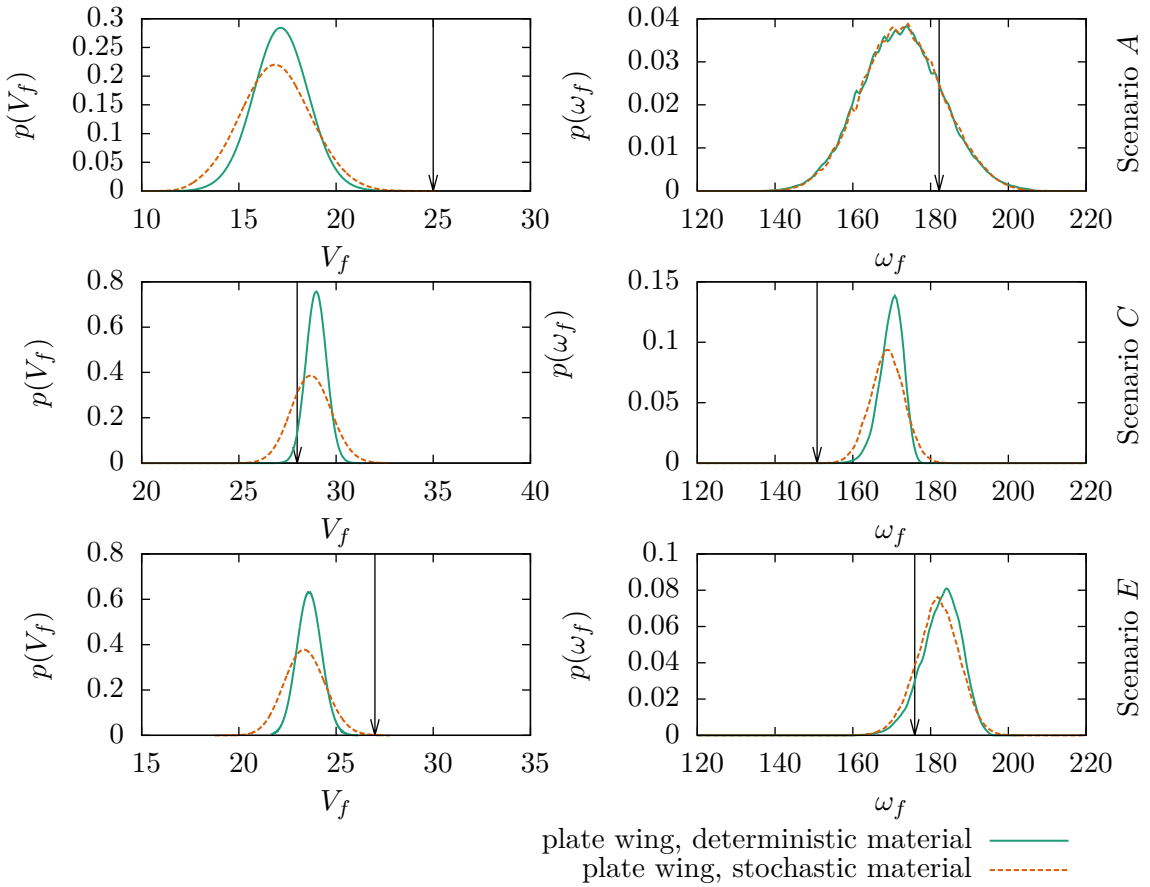

Fig. V.7 *Posterior results for critical flutter velocity and flutter frequency obtained with the Wright model after calibration using plate flutter data from [58] (Table V.4). Distribution obtained using importance sampling with* 10^5 *samples.*

In contrast, the posterior results for the velocities and frequencies shown in Figure V.7 are more clearly affected, especially in the critical flutter velocity. In most cases, the distribution is widened, which comes from the added entropy through the inclusion of the uncertainty in the material stiffness. The biggest effect can be observed in scenario C, in which the velocity was previously resolved best. In the other cases, especially for the frequencies, the difference is smaller, with the extreme in scenario A where the distribution nearly does not change.

In the following, the calibration study will be repeated with the Theodorsen model, for which the parameters calibrated as well as the choices for hyperparameters and datapoints are given in Table V.11. Note that other than for the Wright model, the error standard deviation in frequency has become bigger and is now $3 \cdot 2\pi$ due to the added uncertainty.

Model calibrated $\mathcal{M}$	Theodorsen-type
Calibrated parameters $\boldsymbol{\theta}$	α_1, α_2, β_1, β_2 (aerodynamics), $T_0^{\tilde{D}}, T_1^{\tilde{D}}, R_0^{\tilde{D}}, R_1^{\tilde{D}}, \Phi_0^{\tilde{D}}, \Phi_1^{\tilde{D}}$ (material)
Hyperparameters	$\sigma_{V_f} = 4, \sigma_\omega = 6\pi$
Data used $\mathcal{D}$	[58], scenarios A,C,E (flutter problem) (Table V.4)

Table V.11 – Summary of calibrated parameters, settings and data for the Theodorsen model on the plate wing case from [58], with uncertain material stiffnesses.

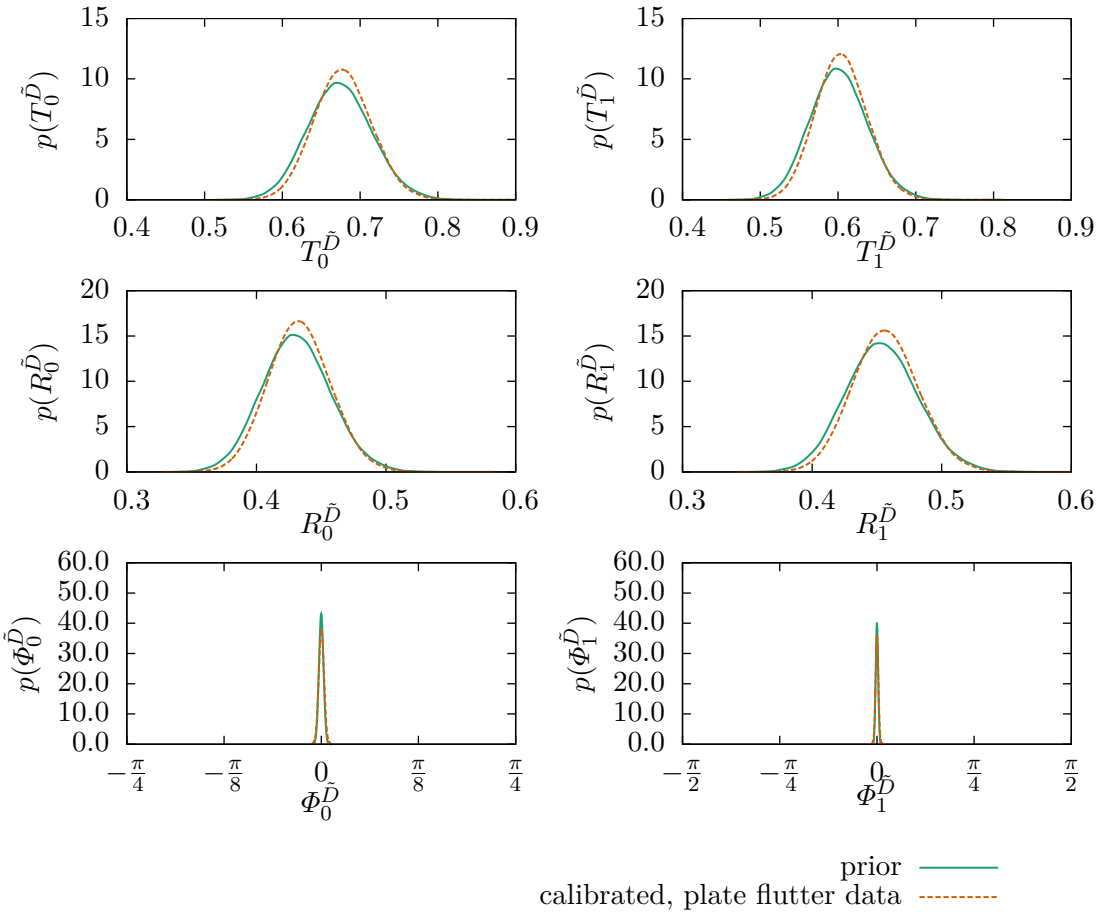

Fig. V.8 *Posterior distributions for the polar parameters for scenario A from [58], calibrated together with the Theodorsen model on scenarios A, C and E, in comparison to the assumed distribution, used here as a prior. Distribution obtained using importance sampling with* 10^5 *samples.*

Again, the calibration results for the material parameters are shown first for the A scenario. The estimates of their probability density functions are given in Figure V.8. As in the previous study using the Wright model (Figure V.8), the distributions of the parameters do not change much with respect to the given prior, but hint again that it may not be a purely aleatory distribution. Moreover, the uncertainty is reduced slightly. How-

ever, instead of a small shift to lower stiffness values as in the case of the Wright model, the curves of the posterior distributions show a tendency towards higher values for the moduli. This indicates that with the Theodorsen model, the material is expected to be globally stiffer. Finally, the polar angles are predicted to be slightly more uncertain than assumed in the prior.

The posterior distribution for the weight parameters α_j gets slightly more flat, which means that the uncertainty in these parameters are increased. Moreover, a clear maximum can no longer be distinguished.

In the distribution of the time scale parameters β_j, two important changes can be noticed. The local peak which was between values of 0.3 and 0.4 when calibrated assuming the composite material to be deterministic has shifted left, with the maximum probability density now to be found between 0.2 and 0.3. Moreover, the second peak at values between 0.0 and 0.1 is not as marked as with calibration assuming a deterministic material. This shift in the β values can be interpreted that the uncertainty in the material has a considerable effect mostly on the time scale of the flutter phenomenon and gives way to lower time scale parameters.

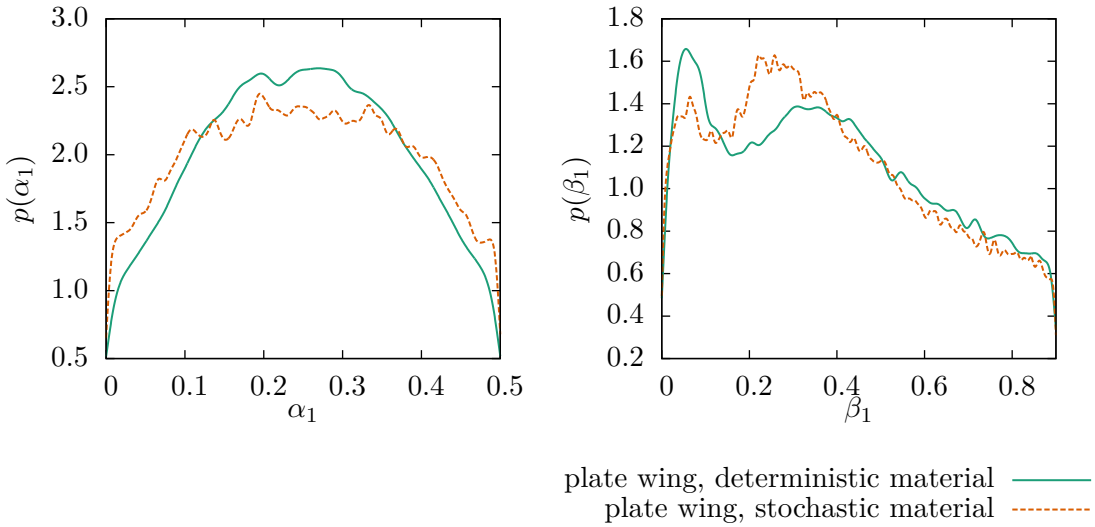

Fig. V.9 *Posterior distributions for the aerodynamic parameters of the Theodorsen-type model, calibrated on scenarios A, C and E with uncertain material parameters, in comparison to the posterior distributions obtained by calibration on the same dataset assuming the nominal values of the polar parameters to be deterministic. Distribution obtained using importance sampling with* 10^5 *samples.*

The results are reflected in the posterior results for the critical flutter velocity and the flutter frequency, which are shown for the Theodorsen model in Figure V.10. While the probability density maximum for the velocity in scenario A and E approaches the experimental result, it shifts away in scenario C, and the frequency adjusts in the "right" way in scenario E. However the probability density maximum shifts away from the experimental result in scenario A, and remains alsmost indifferent in scenario C.

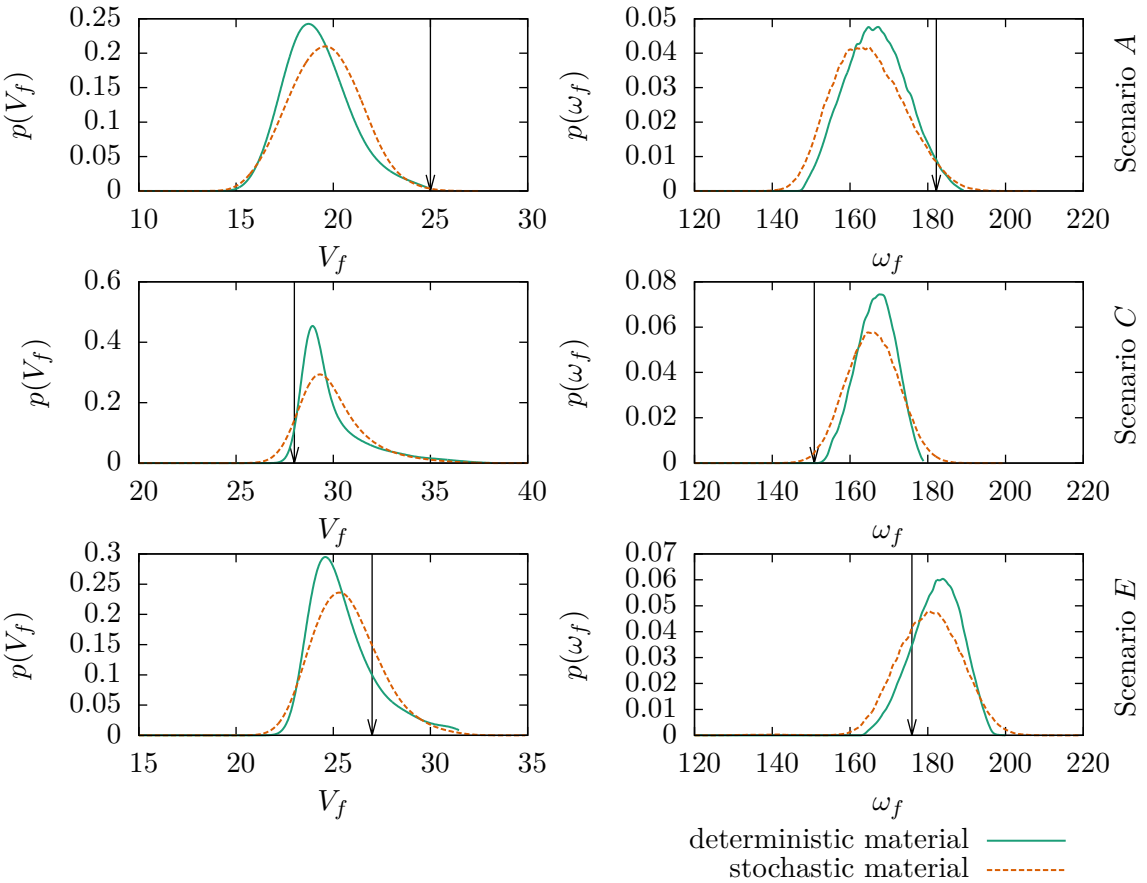

Fig. V.10 *Posterior results for critical flutter velocity and flutter frequency obtained using the Theodorsen type model after calibration using plate flutter data from [58] (Table V.4). Distribution obtained using importance sampling with* 10^5 *samples.*

The model probabilities are re-evaluated for the case of the uncertain material. They are given in Table V.12.

	Wright	Theodorsen
$P(\mathcal{M}\|\mathcal{D})$	0.232	0.768

Table V.12 – Model probabilities for the plate wing problem with stochastic material parameters, calculated using Monte Carlo simulation with 10^5 samples.

The added uncertainty in the material parameters leads to a rise in the model probability for the Wright model compared to the case for the deterministic material (Table V.9). Several explanations can be given for this change. One possibility that the model is more stable in its response to the changes in stiffness. Another possible explanation is that the model probabilities are only able to highlight differences between the models, which are blurred by the added uncertainty in the material parameters. As a consequence, the

model probabilities would be closer to each other.

V.4 Using multiple sources of data

As the material has been shown to have a significant influence on flutter predictions and the material uncertainty having an impact on calibration of the aerodynamic parameters, it will be investigated in the following how the use of the free vibration data can improve the calibration of the aerodynamic parameters.

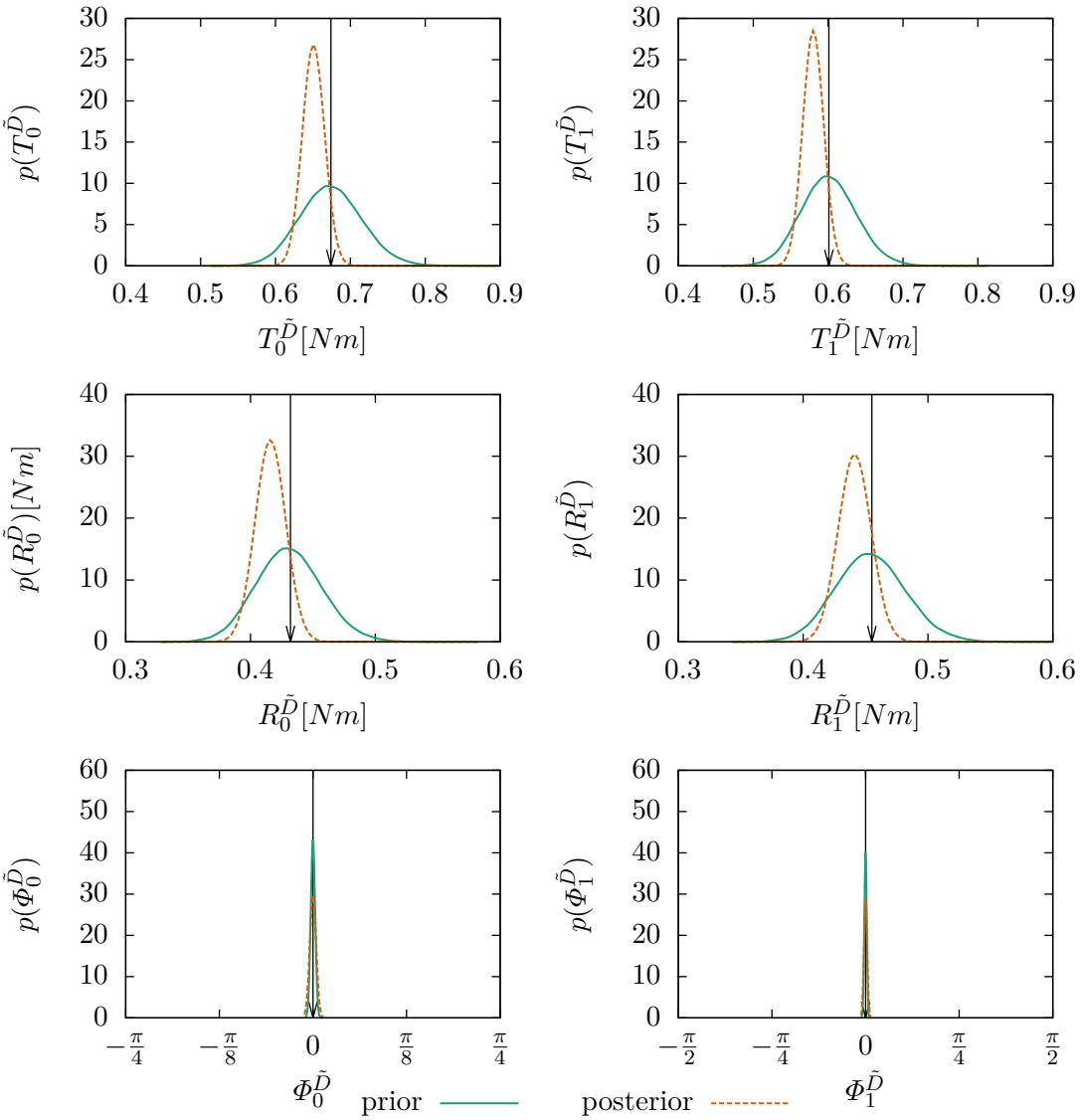

Fig. V.11 *Priors and posteriors obtained using free vibration data from [58] for scenario A as given in Table V.3. The nominal values are indicated by the vertical arrow. Distributions obtained using importance sampling with* 10^5 *samples.*

To have a base for comparison, a calibration of the material parameters has ben carried out using the Bayesian formalism and the free vibration data from Hollowell and Dugundji [58]. The same plate model as for the wing was used to evaluate the frequency response of the first two modes. In Figure V.11, an example is given for scenario *A*. For the modulus parameters, the uncertainty was significantly reduced in that scenario, while the uncertainty in the polar angles augments slightly. Moreover, the material is found to be less stiff than assumed when using the nominal values from the original article. The results for the other layups are similar. A full account of the Bayesian study of the material parameters by exploiting the given free vibration data is given in appendix C.

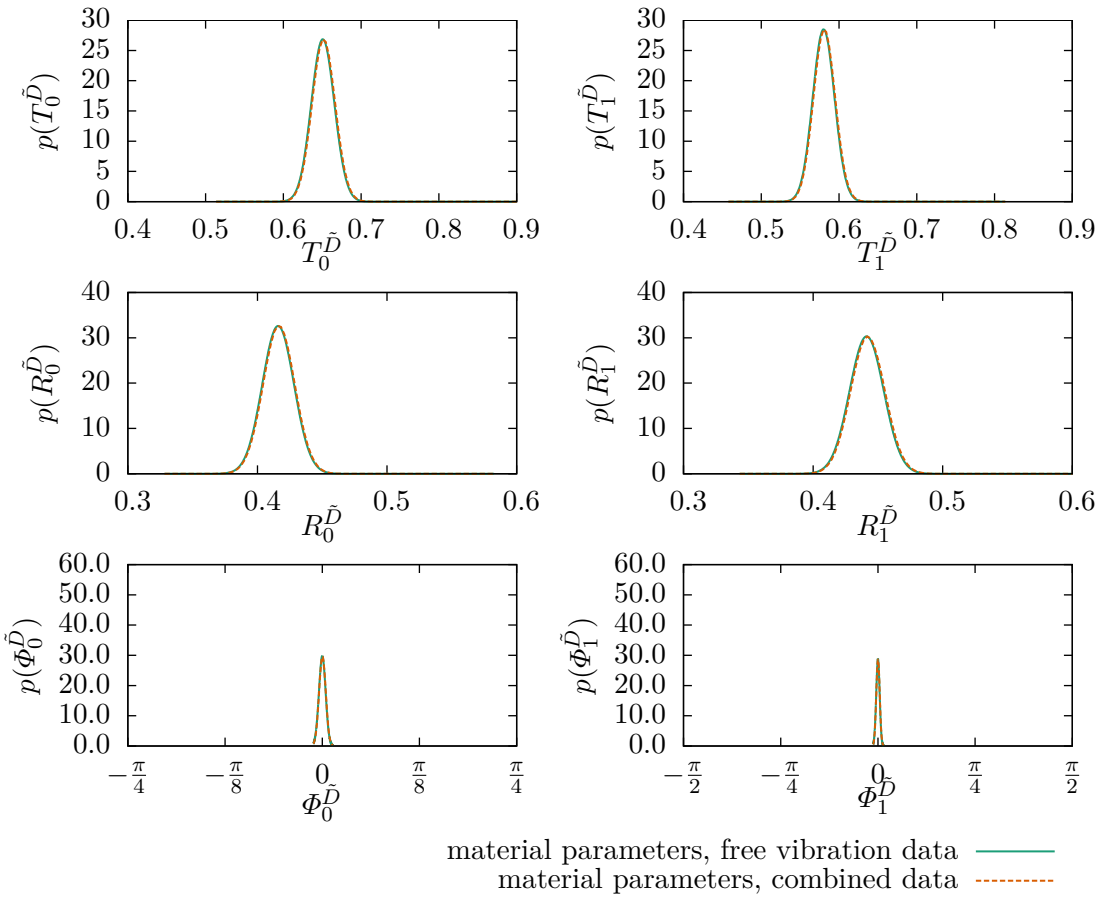

Fig. V.12 *Posteriors obtained for the composite material parameters calibrated together with the Theodorsen model using data from flutter experiments and free vibration experiments from [58] and PAPA flutter experiments from [124], compared to posteriors obtained using [58] free vibration data only. Distribution obtained using importance sampling with* 10^6 *samples.*

As the material parameters can thoroughly be determined from the free vibration data alone and the flutter problem is highly related to the free vibration problem, the changes in the calibration of the aerodynamic model do not affect the composite material distributions. Effectively, the distributions remain virtually unchanged, as is shown in Fig-

ure V.12. Note that for the combined study, for reasons of a convergence problem, 10^6 samples are used instead of 10^5.

This combined calibration can be shown as equivalent to gaining priors using Bayesian techniques and adding them to the model afterwards, provided the errors made in the different experiments are independent.

Consider two sets of epistemically uncertain parameter vectors $\boldsymbol{\theta}_I, \boldsymbol{\theta}_{II}$ which are independent *a priori*. Consider furthermore two sets of data $\mathcal{D}_I$ and $\mathcal{D}_{II}$, where $\mathcal{D}_I$ contains data from experiments where both the parameters from $\boldsymbol{\theta}_I, \boldsymbol{\theta}_{II}$ play a role, whereas $\mathcal{D}_{II}$ contains only data for which only $\boldsymbol{\theta}_{II}$ is relevant. Then, the joint posterior for common calibration is written similarly to Equation (IV.3)

$$p(\boldsymbol{\theta}_I, \boldsymbol{\theta}_{II}|\mathcal{D}_I, \mathcal{D}_{II}, \mathcal{M}) \propto f(\mathcal{D}_I, \mathcal{D}_{II}|\boldsymbol{\theta}_I, \boldsymbol{\theta}_{II}, \mathcal{M}) p(\boldsymbol{\theta}_I|\mathcal{M}) p(\boldsymbol{\theta}_{II}|\mathcal{M}) \tag{V.1}$$

Assuming a posterior for $\boldsymbol{\theta}_{II}$ can be constructed such that

$$p(\boldsymbol{\theta}_{II}|\mathcal{D}_{II}, \mathcal{M}) \propto f(\mathcal{D}_{II}|\boldsymbol{\theta}_{II}, \mathcal{M}) p(\boldsymbol{theta}_{II}|\mathcal{M}) \tag{V.2}$$

and that the errors are independent, the likelihood function may be factorised such that

$$\begin{aligned} p(\boldsymbol{\theta}_I, \boldsymbol{\theta}_{II}|\mathcal{D}_I, \mathcal{D}_{II}, \mathcal{M}) &\propto f(\mathcal{D}_I|\boldsymbol{\theta}_I, \boldsymbol{\theta}_{II}, \mathcal{M}) f(\mathcal{D}_{II}|\boldsymbol{\theta}_{II}, \mathcal{M}) p(\boldsymbol{\theta}_I|\mathcal{M}) p(\boldsymbol{\theta}_{II}|\mathcal{M}) \\ &\propto f(\mathcal{D}_I|\boldsymbol{\theta}_I, \boldsymbol{\theta}_{II}, \mathcal{M}) p(\boldsymbol{\theta}_{II}|\mathcal{D}_{II}, \mathcal{M}) p(\boldsymbol{\theta}_I|\mathcal{M}) \end{aligned} \tag{V.3}$$

which means that $p(\boldsymbol{\theta}_{II}|\mathcal{D}_{II}, \mathcal{M})$ takes the role of a prior.

Consequently, it can be stated that the additional information provided by the flutter experiments does not change a "prior" that would be gained by Bayesian calibration using the free vibration experiments. This reinforces the claim stated before that a well-defined prior does not change further when tried to be calibrated together with other parameters with epistemic uncertainty.

Model calibrated $\mathcal{M}$	Wright-type
Calibrated parameters $\boldsymbol{\theta}$	$M_{\dot{\alpha}}$ (aerodynamics), $T_0^{\check{D}}, T_1^{\check{D}}, R_0^{\check{D}}, R_1^{\check{D}}, \Phi_0^{\check{D}}, \Phi_1^{\check{D}}$ (structure)
Hyperparameters	$\sigma_{V_f} = 5, \sigma_\omega = 4\pi$ (plate flutter problem), $\sigma_{V_f^*} = 1.1$ (PAPA flutter), $\sigma_{\omega_1} = 0.15 \cdot 2\pi$, $\sigma_{\omega_2} = 1.5 \cdot 2\pi$
Data used $\mathcal{D}$	[58], scenarios *A*,*C*,*E* (plate flutter problem, Table V.4), [58], scenarios *A*,*B*,*C*,*D*,*E*,*F* (free vibration problem, Table V.3), [124] *A*,*B*,*C*,*D* (PAPA flutter problem, Table IV.2)

Table V.13 – Summary of calibrated parameters, settings and data for the Wright model for all data points from [58] and [124] combined.

Figure V.13 shows the results of the calibration of the Wright model using all available data points. That is, the flutter results using the PAPA data from [124], the free vibration data from [58] and the plate flutter data from that same article. The results are compared to the previous calibration using only flutter data from [58].

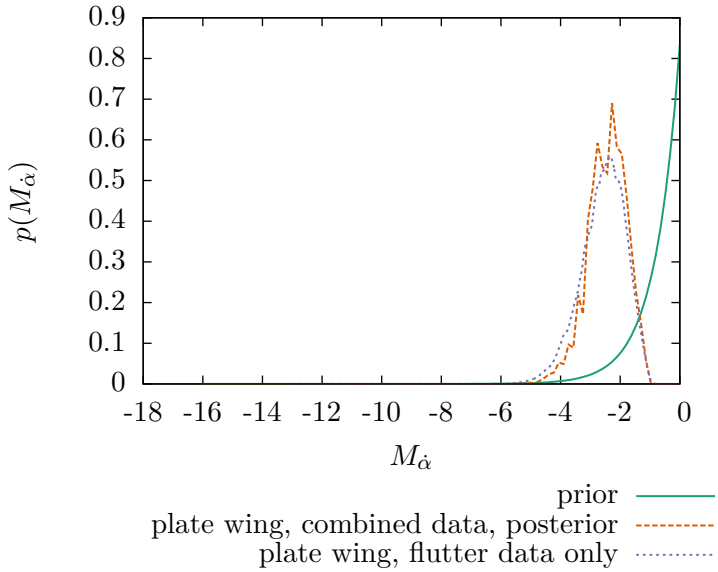

Fig. V.13 *Posterior obtained for the Wright model parameter using data from flutter experiments and free vibration experiments from [58] and PAPA flutter experiments from [124], compared to posteriors obtained using [58] flutter data only. The distributions obtained using importance sampling with* 10^6 *samples.*

It can be observed that the shape of the posterior distribution resembles very strongly the calibrated curve from the previous plate flutter studies and is much narrower than its equivalent only calibrated on the PAPA data. Spikes in the curve may be numerical artefacts.

Figure V.14 shows the results for the four PAPA scenarios defined in [124] obtained with the Wright model, after calibration with all the data available, free vibration data in the plate case included. The results for the PAPA data points can be shown to be improved, as the probability density distributions for the critical flutter velocity all get narrower in place or even move towards the experimental data. This can be interpreted as result of the information gain provided by the plate flutter problem, while the added uncertainty of the material parameters does not play as much of a role. Nevertheless, the "invisible limit" of the model is still preserved, the improvements stopping at an imaginary barrier.

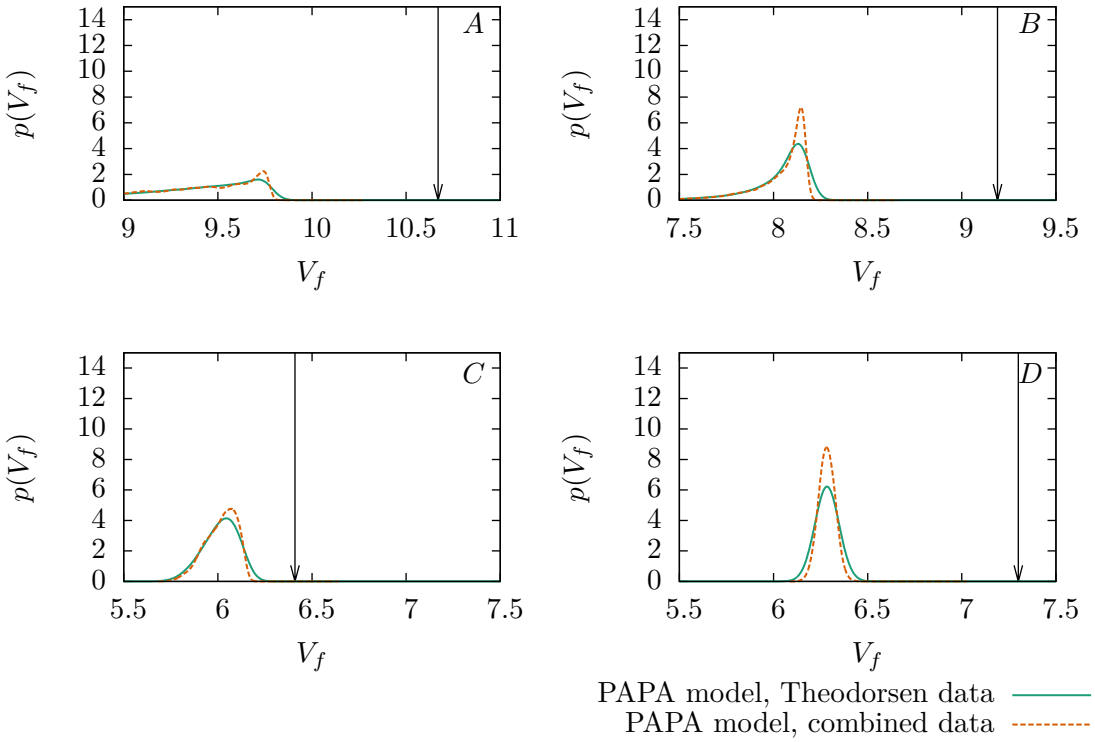

Fig. V.14 *Posterior velocity results for the PAPA datapoints for the Wright model after calibrations using datasets A-D from [124], free vibration datapoints on the first two modes from scenarios A-F from [58] as well as velocity and frequency data from scenarios A,C and E from the same paper, compared to calibration using only the Theodorsen data. The distributions are obtained using importance sampling with* 10^6 *samples.*

Also in the plate flutter case depicted in Figure V.15, improvements are observed after calibration with all the data available, in scenarios C and E. Actually, the experimental values are captured quite well in case of the velocity in scenario C and especially in frequency in scenario E. However, the remaining offsets still point out the model inadequacy discovered earlier. It is remarkable that especially in scenario A, the results do not improve much in neither of the quantities of interest, and even get much worse in the frequency. This could be due to some more complex modal behaviour, which was discovered by [28].

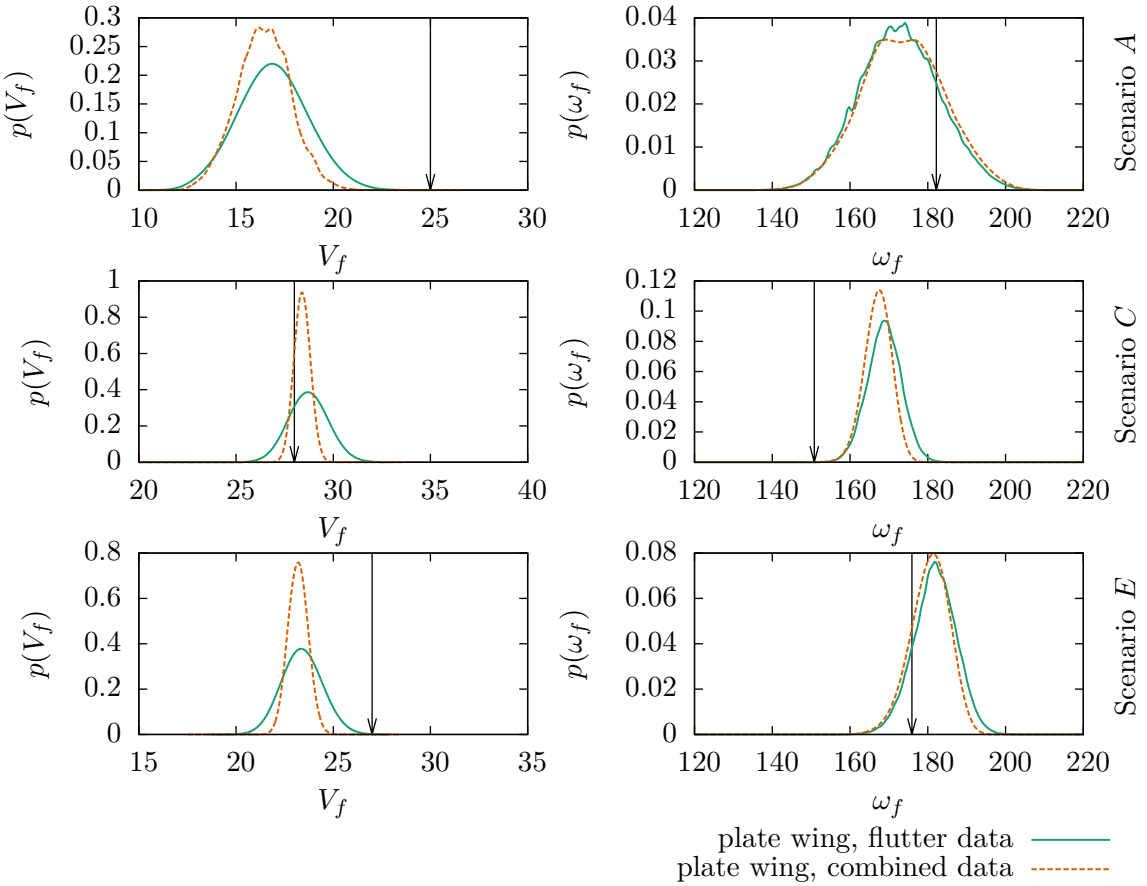

Fig. V.15 *Posterior velocity results for the plate flutter datapoints for the Wright model after calibrations using datasets A-D from [124], free vibration datapoints on the first two modes from scenarios A-F from [58] as well as velocity and frequency data from scenarios A,C and E from the same paper, compared to calibration using only the Theodorsen data.Distribution obtained using importance sampling with* 10^6 *samples.*

Model calibrated $\mathcal{M}$	Theodorsen-type
Calibrated parameters $\boldsymbol{\theta}$	α_1, α_2, β_1, β_2 (aerodynamics), $T_0^{\tilde{D}}, T_1^{\tilde{D}}, R_0^{\tilde{D}}, R_1^{\tilde{D}}, \Phi_0^{\tilde{D}}, \Phi_1^{\tilde{D}}$ (structure)
Hyperparameters	$\sigma_{V_f} = 4, \sigma_\omega = 6\pi$ (plate flutter), $\sigma_{V_f^*} = 1.1$ (PAPA flutter), $\sigma_{\omega_1} = 0.15 \cdot 2\pi$, $\sigma_{\omega_2} = 1.5 \cdot 2\pi$
Data used $\mathcal{D}$	[58], scenarios A,C,E (plate flutter, Table V.4), [58], scenarios A,B,C,D,E,F (free vibration problem, Table V.3), [124] A,B,C,D (PAPA flutter, Table IV.2)

Table V.14 – Summary of calibrated parameters, settings and data for the Theodorsen model for all data points from [58] and [124] combined.

The calibration results of the aerodynamic parameters are presented in Figure V.9. In comparison to the calibration performed with only the plate flutter data taken into account, almost the same distribution for the weight parameters α_j is found. A more important change is noticed in the time scale parameters β_j. The peak for low values of $\beta_j < 0.1$ is strengthened, while the second local probability density maximum situated roughly between $\beta_j = 0.2$ and $\beta_j = 0.3$ gets lower. Other than could be expected, the tendency towards higher time scale parameters found in the calibration of the aerodynamic parameters on the PAPA data cannot be noticed much in the present example.

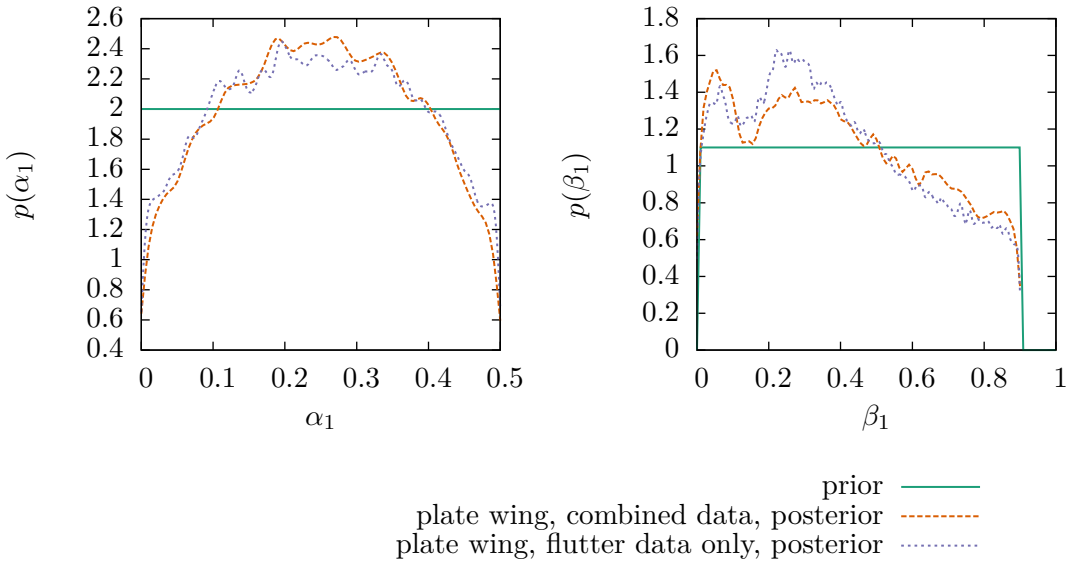

Fig. V.16 *Posteriors obtained for the Theodorsen model parameters using data from flutter experiments and free vibration experiments from [58] and PAPA flutter experiments from [124], compared to posteriors obtained using [58] flutter data only. The distributions are obtained using importance sampling with* 10^6 *samples.*

The PAPA results for the Theodorsen model after calibration using all the data available are shown in Figure V.18. The model does not profit as much from the additional data as the Wright model, which might come from the fact that generally, it is not very well informed by the data.

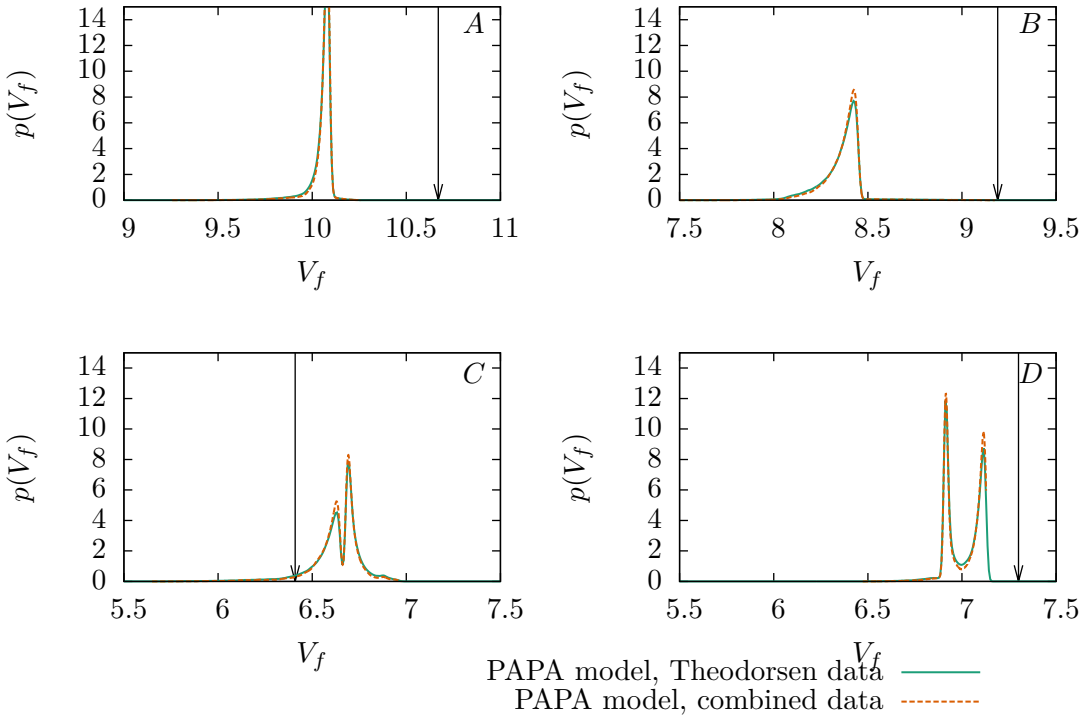

Fig. V.17 *Posterior velocity results for the PAPA datapoints for the Theodorsen model after calibrations using datasets A-D from [124], free vibration datapoints on the first two modes from scenarios A-F from [58] as well as velocity and frequency data from scenarios A,C and E from the same paper, compared to calibration using only the Theodorsen data. The distributions are obtained using importance sampling with* 10^6 *samples.*

On the contrary, the information gain has significant influence on the plate flutter results, which are shown in Figure V.18. However, results are very inconsistent between the scenarios. While the calibration leads to almost perfectly predicting V_f in the scenario C, the critical flutter velocity shifts down in scenarios A and E. While slight shifts in frequency towards the experimental result are observed in all results (small bumps facing from the main mode towards the experimental value can be recognised) and the frequencies get narrowed down, no significant improvement neither in probability density for the experimental value nor in the distance from the maximum to the experimental value can be found, and the distributions do not change that much. However, the updated distribution aligns well with the previously found trend that the Theodorsen model, as its Wright counterpart, tends to underestimate the critical flutter velocity. Moreover, with the additional data, both models become more consistent in their predictions.

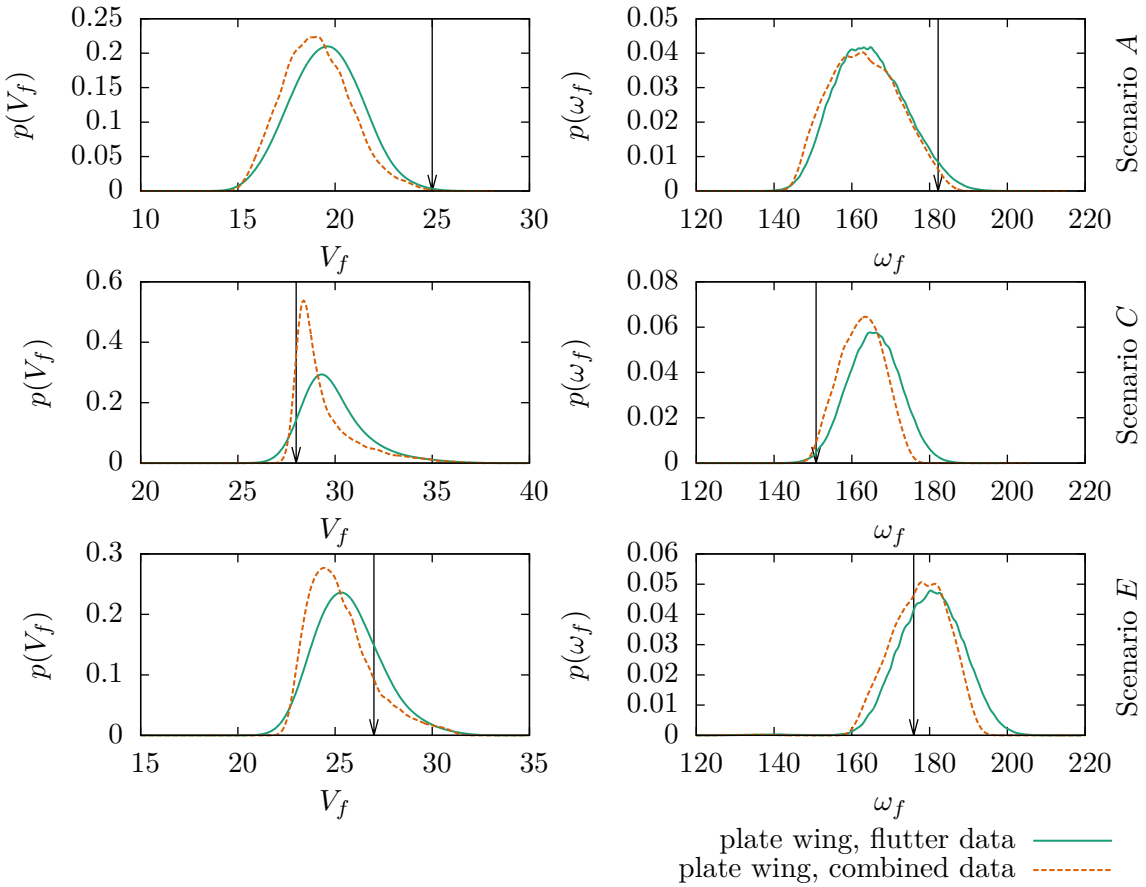

Fig. V.18 *Posterior velocity results for the plate flutter datapoints for the Theodorsen model after calibrations using datasets A-D from [124], free vibration datapoints on the first two modes from scenarios A-F from [58] as well as velocity and frequency data from scenarios A,C and E from the same paper, compared to calibration using only the Theodorsen data. The distributions are obtained using importance sampling with* 10^6 *samples.*

Although the use of multiple data sources improved the results and helped to reduce the uncertainty, the posteriors for the critical flutter velocity and the flutter frequency still show significant deviations from the experimental data for both of the models. These deviations cannot be explained by neither the uncertainty assumed in the parameters of the aerodynamic models, nor the uncertainty in the material. In the previous chapter, an attempt was made to explain parts of the difference by typical flaws of PAPA modelling, which do not apply in the case of a plate. For example, friction is negligible and other than the PAPA used in the study in the previous chapter, the plate does actually not have any profile as assumed by the model. However, different flaws inherent to the modelling of the plate wing are present which could explain parts of the difference.

- Both aerodynamic models require the structural model to assume that the plate is rigid in the chordwise direction. This is a nuisance in modeling the modal behaviour

of the plate. Remaining deviations in the frequency after calibration of the material parameters for the free vibration model could come from this fact. As the aeroelastic flutter problem is also dependent on the modal behaviour of the plate, prediction accuracy is lowered by this fact.

- On lifting surfaces, the lift gets smaller towards their tip due to wingtip vortices coming from air flowing from below the wing to its upper side due to the pressure difference that creates the lift in the first place. The strip theory approaches chosen in this chapter do not reflect that. While there are empirical approaches to mimic that effect (e.g. [123], which was used in the chapter III), these were omitted in this study to be closer to the original article [58].

Nevertheless, it cannot be proven that these would be the only causes of the model discrepancies. For example, the models have a tendency to underestimate the critical flutter velocity in most cases after calibration points regardless of the experiment type. This tendency is also present in the individual calibrations. Consequently, it points to the fact that there might be a common explanation for the discrepancy not to be found in the individual modelling flaws.

Finally, the model probabilities for the two aerodynamic models are given in Table V.15. With all the points from the PAPA data and the plate flutter data combined and the

	Wright	Theodorsen
$P(\mathcal{M}\|\mathcal{D})$	0.0095	0.9905

Table V.15 – Model probabilities for the plate wing problem with stochastic material parameters, calculated using Monte Carlo simulation with 10^6 samples.

additional information provided by the free vibration data, the model probability for the Wright model drops with respect to the previous two studies where only the plate flutter data was taken into account. Again, multiple possible reasons for this can be considered. First, the Wright model was already performing badly with the calibration executed only on the PAPA data. When the cases are combined, this weakness continues to exist in the combined study.

The lower model probability could also indicate that the Wright model does not generalise well in comparison with the Theodorsen type model. As stated before, Theodorsen's PAPA experiments and the plate flutter studied by Hollowell probably belong to different frequency regimes. It is possible that the Theodorsen model is better at taking the two into account at the same time. Finally, the added data from the free vibration problem added information to the flutter problem. This could have the opposite effect of the addition of the material uncertainty, which in the previous example made the model probability rise.

V.5 Conclusion

In this chapter, the Bayesian methods, which were introduced in the previous chapter, have been applied to the plate wing. First, a study with the material of the wing supposed deterministic was conducted. Later, the uncertainty in the material as assumed in the chapter III was added. Differences in the calibration results with the material uncertainty taken into account with respect to the study assuming a deterministic material showed that uncertainties assumed aleatory cannot be omitted in a Bayesian study, even if the calibration does not alter the aleatory distributions.

To conclude the study and to exploit a maximum number of data points, the data from the PAPA case and available free vibration data from [58] are considered. It could be demonstrated in a preliminary study that the uncertainty in the material could be further reduced, even if the information contained in the plate flutter data alone was not sufficient to do so. The free vibration data was then integrated into the common calibration, which could be shown to be equivalent to using the distribution obtained in a previous study as a prior.

The big difference in the calibration results between the calibration using PAPA data only, the plate flutter study and the combined study especially in the Theodorsen model highlights the necessity to combine a maximum number of data points. As the parameters are sensitive to the flutter regime, different experiments help to construct a more general model. The study showed how these different sources can be used. Moreover, with the addition of free vibration data, it could be shown that adding data sources providing information only on partial aspects of the problem can be beneficial.

The number and kind of data also affects the model probabilities, further highlighting the need for data. With a maximum number of data points added to the study, the Theodorsen-type model proved clearly superior with a model probability of nearly one. This could mean that it is more generalisable than the Wright model and can handle the different flutter regimes represented by the different data points better.

While this study could serve as a demonstrator to calibration in aeroelasticity and show a path towards handling different types of uncertainties as well as a path to robust predictions, the limits of the underlying models and the small number of data prevent the study to conclude with usable predictions. The calibrations may be specific to the data and the calculated errors are big. Further studies will aim at diminishing the number of calls to the solver in order to be able to use more advanced models at reasonable cost. These advanced models would also be capable to take into account a bigger number of scenarios, opening up possibilities to use bigger databases.

Chapter VI

Conclusion and perspectives

VI.1 Conclusion

In this work, quantification of aleatory and epistemic uncertainties was performed on example problems in aeroelasticity. The study of the uncertainties was focused primarily on the critical flutter velocity, which is the freestream velocity at which the linearly coupled aeroelastic behaviour of structures subject to aerodynamic loads become unstable.

In a first study, effects of uncertainties in ply angles and ply thicknesses, as they often occur in the manufacturing of composite layups were investigated in the example of a straight rectangular plate wing made of a 16-layer composite laminate. These uncertainties, as they are supposed to be known, were considered as aleatory. The use of the polar method reduced the dimension of the random space from $2 \cdot 16$ to six, making the surrogate modeling step affordable. Compared to earlier studies using the lamination parameters [114], desymmetrisation of the laminates by the uncertainties as well as changes in the thickness of the individual plies could be taken into account.

A preliminary deterministic study in the domain of orthotropic laminates was performed, which, thanks to the polar method, could be achieved by varying only two structural parameters. The analysis of the aeroelastic response revealed a sharp step in critical flutter velocity and frequency due to a mode switch. This step represents a risk in optimisation problems as it was found to be directly next to the point of optimal critical flutter velocity in the plane of study.

The results of the deterministic analysis were used to identify points of interest, for which actual laminate stacking sequences were reconstructed. Then, the ply angle and ply thickness uncertainties were applied to these layup configurations. Important deviations of the critical flutter velocity were found, where the uncertainty in the ply thickness was observed to be the dominating one. Both types of uncertainties were shown to trigger the mode switch when the nominal configuration was close to it. The resulting distribution showed considerable probability for the critical velocity to fall below the classical 15% flutter margin. This means that stochastic methods provide additional safety. The fact that the optimal configuration in terms of critical flutter velocity was

most severely affected by the mode switch points to a need of robust optimisation.

In order to reduce computational cost over plain Monte Carlo simulations, a polynomial chaos surrogate model was developed to model the stochastic response more efficiently. The reduced set of parameters of the polar method was exploited in the computation of the stochastic flutter velocity to avoid the "curse of dimensionality". To deal with the correlation in the random input parameters resulting from the use of the polar method, arbitrary polynomial chaos was used, where a Gram-Schmidt algorithm was employed to construct the necessary orthogonal polynomial bases. In order to deal with the discontinuities in the random space, the response surface was split using a machine learning algorithm and the resulting sub-response surfaces modelled by the arbitrary polynomial chaos algorithm. This way, the number of calls to the solver could be reduced from 10^5 for a plain Monte Carlo simulations to just 1000 samples, while accurately reproducing the resulting multi-modal probability density functions.

Another source of uncertainty is in the need for aerodynamic modelling, which mostly comes from lack of knowledge on the choice of the appropriate model or the choice of parameters. In a first step, the common Pitch And Plunge Airfoil aeroelastic configuration was chosen as example, for which experimental data was retrieved from literature. Two aerodynamic models based on both quasi-steady and fully unsteady potential flow theory in the incompressible regime found in different aeroelastic studies were analysed for parametric uncertainties. Prior distributions were defined summarising prior knowledge on the values of the parameters of each model. On that basis, the models were updated using Bayesian calibration, with importance sampling employed to estimate the distributions of parameters and critical flutter velocity predictions.

In the case of the approximated Theodorsen model, the calibration provided hints that the parameters indeed fall in the combinations that can also be found in the literature. However, most instances of this type of model include one of the parameters chosen very low, which the calibration using the PAPA data does not support. For the quasi-steady Wright model, which also was used in the forward propagation study in a similar form, the calibration led to values for the only model parameter that were significantly lower than what was given in the literature. As expected, the Bayesian Model Averaging procedure to calculate model probabilities gave a much higher model probability for the approximated Theodorsen model. The distributions of the critical flutter velocity samples corresponding to the posterior parameter distributions showed a significant offset to the experimental results. The author tried to compensate this by adding a bias term to the error term which is the basis for the Bayesian methods. Prediction results could be significantly improved. However, the bias has a repercussion on the parameter calibrations and alters the distributions, which can lead to physically questionable parameter values.

The Bayesian method was also applied to the composite plate wing case. First, a study was done with the composite material supposed to be fixed at the nominal value. Generally, the parameters were informed better than in the calibration using the PAPA data. In the case of the Theodorsen model, the choice of low values for the time scale parameters could be confirmed. The better degree of information could be due to the fact that the plate flutter case is richer in features (i. e. it contained frequency data). In a second step, the uncertainty in the stiffness was added to the calibration, where the uncertainty assumed

in the forward propagation case was taken as prior. The addition of this uncertainty changed the calibration results. The corresponding flutter velocity and flutter frequency responses became more uncertain, but in some cases the prediction was improved.

As the uncertainty in the material parameters was shown to be reducible by the flutter data, free vibration data was added to the study in order to narrow down their uncertainty. The calibration of the material parameters was performed together with the aeroelastic models. It could be demonstrated that this is equivalent to perform the calibrations sequentially and to reuse the posteriors of the previous calibrations as prior for the subsequent calibrations, provided the different experiments are assumed to be independent in error. Moreover, it could be shown that when the distribution for the material parameters obtained as posterior from the calibration of the free vibration experiment was used as a prior, it could not be further reduced, thus confirming the aleatory nature of the reduced uncertainty.

Using the methods described above, influences of aleatory and epistemic uncertainties on the critical flutter velocity could be shown. Estimates for the distributions were derived in both cases as well as for scenarios where the two types of uncertainties come into play. The approaches were demonstrated to offer a more rigorous view on the flutter risk than classical security margins, which could be proven to be insufficient in some cases. In addition to providing robust estimates for the critical velocity, Bayesian approaches allow identification or verification of parameter values. With this demonstration of possible solutions to the uncertainty quantification problem, the door is opened to address further challenges.

VI.2 Perspectives

Bayesian studies require a considerable amount of experimental data. The datasets used in the Bayesian studies in this work are quite small, as data in literature is quite limited and not necessarily adapted to suit this kind of study. This means that the results obtained are probably specific to the datasets, which is also shown by the fact that the posterior distributions change when data sets are added. For the results to be generalisable, the datasets would have to be much larger. This could be adressed by specially designing series of experiments to be used for Bayesian calibration, with the aim of having as many realistic scenarios at hand as possible. A specially-designed flutter database could also give acces to information not given in the literature such as mode shapes, which could be used to further improve the calibrations. It would also allow to distinguish between model and experimental error more clearly.

Despite calibration, the models used in the study do not produce very precise stochastic predictions. This can only partially be mitigated by adaption of the error term, which has different drawbacks. Obviously, it can be hoped that more precise predictions could be obtained by using higher fidelity models. The aPC/Machine Learning method developed in this work for the treatment of uncertainty in composite materials paves the way to stochastic studies on more complex computational models. This includes also handling more complex configurations such as swept wings and entire airframes. However, as the

number of polar parameters would increase when loading of the structure goes beyond pure bending, the aPC method has to be developed further to handle the bigger polar parameter space of those problems. The use of sparse quadrature rules instead of the sampling- and fitting-based mechanisms could provide a possible way.

Further work could be done to integrate the surrogate modelling into the Bayesian calibration framework. A simple approach would be to simply construct a polynomial chaos on the prior. However, different approaches exist to adapt the polynomial basis to the posterior, boosting efficiency (e.g. [14]). It has to be investigated if the orthogonalisation method used for the aPC can be used to take the posterior into account. Moreover, as it has been shown that aleatory uncertainties can influence calibration results, measures have to be taken to take into account a higher number of parameters.

As the flutter boundary is an instability limit, it is the lower limit which is interesting. Consequently, the limiting factor in aircraft design would be the lower quantiles of the flutter velocity distribution. Industry requirements on the corresponding confidence intervals are rather strict, for example in "Six Sigma" frameworks, demanding confidence intervals of 99.99966 per cent confidence level. However, the methods presented in this work are not designed with respect to precise estimation of quantiles.

The first necessary improvement would be to eliminate sampling-based methods as far as possible, as high-resolution sampling is computationally expensive. In the aPC method, orthogonalisation and the fitting of the response surfaces would have to be eliminated in favour of quadrature-based methods. The work of Navarro Jimenez et al. [93], who provide a method to derive collocation points for scenarios with correlated variables, could be useful in this setting. First steps to obtain them in the case of the polar method for composite materials have been taken. This step would also enable the development of a multi-element polynomial chaos approach for the composite material uncertainties, which then could help improve the resolution of discontinuous response surface, another important challenge that was demonstrated in this work. A further advantage of quadrature-based polynomial chaos is that error estimates are available. In combination with adaptivity, this feature can help to improve the precision of the stochastic surrogate models.

With augmented precision, stochastic methods like the ones presented in this work could help to reach improved security and performance over classical deterministic security margin methods. Integration of these methods into robust optimisation could help engineers to take into account relevant uncertainties already in the design phase. The Bayesian methodologies can help to identify uncertainties of aleatory and epistemic nature in this framework and make predictions of aeroelastic instabilities robust.

Appendix A

System matrices for the plate wing

In this chapter, the system matrices needed for the calculation of the critical flutter velocity in the case of a rectangular plate wing made of a general anisotropic material are developed. The elements of the approach were already described in chapter II.2. The goal of this chapter is to describe the path from the Lagrange equation (II.1) [117]

$$\frac{d}{dt}\frac{\partial T}{\partial \dot{\mathbf{q}}} - \frac{\partial T}{\partial \mathbf{q}} + \frac{\partial U}{\partial \mathbf{q}} = \frac{\partial(\delta W)}{\partial(\delta \mathbf{q})} \tag{A.1}$$

to the system matrices and provide explicit expressions, using a Rayleigh-Ritz approach of assumed modes in harmonic motion.

The assumed modes were already given in Equation (II.44), but are recalled here [107]

$$w(x,y,t) = \sum_{i=1}^{n_x}\sum_{j=1}^{n_y} \overline{w}_{ij}(t) \left(\frac{x}{S}\right)^{j+1} \left(\frac{y}{c}\right)^{j-1} \tag{A.2}$$

A.1 Mass matrix

The mass matrix describes the inertial behaviour of the wing and thus depends on movement. It is consequently derived from the expression of the kinetic energy T. For the plate wing as described by the scheme II.5, the kinetic energy is given as follows [4]

$$T = \frac{1}{2}\int_{-b}^{b}\int_{0}^{S} \rho t_{total} \dot{w}^2 dxdy \tag{A.3}$$

Using the assumed mode shapes Equation (II.44), the kinetic energy becomes

$$T = \frac{1}{2}\rho d \int_{-b}^{b}\int_{0}^{S} \left[\sum_{i=1}^{n_x}\sum_{j=1}^{n_y} \dot{\overline{w}}_{ij} \left(\frac{x}{S}\right)^{i+1} \left(\frac{y}{c}\right)^{j-1}\right] \left[\sum_{k=1}^{n_x}\sum_{l=1}^{n_y} \dot{\overline{w}}_{kl} \left(\frac{x}{S}\right)^{k+1} \left(\frac{y}{c}\right)^{l-1}\right] dxdy \tag{A.4}$$

Preparing the expression for injection into the Lagrange equation, the derivative by the generalised coordinates is carried out using the product rule

$$\begin{aligned}
\frac{\partial T}{\partial \dot{\overline{w}}_{(mn)}} =& \frac{1}{2}\rho d \int_{-b}^{b}\int_{0}^{S} \sum_{i=1}^{n_x}\sum_{j=1}^{n_y} \frac{\partial \dot{\overline{w}}_{ij}}{\partial \dot{\overline{w}}_{mn}} \left(\frac{x}{S}\right)^{i+1} \left(\frac{y}{c}\right)^{j-1} \left[\sum_{k=1}^{n_x}\sum_{l=1}^{n_y} \dot{\overline{w}}_{kl} \left(\frac{x}{S}\right)^{k+1} \left(\frac{y}{c}\right)^{l-1}\right] \\
&+ \sum_{k=1}^{n_x}\sum_{l=1}^{n_y} \frac{\partial \dot{\overline{w}}_{kl}}{\partial \dot{\overline{w}}_{mn}} \left(\frac{x}{S}\right)^{k+1} \left(\frac{y}{c}\right)^{l-1} \left[\sum_{i=1}^{n_x}\sum_{j=1}^{n_y} \dot{\overline{w}}_{ij} \left(\frac{x}{S}\right)^{i+1} \left(\frac{y}{c}\right)^{j-1}\right] dxdy \\
=& \frac{1}{2}\rho d \int_{-b}^{b}\int_{0}^{S} \sum_{i=1}^{n_x}\sum_{j=1}^{n_y} \delta_{(ij)(mn)} \left(\frac{x}{S}\right)^{i+1} \left(\frac{y}{c}\right)^{j-1} \left[\sum_{k=1}^{n_x}\sum_{l=1}^{n_y} \dot{\overline{w}}_{kl} \left(\frac{x}{S}\right)^{k+1} \left(\frac{y}{c}\right)^{l-1}\right] \\
&+ \sum_{k=1}^{n_x}\sum_{l=1}^{n_y} \delta_{(kl)(mn)} \left(\frac{x}{S}\right)^{k+1} \left(\frac{y}{c}\right)^{l-1} \left[\sum_{i=1}^{n_x}\sum_{j=1}^{n_y} \dot{\overline{w}}_{ij} \left(\frac{x}{S}\right)^{i+1} \left(\frac{y}{c}\right)^{j-1}\right] dxdy
\end{aligned} \tag{A.5}$$

where the $\delta_{(\cdot)(\cdot)}$ are Kronecker's deltas, not to be confounded with variational deltas.

Consolidating the indices such that (ij) is the external index and (kl) the internal summation index, eliminating the Kronecker's deltas in the process and carrying out the integration,

$$\frac{\partial T}{\partial \dot{\overline{w}}_{(ij)}} = \rho t_{total} Sc \sum_{k=1}^{n_x}\sum_{l=1}^{n_y} \dot{\overline{w}}_{kl} \left[\frac{1}{i+k+3}\left(\frac{x}{S}\right)^{i+k+3}\right]_0^S \left[\frac{1}{j+l-1}\left(\frac{y}{c}\right)^{j+l-1}\right]_{-b}^{b} = \mathbf{M}\dot{\overline{\mathbf{q}}} \tag{A.6}$$

where

$$M_{(ij)(kl)} = \rho h Sc \left[\frac{1}{i+k+3}\left(\frac{x}{S}\right)^{i+k+3}\right]_0^S \left[\frac{1}{j+l-1}\left(\frac{y}{c}\right)^{j+l-1}\right]_{-b}^{b} \tag{A.7}$$

is the mass matrix, which multiplies the vector of generalised coordinates $\overline{\mathbf{q}}$ which consists of the $\overline{w}_{kl}$.

A.2 Stiffness matrix

The stiffness matrix describes the elastic part of the system. As the elastic effects are those storing the energy in the system, its associated energy is the potential energy. It can be given as [4]

$$U = \frac{1}{2}\int_{-b}^{b}\int_{0}^{S} \boldsymbol{\kappa}^{\mathsf{T}}\mathbf{D}\boldsymbol{\kappa} dxdy \tag{A.8}$$

where $\boldsymbol{\kappa}$ is the curvature vector in Voigt notation

$$\boldsymbol{\kappa} = \begin{bmatrix} -\frac{\partial^2 w}{\partial x^2} \\ -\frac{\partial^2 w}{\partial y^2} \\ -2\frac{\partial^2 w}{\partial x \partial y} \end{bmatrix} \tag{A.9}$$

and $\mathbf{D}$ is the bending stiffness tensor in Voigt notation, which in turn can be replaced by the modified bending stiffness tensor $\tilde{\mathbf{D}}$.

As fully anisotropic plates will be considered, Equation (A.8) is fully written out, using the tensor symmetry

$$\begin{aligned} U = &\frac{1}{2}\int_{-b}^{b}\int_{0}^{S} \frac{\partial^2 w}{\partial x^2} D_{11} \frac{\partial^2 w}{\partial x^2} + 2\frac{\partial^2 w}{\partial x^2} D_{12} \frac{\partial^2 w}{\partial y^2} + 4\frac{\partial^2 w}{\partial x^2} D_{13} \frac{\partial^2 w}{\partial x \partial y} \\ &+ \frac{\partial^2 w}{\partial y^2} D_{22} \frac{\partial^2 w}{\partial y^2} + 4\frac{\partial^2 w}{\partial y^2} D_{23} \frac{\partial^2 w}{\partial x \partial y} + 4\frac{\partial^2 w}{\partial x \partial y} D_{33} \frac{\partial^2 w}{\partial x \partial y} dxdy \end{aligned} \tag{A.10}$$

Inserting the mode shape functions

$$\begin{aligned} U = &\frac{1}{2}\int_{-b}^{b}\int_{0}^{S} \left[\frac{\partial^2}{\partial x^2}\sum_{i=1}^{n_x}\sum_{j=1}^{n_y} \hat{w}_{ij}\left(\frac{x}{S}\right)^{i+1}\left(\frac{y}{c}\right)^{j-1}\right] D_{11} \left[\frac{\partial^2}{\partial x^2}\sum_{k=1}^{n_x}\sum_{l=1}^{n_y} \hat{w}_{kl}\left(\frac{x}{S}\right)^{k+1}\left(\frac{y}{c}\right)^{l-1}\right] \\ &+2\left[\frac{\partial^2}{\partial x^2}\sum_{i=1}^{n_x}\sum_{j=1}^{n_y} \hat{w}_{ij}\left(\frac{x}{S}\right)^{i+1}\left(\frac{y}{c}\right)^{j-1}\right] D_{12} \left[\frac{\partial^2}{\partial y^2}\sum_{k=1}^{n_x}\sum_{l=1}^{n_y} \hat{w}_{kl}\left(\frac{x}{S}\right)^{k+1}\left(\frac{y}{c}\right)^{l-1}\right] \\ &+4\left[\frac{\partial^2}{\partial x^2}\sum_{i=1}^{n_x}\sum_{j=1}^{n_y} \hat{w}_{ij}\left(\frac{x}{S}\right)^{i+1}\left(\frac{y}{c}\right)^{j-1}\right] D_{13} \left[\frac{\partial^2}{\partial x \partial y}\sum_{k=1}^{n_x}\sum_{l=1}^{n_y} \hat{w}_{kl}\left(\frac{x}{S}\right)^{k+1}\left(\frac{y}{c}\right)^{l-1}\right] \\ &+\left[\frac{\partial^2}{\partial y^2}\sum_{i=1}^{n_x}\sum_{j=1}^{n_y} \hat{w}_{ij}\left(\frac{x}{S}\right)^{i+1}\left(\frac{y}{c}\right)^{j-1}\right] D_{22} \left[\frac{\partial^2}{\partial y^2}\sum_{k=1}^{n_x}\sum_{l=1}^{n_y} \hat{w}_{kl}\left(\frac{x}{S}\right)^{k+1}\left(\frac{y}{c}\right)^{l-1}\right] \\ &+4\left[\frac{\partial^2}{\partial y^2}\sum_{i=1}^{n_x}\sum_{j=1}^{n_y} \hat{w}_{ij}\left(\frac{x}{S}\right)^{i+1}\left(\frac{y}{c}\right)^{j-1}\right] D_{23} \left[\frac{\partial^2}{\partial x \partial y}\sum_{k=1}^{n_x}\sum_{l=1}^{n_y} \hat{w}_{kl}\left(\frac{x}{S}\right)^{k+1}\left(\frac{y}{c}\right)^{l-1}\right] \\ &+4\left[\frac{\partial^2}{\partial x \partial y}\sum_{i=1}^{n_x}\sum_{j=1}^{n_y} \hat{w}_{ij}\left(\frac{x}{S}\right)^{i+1}\left(\frac{y}{c}\right)^{j-1}\right] D_{33} \left[\frac{\partial^2}{\partial x \partial y}\sum_{k=1}^{n_x}\sum_{l=1}^{n_y} \hat{w}_{kl}\left(\frac{x}{S}\right)^{k+1}\left(\frac{y}{c}\right)^{l-1}\right] dxdy \end{aligned} \tag{A.11}$$

Executing the partial derivatives in x and y

$$
\begin{aligned}
U =& \frac{1}{2}\int_{-b}^{b}\int_{0}^{S}\left[\frac{1}{S^2}\sum_{i=1}^{n_x}\sum_{j=1}^{n_y}\overline{w}_{ij}(i+1)i\left(\frac{x}{S}\right)^{i-1}\left(\frac{y}{c}\right)^{j-1}\right]D_{11}\left[\frac{1}{S^2}\sum_{k=1}^{n_x}\sum_{l=1}^{n_y}\overline{w}_{kl}(k+1)k\left(\frac{x}{S}\right)^{k-1}\left(\frac{y}{c}\right)^{l-1}\right] \\
&+\left[\frac{1}{S^2}\sum_{i=1}^{n_x}\sum_{j=1}^{n_y}\overline{w}_{ij}(i+1)i\left(\frac{x}{S}\right)^{i-1}\left(\frac{y}{c}\right)^{j-1}\right]D_{12}\left[\frac{1}{c^2}\sum_{k=1}^{n_x}\sum_{l=1}^{n_y}\overline{w}_{kl}\left(\frac{x}{S}\right)^{k+1}(l-1)(l-2)\left(\frac{y}{c}\right)^{l-3}\right] \\
&+4\left[\frac{1}{S^2}\sum_{i=1}^{n_x}\sum_{j=1}^{n_y}\overline{w}_{ij}(i+1)i\left(\frac{x}{S}\right)^{i-1}\left(\frac{y}{c}\right)^{j-1}\right]D_{13}\left[\frac{1}{Sc}\sum_{k=1}^{n_x}\sum_{l=1}^{n_y}\overline{w}_{kl}(k+1)(l-1)\left(\frac{x}{S}\right)^{k}\left(\frac{y}{c}\right)^{l-2}\right] \\
&+\left[\frac{1}{c^2}\sum_{i=1}^{n_x}\sum_{j=1}^{n_y}\overline{w}_{ij}(j-1)(j-2)\left(\frac{x}{S}\right)^{i+1}\left(\frac{y}{c}\right)^{j-3}\right]D_{22}\left[\frac{1}{c^2}\sum_{k=1}^{n_x}\sum_{l=1}^{n_y}\overline{w}_{kl}(l-1)(l-2)\left(\frac{x}{S}\right)^{k+1}\left(\frac{y}{c}\right)^{l-3}\right] \\
&+4\left[\frac{1}{c^2}\sum_{i=1}^{n_x}\sum_{j=1}^{n_y}\overline{w}_{ij}(j-1)(j-2)\left(\frac{x}{S}\right)^{i+1}\left(\frac{y}{c}\right)^{j-3}\right]D_{23}\left[\frac{1}{Sc}\sum_{k=1}^{n_x}\sum_{l=1}^{n_y}\overline{w}_{kl}(k+1)(l-1)\left(\frac{x}{S}\right)^{k}\left(\frac{y}{c}\right)^{l-2}\right] \\
&+4\left[\frac{1}{Sc}\sum_{i=1}^{n_x}\sum_{j=1}^{n_y}\overline{w}_{ij}(i+1)(j-1)\left(\frac{x}{S}\right)^{i}\left(\frac{y}{c}\right)^{j-2}\right]D_{33}\left[\frac{1}{Sc}\sum_{k=1}^{n_x}\sum_{l=1}^{n_y}\overline{w}_{kl}(k+1)(l-1)\left(\frac{x}{S}\right)^{k}\left(\frac{y}{c}\right)^{l-2}\right]dxdy
\end{aligned}
\tag{A.12}
$$

as the most general expressions for $j \geq 3$. Note that the second derivatives in y become zero for $j < 3$ and the first derivatives in y for $j < 2$ (there are no negative exponents).

Afterwards, the partial derivatives in the generalised coordinates are carried out in order

to simplify the expression. As for the mass matrix, the product rule is applied.

$$
\begin{aligned}
\frac{\partial U}{\partial \overline{w}_{(mn)}} =& \frac{1}{2}\int_{-b}^{b}\int_{0}^{S} \\
&\left[\frac{1}{S^2}\sum_{i=1}^{n_x}\sum_{j=1}^{n_y}\delta_{(ij)(mn)}(i+1)i\left(\frac{x}{S}\right)^{i-1}\left(\frac{y}{c}\right)^{j-1}\right] D_{11}\left[\frac{1}{S^2}\sum_{k=1}^{n_x}\sum_{l=1}^{n_y}\overline{w}_{kl}(k+1)k\left(\frac{x}{S}\right)^{k-1}\left(\frac{y}{c}\right)^{l-1}\right] \\
&+\left[\frac{1}{S^2}\sum_{i=1}^{n_x}\sum_{j=1}^{n_y}\overline{w}_{ij}(i+1)i\left(\frac{x}{S}\right)^{i-1}\left(\frac{y}{c}\right)^{j-1}\right] D_{11}\left[\frac{1}{S^2}\delta_{(kl)(mn)}(k+1)k\left(\frac{x}{S}\right)^{k-1}\left(\frac{y}{c}\right)^{l-1}\right] \\
&+\left[\frac{1}{S^2}\delta_{(ij)(mn)}(i+1)i\left(\frac{x}{S}\right)^{i-1}\left(\frac{y}{c}\right)^{j-1}\right] D_{12}\left[\frac{1}{c^2}\sum_{k=1}^{n_x}\sum_{l=1}^{n_y}\overline{w}_{kl}\left(\frac{x}{S}\right)^{k+1}(l-1)(l-2)\left(\frac{y}{c}\right)^{l-3}\right] \\
&+\left[\frac{1}{S^2}\sum_{i=1}^{n_x}\sum_{j=1}^{n_y}\overline{w}_{ij}(i+1)i\left(\frac{x}{S}\right)^{i-1}\left(\frac{y}{c}\right)^{j-1}\right] D_{12}\left[\frac{1}{c^2}\delta_{(kl)(mn)}\left(\frac{x}{S}\right)^{k+1}(l-1)(l-2)\left(\frac{y}{c}\right)^{l-3}\right] \\
&+4\left[\frac{1}{S^2}\delta_{(ij)(mn)}(i+1)i\left(\frac{x}{S}\right)^{i-1}\left(\frac{y}{c}\right)^{j-1}\right] D_{13}\left[\frac{1}{Sc}\sum_{k=1}^{n_x}\sum_{l=1}^{n_y}\overline{w}_{kl}(k+1)(l-1)\left(\frac{x}{S}\right)^{k}\left(\frac{y}{c}\right)^{l-2}\right] \\
&+4\left[\frac{1}{S^2}\sum_{i=1}^{n_x}\sum_{j=1}^{n_y}\overline{w}_{ij}(i+1)i\left(\frac{x}{S}\right)^{i-1}\left(\frac{y}{c}\right)^{j-1}\right] D_{13}\left[\frac{1}{Sc}\delta_{(kl)(mn)}(k+1)(l-1)\left(\frac{x}{S}\right)^{k}\left(\frac{y}{c}\right)^{l-2}\right] \\
&+\left[\frac{1}{c^2}\delta_{ij}(j-1)(j-2)\left(\frac{x}{S}\right)^{i+1}\left(\frac{y}{c}\right)^{j-3}\right] D_{22}\left[\frac{1}{c^2}\sum_{k=1}^{n_x}\sum_{l=1}^{n_y}\overline{w}_{kl}(l-1)(l-2)\left(\frac{x}{S}\right)^{k+1}\left(\frac{y}{c}\right)^{l-3}\right] \\
&+\left[\frac{1}{c^2}\sum_{i=1}^{n_x}\sum_{j=1}^{n_y}\overline{w}_{ij}(j-1)(j-2)\left(\frac{x}{S}\right)^{i+1}\left(\frac{y}{c}\right)^{j-3}\right] D_{22}\left[\frac{1}{c^2}\delta_{(kl)(mn)}(l-1)(l-2)\left(\frac{x}{S}\right)^{k+1}\left(\frac{y}{c}\right)^{l-3}\right] \\
&+4\left[\frac{1}{c^2}\delta_{(ij)(mn)}(j-1)(j-2)\left(\frac{x}{S}\right)^{i+1}\left(\frac{y}{c}\right)^{j-3}\right] D_{23}\left[\frac{1}{Sc}\sum_{k=1}^{n_x}\sum_{l=1}^{n_y}\overline{w}_{kl}(k+1)(l-1)\left(\frac{x}{S}\right)^{k}\left(\frac{y}{c}\right)^{l-2}\right] \\
&+4\left[\frac{1}{c^2}\sum_{i=1}^{n_x}\sum_{j=1}^{n_y}\overline{w}_{ij}(j-1)(j-2)\left(\frac{x}{S}\right)^{i+1}\left(\frac{y}{c}\right)^{j-3}\right] D_{23}\left[\frac{1}{Sc}\delta_{(kl)(mn)}(k+1)(l-1)\left(\frac{x}{S}\right)^{k}\left(\frac{y}{c}\right)^{l-2}\right] \\
&+4\left[\frac{1}{Sc}\delta_{(ij)(mn)}(i+1)(j-1)\left(\frac{x}{S}\right)^{i}\left(\frac{y}{c}\right)^{j-2}\right] D_{33}\left[\frac{1}{Sc}\sum_{k=1}^{n_x}\sum_{l=1}^{n_y}\overline{w}_{kl}(k+1)(l-1)\left(\frac{x}{S}\right)^{k}\left(\frac{y}{c}\right)^{l-2}\right] \\
&+4\left[\frac{1}{Sc}\sum_{i=1}^{n_x}\sum_{j=1}^{n_y}\overline{w}_{ij}(i+1)(j-1)\left(\frac{x}{S}\right)^{i}\left(\frac{y}{c}\right)^{j-2}\right] D_{33}\left[\frac{1}{Sc}\delta_{(kl)(mn)}(k+1)(l-1)\left(\frac{x}{S}\right)^{k}\left(\frac{y}{c}\right)^{l-2}\right] \\
&dxdy
\end{aligned}
\tag{A.13}
$$

Collecting terms and, as before, renaming the indices such that (ij) is the external index and (kl) the internal summation index during which the Kronecker's deltas are removed, as well as carrying out the integration, gives

$$\begin{aligned}
\frac{\partial U}{\partial \overline{w}_{(ij)}} = &\left[\frac{c}{S^3}\sum_{k=1}^{n_x}\sum_{l=1}^{n_y}\overline{w}_{kl}\frac{(i+1)i(k+1)k}{(i+k-1)(j+l-1)}\left[\left(\frac{x}{S}\right)^{i+k-1}\right]_0^S\left[\left(\frac{y}{c}\right)^{j+l-1}\right]_{-b}^b\right]D_{11}\\
&+2\left[\frac{1}{Sc}\sum_{k=1}^{n_x}\sum_{l=1}^{n_y}\overline{w}_{kl}\frac{(i+1)i(l-1)(l-2)}{(i+k+1)(j+l-3)}\left[\left(\frac{x}{S}\right)^{i+k+1}\right]_0^S\left[\left(\frac{y}{c}\right)^{j+l-3}\right]_{-b}^b\right]D_{12}\\
&+4\left[\frac{1}{S^2}\sum_{k=1}^{n_x}\sum_{l=1}^{n_y}\overline{w}_{kl}\frac{(i+1)i(k+1)(l-1)}{(i+k)(j+l-2)}\left[\left(\frac{x}{S}\right)^{i+k}\right]_0^S\left[\left(\frac{y}{c}\right)^{j+l-2}\right]_{-b}^b\right]D_{13}\\
&+\left[\frac{S}{c^3}\sum_{k=1}^{n_x}\sum_{l=1}^{n_y}\overline{w}_{kl}\frac{(j-1)(j-2)(l-1)(l-2)}{(i+k+3)(j+l-5)}\left[\left(\frac{x}{S}\right)^{i+k+3}\right]_0^S\left[\left(\frac{y}{c}\right)^{j+l-5}\right]_{-b}^b\right]D_{22}\\
&+4\left[\frac{1}{c^2}\sum_{k=1}^{n_x}\sum_{l=1}^{n_y}\overline{w}_{kl}\frac{(j-1)(j-2)(k+1)(l-1)}{(i+k+2)(j+l-4)}\left[\left(\frac{x}{S}\right)^{i+k+2}\right]_0^S\left[\left(\frac{y}{c}\right)^{j+l-4}\right]_{-b}^b\right]D_{23}\\
&+4\left[\frac{1}{Sc}\sum_{k=1}^{n_x}\sum_{l=1}^{n_y}\overline{w}_{kl}\frac{(i+1)(j-1))(k+1)(l-1)}{(i+k+1)(j+l-3)}\left[\left(\frac{x}{S}\right)^{i+k+1}\right]_0^S\left[\left(\frac{y}{c}\right)^{j+l-3}\right]_{-b}^b\right]D_{33}
\end{aligned} \tag{A.14}$$

so that the final stiffness matrix components are

$$\begin{aligned}
K_{(ij)(kl)} = &\left[\frac{c}{S^3}\frac{(i+1)i(k+1)k}{(i+k-1)(j+l-1)}\left[\left(\frac{x}{S}\right)^{i+k-1}\right]_0^S\left[\left(\frac{y}{c}\right)^{j+l-1}\right]_{-b}^b\right]D_{11}\\
&+2\left[\frac{1}{Sc}\frac{(i+1)i(l-1)(l-2)}{(i+k+1)(j+l-3)}\left[\left(\frac{x}{S}\right)^{i+k+1}\right]_0^S\left[\left(\frac{y}{c}\right)^{j+l-3}\right]_{-b}^b\right]D_{12}\\
&+4\left[\frac{1}{S^2}\frac{(i+1)i(k+1)(l-1)}{(i+k)(j+l-2)}\left[\left(\frac{x}{S}\right)^{i+k}\right]_0^S\left[\left(\frac{y}{c}\right)^{j+l-2}\right]_{-b}^b\right]D_{13}\\
&+\left[\frac{S}{c^3}\frac{(j-1)(j-2)(l-1)(l-2)}{(i+k+3)(j+l-5)}\left[\left(\frac{x}{S}\right)^{i+k+3}\right]_0^S\left[\left(\frac{y}{c}\right)^{j+l-5}\right]_{-b}^b\right]D_{22}\\
&+4\left[\frac{1}{c^2}\frac{(j-1)(j-2)(k+1)(l-1)}{(i+k+2)(j+l-4)}\left[\left(\frac{x}{S}\right)^{i+k+2}\right]_0^S\left[\left(\frac{y}{c}\right)^{j+l-4}\right]_{-b}^b\right]D_{23}\\
&+4\left[\frac{1}{Sc}\frac{(i+1)(j-1))(k+1)(l-1)}{(i+k+1)(j+l-3)}\left[\left(\frac{x}{S}\right)^{i+k+1}\right]_0^S\left[\left(\frac{y}{c}\right)^{j+l-3}\right]_{-b}^b\right]D_{33}
\end{aligned} \tag{A.15}$$

A.3 Aerodynamic matrices for the Wright aerodynamic operator

To obtain the aerodynamic matrices for the Wright model detailed in chapter II.1.1, the elements described in chapter II.2.2 are used. However, this description is derived for a 2D wing section. In order to be able to use it for the plate wing, several assumptions have to be made.

The first assumption is the so-called “strip theory” assumption, which describes the aerodynamics of the wing as a series of infinitesimally thin identical “strips” along the wing span, which are not influenced by their neighbour environment.

The infinitesimally small lift and moment "strips" are described as (see also Equations (II.10),(II.11)) [146, 123]

$$dL = 2\rho_a \pi b V^2 \left(\alpha + \frac{\dot{w}}{V}\right) dx \tag{A.16}$$

$$dM = 2\rho_a V^2 b^2 \left[\frac{1}{2}\pi \left(\alpha + \frac{\dot{w}}{V}\right) + M_{\dot{\alpha}} \frac{\dot{\alpha} b}{2V}\right] dx \tag{A.17}$$

where the wing is assumed to be a flat plate with its aerodynamic centre situated at a quarter of the chord from the leading edge.

The virtual work can be obtained by integrating along the half-span of the plate.

$$\delta W = \int_0^S (-\delta w) dL + \int_0^S \delta\alpha dM \tag{A.18}$$

This however is expressed in terms of heave in pitch motion, whereas a plate is much richer in degrees of freedom. To circumvent this problem, a restriction is put on the chordwise modes such that $n_y = 2$. This restricts the assumed mode shapes Equation (A.2) to modes where the chord is rigid. For $j = 1$, the movement of an arbitrary strip of the plate corresponds then to pure plunge motion at midchord, which is taken as the reference axis anyway.

To obtain the angular motion, a small displacement assumption is made. This way, the angle of attack can be approximated via putting

$$\frac{dw}{dy} \approx \sin(\alpha) \approx \alpha \tag{A.19}$$

Inserting the assumed mode shapes,

$$\alpha \approx \sum_{i=1}^{n_x} \overline{w}_{i2} \frac{1}{c} \left(\frac{x}{S}\right)^{i+1} \tag{A.20}$$

The virtual work can then be calculated as

$$\begin{aligned}
\delta W = &\int_0^S 2\rho_a V^2 b\pi \left(\frac{1}{V}\left[\sum_{k=1}^{n_x} \dot{\overline{w}}_{k1} \left(\frac{x}{S}\right)^{k+1}\right] + \frac{1}{c}\left[\sum_{k=1}^{n_x} \overline{w}_{k2} \left(\frac{x}{S}\right)^{k+1}\right]\right) \left[-\sum_{i=1}^{n_x} \delta\overline{w}_{i1} \left(\frac{x}{S}\right)^{i+1}\right] dx \\
&+ \int_0^S 2\rho_a V^2 b^2 \left[\frac{1}{2}\pi \left(\frac{1}{V}\left[\sum_{k=1}^{n_x} \dot{\overline{w}}_{k1} \left(\frac{x}{S}\right)^{k+1}\right] + \frac{1}{c}\left[\sum_{k=1}^{n_x} \overline{w}_{k2} \left(\frac{x}{S}\right)^{k+1}\right]\right)\right. \\
&\left. + M_{\dot{\alpha}} \left(\frac{1}{4V} \sum_{k=1}^{n_x} \dot{\overline{w}}_{k2} \left(\frac{x}{S}\right)^{k+1}\right)\right] \left[\sum_{i=1}^{n_x} \delta\overline{w}_{i2} \frac{1}{c} \left(\frac{x}{S}\right)^{i+1}\right] dx
\end{aligned} \tag{A.21}$$

Collecting terms

$$\begin{aligned}\delta W = &- \int_0^S 2\rho_a V^2 b\pi \left(\frac{1}{V} \left[\sum_{i=1}^{n_x} \sum_{k=1}^{n_x} \dot{\overline{w}}_{k1} \delta \overline{w}_{i1} \left(\frac{x}{S} \right)^{i+k+2} \right] + \frac{1}{c} \left[\sum_{i=1}^{n_x} \sum_{k=1}^{n_x} \overline{w}_{k2} \delta \overline{w}_{i1} \left(\frac{x}{S} \right)^{i+k+2} \right] \right) dx \\ &+ \int_0^S 2\rho_a V^2 b^2 \left[\frac{1}{2}\pi \left(\frac{1}{V} \left[\sum_{i=1}^{n_x} \sum_{k=1}^{n_x} \dot{\overline{w}}_{k1} \delta \overline{w}_{i2} \frac{1}{c} \left(\frac{x}{S} \right)^{i+k+2} \right] + \frac{1}{c} \left[\sum_{i=1}^{n_x} \sum_{k=1}^{n_x} \overline{w}_{k2} \delta \overline{w}_{i2} \frac{1}{c} \left(\frac{x}{S} \right)^{i+k+2} \right] \right) \right. \\ &\left. + M_{\dot{\alpha}} \left(\frac{1}{4V} \sum_{i=1}^{n_x} \sum_{k=1}^{n_x} \dot{\overline{w}}_{k2} \delta \overline{w}_{i2} \left(\frac{x}{S} \right)^{i+k+2} \right) \right] dx \end{aligned} \tag{A.22}$$

Integrating

$$\begin{aligned}\delta W = &- 2\rho_a V^2 b\pi \left(\frac{S}{V} \left[\sum_{i=1}^{n_x} \sum_{k=1}^{n_x} \dot{\overline{w}}_{k1} \delta \overline{w}_{i1} \frac{1}{i+k+3} \left(\frac{x}{S} \right)^{i+k+3} \right] + \frac{S}{c} \left[\sum_{i=1}^{n_x} \sum_{k=1}^{n_x} \overline{w}_{k2} \delta \overline{w}_{i1} \frac{1}{i+k+3} \left(\frac{x}{S} \right)^{i+k+3} \right] \right) \\ &+ 2\rho_a V^2 b^2 \left[\frac{1}{2}\pi \left(\frac{S}{V} \left[\sum_{i=1}^{n_x} \sum_{k=1}^{n_x} \dot{\overline{w}}_{k1} \delta \overline{w}_{i2} \frac{1}{c} \frac{1}{i+k+3} \left(\frac{x}{S} \right)^{i+k+3} \right] + \frac{S}{c} \left[\sum_{i=1}^{n_x} \sum_{k=1}^{n_x} \overline{w}_{k2} \delta \overline{w}_{i2} \frac{1}{i+k+3} \frac{1}{c} \left(\frac{x}{S} \right)^{i+k+3} \right] \right) \right. \\ &\left. + M_{\dot{\alpha}} \left(\frac{S}{4V} \sum_{i=1}^{n_x} \sum_{k=1}^{n_x} \dot{\overline{w}}_{k2} \delta \overline{w}_{i2} \frac{1}{i+k+3} \left(\frac{x}{S} \right)^{i+k+3} \right) \right] \end{aligned} \tag{A.23}$$

To prepare the insertion in the Lagrange equation, the partial derivatives by the generalised coordinates are carried out.

$$\frac{\partial \delta W}{\partial \delta w_{i1}} = -2\rho_a V^2 b\pi \sum_{k=1}^{n_x} \left(\frac{S}{V} \dot{\overline{w}}_{k1} + \frac{S}{c} \overline{w}_{k2} \right) \left[\frac{1}{i+k+3} \left(\frac{x}{S} \right)^{i+k+3} \right] \tag{A.24}$$

$$\begin{aligned}\frac{\partial \delta W}{\partial \delta w_{i2}} = &\ 2\rho_a V^2 b^2 \sum_{k=1}^{n_x} \left[\frac{1}{2}\pi \left(\frac{S}{V} \frac{1}{c} \dot{\overline{w}}_{k1} + \frac{S}{c} \frac{1}{c} \overline{w}_{k2} \right) \right. \\ &\left. + \ 2\rho_a V^2 b^2 \ M_{\dot{\alpha}} \left(\frac{S}{4V} \dot{\overline{w}}_{k2} \right) \right] \left[\frac{1}{i+k+3} \left(\frac{x}{S} \right)^{i+k+3} \right] \end{aligned} \tag{A.25}$$

The components of the aerodynamic "stiffness" matrix **A** and the aerodynamic "damping" matrix **B** can then be given as

$$A_{(i1)(k1)} = A_{(i2)(k1)} = 0 \tag{A.26}$$

$$A_{(i1)(k2)} = -2\rho_a V^2 b\pi \frac{S}{c} \left[\frac{1}{i+k+3} \left(\frac{x}{S} \right)^{i+k+3} \right] \tag{A.27}$$

$$A_{(i2)(k2)} = \rho_a V^2 b^2 \pi \frac{S}{c^2} \left[\frac{1}{i+k+3} \left(\frac{x}{S} \right)^{i+k+3} \right] \tag{A.28}$$

$$B_{(i1)(k1)} = -2\rho_a V^2 b\pi \frac{S}{V}\left[\frac{1}{i+k+3}\left(\frac{x}{S}\right)^{i+k+3}\right] \tag{A.29}$$

$$B_{(i1)(k2)} = 0 \tag{A.30}$$

$$B_{(i2)(k1)} = \rho_a V^2 b^2 \pi \frac{S}{V}\frac{1}{c}\left[\frac{1}{i+k+3}\left(\frac{x}{S}\right)^{i+k+3}\right] \tag{A.31}$$

$$B_{(i2)(k2)} = 2\rho_a V^2 b^2 M_{\dot{\alpha}}\left(\frac{S}{4V}\right)\left[\frac{1}{i+k+3}\left(\frac{x}{S}\right)^{i+k+3}\right] \tag{A.32}$$

A.4 Aerodynamic matrix for the Theodorsen aerodynamic operator

For the Theodorsen approach, a simpler approach to derive the lift and moment expressions is taken. Other than in the Wright approach, the time derivatives are not separated. Instead, they are executed directly and the aerodynamic operator is given as a function of the reduced frequency.

The lift and moment in dimensional form were expressed in Equations (II.22), (II.23) as

$$L = \rho_a \pi b^2 \left(V\dot{\alpha} + \ddot{w} - ba_h\ddot{\alpha}\right) + 2\pi\rho V b C\left[V\alpha + \dot{w} + b\left(\frac{1}{2} - a_h\right)\dot{\alpha}\right] \tag{A.33}$$

$$\begin{aligned} M = {} & -\rho_a b^2\left[\pi\left(\frac{1}{2} - a_h\right)Vb\dot{\alpha} + \pi b^2\left(\frac{1}{8} + a_h^2\right)\ddot{\alpha} - a_h\pi b\ddot{w}\right] \\ & +2\rho_a V b^2\pi\left(a_h + \frac{1}{2}\right)C\left[V\alpha + \dot{w} + b\left(\frac{1}{2} - a_h\right)\dot{\alpha}\right] \end{aligned} \tag{A.34}$$

Assuming harmonic motion and executing the time derivatives, these expressions are reformulated so they can be given in terms of the reduced velocity k and the airspeed V does no longer appear explicitely in the lift and moment terms. Other than in Equations (II.26), (II.27), the dimensions are kept, as certain nondimensional quantities do not exist in the framework of the plate wing.

$$\begin{aligned} dL = {} & \omega^2\rho_a\pi b^2\left(\frac{\imath}{k}b\alpha - w + ba_h\alpha\right) \\ & +\omega^2 2\rho_a\pi b^2 C(k)\left[\frac{1}{k^2}b\alpha + \frac{\imath}{k}w = \frac{\imath}{k}b\left(\frac{1}{2} - a_h\right)\alpha\right] \end{aligned} \tag{A.35}$$

$$\begin{aligned} dM = {} & -\omega^2\rho_a\pi b^2\left[\frac{\imath}{k}\left(\frac{1}{2} - a_h\right)b^2\alpha - b^2\left(\frac{1}{8} + a_h^2\right)\alpha + a_h bw\right] \\ & +\omega_2 2\rho_a\pi b^2\left(a_h + \frac{1}{2}\right)C(k)\left[\frac{1}{k^2}b^2\alpha + \frac{i}{k}bw + \frac{i}{k}b^2\left(\frac{1}{2} - a_h\right)\alpha\right]dx \end{aligned} \tag{A.36}$$

Grouping by degree of freedom results in

$$
\begin{aligned}
dL &= \omega^2\rho_a\pi b^2\left(-1+2C(k)\frac{\imath}{k}\right)wdx \\
&\quad +\omega^2\rho_a\pi b^3\left[\frac{\imath}{k}+a_h+2\left(a_h+\frac{1}{2}\right)C(k)\left[\frac{1}{k^2}+\frac{\imath}{k}\left(\frac{1}{2}-a_h\right)\right]\right]\alpha dx \quad \text{(A.37)} \\
dM &= \omega^2\rho_a\pi b^3\left[-a_h+2\left(a_h+\frac{1}{2}\right)C(k)\frac{\imath}{k}\right]wdx \quad \text{(A.38)} \\
&\quad \omega^2\rho\pi b^4\left[-\left(\frac{1}{2}-a_h\right)\frac{\imath}{k}+\left(\frac{1}{8}+a_h^2\right)\right. \\
&\quad \left.+2\left(a_h+\frac{1}{2}\right)C(k)\left[\frac{1}{k^2}+\frac{\imath}{k}\left(\frac{1}{2}-a_h\right)\right]\right]\alpha dx \quad \text{(A.39)}
\end{aligned}
$$

Using the mode shapes Equation (A.2) and the approximation for the angle Equation (A.20)

$$
\begin{aligned}
\delta W &= \int_0^S -\delta w dL + \int_0^S \delta\alpha dM \\
&= -\int_0^S \omega^2\rho_a\pi b^2\left(-1+2C(k)\frac{\imath}{k}\right)\sum_{i=1}^{n_x}\sum_{m=1}^{n_x}\overline{w}_{i1}\delta\overline{w}_{m1}\left(\frac{x}{S}\right)^{i+1}\left(\frac{x}{S}\right)^{m+1}dx \\
&\quad +\int_0^S \omega^2\rho_a\pi b^3\left[\frac{\imath}{k}+a_h+2\left(a_h+\frac{1}{2}\right)C(k)\left[\frac{1}{k^2}+\frac{\imath}{k}\left(\frac{1}{2}-a_h\right)\right]\right] \\
&\quad \left[\sum_{i=1}^{n_x}\sum_{m=1}^{n_x}\frac{1}{c}\overline{w}_{i2}\delta\overline{w}_{m1}\left(\frac{x}{S}\right)^{i+1}\left(\frac{x}{S}\right)^{m+1}\right]dx \\
&\quad +\int_0^S \omega^2\rho_a\pi b^3\left[-a_h+2\left(a_h+\frac{1}{2}\right)C(k)\frac{\imath}{k}\right]\left[\sum_{i=1}^{n_x}\sum_{m=1}^{n_x}\frac{1}{c}\overline{w}_{i1}\delta\overline{w}_{m2}\left(\frac{x}{S}\right)^{i+1}\left(\frac{x}{S}\right)^{m+1}\right]dx \\
&\quad +\int_0^S \omega^2\rho\pi b^4\left[-\left(\frac{1}{2}-a_h\right)\frac{\imath}{k}+\left(\frac{1}{8}+a_h^2\right)\right. \\
&\quad \left.+2\left(a_h+\frac{1}{2}\right)C(k)\left[\frac{1}{k^2}+\frac{\imath}{k}\left(\frac{1}{2}-a_h\right)\right]\right]\left[\sum_{i=1}^{n_x}\sum_{m=1}^{n_x}\frac{1}{c^2}\overline{w}_{i2}\delta\overline{w}_{m2}\left(\frac{x}{S}\right)^{i+1}\left(\frac{x}{S}\right)^{m+1}\right]dx
\end{aligned}
$$

Collecting terms and executing the integration results in

$$\begin{aligned}
\delta W = &- \omega^2 \rho_a \pi b^2 \left(-1 + 2C(k)\frac{\imath}{k}\right) \sum_{i=1}^{n_x}\sum_{m=1}^{n_x} \overline{w}_{i1}\delta\overline{w}_{m1} S \frac{1}{i+m+3}\left[\left(\frac{x}{S}\right)^{i+m+3}\right]_0^S \\
&+ \omega^2 \rho_a \pi b^3 \left[\frac{\imath}{k} + a_h + 2\left(a_h + \frac{1}{2}\right) C(k)\left[\frac{1}{k^2} + \frac{\imath}{k}\left(\frac{1}{2} - a_h\right)\right]\right] \\
&\left[\sum_{i=1}^{n_x}\sum_{m=1}^{n_x} \frac{1}{c}\overline{w}_{i2}\delta\overline{w}_{m1} S \frac{1}{i+m+3}\left[\left(\frac{x}{S}\right)^{i+m+3}\right]_0^S\right] \\
&+ \omega^2 \rho_a \pi b^3 \left[-a_h + 2\left(a_h + \frac{1}{2}\right) C(k)\frac{\imath}{k}\right] \left[\sum_{i=1}^{n_x}\sum_{m=1}^{n_x} \frac{1}{c}\overline{w}_{i1}\delta\overline{w}_{m2} S \frac{1}{i+m+3}\left[\left(\frac{x}{S}\right)^{i+m+3}\right]_0^S\right] \\
&+ \omega^2 \rho \pi b^4 \left[-\left(\frac{1}{2} - a_h\right)\frac{\imath}{k} + \left(\frac{1}{8} + a_h^2\right)\right. \\
&\left. + 2\left(a_h + \frac{1}{2}\right) C(k)\left[\frac{1}{k^2} + \frac{\imath}{k}\left(\frac{1}{2} - a_h\right)\right]\right] \left[\sum_{i=1}^{n_x}\sum_{m=1}^{n_x} \frac{1}{c^2}\overline{w}_{i2}\delta\overline{w}_{m2} S \frac{1}{i+m+3}\left[\left(\frac{x}{S}\right)^{i+m+3}\right]_0^S\right]
\end{aligned}$$

By executing the partial derivatives by the coefficients of the virtual displacements $\delta\overline{w}_{op}$ as in the previous examples, and again renaming the indices, the components of the aerodynamic matrix can be recovered as

$$A_{(i1)(m1)} = \rho_a \pi b^2 \left(-1 + 2C(k)\frac{\imath}{k}\right) \overline{w}_{i1}\delta\overline{w}_{m1} S \frac{1}{i+m+3}\left[\left(\frac{x}{S}\right)^{i+m+3}\right]_0^S \tag{A.40}$$

$$\begin{aligned}
A_{(i1)(m2)} = &\ \rho_a \pi b^3 \left[\frac{\imath}{k} + a_h + 2\left(a_h + \frac{1}{2}\right) C(k)\left[\frac{1}{k^2} + \frac{\imath}{k}\left(\frac{1}{2} - a_h\right)\right]\right] \\
&\frac{S}{c}\frac{1}{i+m+3}\left[\left(\frac{x}{S}\right)^{i+m+3}\right]_0^S
\end{aligned} \tag{A.41}$$

$$A_{(i2)(m1)} = \rho_a \pi b^3 \left[-a_h + 2\left(a_h + \frac{1}{2}\right) C(k)\frac{\imath}{k}\right] \frac{S}{c}\frac{1}{i+m+3}\left[\left(\frac{x}{S}\right)^{i+m+3}\right]_0^S \tag{A.42}$$

$$\begin{aligned}
A_{(i2)(m2)} = &\ \rho \pi b^4 \left[-\left(\frac{1}{2} - a_h\right)\frac{\imath}{k} + \left(\frac{1}{8} + a_h^2\right) + 2\left(a_h + \frac{1}{2}\right) C(k)\left[\frac{1}{k^2} + \frac{\imath}{k}\left(\frac{1}{2} - a_h\right)\right]\right] \\
&\frac{S}{c^2}\frac{1}{i+m+3}\left[\left(\frac{x}{S}\right)^{i+m+3}\right]_0^S
\end{aligned} \tag{A.43}$$

where the term of ω^2 was factored out of the matrix. In the final system, it is divided by and is finally part of the eigenvalues. Finally, it has to be noticed that plates have no "elastic axis", which means that the parameter a_h has no meaning. Instead, a reference axis is defined. In this work, the reference axis is midchord. a_h is consequently zero $a_h = 0$.

Appendix B

aPC validation

The arbitrary polynomial chaos approach is employed in this work to provide a faster surrogate model for the stochastic response of the aeroelastic problem. The present implementation has been derived following Navarro Jimenez, M.I. et al. [94], who provide a simple test case, consisting in the propagation of a multivariate Gaussian variable through an ODE problem.

In the case of a multivariate Gaussian, the analytical form of the distribution is known, and therefore the polynomial base for the chaos expansion can be computed analytically. Navarro Jimenez, M.I. et al. [94] use moment-generating functions. The equivalent can be achieved using the characteristic function of the multivariate Gaussian, which is its Fourier transform

$$\boldsymbol{\Psi} = \exp\left(\imath \boldsymbol{\mu}^{\mathsf{T}} \boldsymbol{\omega} - \frac{1}{2} \boldsymbol{\omega}^{\mathsf{T}} \boldsymbol{\Sigma} \boldsymbol{\omega}\right) \tag{B.1}$$

where $\mathbf{t}$ is the transformed variable, $\boldsymbol{\mu}$ is the mean and $\boldsymbol{\Sigma}$ is the covariance matrix. The integrals are then calculated by monomial, which is just the moment, which can be retrieved from the characteristic function by [**?**]

$$\int x^n \phi(x) dx = \imath^{-n} \frac{d^n \boldsymbol{\Psi}}{d\mathbf{t}^n} \tag{B.2}$$

However, in the aeroelastic problem, no analytical form of the distribution is available, and therefore, the polynomials cannot be computed analytically. In this work, the orthogonalisation is performed using Monte Carlo integration, and the expansion coefficients are determined by a fitting procedure. Obviously, this represents a compromise in the precision of the method. In order to find how the error due to the Monte Carlo integrations manifests in the expressions of the polynomials, a comparison of the method with Hermite polynomials, of which the expressions are known, is carried out. Furthermore, a comparison is made with the test case of the original paper from [94]. In order to distinguish between the error from the Monte Carlo integration and the fitting, we use the exact polynomial base which is derived using the characteristic function as described above.

B.1 Finding 1D Hermite polynomials

Although in the 1D case, there is no correlation by definition, the 1D study will permit to explore the precision issues and some properties of the proposed approach. In the following, it is assumed without proof that the 1D orthogonal polynomials with respect to a given probability density function are the unique solution. As the test law, a standard normal probability density function is assumed as the weight function for the creation of the polynomials. The result of the Gram-Schmidt algorithm should consequently correspond to the probabilist's Hermite polynomials.

In the following, a 1D polynomial will be noted as

$$p(\xi) = a_0 + a_1\xi + a_2\xi^2 + a_3\xi^3 + a_4\xi^4 + \dots \tag{B.3}$$

The analytical expressions for the six first Hermite polynomials are given in Tab. (B.1).

Polynôme	a_0	a_1	a_2	a_3	a_4	a_5
$H_0(\xi)$	1	0	0	0	0	0
$H_1(\xi)$	0	1	0	0	0	0
$H_2(\xi)$	-1	0	1	0	0	0
$H_3(\xi)$	0	-3	0	1	0	0
$H_4(\xi)$	3	0	-6	0	1	0
$H_5(\xi)$	0	15	0	-10	0	1

Table B.1 – 1D probabilist's Hermite polynomials up to order $p = 5$.

The orthogonal polynomials with respect to the standard normal law are recalculated in the following using the Gram-Schmidt algorithm, where the integrals for the scalar products are evaluated by the Monte Carlo method with 10^4 samples. The results are shown in Tab. (B.2).

Polynôme	a_0	a_1	a_2	a_3	a_4	a_5
$H_0(\xi)$	1.0	0.0	0.0	0.0	0.0	0.0
$H_1(\xi)$	0.0016	1.0	0.0	0.0	0.0	0.0
$H_2(\xi)$	-0.9994	0.0106	1.0	0.0	0.0	0.0
$H_3(\xi)$	-0.0205	-3.0218	0.0278	1.0	0.0	0.0
$H_4(\xi)$	3.0365	-0.2206	-6.0596	0.0835	1.0	0.0
$H_5(\xi)$	0.3875	15.1042	-0.9418	-10.0521	0.1841	1.0

Table B.2 – 1D orthogonal polynomials up to order $p = 5$, calculated using the Gram-Schmidt algorithm. Integrals for the functional scalar products are evaluated using the Monte Carlo method with 10^4 samples.

The structure of Hermite polynomials is clearly recognisable in the results. For low polynomial orders, the errors on the coefficients are small (of the order of 10^{-2}). Contrarily, it can be see that the errors accumulate for higher orders. The problem can be alleviated

using more samples. Increasing the number of samples to 10^6 lowers the errors for the coefficients of the polynomials of order 5 by about 50%, but the general problem of precision limitation persists. Evaluating the integrals analytically, the exact values are found. Thus, the precision issues are not a problem of the Gram-Schmidt method itself.

B.2 Finding 2D Hermite polynomials

In the framework of classical generalised polynomial chaos, the polynomials for higher-dimensional spaces are constructed using tensorial products of 1D base polynomials. However, as the case of interest in this work is composed of correlated variables, the polynomials of higher dimensional spaces cannot be recovered by such tensorial products any more, but the polynomials have to be calculated taking into account multiple dimensions at the same time.

In this section, it is attempted to find 2D Hermite polynomials on a two-dimensional, uncorrelated standard normal distributed random variable using the Gram-Schmidt algorithm without employing a direct tensor product in the process. It has to be noted that the polynomials in 2D are not unique, but depend on the sequence of the input monomials [93]. A set of monomials that produces the polynomials in order is chosen.

The result for a 2D-polynomial of order 3 is shown in Tab. (B.3).

$k=6$				
	b_0	b_1	b_2	b_3
a_0	−0.0247269769	−0.000195823	−0.0192252715	0.0
a_1	−2.93376876	0.0117545865	0.0	0.0
a_2	0.0754135822	1.0	0.0	0.0
a_3	1.0	0.0	0.0	0.0
$k=7$				
	b_0	b_1	b_2	b_3
a_0	−0.01149774	−0.98083283	−0.00176277	0.0
a_1	0.03501909	−0.01840475	0.0	0.0
a_2	0.00853065	1.0	0.0	0.0
a_3	−0.00430495	0.0	0.0	0.0
$k=8$				
	b_0	b_1	b_2	b_3
a_0	0.00990975	−0.03140393	0.00905575	0.0
a_1	−1.06225378	0.03111905	1.0	0.0
a_2	−0.02460403	0.03320619	0.0	0.0
a_3	0.01404496	0.0	0.0	0.0
$k=9$				
	b_0	b_1	b_2	b_3
a_0	0.00135357160	−3.01176333	0.0611448150	1.0
a_1	−0.00736285682	−0.106945128	−0.00316963305	0.0
a_2	−0.0278692908	0.0159679779	0.0	0.0
a_3	−0.00131020290	0.0	0.0	0.0

Table B.3 – The four last polynomials for a 2D orthogonalisation up to polynomials of order 3, calculated by the Gram-Schmidt algorithm. Integrals for the functional scalar products are evaluated by the Monte Carlo method using 10^4 samples.

As there are coefficients for every dimension and also mixed terms are well represented, the algorithm also respects the weights in the 2D space. At the same time, it is noted that the errors already found in 1D spread to the 2D space, but do not seem to accumulate further than in the 1D case. This leads to the expectation that the error will rise more with the order of the polynomials than with a higher dimension of the random space.

B.3 The test case of Navarro et al., 2014

In this section, the test case of the paper [94] is reevaluated using the proposed method. It consists of a solution of the first order decomposition equation [94]

$$y'(t;\alpha,\beta) = -\alpha(y(t;\alpha,\beta) - \beta) \tag{B.4}$$

of which the stochastic parameters are [94]

$$\boldsymbol{\mu} = \begin{pmatrix} 1 \\ 1 \end{pmatrix} \text{ and } \boldsymbol{\Sigma} = \begin{pmatrix} \sigma_\alpha^2 & \rho\sigma_\alpha\sigma_\beta \\ \rho\sigma_\alpha\sigma_\beta & \sigma_\beta^2 \end{pmatrix}, \text{ with } \sigma_\alpha = \sigma_\beta = 0.25 \tag{B.5}$$

B.3.1 Correlated variables

For $\rho \neq 0$, the stochastic input variables are correlated. In this work, only $\rho = 0.5$ is considered.

The polynomial basis for the surrogate model is constructed by evaluating the functional scalar products using Monte Carlo integration with 10^4 samples. Afterwards, the solver is sampled with 100 points. The development coefficients are then fitted using the least-squares method [114].

A histogram of the samples propagated through the surrogate model is shown in Fig. B.1

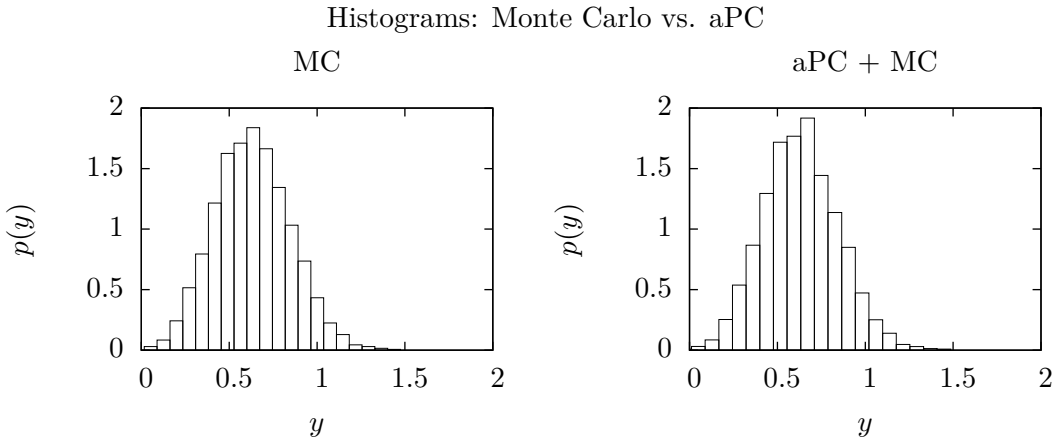

Fig. B.1 *Histograms obtained by direct sampling of the solver for $t = 1.0$, compared with samples propagated through the aPC surrogate, with 10^4 samples each.*

The histograms show that the aPC method reproduces results that are in satisfactory agreement with a direct propagation using Monte Carlo Simulation. The position of the peak and the form of the queues of the distributions match well. In the region used by the sampling, which is shown in Fig. B.2, the surrogate model is apparently sufficiently accurate. As a consequence, the aPC method can be used to obtain samplings of the probability density functions of y.

The low order of the aPC model, which is limited to order two in the example, can clearly be seen in the response surface. It is most notable on the limits of the domain, where the curvature of the surrogate does not correspond to the solver's response surface. However, in the center of the domain, which is the region with high probability density, the surfaces are nevertheless in good agreement.

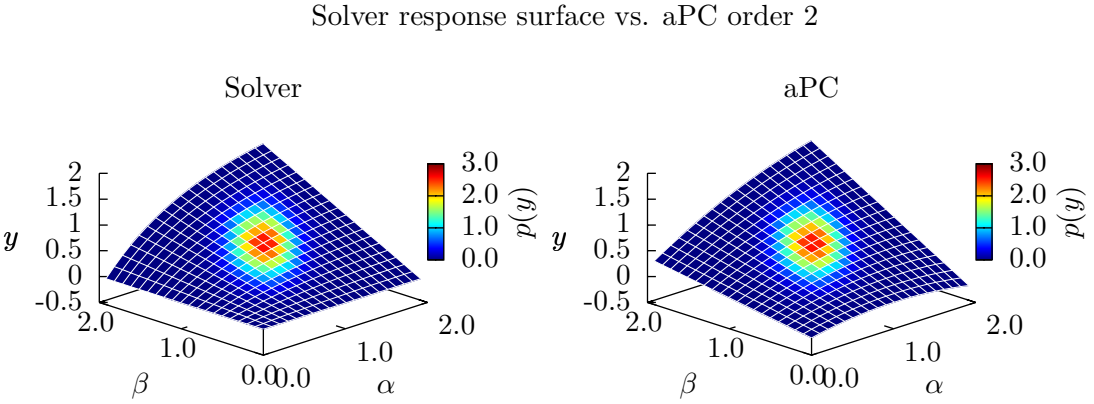

Fig. B.2 *Total aPC response surface in comparison with the response surface by direct calculus using the solver. The color indicates the probablity density of the parameters on the corresponding points on the response surface.*

Fig. B.3 shows the decomposition of the response surface into the individual orthogonal polynomials, which mimics Figs. 1,2 in [94]. Results are similar to those presented in [94].

Finally, the moments are obtained by directly exploiting the weighting coefficients of the polynomial chaos model [82]. The results for the mean and the variance are given in Table B.4 and compared to the results given by Monte Carlo simulation. The results are in satisfactory agreement with the results given graphically in Fig. 3 of [94].

Method	μ	σ
MC	0.6315	0.2147
aPC	0.6335	0.2170

Table B.4 – Moments for $t = 1.0$,$\rho = +0.5$ by Monte Carlo with 10^4 samples and with second-order aPC

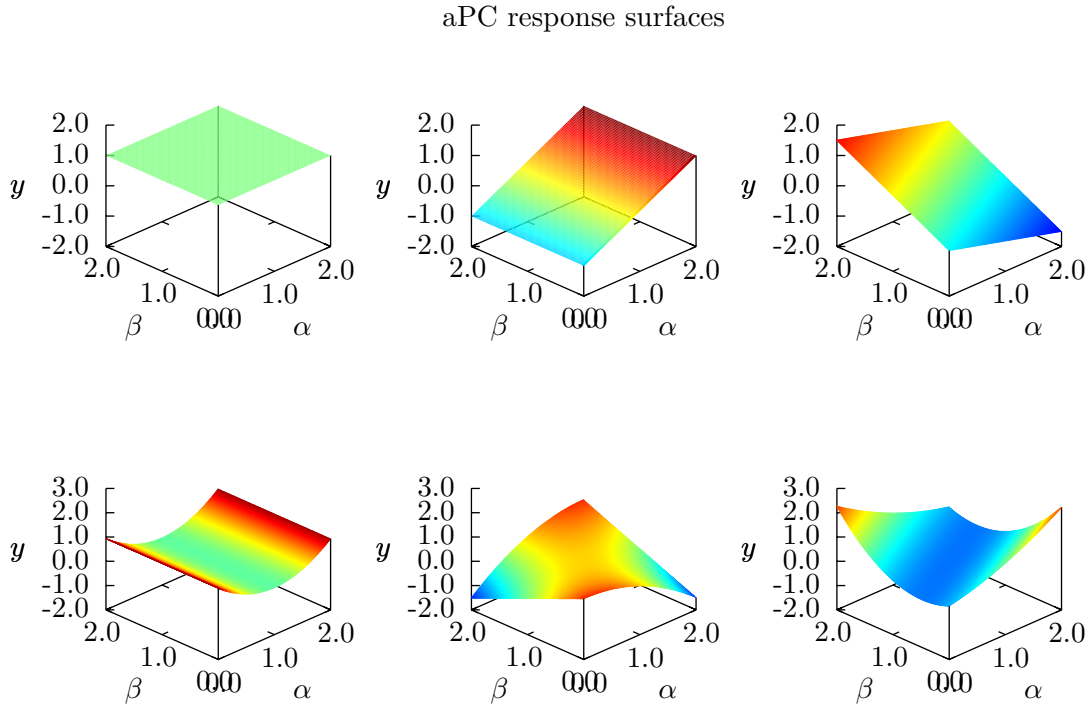

Fig. B.3 *Response surfaces of the individual polynomials without weighting coefficients, obtained for the example from Navarro Jimenez, M.I. et al. [94] with* $\rho = 0.5$

B.4 Decorrelated variables and comparison to classical Hermite Polynomial Chaos

For $\rho = 0$ the input variables become decorrelated, degenerating the input distribution to independent Gaussians. In that particular case, the classical polynomial chaos with Hermite polynomials can be applied. This classical approach will serve as a reference for the convergence properties of the aPC approach. For the construction of the polynomial chaos, [82] is used for the general procedure and [47] for the details on Hermite's polynomials.

Fig. B.4 shows the total response surfaces for fifth order polynomial chaos with 10^4 samples for the evaluation of the integrals and 100 points for the least-squares fit, compared to Hermite polynomial chaos, also of order five. The curves are in good agreement. Due to the higher polynomial order, the curvature of the response surface also matches satisfactorily on the border of the domains.

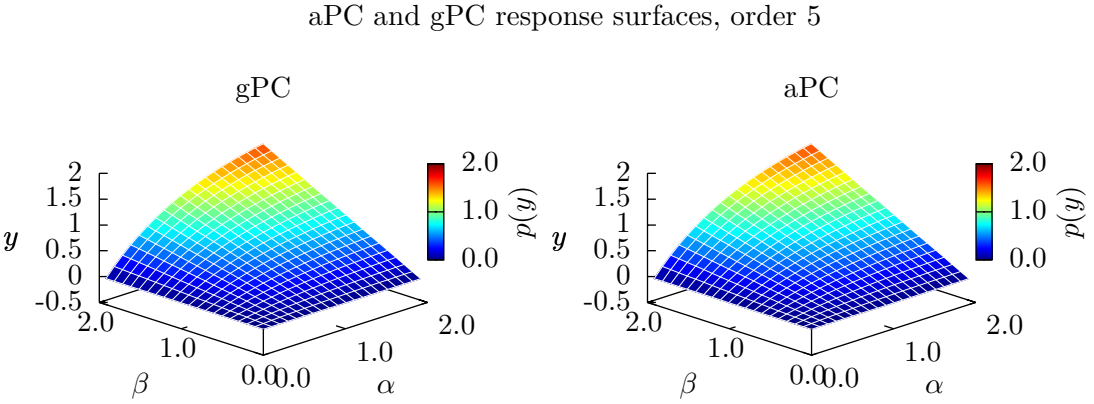

Fig. B.4 *Total aPC response surface (right) in comparison with the corresponding Hermite gPC response surface (left). The polynomial order is* 5 *in both cases.* 10^4 *samples for the evaluation of the integrals for the aPC.*

A comparison of the estimate of the first two moments of the response done with the two methods is given in Table B.5. the corresponding errors are shown in Fig. B.5.

	Wiener-Hermite-PC		Gram-Schmidt-PC, $n_{mc} = 10^4$		Gram-Schmidt-PC, $n_{mc} = 10^6$	
Ordre	μ	σ	μ	σ	μ	σ
1	0.6321206	0	0.6205076	0.1020561	0.6158589	0.0924467
2	0.6205643	0.1823312	0.6221902	0.1852516	0.6203117	0.1832563
3	0.6204436	0.1841526	0.6186309	0.1846591	0.6201870	0.1839390
4	0.6204428	0.1842037	0.6175228	0.1837377	0.6203902	0.1843192
5	0.6204428	0.1842046	0.6186208	0.1845447	0.6200298	0.1841010
10	0.6204428	0.1842046	–	–	0.6203153	0.1842849

Table B.5 – Mean and standard deviation for $\rho = 0.0$ and $t = 1.0$ for polynomial chaos of Wiener-Hermite and arbitrary polynomial chaos of Gram-Schmidt type with least-squares fitting with 100 calls to the solver in comparison

.

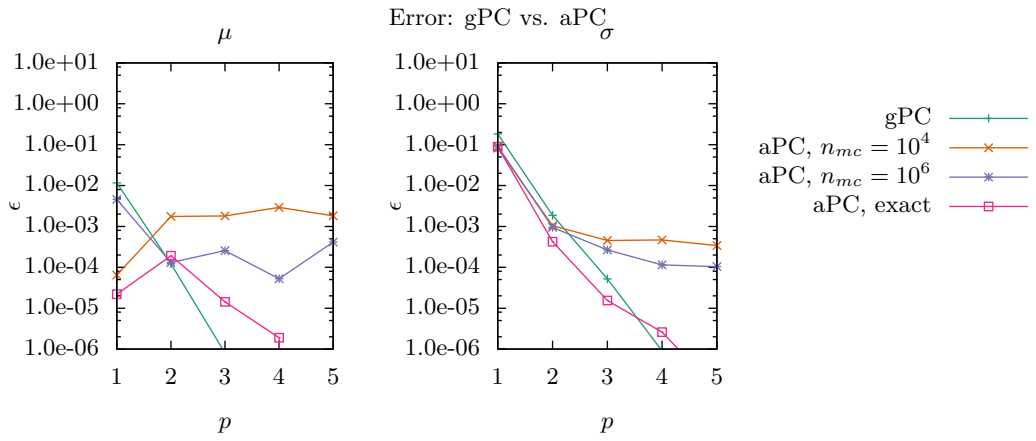

Fig. B.5 *Error between a 10th-order Wiener-Hermite solution, gPC of inferior order and aPC as a function of the order, and, for aPC, the number of samples for evaluating the integrals used in the orthogonalisation process.*

For the Wiener-Hermite polynomial chaos, the result for the mean converges to seven significant digits for an integration order of four. The result for the standard deviation is accurate to the fourth significant digit starting from that order.

It must be noted that the arbitrary polynomial chaos suffers from numeric noise coming from the Monte Carlo integrations used during the orthogonalisation of the polynomials. Using 10^4 samples, the precision does not rise starting from order two. Using 10^6 samples, the precision saturates at order three. Consequently, the noise from the Monte Carlo integration represents a limit for the precision, which seems to be independent from the polynomial order.

Of course, the accuracy of the approximation of the expansion coefficients also plays an important role, but this effect is less strong thatn the noise of the Monte Carlo integration if the system for the least-squares method stays overdetermined. This can be seen if the polynomials for the aPC are calculated analytically, which gives exact values for the polynomial basis. Then, the precision of the arbitrary polynomial chaos only depends on the fitting of the expansion coefficients. Despite the noise in the result and the fact that fitting of polynomial chaos expansion coefficents does not necessarily converge [29], it can be distinguished that the spectral convergence property is kept in this case so the error decreases with rising polynomial order. Contrarily to the development of the aPC using Monte Carlo integration, no saturation effect can be determined for orders inferior to six.

B.5 Conclusion

According to the test case of Navarro Jimenez, M.I. et al. [94] which has been reproduced in this work, the arbitrary polynomial chaos procedure with Monte Carlo integration and least-squares fitting appears to be usable and produces satisfactory results for the given test case. Good results are obtained for the histogram of the result distribution and the

first two moments, which have been compared with the results from the original paper. However, the test case does not challenge the method much, as the response surface is very smooth in the region of interest and can be approximated by polynomial chaos of relatively low order.

The comparison with analytical polynomial chaos shows that the accuracy of the approach is limited by the precision of the integration method chosen for the orthogonalisation of the polynomial base. An analytical development of the polynomial base showed potential for augmenting the precision of the results. Finally, a replacement for the least-squares fitting would be desirable, as convergence of this approach cannot be guaranteed. [94] resort to an intrusive Galerkin approach. Classical polynomial chaos relies on quadrature rules, but depends also in this aspect on the independence of its input variables. An integration strategy that takes into account the correlation between the variables would have to be employed for the aPC approach.

Appendix C

Bayesian study of material parameters using free vibration data

Throughout the thesis, it was difficult to find data on errors. This was also true for the uncertainty in the composite material. Sources could mostly be found for the angular uncertainty [114, 127], where the more optimistic value for the standard deviation was assumed. Concerning the thickness uncertainty, very little data on the standard deviations could be found, with some indications given in U.S. Department of Defense [128]. Based on this data, an educated guess was made for the distribution in the forward propagation study in chapter III.

In this appendix, it will be tried to add data to the Bayesian uncertainty quantification procedure specifically aimed at providing information on the composite material in question. This data will be sourced from the experimental data that on free vibration that is given in the same article as the flutter data used before [58]. Bayesian estimation of material parameters using free vibration has already been performed before, for example by Beck and Au [7],Gogu et al. [49] or [116], with very good results.

It is recalled that the configuration of interest are cantilevered rectangular composite plates with six layers [58], of which the geometry is recalled in Table C.1. The elasticity parameters of the base material AS1-3501 used in the same article are given along with the material density in Table C.2

Half-span $S[m]$	chord $c[m]$	Ply thickness $t[mm]$
0.3048	0.0762	0.134

Table C.1 – Geometric parameters for the plate studied.

$E_1[GPa]$	$E_2[GPa]$	$G_{12}[GPa]$	ν_{12}	Ply material density $\rho[kg/m^3]$
98	7.9	5.6	0.28	1520

Table C.2 – Engineering moduli and density for AS1-3501, the composite material used in [58].

From this material, Hollowell and Dugundji [58] construct six different layups, of which the stacking sequences, together with the stiffness properties in form of polar parameters, are repeated in Table C.3.

Scenario	Layup	$T_0^{\tilde{D}}[Nm]$	$T_1^{\tilde{D}}[Nm]$	$R_0^{\tilde{D}}[Nm]$	$R_1^{\tilde{D}}[Nm]$	$\Phi_0^{\tilde{D}}$	$\Phi_1^{\tilde{D}}$
A	$[0_2/90]_S$	0.674	0.601	0.432	0.455	0	0
B	$[\mp 45/0]_S$	0.674	0.601	0.400	0.219	$-\frac{\pi}{4}$	-0.744
C	$[-45_2/0]_S$	0.674	0.601	0.400	0.473	$-\frac{\pi}{4}$	-0.766
D	$[+45_2/0]_S$	0.674	0.601	0.400	0.473	$\frac{\pi}{4}$	0.766
E	$[-30_2/0]_S$	0.674	0.601	0.408	0.482	-0.515	-0.507
F	$[+30_2/0]_S$	0.674	0.601	0.408	0.482	0.515	0.507

Table C.3 – Layups of [58] and the corresponding polar parameters.

For validation purposes and to have a first idea of the results, a deterministic free vibration study is performed using the framework given in chapter II. To conform to the requirements of the aerodynamic methods, the study is performed with the number of chordwise modes (parallel to the clamping) restricted to $n_y = 2$, while a $n_x = 8$ modes are used in the spanwise direction. The results of this study are presented in Table C.4). It has to be noted that configurations C and D behave in the same way due to symmetry. The same holds for layups E and F.

Case	Layup	$\omega_1[rad/s]$	$\omega_2[rad/s]$	$\omega_3[rad/s]$
A	$[0_2/90]_S$	69.74 (69.54)	263.89 (248.76)	433.54 (435.80)
B	$[\mp 45/0]_S$	38.33 (40.48)	238.76 (252.44)	483.81 (461.54)
C	$[-45_2/0]_S$	30.16 (30.88)	188.50 (190.77)	320.44 (463.15)
D	$[+45_2/0]_S$	30.16 (30.88)	188.50 (190.77)	320.44 (463.15)
E	$[-30_2/0]_S$	37.70 (39.90)	226.19 (238.34)	364.42 (441.06)
F	$[+30_2/0]_S$	37.70 (39.90)	226.19 (238.34)	364.42 (441.06)

Table C.4 – Free vibration experimental results from [58]. Numerical results using eight modes in span-wise and two modes in chord-wise direction given in parentheses. Note the changed signs, which are due to the z axis pointing downwards in the framework of this work.

The results show that the frequencies for the third mode for configurations C-F are overestimated. To get reasonable calibration results, only the first two modes will be used.

First, the assumed measurement error has to be determined. To this end, the evidence method is used and the integrated likelihood is maximised. Hollowell and Dugundji [58]

in his original article gives the values with a precision of $c_{scale} = 0.1[Hz]$ for the first mode and $c_{scale} = 1[Hz]$ for the following modes. Moreover, it is assumed that the experimental error can be determined with a constant scale with respect to the scale that the results are given $\sigma = c_\sigma \cdot c_{scale}$. The logs of the integrated likelihoods are shown in Figure C.1

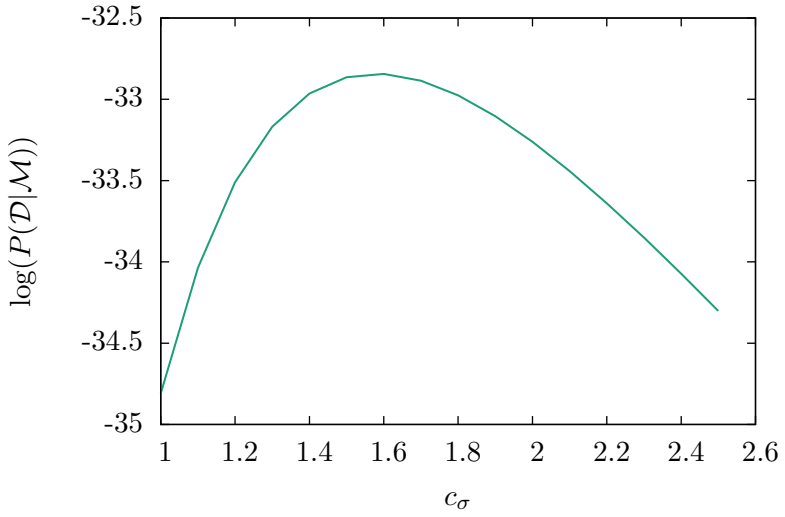

Fig. C.1 *Log likelihoods of assumed values for the experimental error, expressed as a factor for the scale with which the results are given. The maximum is at* 1.6

The evidence method analysis reveals that the maximum is obtained at 1.6 times the minimum scale in the article [58]. For practical reasons, a value of c_σ of $c_\sigma = 1.5$ is adopted in the following. Using this precision parameter, posterior distributions for the polar parameters are obtained.

Model calibrated	Free vibration
Calibrated parameters	$T_0^{\tilde{D}}, T_1^{\tilde{D}}, R_0^{\tilde{D}}, R_1^{\tilde{D}}, \Phi_0^{\tilde{D}}, \Phi_1^{\tilde{D}}$
Hyperparameters	$\sigma_{\omega_1} = 0.15 \cdot 2\pi$, $\sigma_{\omega_2} = 1.5 \cdot 2\pi$
Data used	[58], scenarios A,B,C,D,E,F (free vibration problem) (Table V.3)

Table C.5 – Summary of the data used and the calibrated parameters for the free vibration study on the first two modes.

The results are given in Figures C.2- C.11. Other than in the test case where only data from the flutter experiments are used, an important gain in information can be noted as the distributions generally differ much from the priors. Nevertheless, the shapes of the distributions are globally confirmed. It can be stated that the estimates on the uncertainty were too pessimistic. The uncertainty after calibration is considerably reduced in most cases. However, the maxima of the distributions being shifted to the left in all the modules and thus being below the nominal value given by [58] indicate that the materials may originally be estimated too stiff. This could either be caused by the layers being thinner than given in the original article [58] or a deviation in the stiffness of the base layer material. In the following, specifics will be detailed for each scenario.

The posteriors for scenario A are given in Figure C.2. As described before, the distributions for the moduli shift down and get much narrower than assumed in chapter III. However, the distributions for the polar angles get wider. This could either come from the angular uncertainty contained in the layup or indicate an error in the clamping for the experiment. However, the angular deviations remain small.

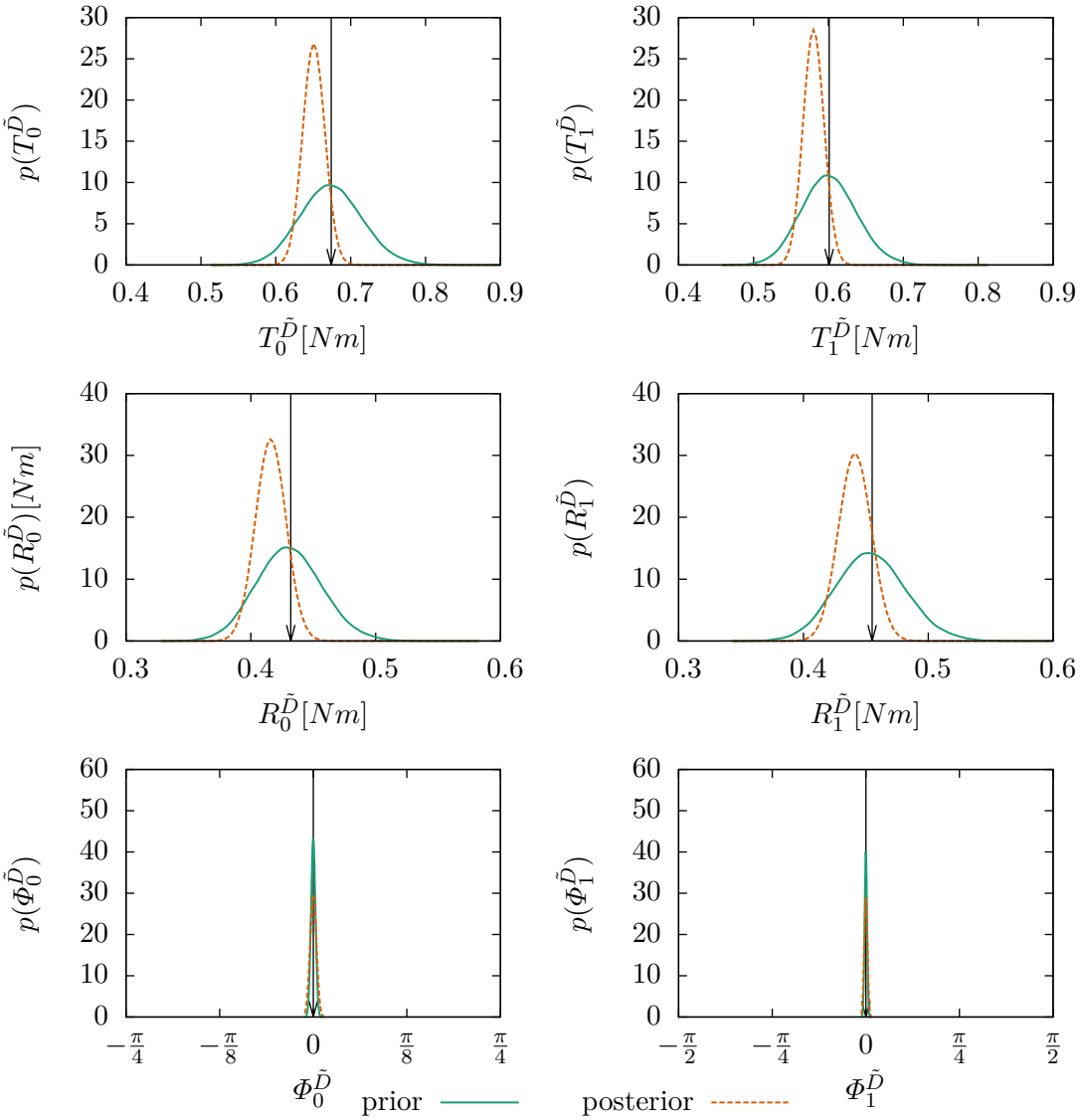

Fig. C.2 *Priors and posteriors obtained using free vibration data from [58] for scenario A as given in Table V.3. The nominal values are indicated by the vertical arrow.*

The corresponding frequency distributions are given in Figure C.3. The figure clearly shows how the frequencies are narrowed down and the uncertainty significantly reduced. The calculation for the first mode matches the experimental value quite well, while the value for the second mode is calibrated to a value significantly below.

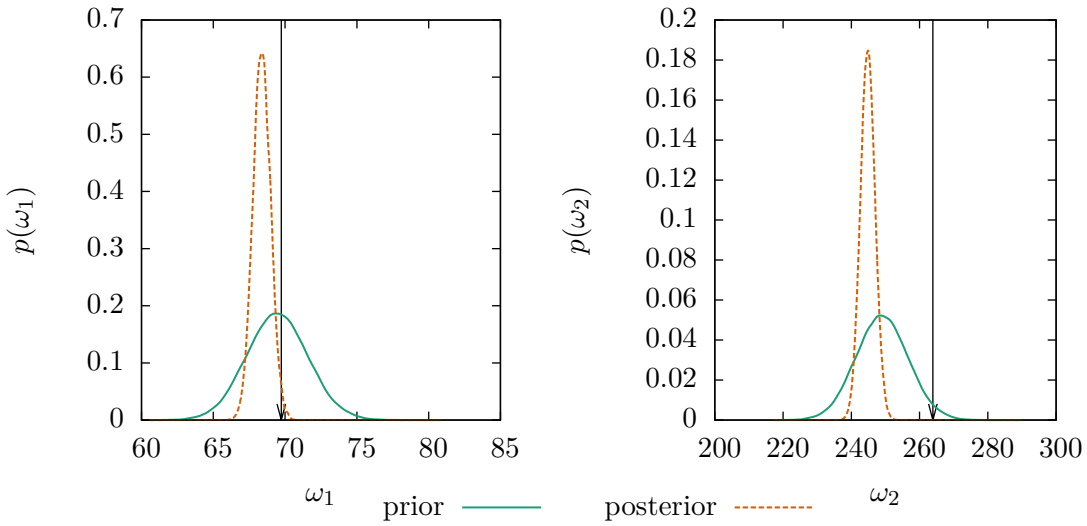

Fig. C.3 *Propagation of prior and posterior distribution for the first two modes using free vibration data from [58] for scenario A as given in Table V.3. The nominal experimental frequency values are indicated by the arrow.*

Scenario B shows essentially the same picture, as can be seen in Figure C.4. Polar parameter $R_0^{\tilde{D}}$, of which the distribution changes only slightly, represents the only exception. A reason for this could be that the mode does not involve much of a $R_1^{\tilde{D}}$-type stiffness. Moreover, the posterior distributions of the polar angles can be found to be slightly off-center, with the offset being oriented in the same direction. It has also to be noted that the uncertainty in $\Phi_0^{\tilde{D}}$ is significantly reduced, while the $\Phi_1^{\tilde{D}}$ distribution does not show such a change. However, polar material parameter $\Phi_0^{\tilde{D}}$ had a much higher coefficient of variation before the calibration, leaving much space for an information gain, while $\Phi_1^{\tilde{D}}$ was less uncertain.

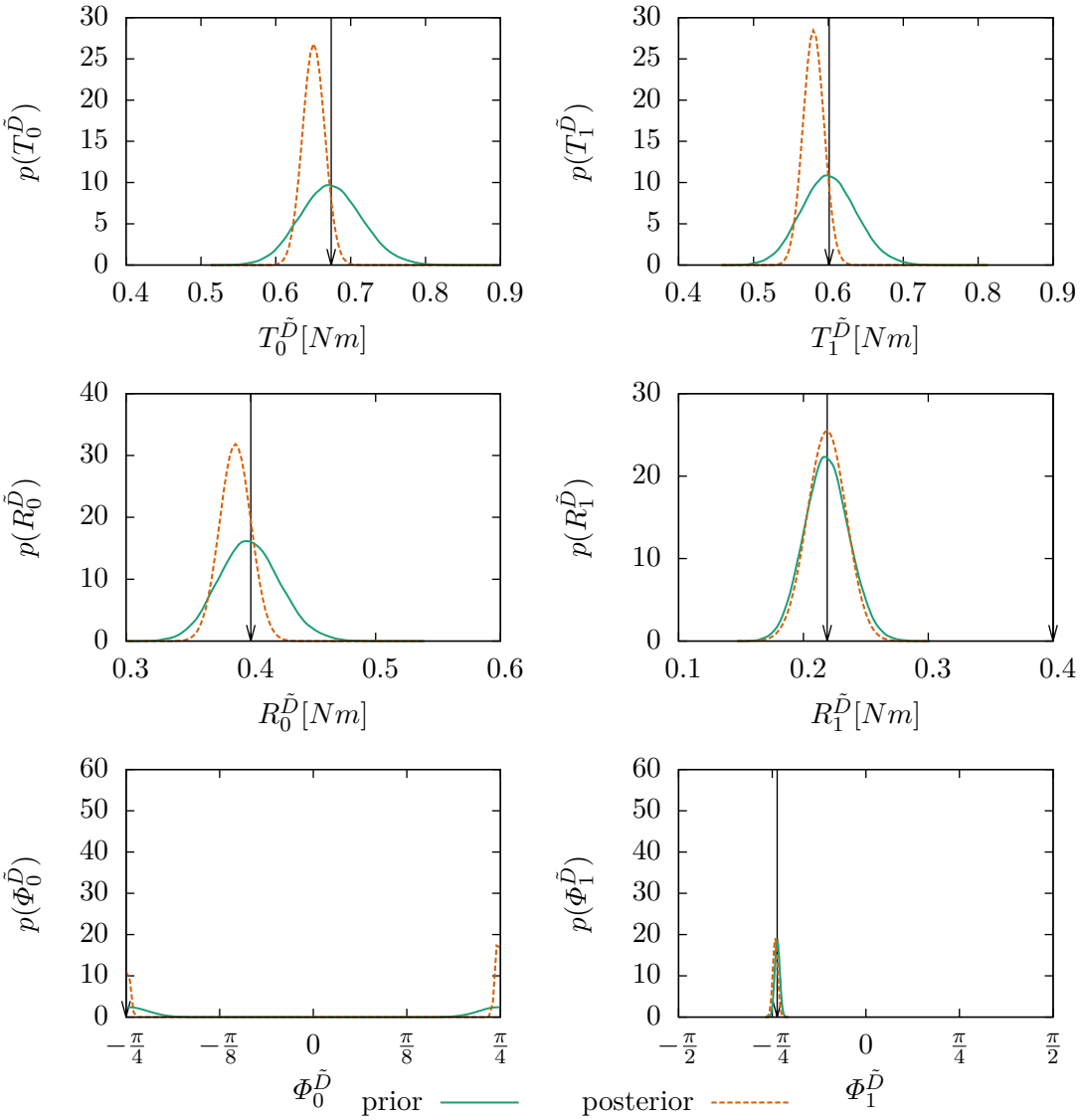

Fig. C.4 *Priors and posteriors obtained using free vibration data from [58] for scenario B as given in Table V.3*

The corresponding frequency distributions for the first two modes are depicted in Figure C.5. In this case, the calibration of the material parameters leads to a clear improvement for the frequency results in both of the first modes, with the probability density maximum shifting towards the experimental values. Again, the uncertainty is significantly reduced.

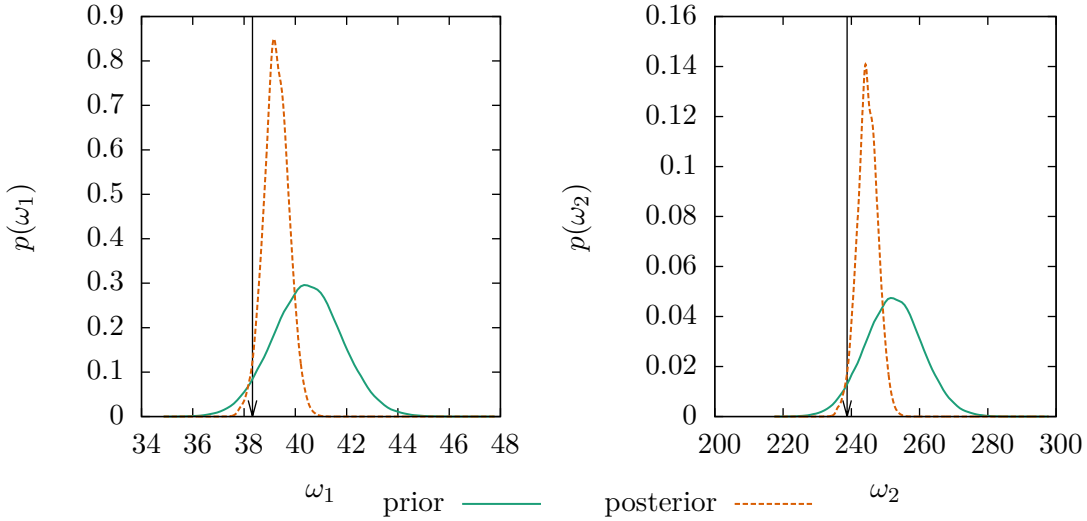

Fig. C.5 *Propagation of prior and posterior distribution for the first two modes using free vibration data from [58] for scenario B as given in Table V.3. The nominal experimental frequency values are indicated by the arrow.*

Scenarios C and D, of which the calibration results are shown in Figure C.6 and Figure C.7, can be evaluated together, as the configurations are just mirrored. Again, the moduli are observed to shift down, but also being narrowed down. Other than in the B configuration, all modules benefit from calibration. Another difference can be observed in the polar angles, where the distributions seem to remain centered. Finally, the uncertainty in the $\Phi_1^{\tilde{D}}$ parameter gets stronger, which is also different from the previous case and the behaviour of its sister parameter $\Phi_0^{\tilde{D}}$, but similar to the behaviour of its counterparts in A, E and F.

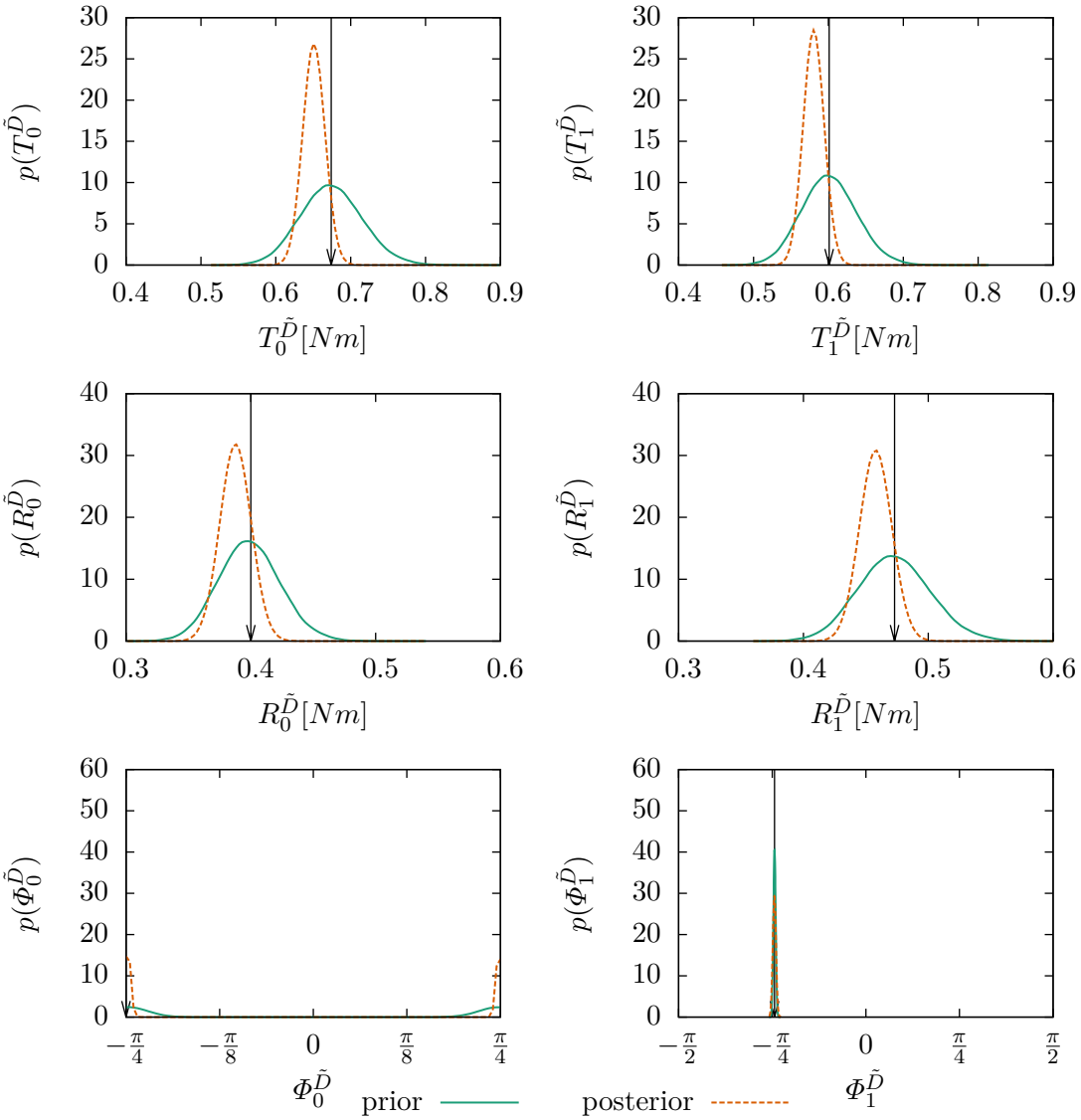

Fig. C.6 *Priors and posteriors obtained using free vibration data from [58] for scenario C as given in Table V.3*

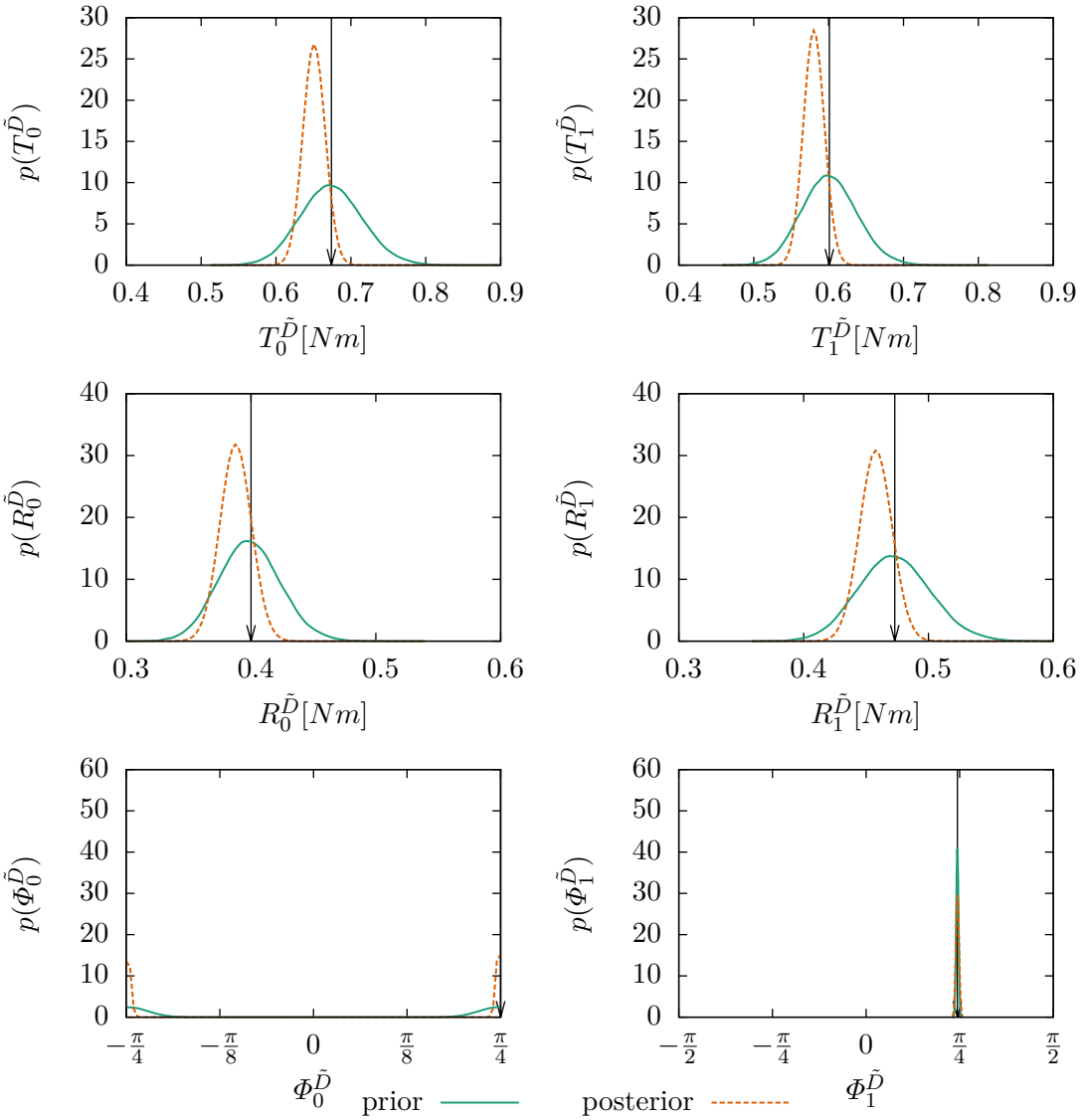

Fig. C.7 *Priors and posteriors obtained using free vibration data from [58] for scenario D as given in Table V.3*

Figures C.8 and C.9 show the corresponding frequency distributions for the first two modes. The uncertainty is again significantly reduced, and the frequency distributions align with the experimental values. In case of the first mode, this works better than in case of the second mode, where the maximum probability density value is still very close to the experimental value.

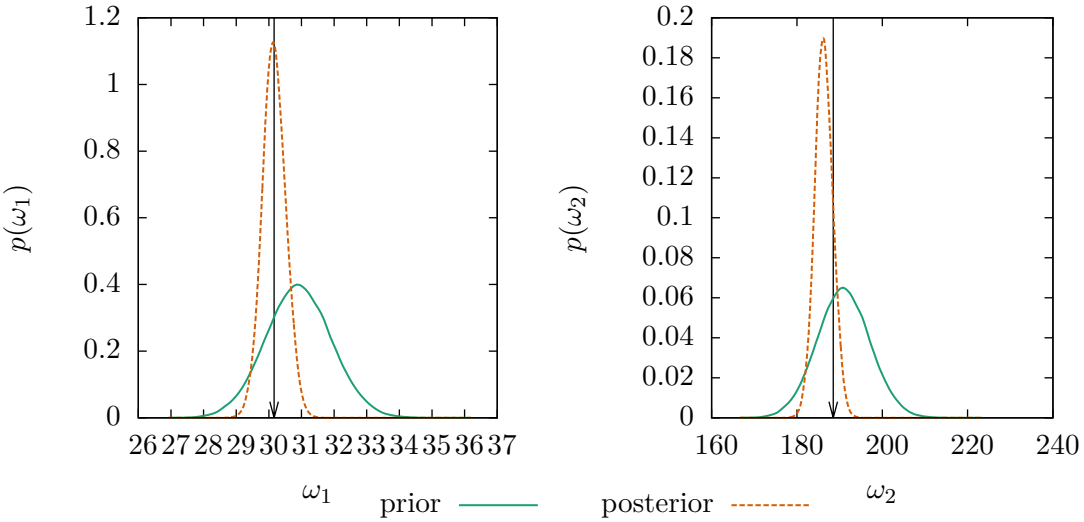

Fig. C.8 *Propagation of prior and posterior distribution for the first two modes using free vibration data from [58] for scenario C as given in Table V.3. The nominal experimental frequency values are indicated by the arrow.*

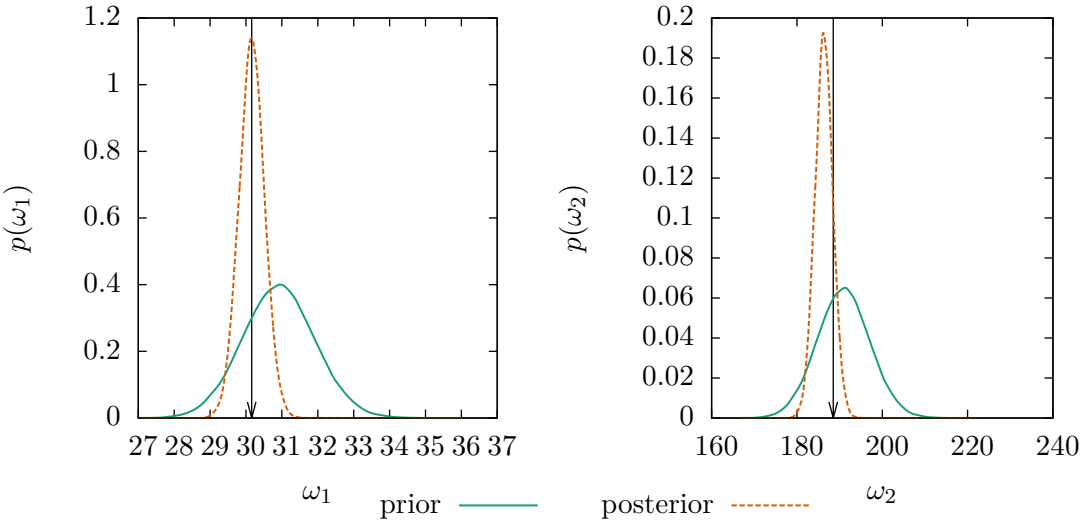

Fig. C.9 *Propagation of prior and posterior distribution for the first two modes using free vibration data from [58] for scenario D as given in Table V.3. The nominal experimental frequency values are indicated by the arrow.*

Finally, scenarios E and F can be evaluated together as C and D were, because again, the layup sequence is just flipped from one example to the other. Their calibration results are shown in Figure C.10 and Figure C.11. As before, uncertainty in the modulus values is reduced and the distribution curves are shifted to the left, indicating that the material is less stiff than nominally given. The angles are slightly more uncertain than expected *a priori*. Also, a slight offset can be remarked, which again goes into the same direction for both angles, but goes to the opposite direction from scenario B.

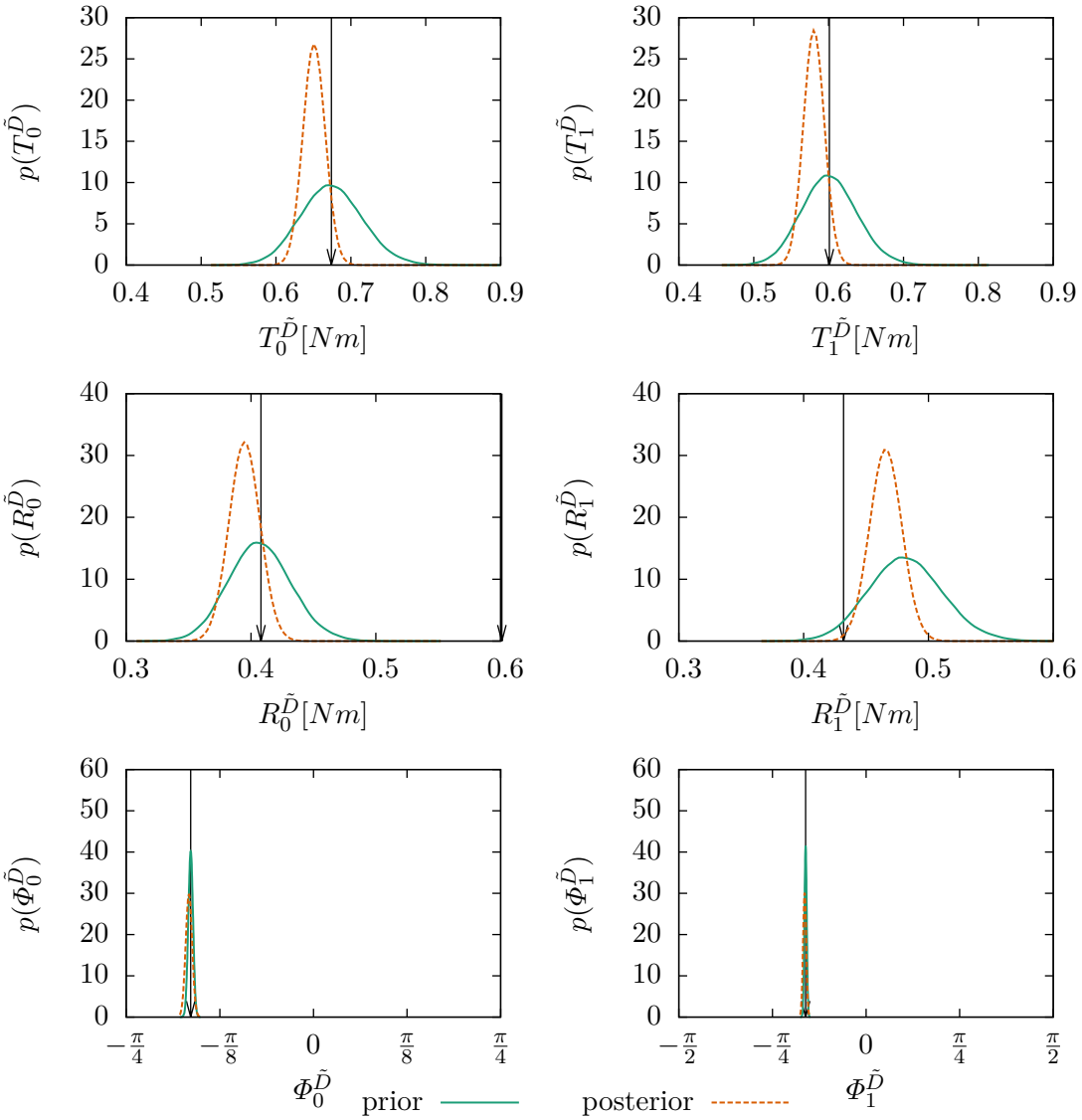

Fig. C.10 *Priors and posteriors obtained using free vibration data from [58] for scenario E as given in Table V.3*

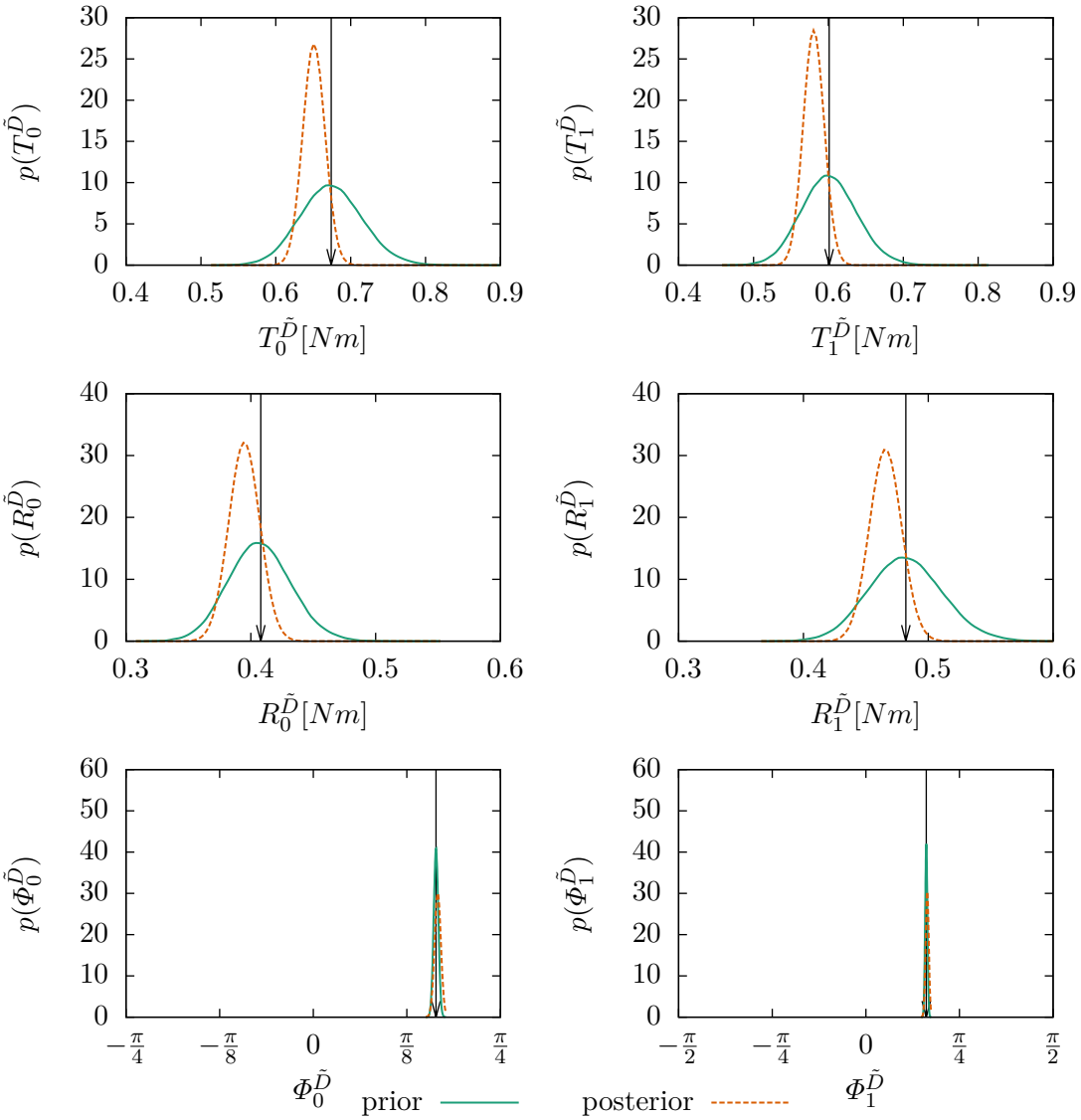

Fig. C.11 *Priors and posteriors obtained using free vibration data from [58] for scenario F as given in Table V.3*

The corresponding frequency distributions for the first two modes are shown in Figure C.12 and C.13. Again, the uncertainty in the frequencies is narrowed down, and both distributions adjust to the experimental values. However, other than in the previous example, in this case, they fail to exactly hit the experimental value. However, the probability density maxima are very close to the experimental value.

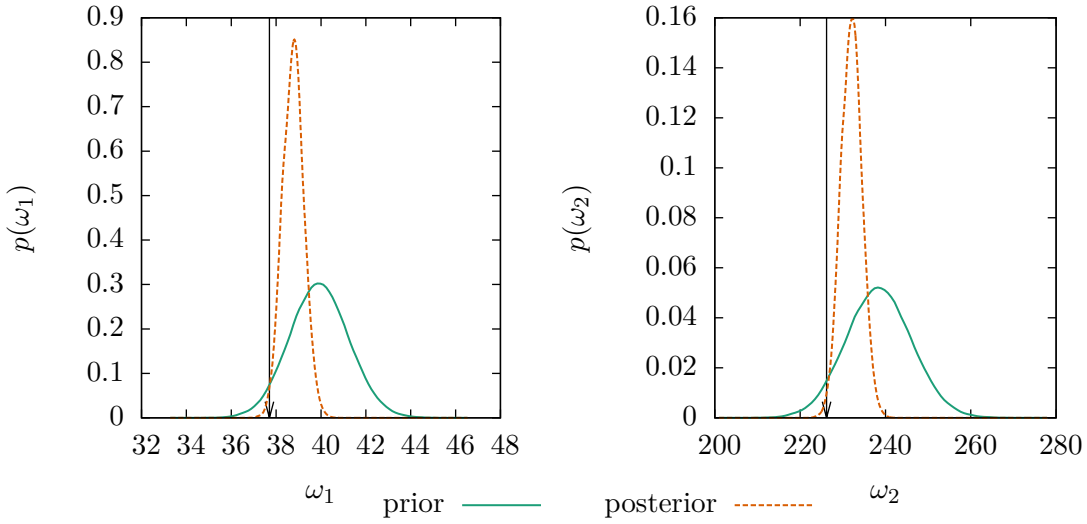

Fig. C.12 *Propagation of prior and posterior distribution for the first two modes using free vibration data from [58] for scenario E as given in Table V.3. The nominal experimental frequency values are indicated by the arrow.*

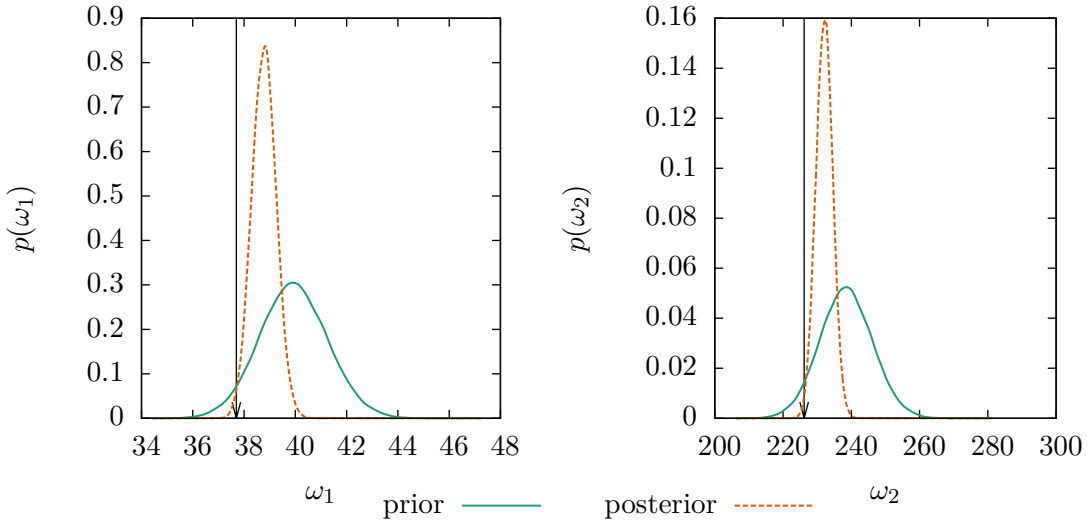

Fig. C.13 *Propagation of prior and posterior distribution for the first two modes using free vibration data from [58] for scenario F as given in Table V.3. The nominal experimental frequency values are indicated by the arrow.*

In this chapter, it could be shown that the guess for the distributions of the error due to manufacturing in the composite material was too pessimistic. Standard deviations of the polar stiffness parameters could be significantly reduced, which means that the amount of information contributed by the free vibration experiments is important. Furthermore, it could be shown that the materials are very likely less stiff than given in Hollowell and Dugundji [58].

The precision of the study could be further augmented by using more modes, notably in the chordwise direction of the plates. This was avoided to be consistent with the model used for flutter analysis in the main part of the thesis. Alternatively, a higher-fidelity finite element model could also be used in future work.

Bibliography

[1] F. Afonso, J. Vale, É. Oliveira, F. Lau, and A. Suleman. A review on non-linear aeroelasticity of high aspect-ratio wings. *Progress in Aerospace Sciences*, 89(Supplement C):40–57, February 2017. ISSN 0376-0421. doi: 10.1016/j.paerosci.2016.12.004. URL http://www.sciencedirect.com/science/article/pii/S037604211630077X. 4

[2] E. Albano and W. P. Rodden. A doublet-lattice method for calculating lift distributions on oscillating surfaces in subsonic flows. *AIAA Journal*, 7(2):279–285, February 1969. ISSN 0001-1452, 1533-385X. doi: 10.2514/3.5086. URL http://arc.aiaa.org/doi/abs/10.2514/3.5086. 3

[3] M. S. Anderson and H. L. Bohon. Role of boundary conditions on flutter of orthotropic panels. *AIAA Journal*, 4(7):1241–1248, July 1966. ISSN 0001-1452, 1533-385X. doi: 10.2514/3.3655. URL http://arc.aiaa.org/doi/abs/10.2514/3.3655. 3

[4] J.E. Ashton and M.E. Waddoups. Analysis of Anisotropic Plates. *Journal of Composite Materials*, 3(1):148–165, January 1969. ISSN 0021-9983. doi: 10.1177/002199836900300111. URL http://jcm.sagepub.com/cgi/doi/10.1177/002199836900300111. 4, 19, 137, 138

[5] A. Attaran, D.L. Majid, S. Basri, A.S. Mohd Rafie, and E.J. Abdullah. Structural optimization of an aeroelastically tailored composite flat plate made of woven fiberglass/epoxy. *Aerospace Science and Technology*, 15(5):393–401, July 2011. ISSN 12709638. doi: 10.1016/j.ast.2010.09.005. URL http://linkinghub.elsevier.com/retrieve/pii/S127096381000129X. 3

[6] D. Barber. *Bayesian reasoning and machine learning*. Cambridge Univ. Press, Cambridge, 2012. ISBN 978-0-521-51814-7. 85

[7] J. L. Beck and S. K. Au. Bayesian updating of structural models and reliability using Markov chain Monte Carlo simulation. *Journal of engineering mechanics*, 128 (4):380–391, 2002. 6, 159

[8] J. L. Beck and L. S. Katafygiotis. Updating of a Model and its Uncertainties Utilizing Dynamic Test Data. In P. D. Spanos and C. A. Brebbia, editors, *Computational Stochastic Mechanics*, pages 125–136. Springer Netherlands, Dordrecht, 1991. ISBN 978-1-85166-698-0 978-94-011-3692-1. URL http://www.springerlink.com/index/10.1007/978-94-011-3692-1_12. DOI: 10.1007/978-94-011-3692-1_12. 6

[9] J. L. Beck and L. S. Katafygiotis. Updating Models and Their Uncertainties. I: Bayesian Statistical Framework. *Journal of Engineering Mechanics*, 124(4):455–461, April 1998. ISSN 0733-9399, 1943-7889. doi: 10.1061/(ASCE)0733-9399(1998)124:4(455). URL http://ascelibrary.org/doi/10.1061/%28ASCE%290733-9399%281998%29124%3A4%28455%29. 78, 79, 82

[10] J.L. Beck and S.K. Au. Updating robust reliability using Markov chain simulation. In *Proceedings of the International Conference on Monte Carlo Simulation*, pages 499–440. Balkema, 2000. 6

[11] S. M. Belotserkovskii. Study of the Unsteady Aerodynamics of Lifting Surfaces Using the Computer. *Annual Review of Fluid Mechanics*, 9(1):469–494, January 1977. ISSN 0066-4189, 1545-4479. doi: 10.1146/annurev.fl.09.010177.002345. URL http://www.annualreviews.org/doi/10.1146/annurev.fl.09.010177.002345. 3

[12] R. M. Bennett, J. T. Batina, and H. J. Cunningham. Wing-flutter calculations with the CAP-TSD unsteady transonic small-disturbance program. *Journal of Aircraft*, 26(9):876–882, September 1989. ISSN 0021-8669, 1533-3868. doi: 10.2514/3.45854. URL http://arc.aiaa.org/doi/10.2514/3.45854. 3

[13] P. Beran, B. Stanford, and C. Schrock. Uncertainty Quantification in Aeroelasticity. *Annual Review of Fluid Mechanics*, 49(1):361–386, January 2017. ISSN 0066-4189, 1545-4479. doi: 10.1146/annurev-fluid-122414-034441. URL http://www.annualreviews.org/doi/10.1146/annurev-fluid-122414-034441. 2, 4, 6, 11

[14] A. Birolleau, G. Poëtte, and D. Lucor. Adaptive Bayesian Inference for Discontinuous Inverse Problems, Application to Hyperbolic Conservation Laws. *Communications in Computational Physics*, 16(01):1–34, 2014. ISSN 1991-7120. doi: 10.4208/cicp.240113.071113a. URL http://journals.cambridge.org/article_S1815240600005442. 6, 136

[15] Raymond L Bisplinghoff and Holt Ashley. *Aeroelasticity*. Addison-Wesley, Cambridge, Mass, 1955. 1, 10

[16] G. Blatman and B. Sudret. Sparse polynomial chaos expansions and adaptive stochastic finite elements using a regression approach. *Comptes Rendus Mécanique*, 336(6):518–523, June 2008. ISSN 16310721. doi: 10.1016/j.crme.2008.02.013. URL http://linkinghub.elsevier.com/retrieve/pii/S1631072108000582. 5

[17] M. T. Bordogna, T. Macquart, D. Bettebghor, and R. De Breuker. Aeroelastic Optimization of Variable Stiffness Composite Wing with Blending Constraints. In *17th AIAA/ISSMO Multidisciplinary Analysis and Optimization Conference*. American Institute of Aeronautics and Astronautics, June 2016. ISBN 978-1-62410-439-8. doi: 10.2514/6.2016-4122. URL http://arc.aiaa.org/doi/10.2514/6.2016-4122. 3

[18] A. S. Boyd, R. T. Murphy, C. Gurney, G. J. Minetty, and W. Gillilland. Aircraft accident report BRANIFF AIRWAYS, T,le., LOCKHEED SLECTRA, N 9705c, BUFFALO, TEXAS, SEPTEMBER 29, 1959. Technical report, Civil Aeronautics Board, May 1961. 2

[19] A. S. Boyd, R. T. Murphy, C. Gurney, G. J. Minetty, and W. Gillilland. Aircraft accident report NORTHWEST AIRLINES LOCKHEED ELECTRA, N 121us, NEAR CANNELTON, INDIANA, MARCH 17, 1960. Technical report, Civil Aeronautics Board, April 1961. 2

[20] S. L. Brunton and C. W. Rowley. Empirical state-space representations for Theodorsen's lift model. *Journal of Fluids and Structures*, 38:174–186, April 2013. ISSN 08899746. doi: 10.1016/j.jfluidstructs.2012.10.005. URL http://linkinghub.elsevier.com/retrieve/pii/S0889974612002010. xii, 3, 7, 14, 80, 82, 83

[21] T. Butler, J. D. Jakeman, and T. Wildey. A Consistent Bayesian Formulation for Stochastic Inverse Problems Based on Push-forward Measures. *arXiv:1704.00680 [math, stat]*, April 2017. arXiv: 1704.00680. 78, 82, 102

[22] S. H. Cheung and J. L. Beck. Bayesian Model Updating Using Hybrid Monte Carlo Simulation with Application to Structural Dynamic Models with Many Uncertain Parameters. *Journal of Engineering Mechanics*, 135(4):243–255, April 2009. ISSN 0733-9399, 1943-7889. doi: 10.1061/(ASCE)0733-9399(2009)135:4(243). URL http://ascelibrary.org/doi/10.1061/%28ASCE%290733-9399%282009%29135%3A4%28243%29. 6

[23] S. H. Cheung, T. A. Oliver, E. E. Prudencio, S. Prudhomme, and R. D. Moser. Bayesian uncertainty analysis with applications to turbulence modeling. *Reliability Engineering & System Safety*, 96(9):1137–1149, September 2011. ISSN 09518320. doi: 10.1016/j.ress.2010.09.013. URL http://linkinghub.elsevier.com/retrieve/pii/S0951832011000664. 6, 77, 78, 79, 96

[24] J. D. Collins, G. C; Hart, T. K. Haselman, and B Kennedy. Statistical Identification of Structures. *AIAA Journal*, 12(2):185–190, February 1974. ISSN 0001-1452, 1533-385X. doi: 10.2514/3.49190. URL http://arc.aiaa.org/doi/abs/10.2514/3.49190. 6

[25] P. M. Congedo, A. Cortesi, and G. El Jannoun. Kriging-sparse Polynomial Dimensional Decomposition surrogate model with adaptive refinement. Research Report RR-9098, INRIA Bordeaux, équipe CARDAMOM, August 2017. URL https://hal.inria.fr/hal-01610195. 6

[26] P.M. Congedo, C. Corre, and J.-M. Martinez. Shape optimization of an airfoil in a BZT flow with multiple-source uncertainties. *Computer Methods in Applied Mechanics and Engineering*, 200(1-4):216–232, January 2011. ISSN 00457825. doi: 10.1016/j.cma.2010.08.006. URL http://linkinghub.elsevier.com/retrieve/pii/S0045782510002392. 5

[27] P.M. Congedo, P. Colonna, C. Corre, J.A.S. Witteveen, and G. Iaccarino. Backward uncertainty propagation method in flow problems: Application to the prediction of rarefaction shock waves. *Computer Methods in Applied Mechanics and Engineering*, 213-216:314–326, March 2012. ISSN 00457825. doi: 10.1016/j.cma.2011.12.009. URL http://linkinghub.elsevier.com/retrieve/pii/S0045782511003884. 6

[28] F. di Donfrancesco. Flutter prediction of composite structures in subsonic flows using the Polar Method. Master's thesis, Arts et Métiers ParisTech, Paris, 2016. 107, 125

[29] A. Doostan and G. Iaccarino. A least-squares approximation of partial differential equations with high-dimensional random inputs. *Journal of Computational Physics*, 228(12):4332–4345, July 2009. ISSN 00219991. doi: 10.1016/j.jcp.2009.03.006. URL http://linkinghub.elsevier.com/retrieve/pii/S0021999109001144. 6, 67, 157

[30] A. Doostan, A. Validi, and G. Iaccarino. Non-intrusive low-rank separated approximation of high-dimensional stochastic models. *Computer Methods in Applied Mechanics and Engineering*, 263:42–55, August 2013. ISSN 00457825. doi: 10.1016/j.cma.2013.04.003. URL http://linkinghub.elsevier.com/retrieve/pii/S0045782513000935. 6

[31] E. H. Dowell. Flutter of infinitely long plates and shells. I - Plate. *AIAA Journal*, 4(8):1370–1377, August 1966. ISSN 0001-1452, 1533-385X. doi: 10.2514/3.3680. URL http://arc.aiaa.org/doi/abs/10.2514/3.3680. 3

[32] E. H. Dowell and H. M. Voss. Theoretical and experimental panel flutter studies in the Mach number range 1.0 to 5.0. *AIAA Journal*, 3(12):2292–2304, December 1965. ISSN 0001-1452, 1533-385X. doi: 10.2514/3.3359. URL http://arc.aiaa.org/doi/abs/10.2514/3.3359. 3

[33] R. Dwight and Z.-H. Han. Efficient Uncertainty Quantification Using Gradient-Enhanced Kriging. In *50th AIAA/ASME/ASCE/AHS/ASC Structures, Structural Dynamics, and Materials Conference*. American Institute of Aeronautics and Astronautics, May 2009. ISBN 978-1-60086-975-4. doi: 10.2514/6.2009-2276. URL http://arc.aiaa.org/doi/10.2514/6.2009-2276. 6

[34] W.N. Edeling, P. Cinnella, and R.P. Dwight. Predictive RANS simulations via Bayesian Model-Scenario Averaging. *Journal of Computational Physics*, 275:65–91, October 2014. ISSN 00219991. doi: 10.1016/j.jcp.2014.06.052. URL http://linkinghub.elsevier.com/retrieve/pii/S0021999114004707. 6, 97

[35] W.N. Edeling, P. Cinnella, R.P. Dwight, and H. Bijl. Bayesian estimates of parameter variability in the k–ϵ turbulence model. *Journal of Computational Physics*, 258:73–94, February 2014. ISSN 00219991. doi: 10.1016/j.jcp.2013.10.027. URL http://linkinghub.elsevier.com/retrieve/pii/S0021999113007031. 78

[36] W.N. Edeling, R.P. Dwight, and P. Cinnella. Simplex-stochastic collocation method with improved scalability. *Journal of Computational Physics*, 310:301–328, April 2016. ISSN 00219991. doi: 10.1016/j.jcp.2015.12.034. URL http://linkinghub.elsevier.com/retrieve/pii/S0021999115008530. 6

[37] M.S. Eldred, L.P. Swiler, and G. Tang. Mixed aleatory-epistemic uncertainty quantification with stochastic expansions and optimization-based interval estimation. *Reliability Engineering & System Safety*, 96(9):1092–1113, September 2011. ISSN

09518320. doi: 10.1016/j.ress.2010.11.010. URL http://linkinghub.elsevier.com/retrieve/pii/S0951832011000639. 7

[38] W. R. English. Aviation Accident Report DCA15ca117. Aviation Accident Report DCA15CA117, National Transportation Safety Board, November 2015. 2

[39] W. R. English. Aviation Accident Report DCA16ca197. Aviation Accident Report DCA16CA197, National Transportation Safety Board, December 2016. 2

[40] M. Ester, H.-P. Kriegel, J. Sander, and X. Xu. A density-based algorithm for discovering clusters in large spatial databases with noise. In *Proceedings of the Second International Conference on Knowledge Discovery and Data Mining*, volume 96, pages 226–231, 1996. 71

[41] Federal Aviation Administration. Aeroelastic Stability Substantiation of Transport Category Airplanes. Advisory Circular 25.629-1B, U.S. Department of Transportation, Federal Aviation Administration, Washington, D.C., October 2014. 2, 4

[42] Y.-C. Fung. *An introduction to the theory of aeroelasticity*. Dover, New York, 1969. ISBN 978-0-486-67871-9. 1, 11, 80

[43] I. E. Garrick. On some reciprocal relations in the theory of nonstationary flows. Technical Report 629, National Aeronautics and Space Administration, January 1938. URL http://ntrs.nasa.gov/search.jsp?R=19930091704. 14, 80, 83

[44] I. E. Garrick and W. H. Reed. Historical Development of Aircraft Flutter. *Journal of Aircraft*, 18(11):897–912, November 1981. ISSN 0021-8669, 1533-3868. doi: 10.2514/3.57579. URL http://arc.aiaa.org/doi/abs/10.2514/3.57579. 2

[45] G. Georgiou, A. Manan, and J.E. Cooper. Modeling composite wing aeroelastic behavior with uncertain damage severity and material properties. *Mechanical Systems and Signal Processing*, 32:32–43, October 2012. ISSN 08883270. doi: 10.1016/j.ymssp.2012.05.003. URL http://linkinghub.elsevier.com/retrieve/pii/S0888327012001872. 4

[46] P. Geuzaine, G. Brown, C. Harris, and C. Farhat. Aeroelastic Dynamic Analysis of a Full F-16 Configuration for Various Flight Conditions. *AIAA Journal*, 41(3):363–371, March 2003. ISSN 0001-1452, 1533-385X. doi: 10.2514/2.1975. URL http://arc.aiaa.org/doi/abs/10.2514/2.1975. 2

[47] R. Ghanem and P. D Spanos. *Stochastic finite elements: a spectral approach*. Springer-Verlag, New York, 1991. ISBN 0-387-97456-3 978-0-387-97456-9 3-540-97456-3 978-3-540-97456-7. 5, 6, 155

[48] C. Gogu, R. Haftka, R. Le Riche, and J. Molimard. Effect of approximation fidelity on vibration-based elastic constants identification. *Structural and Multidisciplinary Optimization*, 42(2):293–304, August 2010. ISSN 1615-147X, 1615-1488. doi: 10.1007/s00158-010-0493-y. URL http://link.springer.com/10.1007/s00158-010-0493-y. 6

[49] C. Gogu, R. Haftka, R. Le Riche, J. Molimard, and A. Vautrin. Introduction to the Bayesian Approach Applied to Elastic Constants Identification. *AIAA Journal*, 48

(5):893–903, May 2010. ISSN 0001-1452, 1533-385X. doi: 10.2514/1.40922. URL http://arc.aiaa.org/doi/10.2514/1.40922. 159

[50] C. Gogu, W. Yin, R. Haftka, P. Ifju, J. Molimard, R. Le Riche, and A. Vautrin. Bayesian Identification of Elastic Constants in Multi-Directional Laminate from Moiré Interferometry Displacement Fields. *Experimental Mechanics*, 53(4):635–648, April 2013. ISSN 0014-4851, 1741-2765. doi: 10.1007/s11340-012-9671-8. URL http://link.springer.com/10.1007/s11340-012-9671-8. 6, 102

[51] Martin Goland. The flutter of a uniform cantilever wing. *Journal of Applied Mechanics-Transactions of the Asme*, 12(4):A197–A208, 1945. 3

[52] G. P. Guruswamy. Unsteady aerodynamic and aeroelastic calculations for wings using Euler equations. *AIAA Journal*, 28(3):461–469, March 1990. ISSN 0001-1452, 1533-385X. doi: 10.2514/3.10415. URL http://arc.aiaa.org/doi/abs/10.2514/3.10415. 3

[53] Z. Gürdal, R. T. Haftka, and P. Hajela. *Design and optimization of laminated composite materials*. A Wiley-Interscience Publication. Wiley, New York, NY, 1999. ISBN 978-0-471-25276-4. 24

[54] G. J. Hancock. *An introduction to the flight dynamics of rigid aeroplanes*. Ellis Horwood series in mechanical engineering. Horwood, New York, 1. edition, 1986. ISBN 978-0-13-319450-0 978-0-13-319443-2. 11, 85

[55] D. H. Hodges and G. A. Pierce. *Introduction to structural dynamics and aeroelasticity*. Number 15 in Cambridge aerospace series. Cambridge University Press, Cambridge, [England] ; New York, 2002. ISBN 0-521-80698-4. iii, 1, 10, 12, 13, 14, 16, 17, 79, 80

[56] J. A. Hoeting, D. Madigan, A. E. Raftery, and C. T. Volinsky. Bayesian model averaging: A tutorial. *Statistical Science*, 14(4):382–417, November 1999. ISSN 0883-4237. doi: 10.1214/ss/1009212519. URL http://projecteuclid.org/euclid.ss/1009212519. 6, 78, 79, 94

[57] S. J. Hollowell. Aeroelastic Flutter and Divergence of Graphite/Epoxy Cantilevered Plates with Bending-Torsion Stiffness Coupling. Master's thesis, Massachusetts Institute of Technology, Cambridge, Massachusetts, USA, January 1981. 4, 24, 80, 107, 108

[58] S. J. Hollowell and J. Dugundji. Aeroelastic flutter and divergence of stiffness coupled, graphite/epoxy cantilevered plates. *Journal of Aircraft*, 21(1):69–76, January 1984. ISSN 0021-8669, 1533-3868. doi: 10.2514/3.48224. URL http://arc.aiaa.org/doi/abs/10.2514/3.48224. viii, ix, x, xi, xii, xiii, 8, 105, 106, 107, 108, 109, 110, 111, 112, 113, 114, 115, 117, 118, 120, 121, 122, 123, 124, 125, 126, 127, 128, 129, 130, 131, 159, 160, 161, 162, 163, 164, 165, 166, 167, 168, 169, 170, 171, 172

[59] S. C. Hora. Aleatory and epistemic uncertainty in probability elicitation with an example from hazardous waste management. *Reliability Engineering & System Safety*, 54(2-3):217–223, November 1996. ISSN 09518320. doi: 10.1016/

S0951-8320(96)00077-4. URL http://linkinghub.elsevier.com/retrieve/pii/S0951832096000774. 4

[60] S. S. Isukapalli. *UNCERTAINTY ANALYSIS OF TRANSPORT-TRANSFORMATION MODELS*. PhD thesis, Rutgers University, New Brunswick, NJ, January 1999. 5

[61] J. Jakeman, M. S. Eldred, and D. Xiu. Numerical approach for quantification of epistemic uncertainty. *Journal of Computational Physics*, 229(12):4648–4663, June 2010. ISSN 00219991. doi: 10.1016/j.jcp.2010.03.003. URL http://linkinghub.elsevier.com/retrieve/pii/S0021999110001130. 7, 114

[62] D.W. Jensen, E.F. Crawley, and J. Dugundji. Vibration of Cantilevered Graphite/Epoxy Plates With Bending-Torsion Coupling. *Journal of Reinforced Plastics and Composites*, 1(3):254–269, July 1982. ISSN 0731-6844. doi: 10.1177/073168448200100305. URL http://jrp.sagepub.com/cgi/doi/10.1177/073168448200100305. 24

[63] R. T Jones. Operational treatment of the nonuniform-lift theory in airplane dynamics. Technical Note 667, National Advisory Committee for Aeronautics, 1938. 80, 82

[64] W. P. Jones. Aerodynamic forces on wings in non-uniform motion, 1945. 80, 82, 83

[65] Pascal Joubert De La Motte. *Characteristic Time-Step Scheme for Transonic Flows and Optimum Aeroelastic Design of Wing with a Large Aspect Ratio*. Theses, Arts et Métiers ParisTech, April 2007. URL https://pastel.archives-ouvertes.fr/tel-00144844. 3

[66] Cédric Julien. *Conception Optimale de l'Anisotropie dans les Structures Stratifiées à Rigidité Variable par la Méthode Polaire-Génétique*. PhD thesis, Sorbonne Universités, Université Pierre et Marie Curie Paris 6/CNRS, UMR 7190, Paris, February 2010. 24, 26

[67] R. Kamakoti. *COMPUTATIONAL AEROELASTICITY USING A PRESSURE-BASED SOLVER*. PhD thesis, University of Florida, Gainesville, 2004. 3

[68] M. Karpel. *Design for active and passive flutter suppression and gust alleviation*. PhD thesis, Stanford University, Stanford, CA, November 1981. URL https://ntrs.nasa.gov/search.jsp?R=19820005274. Report/Patent Number: NASA-CR-3482. 3

[69] M. Kennedy and A. Gramfort. talkpython.fm episode 31: Machine Learning with Python and scikit-learn. https://talkpython.fm/episodes/show/31/machine-learning-with-python-and-scikit-learn, October 2015. Last retrieved on 20th of octobre, 2017. 102

[70] Armen Der Kiureghian and Ove Ditlevsen. Aleatory or epistemic? Does it matter? *Structural Safety*, 31(2):105–112, March 2009. ISSN 01674730. doi: 10.1016/j.strusafe.2008.06.020. URL http://linkinghub.elsevier.com/retrieve/pii/S0167473008000556. 4

[71] P. Konstadinopoulos, D. F. Thrasher, D. T. Mook, A. H. Nayfeh, and L. Watson. A vortex-lattice method for general, unsteady aerodynamics. *Journal of Aircraft*, 22 (1):43–49, January 1985. ISSN 0021-8669, 1533-3868. doi: 10.2514/3.45078. URL http://arc.aiaa.org/doi/10.2514/3.45078. 3

[72] A. Kotikalpudi, H. Pfifer, and G. J. Balas. Unsteady Aerodynamics Modeling for a Flexible Unmanned Air Vehicle. In *AIAA Atmospheric Flight Mechanics Conference*. American Institute of Aeronautics and Astronautics, June 2015. ISBN 978-1-62410-358-2. doi: 10.2514/6.2015-2854. URL http://arc.aiaa.org/doi/10.2514/6.2015-2854. 1, 3

[73] George C. Larson. How Things Work: Winglets, 2001. URL http://www.airspacemag.com/flight-today/how-things-work-winglets-2468375/. 2

[74] O.P. Le Maître, O.M. Knio, H.N. Najm, and R.G. Ghanem. Uncertainty propagation using Wiener–Haar expansions. *Journal of Computational Physics*, 197 (1):28–57, June 2004. ISSN 00219991. doi: 10.1016/j.jcp.2003.11.033. URL http://linkinghub.elsevier.com/retrieve/pii/S0021999103006181. 6

[75] J. Le Meitour, D. Lucor, and J.-C. Chassaing. Prediction of stochastic limit cycle oscillations using an adaptive Polynomial Chaos method. *Journal of Aeroelasticity and Structural Dynamics*, 2(1):1–20, 2010. ISSN 1974-5117. doi: 10.3293/asdj.2010.4. URL http://journals.aero.polimi.it/index.php/ASD/article/viewFile/4/Chassaing_asdj2010.pdf. 5, 67, 69

[76] E. E. Leamer. *Specification Searches: Ad Hoc Inference with Nonexperimental Data*. Wiley, 1978. ISBN 0471015202. 97

[77] E. Lebarbier and T. Mary-Huard. Le critère BIC : fondements théoriques et interprétation. Research Report RR-5315, INRIA, 2004. URL https://hal.inria.fr/inria-00070685. 97

[78] B.H.K. Lee, S.J. Price, and Y.S. Wong. Nonlinear aeroelastic analysis of airfoils: bifurcation and chaos. *Progress in Aerospace Sciences*, 35(3):205–334, April 1999. ISSN 03760421. doi: 10.1016/S0376-0421(98)00015-3. URL http://linkinghub.elsevier.com/retrieve/pii/S0376042198000153. 9

[79] Daniel Levin and Joseph Katz. Vortex-Lattice Method for the Calculation of the Nonsteady Separated Flow over Delta Wings. *Journal of Aircraft*, 18(12):1032–1037, December 1981. ISSN 0021-8669, 1533-3868. doi: 10.2514/3.57596. URL http://arc.aiaa.org/doi/10.2514/3.57596. 3

[80] J. Li and Y. Narita. Multi-objective design for aeroelastic flutter of laminated shallow shells under variable flow angles. *Composite Structures*, 111:530–539, May 2014. ISSN 02638223. doi: 10.1016/j.compstruct.2014.01.026. URL http://linkinghub.elsevier.com/retrieve/pii/S0263822314000397. 4

[81] J. H. C. Lisman and M. C. A. van Zuylen. Note on the generation of most probable frequency distributions. *Statistica Neerlandica*, 26(1):19–23, March 1972. ISSN 0039-0402, 1467-9574. doi: 10.1111/j.1467-9574.1972.tb00152.x. URL http://doi.wiley.com/10.1111/j.1467-9574.1972.tb00152.x. 83, 85

[82] D. Lucor. Introduction to Uncertainty Quantification in Computational Fluid Dynamics. Lecture Notes of NSE22 2012, held at Université Pierre et Marie Curie Paris 6, 2012. 67, 154, 155

[83] D. Lucor and G.E. Karniadakis. Stochastic flow-structure interactions. In *Computational Fluid and Solid Mechanics 2003*, pages 1426–1429. Elsevier, 2003. ISBN 978-0-08-044046-0. URL http://linkinghub.elsevier.com/retrieve/pii/B9780080440460503493. 5

[84] A. Manan and J.E. Cooper. Prediction of uncertain frequency response function bounds using polynomial chaos expansion. *Journal of Sound and Vibration*, 329 (16):3348–3358, August 2010. ISSN 0022460X. doi: 10.1016/j.jsv.2010.01.008. URL http://linkinghub.elsevier.com/retrieve/pii/S0022460X10000106. 5

[85] Y. M. Marzouk, H. N. Najm, and L. A. Rahn. Stochastic spectral methods for efficient Bayesian solution of inverse problems. *Journal of Computational Physics*, 224(2):560–586, June 2007. ISSN 00219991. doi: 10.1016/j.jcp.2006.10.010. URL http://linkinghub.elsevier.com/retrieve/pii/S0021999106004839. 6

[86] L. Mathelin and M. Y. Hussaini. A Stochastic Collocation Algorithm for Uncertainty Analysis. Technical report, National Aeronautics and Space Administration, February 2003. URL https://ntrs.nasa.gov/search.jsp?R=20030016674. 6

[87] D. R. Millman, P. I. King, and P. S. Beran. Airfoil Pitch-and-Plunge Bifurcation Behavior with Fourier Chaos Expansions. *Journal of Aircraft*, 42(2):376–384, March 2005. ISSN 0021-8669, 1533-3868. doi: 10.2514/1.5550. URL http://arc.aiaa.org/doi/10.2514/1.5550. 6

[88] M. D. Minich and C. C. Chamis. Analytical displacements and vibrations of cantilevered unsymmetric fiber composite laminates. In *Proceedings of the 16th Structural Dynamics, and Materials Conference, Structures, Structural Dynamics, and Materials and Co-located Conferences*, Denver, Colorado, January 1975. 19

[89] M. Montemurro, A. Vincenti, and P. Vannucci. Design of the elastic properties of laminates with a minimum number of plies. *Mechanics of Composite Materials*, 48(4):369–390, September 2012. ISSN 0191-5665, 1573-8922. doi: 10.1007/s11029-012-9284-4. URL http://link.springer.com/10.1007/s11029-012-9284-4. 26, 32

[90] M. Montemurro, A. Vincenti, and P. Vannucci. A Two-Level Procedure for the Global Optimum Design of Composite Modular Structures—Application to the Design of an Aircraft Wing: Part 2: Numerical Aspects and Examples. *Journal of Optimization Theory and Applications*, 155(1):24–53, October 2012. ISSN 0022-3239, 1573-2878. doi: 10.1007/s10957-012-0070-1. URL http://link.springer.com/10.1007/s10957-012-0070-1. 32

[91] D. J. Mourey. Study of the feasibility aspects of flight testing an aeroelastically tailored forward swept research wing on a BQM-34f drone vehicle. Contractor Report 159149, National Aeronautics and Space Administration, September 1979. URL https://ntrs.nasa.gov/search.jsp?R=19800001956. 4

[92] J. Murua, R. Palacios, and J. M. R. Graham. Applications of the unsteady vortex-lattice method in aircraft aeroelasticity and flight dynamics. *Progress in Aerospace Sciences*, 55:46–72, November 2012. ISSN 03760421. doi: 10.1016/j.paerosci.2012.06.001. URL http://linkinghub.elsevier.com/retrieve/pii/S0376042112000620. 3

[93] M. I. Navarro Jimenez, J. A. S. Witteveen, and J. G. Blom. STOCHASTIC COLLOCATION FOR CORRELATED INPUTS. In *Proceedings of the 1st International Conference on Uncertainty Quantification in Computational Sciences and Engineering (UNCECOMP) 2015*, pages 218–236. Institute of Structural Analysis and Antiseismic Research School of Civil Engineering National Technical University of Athens (NTUA) Greece, 2015. ISBN 978-960-99994-9-6. doi: 10.7712/120215.4266.544. URL http://www.eccomasproceedia.org/conferences/thematic-conferences/uncecomp-2015/4266. 6, 136, 151

[94] Navarro Jimenez, M.I., Witteveen, J.A.S., and Blom, J.G. Polynomial Chaos Expansion for general multivariate distributions with correlated variables. Technical report, Centrum Wiskunde & Informatica, 2014. URL https://repository.cwi.nl/noauth/search/fullrecord.php?publnr=22484. x, 5, 68, 149, 152, 154, 155, 157, 158

[95] A. Nayfeh, B. Hammad, and M. Hajj. Discretization effects on flutter aspects and control of wing/store configurations. *Journal of Vibration and Control*, 18(7):1043–1055, June 2012. ISSN 1077-5463, 1741-2986. doi: 10.1177/1077546311408468. URL http://jvc.sagepub.com/cgi/doi/10.1177/1077546311408468. 3

[96] C. Nitschke, J Maruani, A. Vincenti, D. Lucor, and J.-C. Chassaing. UNCERTAINTY QUANTIFICATION IN AEROELASTIC RESPONSE OF AN IDEALIZED COMPOSITE WING. In *International Forum on Aeroelasticity and Structural Dynamics*, volume 2, pages 970–983, Moscow, Russia, 2016. Central Aerohydrodynamic Institute. Presentation held on July 1st, 2015 at IFASD, St. Petersburg, Russia. 7, 24

[97] C.T. Nitschke, P. Cinnella, D. Lucor, and J.-C. Chassaing. Model-form and predictive uncertainty quantification in linear aeroelasticity. *Journal of Fluids and Structures*, 73:137–161, August 2017. ISSN 08899746. doi: 10.1016/j.jfluidstructs.2017.05.007. URL http://linkinghub.elsevier.com/retrieve/pii/S0889974616300809. vii, 82, 90, 96, 97, 102

[98] F. Nobile, R. Tempone, and C. G. Webster. A Sparse Grid Stochastic Collocation Method for Partial Differential Equations with Random Input Data. *SIAM Journal on Numerical Analysis*, 46(5):2309–2345, January 2008. ISSN 0036-1429, 1095-7170. doi: 10.1137/060663660. URL http://epubs.siam.org/doi/10.1137/060663660. 6

[99] A. K. Noor. Free vibrations of multilayered composite plates. *AIAA Journal*, 11 (7):1038–1039, July 1973. ISSN 0001-1452, 1533-385X. doi: 10.2514/3.6868. URL http://arc.aiaa.org/doi/abs/10.2514/3.6868. 4

[100] T. Oden, R. Moser, and O. Ghattas. Computer predictions with quantified uncertainty, part I. *SIAM News*, 43(9):1–3, 2010. 7

[101] S. Oladyshkin and W. Nowak. Data-driven uncertainty quantification using the arbitrary polynomial chaos expansion. *Reliability Engineering & System Safety*, 106:179–190, October 2012. ISSN 09518320. doi: 10.1016/j.ress.2012.05.002. URL http://linkinghub.elsevier.com/retrieve/pii/S0951832012000853. 68

[102] G.M. Oosterhout, P.J.M. van der Hoogt, and R.M.E.J. Spiering. Accurate calculation methods for natural frequencies of plates with special attention to the higher modes. *Journal of Sound and Vibration*, 183(1):33–47, May 1995. ISSN 0022460X. doi: 10.1006/jsvi.1995.0237. URL http://linkinghub.elsevier.com/retrieve/pii/S0022460X85702374. 19

[103] Jon Ostrower. Boeing locks out 747-8 tail fuel tanks on flutter concerns, January 2012. URL https://www.flightglobal.com/news/articles/boeing-locks-out-747-8-tail-fuel-tanks-on-flutter-concerns-367148/. 2

[104] F. Pedregosa, G. Varoquaux, A. Gramfort, V. Michel, B. Thirion, O. Grisel, M. Blondel, P. Prettenhofer, R. Weiss, V. Dubourg, J. Vanderplas, A. Passos, D. Cournapeau, M. Brucher, M. Perrot, and E. Duchesnay. Scikit-learn: Machine Learning in Python. *Journal of Machine Learning Research*, 12:2825–2830, 2011. 71

[105] C.L. Pettit and P.S. Beran. Spectral and multiresolution Wiener expansions of oscillatory stochastic processes. *Journal of Sound and Vibration*, 294(4-5):752–779, July 2006. ISSN 0022460X. doi: 10.1016/j.jsv.2005.12.043. URL http://linkinghub.elsevier.com/retrieve/pii/S0022460X06000307. 6

[106] R.L. Ramkumar and T.A. Weisshaar. Flutter of flat rectangular anisotropic plates in high mach number supersonic flow. *Journal of Sound and Vibration*, 50(4):587–597, February 1977. ISSN 0022460X. doi: 10.1016/0022-460X(77)90505-3. URL http://linkinghub.elsevier.com/retrieve/pii/0022460X77905053. 4, 23

[107] J. N Reddy. *Theory and analysis of elastic plates*. Taylor & Francis, Philadelphia, PA, 1999. ISBN 1-56032-705-7 978-1-56032-705-9. 19, 137

[108] C. Rehbach. Calcul d'écoulements tri-dimensionnels instationnaires de fluide parfait avec nappes tourbillonnaires. *La Recherche Aerospatiale, Sept.-Oct. 1977, p. 289-298*, pages 289–298, 1977. 3

[109] M. E. Riley. *Quantification of Model-Form, Predictive, and Parametric Uncertainties in Simulation-Based Design*. PhD thesis, Wright State University, 2011. xii, 6, 80, 82, 94

[110] M. E. Riley and R. V. Grandhi. Quantification of model-form and predictive uncertainty for multi-physics simulation. *Computers and Structures*, 89:1206 – 1213, 2011. 78

[111] B. A. Robinson, H. T. Y. Yang, and J. T. Batina. Aeroelastic analysis of wings

using the Euler equations with a deforming mesh. *Journal of Aircraft*, 28(11):781–788, November 1991. ISSN 0021-8669, 1533-3868. doi: 10.2514/3.46096. URL http://arc.aiaa.org/doi/10.2514/3.46096. 3

[112] R. Sandhu, M. Khalil, A. Sarkar, and D. Poirel. Bayesian model selection for nonlinear aeroelastic systems using wind-tunnel data. *Computer Methods in Applied Mechanics and Engineering*, 282:161–183, December 2014. ISSN 00457825. doi: 10.1016/j.cma.2014.06.013. URL http://linkinghub.elsevier.com/retrieve/pii/S0045782514001996. 94

[113] R. Sandhu, D. Poirel, C. Pettit, M. Khalil, and A. Sarkar. Bayesian inference of nonlinear unsteady aerodynamics from aeroelastic limit cycle oscillations. *Journal of Computational Physics*, 316:534–557, July 2016. ISSN 00219991. doi: 10.1016/j.jcp.2016.03.006. URL http://linkinghub.elsevier.com/retrieve/pii/S0021999116001571. 83, 101

[114] C. Scarth, J.E. Cooper, P.M. Weaver, and G.H.C. Silva. Uncertainty quantification of aeroelastic stability of composite plate wings using lamination parameters. *Composite Structures*, 116:84–93, September 2014. ISSN 02638223. doi: 10.1016/j.compstruct.2014.05.007. URL http://linkinghub.elsevier.com/retrieve/pii/S0263822314002074. 5, 12, 19, 24, 27, 67, 69, 70, 75, 92, 133, 153, 159

[115] D. M. Schuster, J. Vadyak, and E. Atta. Static aeroelastic analysis of fighter aircraft using a three-dimensional Navier-Stokes algorithm. *Journal of Aircraft*, 27(9):820–825, September 1990. ISSN 0021-8669, 1533-3868. doi: 10.2514/3.45942. URL http://arc.aiaa.org/doi/10.2514/3.45942. 3

[116] K. Sepahvand and S. Marburg. Non-sampling inverse stochastic numerical–experimental identification of random elastic material parameters in composite plates. *Mechanical Systems and Signal Processing*, 54-55:172–181, March 2015. ISSN 08883270. doi: 10.1016/j.ymssp.2014.09.011. URL http://linkinghub.elsevier.com/retrieve/pii/S0888327014003537. 159

[117] J. C. Slater and N. H. Frank. *Mechanics*. International series in pure and applied physics. McGraw-Hill, New York, London, 1947. 9, 137

[118] C. Soize and R. Ghanem. Physical Systems with Random Uncertainties: Chaos Representations with Arbitrary Probability Measure. *SIAM Journal on Scientific Computing*, 26(2):395–410, January 2004. ISSN 1064-8275, 1095-7197. doi: 10.1137/S1064827503424505. URL http://epubs.siam.org/doi/abs/10.1137/S1064827503424505. 5, 68

[119] S. Sriramula and M. K. Chryssanthopoulos. Quantification of uncertainty modelling in stochastic analysis of FRP composites. *Composites Part A: Applied Science and Manufacturing*, 40(11):1673–1684, November 2009. ISSN 1359835X. doi: 10.1016/j.compositesa.2009.08.020. URL http://linkinghub.elsevier.com/retrieve/pii/S1359835X09002577. 36

[120] B. K. Stanford and P. S. Beran. Analytical Sensitivity Analysis of an Unsteady

Vortex-Lattice Method for Flapping-Wing Optimization. *Journal of Aircraft*, 47 (2):647–662, March 2010. ISSN 0021-8669, 1533-3868. doi: 10.2514/1.46259. URL http://arc.aiaa.org/doi/10.2514/1.46259. 3

[121] W. Stein. A summary of Classical Lamination Theory, 2010. URL http://wstein.org/edu/2010/480b/projects/05-lamination_theory/A%20summary%20of%20Classical%20Lamination%20Theory.pdf. 18, 19, 24

[122] B. Stickan, J. Dillinger, and G. Schewe. Computational aeroelastic investigation of a transonic limit-cycle-oscillation experiment at a transport aircraft wing model. *Journal of Fluids and Structures*, 49:223–241, August 2014. ISSN 08899746. doi: 10.1016/j.jfluidstructs.2014.04.014. URL http://linkinghub.elsevier.com/retrieve/pii/S0889974614000905. 3, 4

[123] O. Stodieck, J. E. Cooper, P. M. Weaver, and P. Kealy. Improved aeroelastic tailoring using tow-steered composites. *Composite Structures*, 106:703–715, December 2013. ISSN 02638223. doi: 10.1016/j.compstruct.2013.07.023. URL http://linkinghub.elsevier.com/retrieve/pii/S0263822313003462. iii, 12, 20, 21, 27, 92, 130, 143

[124] T. Theodorsen. General Theory of Aerodynamic Instability and the Mechanism of Flutter. Technical Report 496, National Advisory Committee for Aeronautics, 1935. iii, vii, viii, ix, x, xii, xiii, 2, 3, 7, 14, 15, 79, 80, 81, 82, 84, 85, 87, 88, 89, 90, 92, 93, 98, 99, 100, 101, 102, 108, 110, 112, 113, 122, 123, 124, 125, 126, 127, 128, 129

[125] F. Tisseur and K. Meerbergen. The Quadratic Eigenvalue Problem. *SIAM Review*, 43(2):235–286, January 2001. ISSN 0036-1445, 1095-7200. doi: 10.1137/S0036144500381988. URL http://epubs.siam.org/doi/10.1137/S0036144500381988. 13

[126] S. W. Tsai and H. T. Hahn. *Introduction to composite materials*. Technomic Publ, Lancaster, Pa., 1980. ISBN 978-0-87762-288-8. 5, 24, 28

[127] M. Uhart, O. Patrouix, and Y. Aoustin. Improving accuracy in robotized fibre placement using force and visual servoing external hybrid control scheme. 44 pages, submitted to journal ROBOTICA, July 2014. URL https://hal.archives-ouvertes.fr/hal-01060750. 36, 159

[128] U.S. Department of Defense. *COMPOSITE MATERIALS HANDBOOK*. U.S. Department of Defense, June 2002. 28, 159

[129] R. Vaicaitis, E.H. Dowell, and C.S. Ventres. Nonlinear Panel Response by a Monte Carlo Approach. *AIAA Journal*, 12(5):685–691, May 1974. ISSN 0001-1452, 1533-385X. doi: 10.2514/3.49320. URL http://arc.aiaa.org/doi/abs/10.2514/3.49320. 4

[130] E. Valot and P. Vannucci. Some exact solutions for fully orthotropic laminates. *Composite Structures*, 69(2):157–166, July 2005. ISSN 02638223. doi: 10.1016/j.compstruct.2004.06.007. URL http://linkinghub.elsevier.com/retrieve/pii/S0263822304002144. 30

[131] L.M.M. van den Bos, B. Koren, and R.P. Dwight. Non-intrusive uncertainty quantification using reduced cubature rules. *Journal of Computational Physics*, 332: 418–445, March 2017. ISSN 00219991. doi: 10.1016/j.jcp.2016.12.011. URL http://linkinghub.elsevier.com/retrieve/pii/S0021999116306647. 6

[132] P. Vannucci. A Special Planar Orthotropic Material. *Journal of elasticity and the physical science of solids*, 67(2):81–96, 2002. ISSN 1573-2681. doi: 10.1023/A:1023949729395. URL http://dx.doi.org/10.1023/A:1023949729395. 25, 26

[133] P. Vannucci. Plane Anisotropy by the Polar Method*. *Meccanica*, 40(4-6):437–454, December 2005. ISSN 0025-6455, 1572-9648. doi: 10.1007/s11012-005-2132-z. URL http://link.springer.com/10.1007/s11012-005-2132-z. xi, 5, 25, 26

[134] P. Vannucci. A Note on the Elastic and Geometric Bounds for Composite Laminates. *Journal of Elasticity*, 112(2):199–215, July 2013. ISSN 0374-3535, 1573-2681. doi: 10.1007/s10659-012-9406-1. URL http://link.springer.com/10.1007/s10659-012-9406-1. 26

[135] P. Vannucci and G. Verchery. Stiffness design of laminates using the polar method. *International Journal of Solids and Structures*, 38(50-51):9281–9294, December 2001. ISSN 00207683. doi: 10.1016/S0020-7683(01)00177-9. URL http://linkinghub.elsevier.com/retrieve/pii/S0020768301001779. 30

[136] P. Vannucci and G. Verchery. A new method for generating fully isotropic laminates. *Composite Structures*, 58(1):75–82, October 2002. ISSN 02638223. doi: 10.1016/S0263-8223(02)00038-7. URL http://linkinghub.elsevier.com/retrieve/pii/S0263822302000387. 30

[137] R. Vepa. Finite state modeling of aeroelastic systems. Contractor Report 2779, National Aeronautics and Space Administration, 1977. 80, 82

[138] G. Verchery. Les Invariants des Tenseurs d'Ordre 4 du Type de l'Élasticité. In Jean-Paul Boehler, editor, *Mechanical Behavior of Anisotropic Solids / Comportment Méchanique des Solides Anisotropes*, pages 93–104, Dordrecht, 1982. Springer Netherlands. ISBN 978-94-009-6829-5 978-94-009-6827-1. URL http://www.springerlink.com/index/10.1007/978-94-009-6827-1_7. Presentation held at 115th Colloque Euromech at Villard-de-Lans, 1979. 5, 23, 24

[139] H. Wagner. Über die Entstehung des dynamischen Auftriebes von Tragflügeln. *ZAMM - Zeitschrift für Angewandte Mathematik und Mechanik*, 5(1):17–35, 1925. ISSN 00442267, 15214001. doi: 10.1002/zamm.19250050103. URL http://doi.wiley.com/10.1002/zamm.19250050103. 2, 14

[140] X. Wan and G. E. Karniadakis. Beyond Wiener–Askey Expansions: Handling Arbitrary PDFs. *Journal of Scientific Computing*, 27(1-3):455–464, June 2006. ISSN 0885-7474, 1573-7691. doi: 10.1007/s10915-005-9038-8. URL http://link.springer.com/10.1007/s10915-005-9038-8. 5

[141] Q. Wang. *Uncertainty quantification for unsteady fluid flow using adjoint-based approaches*. PhD thesis, Stanford University, December 2008. 5

[142] T. A. Weisshaar. Aeroelastic Tailoring of Forward Swept Composite Wings. *Journal of Aircraft*, 18(8):669–676, August 1981. ISSN 0021-8669, 1533-3868. doi: 10.2514/3.57542. URL http://arc.aiaa.org/doi/abs/10.2514/3.57542. 4, 23

[143] N. Wiener. The Homogeneous Chaos. *American Journal of Mathematics*, 60(4):897–936, 1938. ISSN 00029327. URL http://www.jstor.org/stable/2371268. 5

[144] J. A.S. Witteveen, S. Sarkar, and H. Bijl. Modeling physical uncertainties in dynamic stall induced fluid–structure interaction of turbine blades using arbitrary polynomial chaos. *Computers & Structures*, 85(11-14):866–878, June 2007. ISSN 00457949. doi: 10.1016/j.compstruc.2007.01.004. URL http://linkinghub.elsevier.com/retrieve/pii/S0045794907000168. 5

[145] Jeroen A. S. Witteveen and Gianluca Iaccarino. Simplex Stochastic Collocation with Random Sampling and Extrapolation for Nonhypercube Probability Spaces. *SIAM Journal on Scientific Computing*, 34(2):A814–A838, January 2012. ISSN 1064-8275, 1095-7197. doi: 10.1137/100817504. URL http://epubs.siam.org/doi/10.1137/100817504. 6

[146] J. R. Wright and J. E. Cooper. *Introduction to aircraft aeroelasticity and loads*. Wiley, Chichester, 2. ed edition, 2015. ISBN 978-1-118-48801-0 978-1-118-48801-0 978-1-118-70042-6. 1, 2, 7, 11, 12, 13, 14, 20, 79, 84, 85, 92, 102, 110, 143

[147] D. Xiu and G. E. Karniadakis. The Wiener–Askey Polynomial Chaos for Stochastic Differential Equations. *SIAM Journal on Scientific Computing*, 24(2):619–644, January 2002. ISSN 1064-8275, 1095-7197. doi: 10.1137/S1064827501387826. URL http://epubs.siam.org/doi/abs/10.1137/S1064827501387826. 5

[148] D. Xiu and G. E. Karniadakis. Modeling uncertainty in steady state diffusion problems via generalized polynomial chaos. *Computer Methods in Applied Mechanics and Engineering*, 191(43):4927–4948, September 2002. ISSN 00457825. doi: 10.1016/S0045-7825(02)00421-8. URL http://linkinghub.elsevier.com/retrieve/pii/S0045782502004218. 5

[149] D. Xiu, D. Lucor, C.-H. Su, and G. E. Karniadakis. Stochastic Modeling of Flow-Structure Interactions Using Generalized Polynomial Chaos. *Journal of Fluids Engineering*, 124(1):51, 2002. ISSN 00982202. doi: 10.1115/1.1436089. URL http://FluidsEngineering.asmedigitalcollection.asme.org/article.aspx?articleid=1429472. 5

[150] J. S. Xiu, D.and Hesthaven. High-Order Collocation Methods for Differential Equations with Random Inputs. *SIAM Journal on Scientific Computing*, 27(3):1118–1139, January 2005. ISSN 1064-8275, 1095-7197. doi: 10.1137/040615201. URL http://epubs.siam.org/doi/10.1137/040615201. 6

[151] L. Yi, Y. Jun, and K. Bin. Static aeroelastic optimisation to wing structural weight estimation of an extremely manoeuvrable UAV. *The Aeronautical Journal*, 119(1218):1033–1043, August 2015. ISSN 0001-9240, 2059-6464. doi: 10.1017/S0001924000004310. URL https://www.cambridge.org/core/product/identifier/S0001924000004310/type/journal_article. 4

Christian Thomas Nitschke **1er février 2018**

Sujet : Quantification d'incertitudes aléatoires et épistémiques dans la prédiction d'instabilités aéroélastiques

Résumé : La vitesse critique de flottement est un facteur essentiel à la conception aéronautique car elle caractérise le régime de vol au-delà duquel l'aéronef risque de subir un mécanisme de ruine. L'objectif de cette thèse est d'étudier l'impact des incertitudes d'origines aléatoires et épistémiques sur la limite de stabilité linéaire pour des configurations aéroélastiques idéalisées. Dans un premier temps, un problème de propagation directe d'incertitudes aléatoires relatives à des paramètres de fabrication d'une aile en forme de plaque en matériau composite stratifié a été considéré. La représentation du matériau par la méthode polaire lève la contrainte de grande dimensionnalité du problème stochastique initial et permet l'utilisation du Chaos Polynômial. Cependant, la corrélation introduite par cette paramétrisation nécessite une adaptation de la base polynômiale. Enfin, un algorithme d'apprentissage automatique a été employé pour traiter des discontinuités dans le comportement modal des instabilités aéroélastiques. Le second volet de la thèse concerne la quantification d'incertitudes de modélisation de caractère épistémique qui sont introduites au niveau de l'opérateur aérodynamique. Ces travaux, menés à partir d'un formalisme Bayésien, permettent non seulement d'établir des probabilités de modèle, mais aussi de calibrer les coefficients des modèles dans un contexte stochastique afin d'obtenir des prédictions robustes pour la vitesse critique. Enfin, une étude combinée des deux types d'incertitude permet d'améliorer le processus de calibration.

Mots clés : quantification d'incertitude, aéroelasticité, incertitudes aléatoires, incertitudes épistémiques, matériaux composites, calibration bayésienne, melange bayésien de modèles, chaos polynômial

Subject : Quantification of aleatory and epistemic uncertainties in the prediction of aeroelastic instabilities

Abstract: The critical flutter velocity is an essential factor in aeronautic design because it caracterises the flight envelope outside which the aircraft risks to be destroyed. The goal of this thesis is the study of the impact of uncertainties of aleatory and epistemic origin on the linear stability limit of idealised aeroelastic configurations. First, a direct propagation problem of aleatory uncertainties related to manufacturing parameters of a rectangular plate wing made of a laminated composite material was considered. The representation of the material through the polar method alleviates the constraint of the high number of dimensions of the initial stochastic problem, which allows the use of polynomial chaos. However, the correlation which is introduced by this parametrisation requires an adaption of the polynomial basis. Finally, a machine learning algorithm is employed for the treatment of discontinuities in the modal behaviour of the aeroelastic instabilities. The second part of the thesis is about the quantification of modelling uncertainties of epistemic nature which are introduced in the aerodynamic operator. This work, which is conducted based on a Bayesian formalism, allows not only to establish model probabilities, but also to calibrate the model coefficients in a stochastic context in order to obtain robust predictions for the critical velocity. Finally, a combined study of the two types of uncertainty allows to improve the calibration process.

Keywords : Uncertainty Quantification, Aeroelasticity, Aleatory Uncertainty, Epistemic Uncertainty, Composite Materials, Bayesian Calibration, Bayesian Model Averaging, Polynomial Chaos